Progress in Energy

TOPICAL REVIEW

Pushing the boundaries of lithium battery research with atomistic modelling on different scales

Lucy M Morgan[1,2,*], Michael P Mercer[2,3,*], Arihant Bhandari[2,4], Chao Peng[2,5], Mazharul M Islam[1,2], Hui Yang[2,6], Julian Holland[2,4], Samuel W Coles[1,2], Ryan Sharpe[1], Aron Walsh[2,6,7], Benjamin J Morgan[1,2], Denis Kramer[2,5,8], M Saiful Islam[1,2,11], Harry E Hoster[2,3,10], Jacqueline Sophie Edge[2,9,**] and Chris-Kriton Skylaris[2,4,**]

[1] Department of Chemistry, University of Bath, Claverton Down, Bath BA2 7AY, United Kingdom
[2] The Faraday Institution, Quad One, Harwell Campus, Didcot OX11 0RA, United Kingdom
[3] Department of Chemistry, Lancaster University, Bailrigg, Lancaster LA1 4YB, United Kingdom
[4] School of Chemistry, University of Southampton, Southampton SO17 1BJ, United Kingdom
[5] School of Engineering, University of Southampton, Southampton SO17 1BJ, United Kingdom
[6] Department of Materials, Imperial College London, London SW7 2AZ, United Kingdom
[7] Department of Materials Science and Engineering, Yonsei University, Seoul 03722, Republic of Korea
[8] Faculty of Mechanical Engineering, Helmut-Schmidt University, Holstenhofweg 85 22043 Hamburg, Germany
[9] Department of Mechanical Engineering, Imperial College London, London SW7 2AZ, United Kingdom
[10] Department of Mechanical and Process Engineering, University Duisburg-Essen, Lotharstraße 1, Duisburg 47057, Germany
[11] Department of Materials, University of Oxford, Parks Road, Oxford OX1 3PH, United Kingdom
[*] The two authors contributed equally to this review.
[**] Authors to whom any correspondence should be addressed.

E-mail: j.edge@imperial.ac.uk **and** c.skylaris@soton.ac.uk

Keywords: lithium ion batteries, Li-ion, liquid electrolytes, solid electrolytes, solid electrolyte interphase, cathode electrolyte interphase, atomistic modelling

OPEN ACCESS

RECEIVED
11 June 2021

REVISED
15 October 2021

ACCEPTED FOR PUBLICATION
10 November 2021

PUBLISHED
7 December 2021

Abstract

Computational modelling is a vital tool in the research of batteries and their component materials. Atomistic models are key to building truly physics-based models of batteries and form the foundation of the multiscale modelling chain, leading to more robust and predictive models. These models can be applied to fundamental research questions with high predictive accuracy. For example, they can be used to predict new behaviour not currently accessible by experiment, for reasons of cost, safety, or throughput. Atomistic models are useful for quantifying and evaluating trends in experimental data, explaining structure-property relationships, and informing materials design strategies and libraries. In this review, we showcase the most prominent atomistic modelling methods and their application to electrode materials, liquid and solid electrolyte materials, and their interfaces, highlighting the diverse range of battery properties that can be investigated. Furthermore, we link atomistic modelling to experimental data and higher scale models such as continuum and control models. We also provide a critical discussion on the outlook of these materials and the main challenges for future battery research.

Contents

1. Introduction

Lithium-ion (Li-ion) batteries (LiBs) were first commercialised by Sony in 1991 [1]. They are ubiquitous in portable electronic devices, are emerging in hybrid and all-electric vehicles (EVs) [2], and are starting to play a role in large scale stationary storage [3]. Despite over 30 years of commercialisation and longer for development, not all factors dictating their capacity, performance, safety, and longevity are completely understood. The complexity of battery systems makes it time consuming and impractical to directly measure all of their physical attributes. The grand challenge is to construct a multiscale model, incorporating inputs across length- and time scales that can not only describe, but also predict, changes in behaviour.

To build a truly predictive modelling framework, a physical underpinning to battery models is required, incorporating physically correct descriptions of thermodynamic and kinetic battery behaviour. With sufficient accuracy built in, these models can provide insights on difficult-to-measure internal states, such as degree of Li intercalation and local electrolyte and ionic concentrations, as determined by the nanostructure of the materials used. By contrast, empirical models, which fit a curve to experimental data, are widely used in battery research, but have only a limited physical basis or, in some cases, no physical basis at all. For example, equivalent circuit models, which are widely used in industry, cannot be relied upon to predict battery behaviour over several charge–discharge cycles.

Physics-based continuum models attempt to describe the behaviour of whole cells, for example the widely used Doyle–Fuller–Newman (DFN) model [4–8]. These models need to use drastic simplifications to enable them to run in real time, but their accuracy can be greatly improved by adopting parameters measured using more detailed, microscopic simulations. Atomistic models are key to building truly physics-based models and form the foundation of the multiscale modelling (MSM) chain, leading to more robust and predictive models.

Atomistic models can also be applied to fundamental research questions with high predictive accuracy. For example, they can be used to predict new behaviour not currently accessible by experiment, for reasons of cost, safety, or throughput. They can be used to optimise experimental design and use resources more efficiently, determining whether particular experiments are even worth performing and also provide unique insights into the behaviour of materials that may not even be accessible, or are impractical to obtain, by experimental probes. Atomistic models are useful for quantifying and evaluating trends in experimental data, explaining structure-property relationships and informing materials design strategies and libraries.

With the above in mind, we target this review to the following audiences. Non-atomistic battery modellers, such as continuum and control modellers, who would benefit from an easily accessible summary of atomistic methods and how they connect with longer length scale models. As atomistic models comprise a range of methods, it is also beneficial to summarise how these interlink, since it is possible to be an expert in one area, whilst being unfamiliar with another. For this reason, it is instructive to summarise these different methods in one place, so that non-specialists can understand these links. Recent developments in these techniques, such as linear scaling density functional theory (DFT), require summarising standard DFT techniques. Likewise, longer length scale atomistic techniques can be parameterised using *ab initio* data. While DFT and other atomistic methods are widely known and utilised individually, their other applications and connections to one another are often not as thoroughly described, nor do these descriptions account for more recent developments.

This review also aims to reach those working in the battery area, such as experimentalists, who may not be experts in atomistic modelling and want to understand how atomistic models can help to understand experimental behaviour. Likewise, we show examples of behaviour currently out of reach with experiments. Similarly, this review is of benefit to junior researchers new to the battery area, and those who are already familiar with atomistic methods but are new to lithium batteries. With these audiences in mind, we have summarised applications of atomistic methods in LiBs and all solid-state batteries (ASSBs), which represent the most technologically advanced rechargeable battery systems currently available.

The family of atomistic models itself represents a range of different length- and time scales, from the level of electronic structure calculations through conventional and linear-scaling DFT, to *ab initio* molecular dynamics (MD) and on to longer length scale models, such as classical MD, Monte Carlo (MC), and kinetic Monte Carlo (kMC) calculations, which are parameterised by force field potentials or *ab initio* data. These techniques, along with recent method developments and battery-specific observable properties, are summarised in the methods section of this review, section 2.1. Specific applications to anodes, liquid and solid electrolytes, and cathodes are broken down in the following sections. Links between different methodologies are emphasised and this review may thus be of particular interest to those looking, for example, to link DFT calculations to MC calculations, or apply linear-scaling DFT to MD, bridging possible gaps in nomenclature at different length scales. Atomistic models linking to *ab initio* calculations are summarised by Van der Ven *et al* [9]; also noteworthy in this area is a review by Shi *et al* [10], and an older

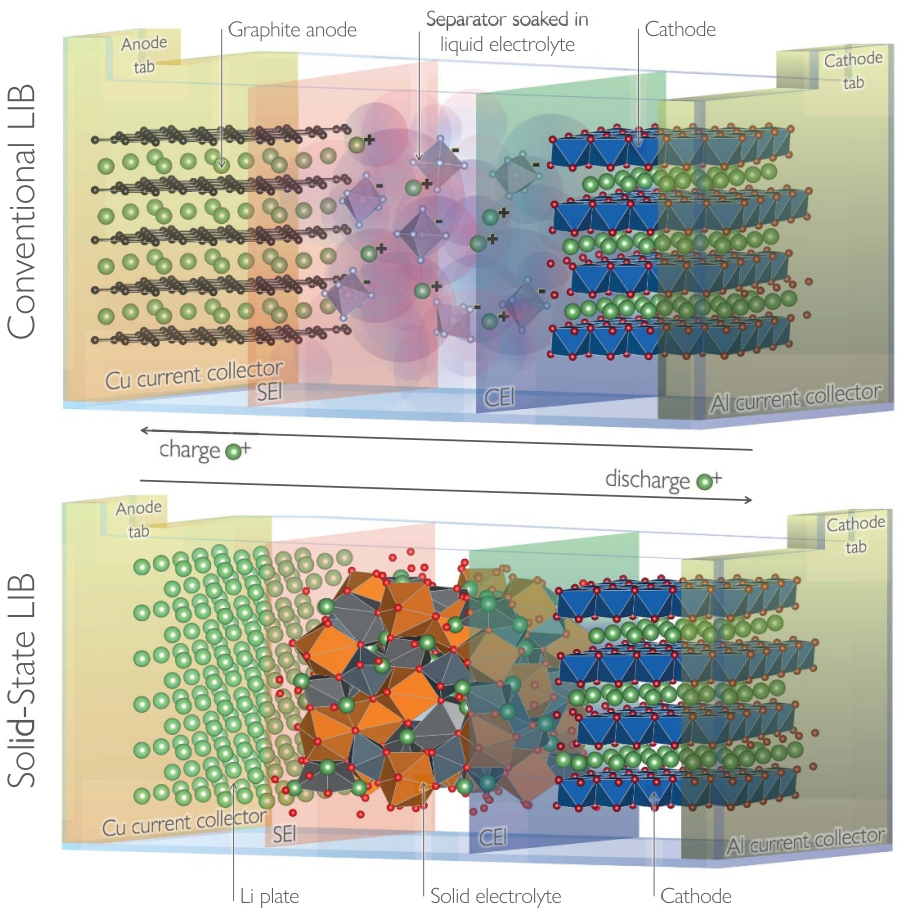

Figure 1. A schematic of a single cell of a conventional, liquid-based LiB and a solid-state LiB. The conventional LiB comprises an anode composed of a Cu current collector and an active anode material (graphite), a separator soaked in an organic electrolyte, and a cathode composed of a Al current collector and an active cathode material, for example, $LiCo_2$, as shown here. The solid-state LiB comprises a similar cathode, a solid electrolyte, and an anode composed of a Li-ion plate and Cu current collector. The anode-electrolyte interphase (SEI) and cathode-electrolyte interphase (CEI) for both LiBs are represented as pink and blue transparent layers, respectively. The tabs are shown protruding from the top of the current collectors. Both LiB cells show all components as fully lithiated, with directional Li^+ movement during (dis) charge indicated with arrows.

review by Franco [11]. A recent review of method development in the area of hybrid quantum-continuum solvation models is presented by Herbert [12].

The review covers mechanisms in both the conventional liquid electrolyte based and solid-state based LiB, as shown schematically in figure 1. In a single cell of a conventional LiB, as shown here, the anode, or negative electrode, comprises a copper current collector and the primary active material is graphite in the vast majority of commercial LiBs. Increasingly, small amounts of silicon are being added to boost the gravimetric capacity. The electrode material also comprises a binder, such as polyvinylidene fluoride (PVDF), and sometimes a small fraction of conductive carbon is added to boost conductivity. The two electrodes are divided by a separator soaked in an organic electrolyte, which is usually a mixture of carbonates with dissolved $LiPF_6$ salt. The cathode, or the positive electrode, has an aluminium current collector. Various different types of cathode material are utilised in commercial LiBs, with the example shown here being the classic 'rocking-chair' battery with a $LiCO_2$ cathode [13]. The low conductivity of these transition metal (TM) oxides requires addition of conductive carbon and, as with the anode material, the active cathode material is held together with a binder, such as PVDF. When the cell is assembled, the cathode starts fully lithiated and the anode is completely delithiated. On the first cell charge cycle (also known as the formation cycle) lithium is removed from the cathode and the anode becomes filled with lithium while the solid electrolyte interphase (SEI) and cathode electrolyte interphase (CEI) are formed. While figure 1 shows both electrodes in a fully lithiated state, Li is transferred between the electrodes reversibly during (dis)charging, therefore allowing this system to be rechargeable.

Although not yet commercialised, ASSBs are a promising future alternative to conventional liquid electrolyte LiBs. Their anode, or negative electrode, comprises a copper current collector and either a a metallic lithium plate (Li-metal), as shown in figure 1, or less commonly a graphite-based material (Li-ion).

As there is no liquid, there is no longer a need for separators, with the two electrodes being separated by the solid electrolyte material, shown here with $Li_7La_3Zr_2O_2$ (LLZO). The cathode, or positive electrode, has an aluminium current collector and, as with the conventional LiB, can accommodate various cathode materials, such as $LiCo_2$. The interfacial regions between the electrodes and the solid electrolyte are known as the solid–solid interphase, or anode/cathode-solid interphase. Figure 1 shows both electrodes in a fully lithiated state; however, the Li is transferred between the electrodes reversibly, as in conventional LiBs.

The anodes section, section 3, heavily focuses on graphite, which is still the predominant anode material in Li-ion cells. The section describes atomistic modelling of bulk graphite, graphite edges where initial Li-ion insertion occurs, and the SEI. The bulk modelling discussion includes a direct comparison between experimental and theoretical thermodynamic parameters, such as the open circuit voltage (OCV) and entropy, which will also be of interest to battery control modellers. Kinetic predictions are made and linked to DFT predictions of the influence of graphite edge morphology on surface states, which may be of interest to those working on battery material development and discovery. Recent work applying linear scaling DFT to complex interfaces will be of interest to those at the forefront of DFT method development, focusing on the boundary between atomistic and continuum modelling. Lastly, recent developments in silicides to boost anode gravimetric capacity, along with their associated challenges, are summarised in the outlook. Recent reviews in this area include Asenbauer *et al* [14], summarising aspects of lithiation/delithiation mechanisms and morphological aspects in graphite and silicon oxide composites, and Zhang *et al* [15], similar in scope but providing a more *ab initio* focus. Here, our review here covers graphite structure and lithiation/delithiation mechanisms, including surfaces and interfaces, which have tended to be neglected, although aspects of modelling the SEI have been reviewed by Wang *et al* [16].

The liquid electrolyte section, section 4.2, has a strong focus on the development of atomistic models, both *ab initio* and force field-based. This includes a pivotal discussion on the atomic interactions between the components and method development to study electrolytes via classical MD simulations. This will be of particular interest to those at the forefront of classical MD method development. Liquid electrolytes are known to be limited by narrow electrochemical windows, solvent toxicity, and material flammability/safety concerns. The latter parts of this section describe the atomistic modelling of the bulk structure and landscaping, Li-ion diffusion, solvation energies, and activity coefficients of liquid electrolytes, and the interfacial nanostructure relating to the interface with a solid electrode. These topics cover the major aspects for improving liquid electrolytes for use in a battery and research towards circumventing critical safety [17, 18] and energy density [19] limitations. The challenges and potential avenues for solving these issues are summarised in the outlook, including recent developments to resolve these within the liquid electrolyte family and alternative materials. Recent reviews in this area include Galiński *et al* [20], summarising the field of ionic liquids, Wang *et al* [21] reviewing the recent progress in water in salts electrolytes, and Logan and Dahn [22] giving some recent developments in conventional electrolytes. Here, our review covers the continued development of interatomic potentials for liquid electrolytes and a description of the solid electrode-liquid electrolyte interface from the perspective of the liquid, which is not the conventional frame of reference.

Solid state electrolytes (SSEs) are becoming an increasingly popular avenue of research, motivated by the rise of the EV [23]. They have been proposed as an alternative to liquid electrolytes to resolve safety issues pertaining to the flammable organic liquid electrolytes that are currently used [17, 18], and also as a route to increased energy density [19]. In the solid electrolyte section, section 4.3, we review a selection of the promising candidate materials currently being investigated. Each material discussed has a different focus, highlighting a range of properties applicable to different SSE materials. In this section, we focus on four material families, grouping them into sulfide and oxide based SSEs. Sulfide based SSEs typically have a high Li-ion conductivity and poor electrochemical stability against Li metal (the anode typically used in combination with SSEs) [24, 25]. $Li_{10}GeP_2S_{12}$ (LGPS) is reviewed, with a focus on how atomistic methods reveal the isotropic ion pathways, while Li_6PS_5X based Li-argyrodites are focused towards the relationship between ionic conductivity and anion substitution, as well as atomistic predictions of occupied Li sites. Oxides typically have a higher electrochemical stability but still suffer from dendrite formation, amongst other issues [24]. LLZO is also reviewed, with a focus on how multiple atomistic methods have been applied to probe dendrite formation and ionic transport in the material. State-of-the-art models of interfaces in oxide nanocomposites are reviewed. Lastly, the challenges of the SEI are discussed and an outlook to future modelling of SSEs is given. Related reviews in the area include Zhang *et al* [26], summarising the future directions of ASSBs, and Gurung *et al* [27] highlighting the advances and challenges in SSEs and ASSBs. Xiao *et al* [28] and others [29, 30] provide a more specific review of the SEI. Ceder *et al* [31] outlines the principles that should be employed when modelling SSEs. Here, our review discusses a broad range of SSE properties, following the notion that these properties are applicable to range of materials.

The cathodes section, section 5, covers a range of different cathode materials used in a variety of Li-ion cells. This section describes atomistic modelling in the bulk, at the surfaces, and the CEI. In discussing bulk modelling, a comparison of the different cathode crystal structures, micro-structuring, and available diffusion pathways within the material are covered, as well as important properties, including redox and electronic properties, TM ordering, and vibrational and thermal properties. Use of electronic structure methods modelling techniques has been essential for investigating crystalline structure, so will be of great interest to those who utilise DFT in their research. Surface structures and morphologies of cathode particles can be difficult to determine using experimental methods alone, which is where *ab initio* and potentials-based MD can provide vital insight. As with the SEI, linear-scaling DFT has recently been applied to CEI, where discussions on CEI will be of interest to those doing state-of-the-art DFT method development. Related reviews in the area include Ma [32], summarising modelling Li-ion battery cathode materials, Yan *et al* [33] focusing on DFT calculations of cathode materials, and Wang *et al* [34] discussing closing the gap between theoretical and practical capacities in layered oxide cathode materials. Our review includes a discussion on the CEI, which has recently been reviewed by Maleki Kheimeh Sari and Li [35]. Here, our review covers thermal, electronic, dynamic, and structural properties for a range of prominent cathode materials in terms of both electronic structure methods and potential-based modelling, which have tended to be more isolated in other reviews.

Finally, we provide an outlook on the key remaining challenges for atomistic modelling of LiBs and promising future directions for resolving them.

2. Methods

2.1. Method overview

2.1.1. Density functional theory

DFT is amongst the most accurate methods for atomistic simulations of materials, as it is a quantum mechanical method. This means that it is able to simulate the electrons in materials and how they result in all the observable processes and properties of a material. As electrons are microscopic particles, to simulate their properties we need to use the theory of quantum mechanics. However, the computational cost of calculations with this theory is very high, as all the observable properties are obtained from the wave function: a highly complicated function of many variables (proportional to the number of particles we are simulating) and, for exact solution, the computational effort scales exponentially with the number of particles. Approximate wave function based theories with more favourable computational scaling (such as $\sim N_e^5$ or $\sim N_e^7$, where N_e is the number of electrons in the calculation) have been developed, but the computational effort is still so high that they cannot be applied to molecules with more than a few atoms.

DFT is a reformulation of quantum electronic structure theory, where the central quantity is no longer the wave function, but instead the electronic density, $\rho(\mathbf{r})$, which is a comparatively simpler function of only one position variable, $\mathbf{r}$. As a result, DFT has lower computational scaling, allowing simulations of much larger systems (up to a few hundred atoms on supercomputers). Another advantage of DFT is that it is formally an exact theory. Due to these two significant advantages, DFT is today the method of choice for most simulations.

DFT was originally developed by Hohenberg and Kohn [36, 37] and reformulated by Kohn and Sham [38] into the mathematical description we use today, often called KS-DFT, where the energy of a material is expressed as:

$$E[\rho] = T_{KS}[\rho] + E_{\text{ext}}[\rho] + E_H[\rho] + E_{xc}[\rho]. \tag{1}$$

Here all the terms are expressed as functionals of the density and $T_{KS}[\rho]$ is the kinetic energy of the electrons, $E_{\text{ext}}[\rho]$ is the energy of attraction of the electrons to nuclei (also called external potential energy), $E_H[\rho]$ is the classical (Coulomb) electrostatic energy of the electronic density charge distribution (also called Hartree energy), and E_{xc} describes the purely quantum effects of exchange and correlation.

DFT calculations are performed in an iterative fashion, with electron density expressed as a sum of one-electron wave functions, $\{\psi_i\}$, called molecular orbitals (MOs):

$$\rho(\mathbf{r}) = \sum_{i=1}^{N_e} |\psi_i(\mathbf{r})| \tag{2}$$

and these MOs are obtained by solving the Kohn–Sham eigenvalue equation:

$$\left[-\frac{1}{2}\nabla^2 + v_{\text{ext}}(\mathbf{r}) + v_{\text{H}}[\rho](\mathbf{r}) + v_{\text{xc}}[\rho](\mathbf{r})\right] = \varepsilon_i\psi_i(\mathbf{r}). \tag{3}$$

As we can see from equation (3), the Hartree, $v_{\text{H}}[\rho]$, and exchange-correlation, $v_{\text{xc}}[\rho]$, potentials are functionals of the density, thus ultimately functionals of the MOs, which provide the solutions of the equation. This equation cannot be solved directly, but must follow an iterative procedure called the *self-consistent field (SCF)* process. The simplest SCF method is to guess a set of $\{\psi_i\}$ and use these to build and solve (equation (3)), obtaining a new set of $\{\psi_i\}$ and repeating this process until the $\{\psi_i\}$ and the energy (equation (1)) no longer change.

KS-DFT is formally an exact theory, but it does not provide an explicit expression for the exchange-correlation energy, $E_{\text{xc}}[\rho]$. The exact exchange-correlation functional is unknown or, more precisely, unknowable. Thus a very active area of DFT development is to construct approximations of increasing accuracy for $E_{\text{xc}}[\rho]$. The simplest approximation is the local density approximation (LDA), where $E_{xc}[\rho(\mathbf{r})]$ is expressed as:

$$E_{xc}^{LDA}[\rho(\mathbf{r})] = \int \rho(\mathbf{r})\epsilon_{\text{xc}}[\rho(\mathbf{r})]\, d\mathbf{r}. \tag{4}$$

The value of ϵ_{xc} at some position, $\mathbf{r}$, is computed exclusively from the value of ρ at that position. In practice, $\epsilon_{\text{xc}}[\rho(\mathbf{r})]$ describes the exchange and correlation energy per particle of a uniform electron gas of density ρ [39].

In general, the electron density in a molecular system is not spatially uniform, even at small volumes of space, limiting the applicability of LDA. More accurate functionals are obtained by the inclusion of a density gradient correction, known as the generalised gradient approximation (GGA), or semi-local functionals. In the GGA, the functionals depend on both the density and the gradient of the density, i.e. $v_{xc}^{\text{GGA}} = f(\rho, \nabla\rho)$. Popular examples of GGA functionals are Perdew-Wang GGA (both exchange and correlation) [40], Perdew–Burke–Ernzerhof GGA [41], and Becke–Lee–Yang–Parr [42, 43]. Functionals including contributions from the second derivative of the density are called *meta*-GGA functionals [44].

Standard DFT methods fail to describe dispersion effects that are of a non-local electron correlation nature. Consequently, DFT methods are often inaccurate for the investigation of molecular crystals, adsorption on surfaces, and other systems in which dispersion forces due to van der Waals (vdW) gaps between layers play a significant role. Several versions of dispersion corrected DFT (DFT-D) approaches are available, e.g. DFT-D2 [45], DFT-D3 [46], DFT-D4 [47], DFT-D3BJ [48, 49], etc.

GGA functionals, however, still have problems with self interaction. The hybrid functionals usually offer some improvement over the corresponding pure DFT functionals. Of all modern functionals, the B3LYP method is the most popular to date [43, 50]. It works well both for structural investigations and for the computation of electronic properties [51]. Another popular hybrid functional, PW1PW [52, 53], was parameterised to reproduce structural, energetic, and electronic properties of solids. A more recent and popular hybrid functional is HSE06, where the correlation part is defined by a PBE functional and a range-separation approach is used for the exchange part [54].

The applicability of the hybrid functionals depends mainly on the type, size, and complexity of the studied systems, as these functionals incur a huge computational cost. An alternative approach is the DFT+U method, where the effects of strong intra-atomic electronic correlations are modelled by adding an on-site Coulomb repulsion, U, and site exchange term, J, to the DFT Hamiltonian [55–57]. Parameters U and J can be extracted from *ab initio* calculations, but are usually obtained semi-empirically. Inspired by the Hubbard model, the DFT+U method is formulated to improve the ground state description of strongly correlated systems. The Hubbard Hamiltonian describes the strongly correlated electronic states (d and f orbitals), while the rest of the valence electrons are treated by normal DFT approximations.

2.1.2. Linear-scaling DFT

In conventional DFT, solving the Kohn–Sham eigenvalue equations, equation (3), subject to the required orthonormality constraint, results in a computational cost scaling with the third power (it is an $\mathcal{O}(N^3)$ procedure) with the number of atoms, N. This is demonstrated in the example of figure 2, showing the computation time as a function of the number of atoms for slabs of graphite of increasing size. This unfavourable scaling is the reason why conventional KS-DFT is practically unfeasible beyond several hundred atoms. However, there are many grand challenges in materials research, where, due to their inherent

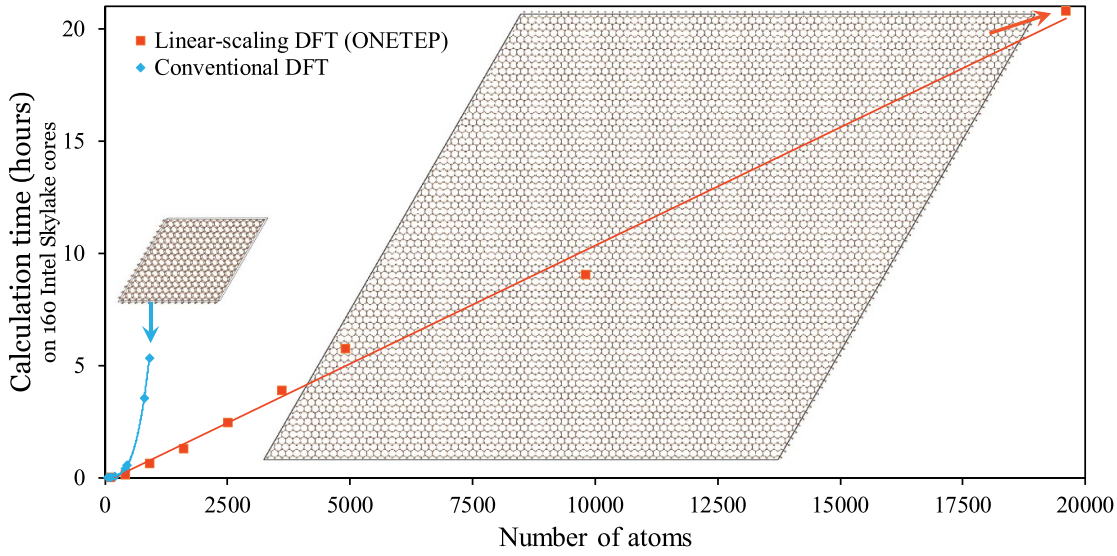

Figure 2. Comparison of the computational time with the number of atoms for slabs of graphite of increasing size using the ONETEP linear-scaling DFT code versus a conventional plane wave DFT code. The computations were performed on the Iridis 5 supercomputer at the University of Southampton on 40 MPI processes, with 4 OpenMP threads each (160 cores in total). Reprinted from [66], with the permission of AIP Publishing.

complexity, building realistic models requires thousands of atoms, such as simulations of defects, complex structures of the SEI, and metallic and semiconductor nanoparticles used in catalysis and battery electrodes, among others. This need for large-scale DFT calculations has motivated the development of new theoretical methods which can scale linearly with system size [58]. In these linear-scaling methods, conventional KS-DFT is reformulated in terms of the one-particle density matrix, γ:

$$\gamma(\mathbf{r},\mathbf{r}') = \sum_i f_i \psi_i(\mathbf{r})\,\psi_i^*(\mathbf{r}')\,, \tag{5}$$

allowing us to exploit the principle of 'nearsightedness of electronic matter' [59], because the density matrix decays exponentially with the distance, $|\mathbf{r}-\mathbf{r}'|$ [59], while the MOs, $\{\psi_i\}$, are, in general, fully delocalised over the entire electronic system (molecule, nanoparticle, slab, etc) and do not decay. The exponentially-decaying tail of the density matrix can be truncated to develop methods with reduced or linear-scaling computational cost. As the system size (number of atoms) is increased, it reaches a point where the remaining amount of information increases linearly with the size of the system. This can be implemented more efficiently with non-orthogonal, localised orbitals, $\{\phi_\alpha\}$ [60, 61]. In this representation, the density matrix can be written as:

$$\gamma(\mathbf{r},\mathbf{r}') = \phi_\alpha(\mathbf{r})\,K^{\alpha\beta}\,\phi_\beta^*(\mathbf{r}')\,. \tag{6}$$

Here, the density kernel matrix, **K**, is a generalisation of the MO occupancies, $\{f_i\}$, of equation (5), while implicit summation (Einstein convention) is assumed for repeated Greek indices.

The development of linear-scaling methods has proven to be a very challenging research topic, as the goal of developing methods that accommodate the conflicting requirements of orbital localisation with high accuracy is extremely difficult to achieve. Recent developments towards this goal have made this possible by using a dual resolution approach, where both $\{\phi_\alpha\}$ and **K** are optimised self-consistently during the calculation, while subject to localisation constraints [62–64]. The $\mathcal{O}(N)$ Electronic Total Energy Package (ONETEP) [65], has the unique capability of achieving linear-scaling computational cost, while maintaining the near-complete basis set accuracy of conventional DFT. The computational efficiency of this code is demonstrated on the graphite example in figure 2, where the linear-scaling behaviour can be clearly seen. DFT calculations with tens of thousands of atoms can be performed with ONETEP, opening avenues for simulating realistic models of materials and interfaces in LiBs with DFT-scale accuracy. ONETEP is being actively developed and offers a large and diverse range of capabilities, including: different boundary conditions, various exchange–correlation functionals, finite electronic temperature methods for metallic systems, methods for strongly correlated systems, MD, vibrational calculations, time-dependent DFT,

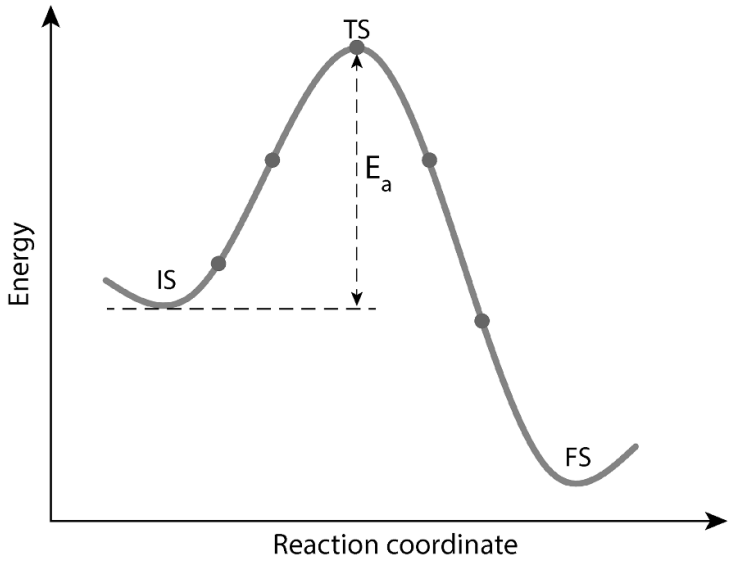

Figure 3. Energy profile of NEB calculation. The IS, TS, and FS are the initial state, transition state and final state, respectively. E_a denotes the activation barrier along the reaction path. The grey circles are the 'images' in the NEB calculation.

electronic transport, core loss spectroscopy, implicit solvation, density of states calculations, and distributed multipole analysis [65]. Recent focus in ONETEP is on developing specific electrochemistry tools for battery simulations, aiming to develop the first atomistic simulation platform (in particular, the first linear-scaling DFT platform) for electrochemistry. Some of these developments are described in this review, in section 2.2.1.

2.1.3. Nudged elastic band

Nudged elastic band (NEB) theory is a useful method based on transition state theory, seeking the minimum energy path and the saddle point (or transition state) between two minima (initial and final states) [67–69]. The energy difference between the lowest energy state and the saddle point is defined as the activation barrier (E_a), figure 3 [69].

The NEB approach initially guesses a number of configurations of several possible intermediate 'images' that may occur along the reaction coordinate or diffusion path. This set of images can be created by linear interpolation between the initial and final states. The NEB algorithm further conducts constrained optimisation and converges those images along the minimum energy path. Furthermore, fictional spring forces are added between adjacent images to maintain the spacing and the continuity of the reaction or diffusion path. The NEB approach is widely applied in the studies of chemical transformations, such as catalytic reactions or ion diffusion in solid materials. The determined chemical reaction energy barriers can then be used in further, larger time- and length-scale models, such as microkinetic models [70, 71].

2.1.4. Cluster expansion

The cluster expansion method enables a statistical approach to sample configurational phase space at finite temperature [72–74]. This method aims to capture the energetics of mixing two or more atoms on a given set of lattice sites, typically with an accuracy close to DFT calculations. The approach borrows ideas from the Ising model [75], where each lattice site is assigned as a spin variable to simulate the magnetic properties, but maps site occupancy onto spin variables instead [76]. For example, for a binary alloy system with atom types A and B, the occupation of each site can be described by a spin-like variable, i.e. $\sigma_i = +1$, if the site is occupied by atom A, and $\sigma_i = -1$ if the site is occupied by atom B, as shown in figure 4. A configuration can then be written as $\sigma = (\sigma_1, \ldots, \sigma_n)$. Accordingly, the energy of each configuration can be expressed as: $E \equiv E(\sigma_1, \ldots, \sigma_n)$.

To compute E(σ), all relevant interactions should be sampled. A set of interactions should be considered, such as nearest neighbouring pair interactions, second nearest neighbouring pair interactions, triplet interactions, quadruplet interactions, and so on, up to many body interactions (figure 4). Further, all symmetry-equivalent interactions (including translations) can be grouped into 'clusters (α)'. Including all relevant cluster interactions, the energy can be expressed as:

$$E_\alpha = \sum_\alpha m_\alpha J_\alpha \bar{\Pi}_\alpha(\sigma), \tag{7}$$

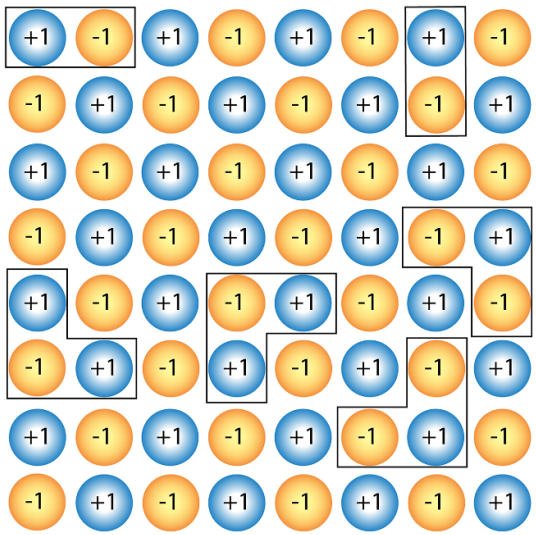

Figure 4. A 2D (8 × 8) structure including several clusters. +1 and −1 are the lattice sites assigned with different spins.

where m_α is the multiplicity of the cluster, α, and can be obtained by considering all the point symmetries in the lattice cell. J_α is the effective cluster interaction (ECI) associated with a cluster, α. $\bar{\Pi}_\alpha(\sigma)$ is the correlation matrix of normalised spin-products for a particular cluster of the entire lattice, obtained via:

$$\bar{\Pi}_\alpha(\sigma) = \frac{1}{Nm_\alpha}\sum_{i\in\alpha}\Pi\sigma_i, \tag{8}$$

where N is the number of parent lattice cells required to generate the configuration σ. Theoretically, the expansion should include all possible clusters. However, that is not practical and one of the key features of cluster expansions is that they usually converge quickly after including a handful of terms [77]. Consequently, only a relatively small number of DFT calculations are therefore required to parameterise a handful of ECIs. For example, if we calculate the energy of an A-B alloy system and consider only four clusters and four configurations, the energy of each configuration can be expressed as:

$$\begin{pmatrix} E_1 \\ E_2 \\ E_3 \\ E_4 \end{pmatrix} = \begin{pmatrix} \Pi_1(1) & \Pi_2(1) & \Pi_3(1) & \Pi_4(1) \\ \Pi_1(2) & \Pi_2(2) & \Pi_3(2) & \Pi_4(2) \\ \Pi_1(3) & \Pi_2(3) & \Pi_3(3) & \Pi_4(3) \\ \Pi_1(4) & \Pi_2(4) & \Pi_3(4) & \Pi_4(4) \end{pmatrix} \begin{pmatrix} J_1 \\ J_2 \\ J_3 \\ J_4 \end{pmatrix}. \tag{9}$$

In principle, the effective interaction coefficients, J_α, can be obtained via inverting the matrix above and using the energies from DFT calculations, but this is not commonly done. Rather, a larger training set is generated from DFT and the ECIs are fitted in a least-square sense. The set of considered clusters is usually obtained by cross-validation: the set of clusters with the highest accuracy for predicting configurations achieves the highest cross-validation score and is selected.

Various codes exist to link the results of DFT calculations with cluster expansion codes, such as the alloy theoretic automated toolkit (AT-AT) [78–80], the clusters approach to statistical mechanics [81], *ab initio* random structure search) [82], Integrated Cluster Expansion Toolkit [83], and CLuster Expansion in Atomic Simulation Environment [84]. These codes usually provide a means to fit ECIs and include MC features to sample phase spaces. They also allow the generation of DFT calculations to expand the training set. MC methods are explained in the next section.

2.1.5. Lattice gas and MC

Lattice gas methods simulate the system state as an array of points [85]. This data structure is ideally suited to represent periodic, crystalline systems, but extensions to more complex systems are possible. In atomistic simulations, the array values denote the occupation of particular sites by certain types of atoms. The evolution of the system state can then be computed in terms of changes in those array values, i.e. site occupancies [85].

In the Ising Hamiltonian described in the previous section, each site can be in either a +1 or −1 state [86]. This data structure is suited to studying the thermodynamics and kinetics of binary alloys [87, 88].

Simplistically, a LiB intercalation material can be represented as a binary alloy of lithium atoms and vacancies within an Ising model [76, 89, 90].

The interaction Hamiltonian describes how the energy of the system depends on the configuration of the lattice. For a simple interaction model, it is possible to perform a direct evaluation of the partition function, Z, via:

$$Z = \sum_i e^{-\beta E_i}, \tag{10}$$

where E_i is the energy of state i, and $\beta = 1/kT$ (k = Boltzmann constant; T = absolute temperature). Once Z is known, the rest of the thermodynamic properties of the system can easily be determined [91–93]. In a two-level system [92], the number of states in equation (10) can be reduced to scale linearly with the number of particles in the system, making the summation computationally tractable [91–93]. Measurable quantities, like the OCV, voltammograms, and partial molar enthalpy and entropy can be simulated [91–93]. This approach has been applied to lithium intercalation in lithium manganese oxide (LMO) [93] and graphite [91, 92], as demonstrated in section 3.2.3. The interactions between the particles can be approximated by taking the average occupation in two levels, allowing ordered structures like graphite stages to be modelled. This approach represents a step in complexity beyond the assumption of simple solid solution behaviour, which is still commonly applied in continuum level models [94]. The approach is closely related to the phase field models applied by Bazant to systems such as lithium iron phosphate and graphite [95–97].

For a more general and realistic interaction Hamiltonian, the number of energy states precludes direct evaluation of equation (10). In that case, MC methods are useful for calculating thermodynamic properties. This is true for the Ising model defined in section 2.1.4, when represented in more than one dimension, as is the case in most practical systems. It is then more practical to obtain the thermodynamic properties by the Metropolis algorithm [98]. Following the Markov chain of states, the limiting distribution equals the probability distribution of the thermodynamic ensemble. Properties of interest can be obtained from taking the average of sampled configurations once the distribution has reached equilibrium [88].

Inputting a chemical potential, μ, in the grand canonical ensemble, the ground state properties of the system are obtained as follows. For a LiB, μ represents the chemical potential of intercalated Li in the host, i.e. the electrode potential, described in section 2.3.1. Computing the average occupation, $\langle N \rangle$, of particles in the system at each μ value, therefore allows the equilibrium potential to be simulated at any input temperature, T. Along with $\langle N \rangle$, the average internal energy, $\langle E \rangle$, is a useful parameter to check the convergence of the simulation results with respect to the system size [85, 89, 90, 99].

Variances can be computed to check the system size convergence and derive experimentally measurable parameters. For example, the configurational component of the heat capacity at constant volume, C_V, given by:

$$C_V = \frac{\beta}{T}\left(\langle E^2 \rangle - \langle E \rangle^2\right) = \frac{\beta}{T}\mathrm{var}(E), \tag{11}$$

where $\mathrm{var}(E)$ is the variance of E. The vibrational and electronic components of C_V must be determined by other means, such as the approaches outlined in section 2.3.4.

It is also possible to determine voltammograms from $\mathrm{var}(N)$, as explained by Darling and Newman [99] and Mercer *et al* [89]. If the covariance of U and N is also known, the partial molar internal energy, $\partial U/\partial N$ and partial molar entropy $\partial S/\partial N$ can be obtained, as defined elsewhere [89, 90]. These parameters can be compared with experimental parameters from 'entropy profiling' or calorimetry [89, 91, 93, 100, 101] and input into a dynamic model such as kMC [76, 99, 102, 103], or MD to describe temperature dependent behaviour. A review of kMC has recently been published [104]; the technique is also briefly described by Van der Ven *et al* [9]. MD is described in the following section.

2.1.6. Molecular dynamics

MD is an approach which probes the dynamic evolution of a system over time. The crucial input for these simulations is the potential energy surface, describing the interactions between atoms. In *ab initio* MD (AIMD), this is described by solving the Schrödinger equation, whereas in a classical (potentials-based) mechanics framework the interactions are described using parameterised interatomic potentials. Here, we give an overview of both frameworks.

AIMD is able to capture events that potentials-based MD cannot, including bond breaking, and bond formation. AIMD also assumes that the dynamics of particles can be treated classically and that the equation of motion for all particles can be written as:

$$M_I \ddot{\mathbf{R}}_I = -\nabla_I \left[\varepsilon_0(\mathbf{R}) + V_{NN}(\mathbf{R})\right], \tag{12}$$

where M_I is the mass of a given nucleus, $\mathbf{R}$ denotes all nuclear coordinates, ∇_I is the Laplacian operator of a given nucleus, $\varepsilon_0(\mathbf{R})$ represents the ground state energy of the system at that given nuclear configuration, and $V_{NN}(\mathbf{R})$ represents the nuclear-nuclear coulomb repulsion at that given nuclear configuration.

Most modern techniques use KS-DFT (cf section 2.1.1) to solve the Schrödinger equation which finds the ground state energy. AIMD can be broadly split up into two main categories: Born–Oppenheimer dynamics and Car–Parrinello extended Lagrangean. The Born–Oppenheimer dynamics method uses a symplectic integrator to numerically integrate the equation of motion in equation (12) for each time step. The Car–Perrinello extended Lagrangean method gives the Kohn–Sham orbitals an artificial time-dependence. To attain a minimum energy with each new $\mathbf{R}$, the orbital dynamics are kept at a temperature much lower than that of the nuclei, but still high enough for the orbitals to quickly relax as the equation of motion proceeds. The new orbitals and their dynamics can then be defined by the Lagrangean equation [105]:

$$L = \mu \sum_i f_i \int d\mathbf{r} |\psi_i(\mathbf{r},t)|^2 + \frac{1}{2}\sum_{I=1}^{N} M_I \dot{\mathbf{R}}_I^2(t) - E[\psi(t),\mathbf{R}(t)] + \sum_{i,j}\Lambda_{ij}\left[\int d\mathbf{r}\psi_i^*(\mathbf{r},t)\psi_j(\mathbf{r},t) - \delta_{ij}\right], \quad (13)$$

where μ is an artificial kinetic energy term (discussed further in [106, 107]), $\psi_x(\mathbf{r},t)$ are the time-dependent Kohn–Sham orbitals, and Λ_{ij} contains a set of Lagrange multipliers to implement the orthonormality constraint on the orbitals.

Potentials-based MD is not able to capture some of the finer details of the system dynamics that AIMD is able to, however, it is able to reach longer time- and length- scales, providing information on long range diffusion properties. In classical potentials-based MD, the atomic interactions are described using parameterised interatomic potentials. There are multiple forms interatomic potentials can take, with their relevancy and accuracy relating to the system and study being conducted. Atoms are either attracted or repelled by one another based on their interatomic distance, r, to reduce their potential energy to a minimum, r_{eq}. This is known as a pair-interaction, which can be used to calculate the force, $\overrightarrow{\mathrm{F}}$, acting on each atom, given by:

$$\overrightarrow{\mathrm{F_i}} = \sum_j \overrightarrow{\nabla} E(r_{ij}). \quad (14)$$

In complex systems, there is a 'net effect' of the N surrounding atoms which can be accounted for by calculating the vector summation of each pair interaction contribution. Within ionic materials, the pair interactions are dominant and therefore it is computationally tractable to truncate the expression after the first term [108] to give an approximation of the pair potential. The charged nature of ions forms a coulombic interaction, where the relatively slow decay of $\frac{1}{r}$ as r increases, gives rise to the long range component of the potential. The general term for the total potential can therefore be written as:

$$E(r_{ij}) = \frac{Q_i Q_j}{4\pi\varepsilon_0\, r_{ij}} + \Phi_{sr}, \quad (15)$$

where i and j are ions of charge Q_i and Q_j at a distance of r_{ij}, and ε_0 is the permittivity of free space. Φ_{sr} is used to denote the remaining short-range interactions.

For ionic solids, including cathode materials, a common choice for an interatomic potential is a Coulomb–Buckingham potential [109], derived from the Born model of the ionic solid [110, 111], where the potential energy of the system can be expressed as:

$$E(r_{ij}) = \sum_{ij} \frac{Q_i Q_j}{4\pi\varepsilon_0\, r_{ij}} + \sum_{ij} A\, \exp\left(\frac{-r_{ij}}{\rho}\right) - C r_{ij}^{-6}, \quad (16)$$

where, A, ρ, and C are constants.

MD simulations can be performed using a range of ensembles, with the most commonly used being microcanonical (NVE), canonical (NVT), and isothermal-isobaric (NPT) ensembles [112–114]. Here, the number of atoms (N), volume (V), energy (E), temperature (T), and pressure (P) are conserved within the respective ensembles. Within the NVT and NPT ensembles the energy of endothermic and exothermic processes is exchanged with a thermostat. A variety of thermostat algorithms are available, with some of the most popular methods including the Nosé-Hoover, Berendsen, and Andersen thermostats [112–114]. For NPT ensembles, a barostat is also applied to control pressure.

The choice between AIMD and potentials-based MD is a trade-off between computational cost, accuracy, and transferability. AIMD is highly accurate, however, it is computationally expensive and scales poorly ($>O(N^3)$), making reachable system sizes and timescales relatively small ($<$1000 atoms, $\sim$100 ps). On the

other hand, potentials-based MD is less computationally expensive and can be applied to much larger system sizes, up to millions of atoms, with longer reachable time scales in the range of nanoseconds. However, the potentials-based approach is generally less accurate, as developing an interatomic potential which is sufficiently accurate enough to describe the specific system chemistry is challenging. The development of interatomic potentials is discussed in greater detail in section 2.2.2. More recently, development of linear-scaling DFT approaches, as discussed in section 2.1.2, has worked towards reducing this trade-off.

2.2. Method development

2.2.1. Continuum models of electrolyte solutions within DFT

Electrode-electrolyte interfaces are an important part of LiBs and an area of active research [115, 116]. The complexity of the structure and formation of electrical double layers at the interface has hindered the understanding of important electrochemical processes. While DFT-based electronic structure methods have been successfully used to study the solid-state physics in the bulk electrodes of LiBs, they are inadequate to describe the liquid state, which lacks structural order. This has led to rapid development of methods to describe the electrode-electrolyte interfaces [117].

The liquid state can be described mainly via explicit solvation [118], implicit solvation [119], or both [120]. In the former, the surrounding solvent and electrolyte molecules are considered at the same level of chemical accuracy as the electrode atoms. The surrounding solvent and electrolyte molecules can not only neutralise the excess charge on the electrode surface, but also form bonds and adsorb on the electrode surface [121–123]. The addition of a large number of solvent and electrolyte molecules to describe the liquid state drastically increases the configurational degrees of freedom. Sampling this large configurational space is computationally demanding and often leads to loss of focus on the main region of interest: the interface. While consideration of the first bonding layer of explicit solvent and electrolyte molecules is necessary to describe the local effects of bonding and electric field [124], the degrees of freedom of the non-participating solvent and electrolyte molecules far away can be averaged out via an implicit model of the electrolyte solution [125, 126]. The electrostatic potential in these hybrid quantum-continuum models is obtained from the solution of the Poisson–Boltzmann equation (P-BE) [127]. Recently, many DFT codes have integrated P-BE based continuum models [66, 128–135].

The continuum electrolyte ions with space-dependent concentrations, $c_i(\mathbf{r}), i = 1 \ldots p$, and charges, $\{z_i\}$, create a mobile electrolyte density, $\rho_{\text{mob}}(\mathbf{r}) = \sum_{i=1}^{p} z_i c_i(\mathbf{r})$, which interacts with the quantum charge density, $\rho(\mathbf{r})$, within a mean-field electrostatic potential, $\nu(\mathbf{r})$. This effect can be included in standard DFT by extending the standard free energy functional to include the mean-field electrostatic potential, $\nu(\mathbf{r})$, and the mobile charge concentrations, $c_i(\mathbf{r})$, as [135]:

$$E[\rho(\mathbf{r})] \rightarrow \Omega[\rho(\mathbf{r}), \nu(\mathbf{r}), c_i(\mathbf{r})]. \tag{17}$$

The variation of the free energy functional with the electrostatic potential, $\nu(\mathbf{r})$, gives the P-BE:

$$\nabla \cdot [\varepsilon(\mathbf{r}) \nabla \nu(\mathbf{r})] = -4\pi [\rho(\mathbf{r}) + \rho_{\text{mob}}(\mathbf{r})]. \tag{18}$$

The P-BE not only includes the quantum charge density, $\rho(\mathbf{r})$, as in standard DFT calculations in vacuum, but also the effect of the solvent in terms of a continuum dielectric with permittivity function, $\varepsilon(\mathbf{r})$, and mobile charge density of electrolyte ions, $\rho_{\text{mob}}(\mathbf{r})$. The permittivity function is chosen as a smooth function with value varying from 1 in the quantum region to ε^{∞} in the solvent region [131]:

$$\varepsilon(\mathbf{r}) = 1 + (\varepsilon^{\infty} - 1) s(\mathbf{r}), \tag{19}$$

where $s(\mathbf{r})$ is a smooth interface function varying from 0 in the quantum region to 1 in the solvent. Several choices for the interface function have been discussed by Andreussi *et al* [136]. The variation of the free energy functional with ion concentrations, $c_i(\mathbf{r})$, gives the Boltzmann expression for ionic concentrations:

$$c_i(\mathbf{r}) = c_i^{\infty} \lambda(\mathbf{r}) \exp\left(-\frac{z_i \nu(\mathbf{r})}{k_B T} + \frac{\mu_i^{\text{ex}}}{k_B T}\right), \; i = 1 \ldots p, \tag{20}$$

where $\{c_i^{\infty}\}$ and $\{\mu_i^{\text{ex}}\}$ are the bulk concentrations and excess chemical potentials of the electrolyte ions. The mobile charge density of electrolyte ions, $\rho_{\text{mob}}(\mathbf{r}) = \sum_{i=1}^{p} z_i c_i(\mathbf{r})$, is shown schematically in figure 5. As the interaction with mobile electrolyte charge is purely electrostatic and excludes any quantum effects such as Pauli repulsion, there is a problem of electrolyte charge accumulating infinitely close to the electrode. In order to prevent this problem, the models include an electrolyte accessibility function, $\lambda(\mathbf{r})$, which varies

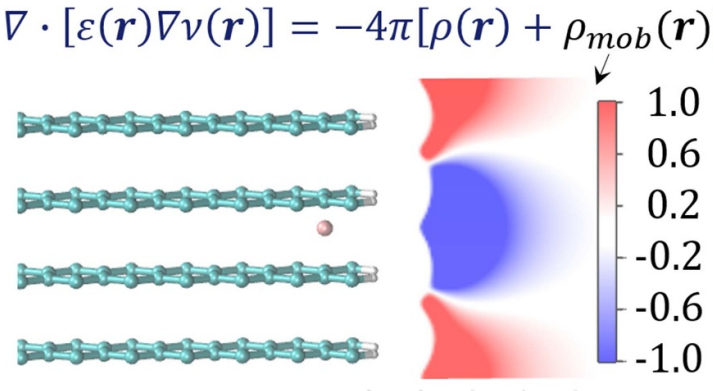

Figure 5. DFT simulation of a lithiated graphite interface in contact with an implicit electrolyte solution, based on the solution of the P-BE. Reprinted with permission from [135]. Copyright (2020) American Chemical Society.

from 0 near the electrode to 1 in the bulk electrolyte region [133, 137, 138]. One of the ways of defining such an accessibility function is as a product of atom-centred interlocking spheres of error functions [135]:

$$\lambda(\mathbf{r}) = \prod_{k}^{n_{\text{atoms}}} \frac{1}{2}\left[1 + \text{erf}\left(\frac{|\mathbf{r} - \mathbf{R}_k| - R_k^{\text{solute}}(\rho_e^{\lambda}) - R_k^{\text{solvent}}}{\sigma}\right)\right], \tag{21}$$

where σ is a smearing width ($0 < \sigma < 0.5\ a_0$). This description of the ion exclusion region derives from a physical picture: the electrolyte ions are moved away from the quantum electrode, up to a distance that incorporates not only the size of the species but also a solvation shell radius around the electrolyte ions. The species size can be described in terms of an isoradius of electronic density, ρ_e^{λ}. The solvation shell radius, R_k^{solvent}, depends on the solvent and is added to the species size, to calculate the overall radius of interlocking spheres for the accessibility function.

The electrostatic potential, $\nu(\mathbf{r})$, obtained from equation (18) is due to the entire electrode-electrolyte interface, where the electrode is treated quantum mechanically and the electrolyte solution as a continuum. Variation of the free energy functional with electronic density gives the Kohn–Sham equations in the total electrostatic potential, with additional terms for the variation of interface function with electronic density [130, 139]. Solvation energies are defined as [130, 133]:

$$\Delta\Omega = \Omega - \Omega_{\text{vac}} - \Omega_{\text{electrolyte}} \tag{22}$$

$$\begin{aligned} &= \Omega\left[\rho(\mathbf{r}), \{c_i(\mathbf{r})\}, \nu(\mathbf{r})\right] \\ &\quad - \Omega\left[\rho_{\text{vac}}(\mathbf{r}), \{c_i(\mathbf{r})\} = 0, \nu_{\text{vac}}(\mathbf{r})\right] \\ &\quad - \Omega\left[\rho(\mathbf{r}) = 0, \{c_i(\mathbf{r})\} = \{c_i^{\infty}\}, \nu(\mathbf{r}) = 0\right] \end{aligned} \tag{23}$$

where the respective terms can be computed as the total free energy in the electrolyte solution, the total free energy in vacuum, and the total free energy of the pure electrolyte [135]. The electrolyte effect on solvation energies can be computed as the difference of solvation energy in electrolyte at $\{c_i^{\infty}\}$ and solvation energy in pure solvent at $\{c_i^{\infty} = 0\}$:

$$\Delta\Delta\Omega = \Delta\Omega\left[\{c_i^{\infty}\}\right] - \Delta\Omega\left[\{c_i^{\infty} = 0\}\right] \tag{24}$$

$$= \Omega - \Omega_{\text{sol}} - \Omega_{\text{electrolyte}}, \tag{25}$$

where the respective terms are computed as the total free energy in the electrolyte solution, $\{c_i^{\infty}\}$, the total free energy in pure solvent, $\{c_i^{\infty} = 0\}$, and the total free energy of the pure electrolyte.

2.2.2. Fitting potentials for classical MD

The development of sufficiently accurate interatomic potentials for a specific chemistry is quite challenging. Interatomic potentials are traditionally based on mathematical functions that have been parameterised using experimental and/or electronic structure methods derived data [109, 140]. There are a limited number of codes available with the explicit purpose or functionality for fitting potentials. Here, we present several

available codes and discuss the complexities and considerations involved in deriving accurate interatomic potentials.

GULP [141], the General Utility Lattice Program, is a widely used code for performing a variety of simulation types on materials using boundary conditions [114]. Within this code, there is the functionality to fit interatomic potentials to either experimental measurements or electronic structure methods data [142]. GULP is capable of simultaneous fitting to multiple structures and can also handle core–shell models (which capture polarisation of atoms).

Atomicrex [143], dftfit [144], and potfit [145, 146] are codes designed to fit potentials to electronic structure methods data. Each of these codes have different levels of flexibility and their own unique features, however, a joint limitation is the ability to fit empirical potentials is limited to rigid ions and cannot fit a core–shell model.

During the process of developing potentials for $Li(Ni_xMn_yCo_z)O_2$ (NMC), and its ternary system $LiNiO_2$, it was found that none of these codes are able to accurately produce potentials for these materials. The complex nature of Ni chemistry in a layered oxide material is challenging, and to the best of our knowledge, no interatomic potentials exist for Ni^{3+}. Oxide systems are widely described using a Buckingham potential form, as given in equation (16), and for layered structures, including NMC and its ternary systems, variations of the Buckingham potentials are presented. Some use rigid ion models [147–150], others use core–shell models [147, 151–156], and a mixture of formal and partial charges have been implemented. With literature in disagreement over which variation of the Buckingham potential is the most accurate for representing the system, a code capable of fitting different permutations of the Buckingham potential is needed.

Structure and composition of a material are crucial to determine the functional form of the potential. For example, for a layered structure such as NMC-811, it is crucial to consider polarisability. Polarisability is described in classical (potentials-based) MD using a core–shell model. There are predominately two types of core–shell models: the relaxed (massless shells) model [157] and the dynamic (adiabatic shells) model [158]. The adiabatic shell model is more widely used in literature, including all core–shell related cited works in this section [147, 151–156], for calculating long trajectories, as it is less computationally taxing. In the adiabatic shell model, a fraction of the atomic mass is assigned to the shell. There is no defined fraction size; however, placing 10% of the atomic mass on the shell is considered common practice [112, 113]. An additional consideration for using a core–shell model is the separation of the formal atomic charge across the core and shell. However, determined numerical values of the core–shell charge separation are inconsistent [156, 159–162]. In some systems, where there is high polarisability, such as in LMO, the short-range interactions are overwhelmed by the longer-range coulombic term. In these cases, the system charges can be scaled to increase the influence of the short-range interactions, and are termed partial charges. The scaling factor is system dependent therefore no specific value is ideal in all cases, however 60% formal charge is commonly adopted [163].

POtential Parameter Optimisation for Force-Fields (PopOff) [164], a code developed within the Faraday institution, was specifically created for fitting different permutations of the Buckingham potential. It is unique in its ability to consider all the factors discussed above (rigid ion/core–shell/charge separation/charge scaling) in a modular design, allowing flexible fitting to suit individual systems. The code has been developed in Python, using a training set consisting of DFT derived data (*DFT*) and utilising the Large-scale Atomic/Molecular Massively Parallel Simulator [113]. The potential is fitted by minimising the mean squared error (χ^2) between the DFT forces, F^{DFT}, and stress tensors, σ^{DFT}, and those produced using the fitted interatomic potential (F^{IP}, σ^{IP}), defined as:

$$\chi^2 = \sum_{i,\alpha}^{N} \frac{(F_{i,\alpha}^{DFT} - F_{i,\alpha}^{IP})^2}{N_i} + \sum_{\beta} \frac{(\sigma_{\beta}^{DFT} - \sigma_{\beta}^{IP})^2}{6}. \tag{26}$$

This modular design allows the construction of a Buckingham potential able to accommodate the considerations and complexities of different systems. PopOff also allows for individual parameters to be fixed/excluded from the fit, lowering the fit dimensionality and computational cost. This is particularly useful for excluding dispersion terms, which are known to be zero or close to, for a range of elements [161, 165].

2.3. Calculating observable properties

2.3.1. Equilibrium voltage

The equilibrium cell voltage, $E(x)$, where $0 < x < 1$ denotes the fraction of sites occupied by lithium in the intercalation host, is a fundamental thermodynamic quantity related to the energy density of a cell [9, 166, 167]. $E(x)$ can be probed through experimental measurements of the OCV, that is, the voltage between the cathode and anode terminals under zero current flow, assuming that the system has been given

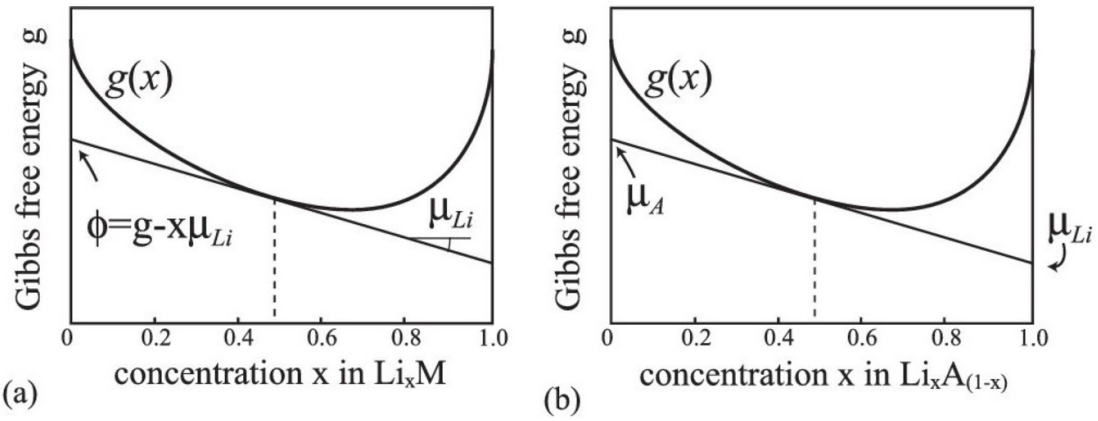

Figure 6. Representation of the connection between the Gibbs free energy, $G(x)$, the lithium chemical potential $\mu(x)$ in (a) an intercalation electrode and (b) an alloy electrode. Reprinted with permission from [9]. Copyright (2020) American Chemical Society.

sufficient time for the OCV to relax to the value of $E(x)$. Computationally, the equilibrium cell voltage can be modelled through DFT calculations at $T = 0$ K [9, 166, 167]; the effect of thermal fluctuations can be included by modelling using MC calculations [89, 90].

There is a fundamental relationship between the Gibbs free energy of lithium dissolution into the host, $G(x)$, the chemical potential of Li intercalation in the host, $\mu(x)$, and the cell voltage $E(x)$. Knowledge of $G(x)$ also provides information about the evolution of the phase behaviour dependent on the fraction of intercalated Li [9, 76, 167, 168], enabling the construction of phase diagrams from DFT. The relationships are represented schematically in figure 6. In essence: the tangent to the free energy curve, $G(x)$, allows $\mu(x)$ and hence the cell voltage to be obtained. Alternatively, integration of $\mu(x)$ can be used to derive free energy curves.

In the case of a Li-ion cell, the equilibrium cell voltage, $\phi(x)$, and the chemical potential of intercalated Li, $\mu(x)$, are related by:

$$\phi(x) = -\frac{\mu(x) - \mu_{\mathrm{Li}}^{\mathrm{ref}}}{nF}, \tag{27}$$

where $\mu_{\mathrm{Li}}^{\mathrm{ref}}$ is the chemical potential of the reference electrode, n is the number of electrons transferred per formula unit of intercalation host ($n = 1$ for Li-ion cells), and F is the Faraday constant. The most convenient reference potential, both from the point of view of simulations and for comparison with experimental measurements of Li-ion half cells, is the bcc metallic Li anode. With a suitable choice of units for all potentials (μ expressed in eV per formula unit of intercalation host), equation (27) can be written much more simply as [167]:

$$\phi(x) = -\mu(x). \tag{28}$$

The intercalated Li chemical potential is defined by:

$$\mu(x) = \left(\frac{\partial \underline{G}(x)}{\partial N_{Li}}\right)_{p,T,N_{\mathrm{host}}} = \left(\frac{\partial G(x)}{\partial x}\right)_{p,T,N_{\mathrm{host}}}, \tag{29}$$

where $\underline{G}$ is the absolute (i.e. extensive) Gibbs free energy of Li dissolution into the host, p is pressure, T is the absolute temperature, and N_{host} and N_{Li} are the number of host and lithium atoms in the system, respectively. The subscripts p, T, and N_{host} will be implicitly assumed to be constant from now on and dropped, to simplify notation.

Similarly, it is well known that:

$$\frac{\partial G(x)}{\partial x} = \frac{\partial H(x)}{\partial x} - T\frac{\partial S(x)}{\partial x}, \tag{30}$$

where $H(x)$ and $S(x)$ are the enthalpy and entropy, respectively, per formula unit of host material.

We can use equations (28)–(30) to get $\partial G/\partial x = -E_{\mathrm{OCV}}$, then, taking the derivative of the OCV with respect to T and using the chain rule, we obtain:

$$\frac{\partial S(x)}{\partial x} = \frac{\partial E_{\mathrm{OCV}}(x)}{\partial T} \tag{31}$$

and so:

$$\frac{\partial H(x)}{\partial x} = T\frac{\partial E_{\mathrm{OCV}}(x)}{\partial T} - E_{\mathrm{OCV}}(x). \tag{32}$$

Due to the units of electron Volts (eV) per formula unit for the potentials $H(x)$ and $TS(x)$, i.e. as in the conversion between equations (27) and (28), the usual factors of F have been omitted. In this way it is possible to simulate not only the equilibrium voltage, but split its contributions into enthalpy and entropy components. Both components can be experimentally measured [91, 93, 100, 169, 170] and modelled through MC or mean field methods [89, 91–93], providing additional properties for model validation purposes and to check the temperature dependence of those properties is modelled accurately. A good thermodynamic basis can then be used to derive dynamic properties, as outlined in the subsequent sections.

2.3.2. Activity coefficients of electrolytes

The activity coefficients of electrolytes ($\gamma_j, j = 1 \ldots p$) describe the thermodynamics of non-ideal solutions [171]. The activity coefficient of electrolytes can be computed from DFT+P-BE models, as described in section 2.2.1, by computing the electrolyte effect on solvation energies, $\Delta\Delta\Omega$ [130, 135]:

$$\ln \gamma_j = \frac{\Delta\Delta\Omega_j[\{c_i^{\infty}\}]}{k_{\mathrm{B}}T}, \; j = 1 \ldots p. \tag{33}$$

For an electrolyte dissociating into p species, the mean activity coefficient can be calculated as:

$$\ln \gamma_{\mathrm{mean}} = \frac{1}{p}\sum_{j=1}^{p} \ln \gamma_j. \tag{34}$$

2.3.3. Diffusion coefficients

The *diffusion coefficient* is a term used to describe the rate of ion transport within a system. This term, however, has been used in literature to express several forms of diffusion, which characterise diffusion in a material in different ways. Here, we describe several commonly used forms of *diffusion coefficient*, in context of where they are used, focusing on bulk diffusion. Heitjans and Kärger gives a detailed description of diffusion along grain boundaries and along surfaces (chapters 7 and 8) [172].

Ionic transport within the electrodes and electrolyte plays a vital role in the kinetics of a battery. It can be described fundamentally with flux expressions that relate ion fluxes to chemical or electrochemical potential gradients. This is related by Fick's first law, where the diffusion flux, $\boldsymbol{\jmath}$, is described using the gradient of the concentration, c, via:

$$\boldsymbol{\jmath} = -\mathcal{D}\nabla c, \tag{35}$$

where $\mathcal{D}$ is denoted as the diffusion coefficient tensor or diffusivity tensor and implies that $\mathcal{D}$ varies with direction. In general, the diffusion flux and concentration gradient are not always antiparallel. They are antiparallel for isotropic mediums. Heitjans and Kärger discusses this in more detail [172].

Steady state methods for measuring diffusion coefficients, like the permeation method, are directly based on Fick's first law [173]. In non-steady states, the diffusion flux and concentration vary with time, t, and position x, and a balanced equation is necessary. For particles which undergo no reaction this become the continuity equation:

$$\frac{\partial c}{\partial t} + \nabla \boldsymbol{\jmath} = 0. \tag{36}$$

Combining equations (35) and (36) leads to Fick's second law, also called the diffusion equation, which predicts how diffusion causes the concentration to change with time:

$$\frac{\partial c}{\partial t} = \nabla(\mathcal{D}\nabla c). \tag{37}$$

In diffusion studies with trace elements the material composition does not practically change and $\mathcal{D}$ is independent of the tracer concentration, presenting a concentration-independent diffusion coefficient. For diffusion in multiple dimensions Fick's second law becomes [174]:

$$\frac{\partial c}{\partial t} = \mathcal{D}\nabla^2 c. \tag{38}$$

The temperature dependence of the diffusion coefficient is often described empirically by an Arrhenius relation:

$$\mathcal{D} = \mathcal{D}_0 \cdot \exp\left(-\frac{E_A}{k_B T}\right), \tag{39}$$

where E_A is the activation energy for the mass transport, D_0^T is the pre-exponential factor, k_B is the Boltzmann constant, and T is the temperature.

From the microscopic point of view, the tracer diffusion coefficient can be defined by the Einstein–Smoluchowski relation [175, 176]:

$$\mathcal{D} = \lim_{t\to\infty} \frac{\left\langle r^2(t)\right\rangle}{2dt}, \text{where} \left\langle r^2(t)\right\rangle = \left\langle (x(t) - x_0)^2 \right\rangle, \tag{40}$$

where, $\left\langle r^2(t)\right\rangle$ is the mean square displacement (MSD) of the particles after time t and d is the dimensionality of the movement. This is also known as the *self diffusion coefficient* and is the main approach used to calculate the diffusion coefficient in kMC and MD from the atom trajectories. Van der Ven *et al* discusses in greater detail [9].

In atomistic modelling, diffusion coefficients can also be calculated using other approaches, such as Green–Kubo. The Green–Kubo approach is linked to the Einstein–Smoluchowski relation approach, equation (40). Both approaches assume that particle dynamics can be well approximated by Brownian motion. As described in equation (40), Brownian motion of independent particles can be expressed by the MSD of a particle proportional to time. This can also be termed as the integral of the velocity. The Green–Kubo approach is derived from the integration of the velocity (or current) autocorrelation function. Assuming that dynamics is ergodic, the diffusion coefficient can be calculated using a linear fit to the velocity autocorrelation function. Averaging is applied to this, for example, a time average for a selected particle type, a sample average, or an ensemble average.

2.3.4. Vibrational and thermal properties

While MD simulates the evolution of a chemical system over time, lattice dynamics is an approach that models the underlying vibrations. In crystalline solids, extended vibrations can be described as phonons with a characteristic frequency and wavevector, $\omega(q)$. A unit cell with N atoms contains $3N$ phonon modes. The theory of phonons provides a direct connection between microscopic atomic motion and macroscopic properties including specific heat capacity, IR and Raman spectra, and thermal expansion [177–179].

While assuming that phonons are harmonic simplifies the theoretical description, it is necessary to include anharmonic effects to describe phenomena such as heat transport. The lattice thermal conductivity, κ, depends on the lifetime of each phonon, i.e. how long it persists before decaying, which is an anharmonic process. Formally, the thermal conductivity given by the product of the modal heat capacity, (C_V), the group velocity, v, and the phonon mean free path, $v \times \tau$ (where τ is the phonon lifetime). The macroscopic κ is obtained by summing over band indices, ν, averaging over wavevectors, q, and normalising by the unit cell volume:

$$\kappa = \frac{1}{NV_0} \sum_{q\nu} C_{V,q\nu} v_{q\nu} \otimes v_{q\nu} \tau_{q\nu}, \tag{41}$$

where N is the number of unit cells in the crystal (number of wavevectors in the Brillouin zone summation) and V_0 is the volume of the crystallographic unit cell.

The heat capacity and group velocity can be extracted from the harmonic phonons, which are readily accessible from calculations based on electronic structure methods or potentials-based potential methods. The lifetime of each phonon mode is more demanding to compute and is often performed within a many-body perturbation theory expansion of phonon–phonon interactions. One approximation is to consider only the leading term of three-phonon creation and annihilation [180]. However, higher-order processes may limit the lifetimes, depending on the material and temperature. There are a range of packages available to compute the terms in equation (41) including PHONO3PY [180] (recently applied to $LiCoO_2$ and NMC cathodes) [181, 182], ALAMODE [183], and SHENGBTE [184].

3. Anodes

3.1. Introduction

Critical to the success of LiBs was the development of graphite-based anodes. Graphite proved to be ideal for this application, due to its low (de)-intercalation potential, only slightly higher than that of metallic lithium, and high theoretical gravimetric capacity of 372 mAh g^{-1}. However, many key degradation mechanisms in present-day LiBs that lead to their eventual failure, including cracking/reformation of the SEI and lithium plating, are still intimately connected with graphite-based anodes [185, 186]. The understanding of these mechanisms is still far from complete and leads to complex, non-linear degradation behaviour that is difficult to predict [187], motivating the development of multiscale models with a descriptive and predictive capability. A critical starting point for these models is a physically accurate atomistic description of the graphite and its interface with organic electrolytes.

The possibility to form Li-graphite intercalation compounds (Li-GICs), also known as 'stages', up to a stoichiometry of LiC_6, was known in 1975, albeit at that time it was only possible to form them by heat treating powders [188–190]. Initial attempts to electrochemically intercalate lithium into graphite resulted in co-intercalation of the organic solvent and exfoliation of the graphite [191]. In 1983, Yazami and Touzain reported the first successful intercalation into graphite using a solid polymer electrolyte [192]. Fong *et al* found that reversible lithium intercalation could be achieved in liquid organic electrolytes using ethylene carbonate (EC) as part of the solvent, which finally enabled the formation of a stable SEI on the graphite surface [193]. Mixtures of EC and dimethyl carbonate (DMC) were developed by Tarascon and Guyomard [194] and present-day graphite-based LiBs are still primarily based on this electrolyte mixture. The key challenge was finding a solvent chemistry that provided sufficient ionic conductivity, did not decompose significantly at the ∼4 V cathode potential, while also avoiding co-intercalation into the graphite and producing a stable SEI on its surface. Further incremental improvements in performance have since been achieved through additional additives and, more recently, the inclusion of small amounts of silicon in the anode as a secondary material.

This section predominantly focuses on graphite, since it remains the primary anode electrode material in the majority of commercial lithium ion (Li-ion) cells [14]. Here, the experimentally confirmed Li-graphite stages and the nomenclature necessary for atomistic models of bulk behaviour are defined. Atomistic modelling in the graphite bulk is outlined, including both thermodynamic and kinetic properties. The key graphite surfaces relevant to understanding the initial intercalation are described, then moving to modelling at the graphite edges and the interface with the electrolyte. Throughout, it is shown how these models enable quantitative understanding of the physical mechanisms of Li intercalation in the graphite bulk, the initial insertion at the graphite edges, and the interface between graphite and the electrolyte. Along the way, the key experimentally observable parameters are outlined, showing success stories of atomistic models to not only quantify and describe those parameters but to also predict new behaviour. In some cases, quantitative disagreement between model and experimental observations is also informative and can create new research directions. Work linking atomistic and continuum models is presented in the case of the technologically important SEI. Given the emerging importance of C/Si and C/SiO_x composites in commercial anode materials, some of the challenges in atomistic modelling of Si and related materials are summarised at the end. In the outlook, key remaining challenges are presented for modelling not only graphite, but also next generation materials such as silicides. Challenges related to metallic Li formation on graphite anodes, and the use of metallic Li as an anode material, are also summarised in the outlook.

3.2. Bulk properties

3.2.1. Graphite structure and Li-graphite stages

Graphite possesses a layered structure with carbon atoms forming a network of hexagons in each layer. The carbon atoms located within one layer are covalently bonded to each other, whereas the weak interlayer binding arises from the dispersion or vdW interactions [76, 188, 189, 189, 195–197]. The lowest energy stacking of the carbon layers is AB stacked (figure 7(b)), but synthesised graphite structures also contain a small amount of rhombohedral (ABC-stacked) domains [198].

Li-graphite stages, also known as Li-GICs, are lithium concentration-dependent structures of various stoichiometries [188, 189, 195, 197, 199]. In Li-GICs, Li atoms form a 2D hexagonal $(\sqrt{3} \times \sqrt{3})$R 30° superstructure, with Li atoms sitting directly above each other, as shown in figure 7(a). The stage number, n, denotes the number of graphene layers between each lithium-filled layer [188, 195, 197, 200]. The experimentally confirmed stages adopt different stackings in the carbon host lattice, as shown in figure 7. The standard nomenclature for GICs [189] denotes the carbon stacking and Li occupancies: periodic carbon layer stackings along the [001] axis are designated by uppercase letters separated by Greek lowercase letters, if

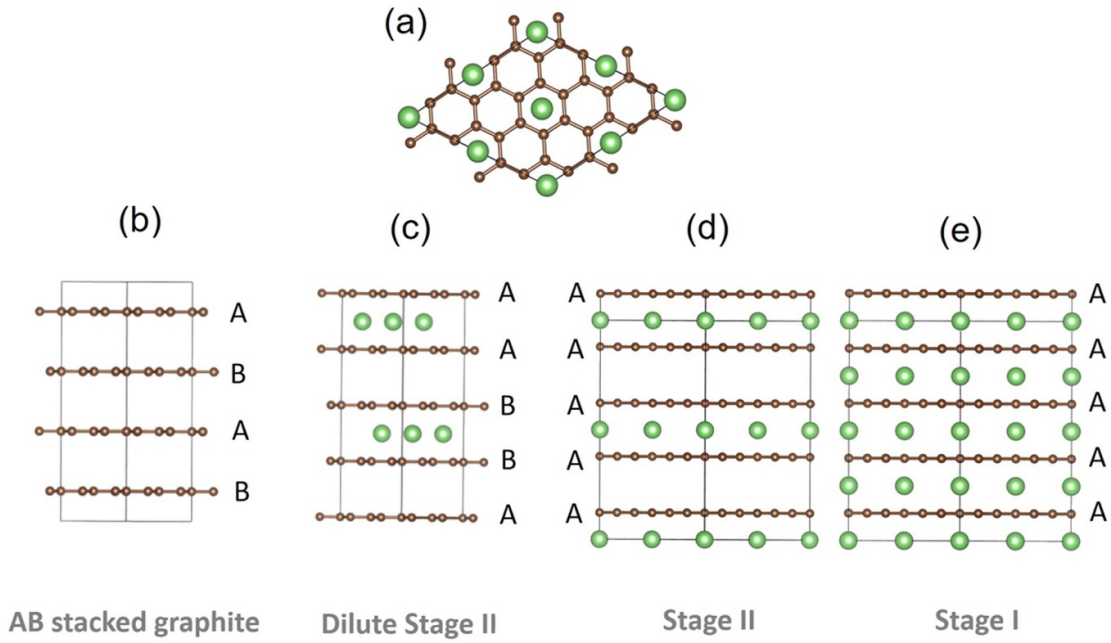

Figure 7. Structural representations of different carbon stackings in experimentally confirmed stages of graphite. (a) Top down view of carbon and lithium arrangements in Stages I and II. (b)–(e) Side views, showing the layers occupied with Li and carbon stackings in (b) empty AB stacked graphite, (c) AαABβB stacked dilute Stage II, with β indicating a lithium layer translated with respect to α, (d) AαAAαA Stage II and (e) Aα stacked Stage I. Green represent Li atoms, while the brown indicate C atoms. Reproduced from [71]. CC BY 3.0.

Table 1. Overview of carbon stackings and stoichiometries of Li-graphite stages from the literature, where Latin characters denote carbon stackings and Greek characters denote Li-filled layers [188, 189, 195, 197, 200, 202–206].

Stage	Stacking	x in Li_xC_6
Stage I	AαAα	$x = 1$ (LiC_6)
Stage II	AαAAαA	$x = 0.5$ (LiC_{12})
Dilute stage II (IID)	AαABβB	$x \approx 0.33$ (LiC_{18})
Stage III	AαAB/AαABAαAC	$x \approx 0.22$ (LiC_{27})
Stage IV	Unknown	$x \approx 0.17$ (LiC_{36})
Dilute stage I (ID)	AB	$x \approx 0.083$ (LiC_{72})
Graphite	AB	$x = 0$

Li is intercalated between planes. For instance, fully lithiated Stage I LiC_6 ($x = 1$) adopts AαAαAα stacking [170, 197, 201]. Here α denotes a lithium filled layer and x is the fraction of Li in Li_xC_6 ($0 \leqslant x \leqslant 1$).

Li-GICs vary not only in their lithium concentrations, but also in their carbon stackings. The current consensus of all known stages, including their carbon stackings and lithium stoichiometries, is tabulated in table 1.

Experimental observation of these stages relies largely on probing the average interlayer carbon spacing through diffraction measurements. Probing the lithium orderings of Li-GICs through experimental techniques remains very difficult [71, 91, 197, 207–209], but as shown in section 3.2.3, atomistic techniques shed light on these orderings.

Thermodynamic and kinetic properties of Li-GICs have been studied by considering various structures of LiC_{6n} using DFT [70, 76, 196, 196, 210–216], mean field [91, 92, 217], canonical and grand canonical MC [76, 218, 219], and kMC simulation techniques [76, 102, 103, 214, 220]. The rest of the section outlines electronic structure based studies of experimentally measurable bulk thermodynamic properties, before describing atomistic modelling of kinetic properties.

3.2.2. Equilibrium potential and measured OCV

Knowledge of the correct phase behaviour of an intercalation electrode is an important pre-requisite to building a dynamic model of the intercalation process. One of the most directly measurable observables is the experimental OCV, which is related to the equilibrium potential determinable from atomistic methods (cf Methods section 2.3.1). The OCV is an important input parameter in continuum models and is also used in control models, for example, to determine the state of charge of a battery within a battery management

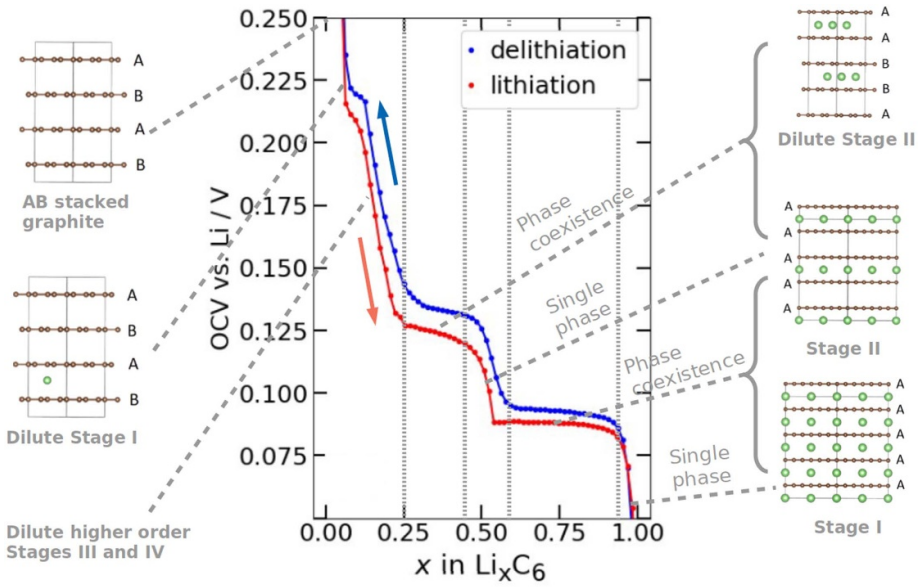

Figure 8. Illustration of OCV features of lithium in graphite using experimental data from [91]. Lithiation and delithiation behaviour is overlaid; labelled stages are linked to the lithiation profile, which is closer to the true equilibrium potential. Reproduced from [71]. CC BY 3.0.

system (BMS) [221]. Inputting a polynomial fit to the experimental OCV at an arbitrary temperature without physical meaning could lead to incorrect predictions of temperature-dependent behaviour in these models. Therefore, to attain predictive, dynamic models on longer length scales, atomistic models of the OCV and equilibrium potential are important and can contribute to physically more robust and more predictive temperature dependence in continuum and control models [9, 166].

In any intercalation electrode, ordered phases give rise to steps in the OCV. In the lithium-graphite system, the ordered stages described in section 3.2.1 therefore give rise to characteristic features in OCV versus x curves [195, 200] as shown in figure 8. The influence of the Li-graphite stages on the measured OCV at $T \approx 25$ °C has been well characterised [195, 199, 200, 207–209, 222–224], although a more thorough study of the temperature dependence of the OCV has only been conducted more recently [71]. Each OCV plateau represents a different two-phase equilibrium. At zero Kelvin, there is no contribution from configurational entropy and each step represents a sudden transition between two different two-phase equilibria. This is the behaviour that can be captured using DFT code. The cluster expansion framework, described in more detail in the Methods section 2.1.4, allows the accuracy of DFT to be retained to explore configurational degrees of freedom. Thermal fluctuations can be included by determining ECIs from fitting DFT data and using these as parameters within an MC method (section 2.1.5). The entropy contribution at temperature, $T > 0$ K has the effect of smoothing out those steps [71, 91, 217, 225], which is caused by some limited single phase solubility around the stoichiometric composition. This can be seen in experimentally measured OCV profiles at $T \approx 300$ K, such as the ones shown in figure 8.

The equilibrium potential versus x can be modelled through atomistic techniques. For example, Li-graphite phase diagrams were constructed and the equilibrium potential was modelled by Persson *et al* [76]. They performed a cluster expansion of Li degrees of freedom from total energy DFT calculations, by fixing the carbon stacking degrees of freedom. Those degrees of freedom represent the host lattice stackings in the experimentally confirmed stages shown in figure 7. Typically, different cluster expansions are performed in Li-vacancy lattices of the respective hosts [71, 76, 196], to account for carbon stacking degrees of freedom with the result from a more recent work [71] represented in figure 9(a). Within this work, AA, AABB, and AB stackings of the host lattice were considered, representing all stages of order up to II (cf figure 7). Reference states at $x = 0$ and $x = 1$ were used in AB and AA stackings, respectively, to linearly correct the free energy and thus obtain the formation energies at each lithium concentration. The convex hull over all stackings represents the lowest energy structure for a given x value. A common tangent construction between the different stackings represents two-phase coexistence. The slope of the resultant ground state free energy profile, $dG(x)/dx$, (equation (29)) equals the intercalated Li chemical potential, μ, where $-\mu$ is equivalent to the equilibrium potential at $T = 0$ K, as represented more generally in figure 6 and the surrounding discussion in the Methods section.

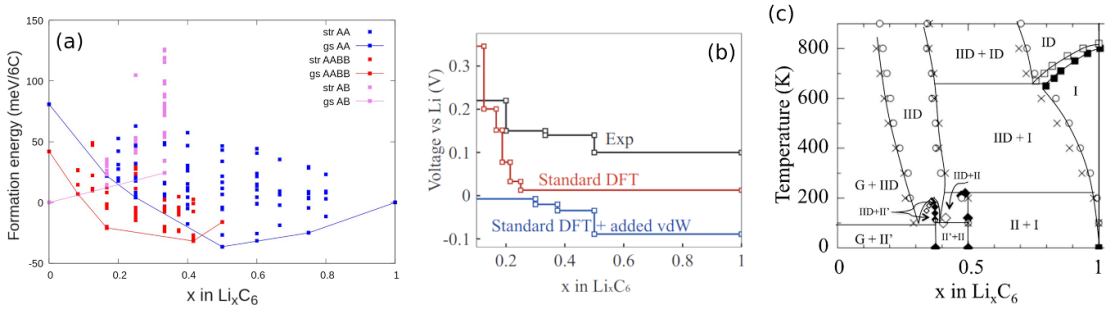

Figure 9. (a) Formation energies of lithium in graphite performed with different carbon stackings. All calculated structures are denoted 'str' while the 'gs' represent the ground state structures in each of the three carbon stackings: AB, AABB, AA. (b) Phase diagram of lithium in graphite, determined by performing MC calculations parameterised by ECIs from DFT calculations. (c) Zero kelvin equilibrium potential profiles dependent on different levels of vdW corrections. (a) Reproduced from [71]. CC BY 3.0. (b), (c) Reprinted figure with permission from [76], Copyright (2010) by the American Physical Society.

The phase behaviour of the lithium-graphite system, and therefore the voltage profile, is sensitive to the vdW interactions between the carbon planes [76, 210, 211]. Conventional DFT approaches without accounting for vdW interactions do not correctly reproduce the structure and energetics of graphite and Li-GICs [76, 210, 211] (figure 9(b)). Therefore, vdW-corrected DFT approaches, for example DFT-D2 [45] and DFT-D3 [47], are important for correctly describing the phase behaviour and dynamics of graphite and Li-GICs. Persson *et al* considered the vdW interaction as a constant [76]. This approximation can accurately describe the step height at $x = 0.5$ (the height difference represents the difference between the chemical potentials in the Stage I–Stage II and Stage II–Stage IID coexistence regions). The simulated voltage profile figure 9(b) (blue line), shows that the constant vdW interaction results in a systematic error in the voltage scale.

Voltage profiles like the ones shown in figure 9(b) represent the ground state behaviour, at $T = 0$ K. As an additional step, cluster expansions can be used to parameterise an MC simulation (section 2.1.5) and therefore include thermal fluctuations. The lithium-graphite phase diagram, figure 9(c), has been constructed by performing a combination of canonical and grand canonical MC simulations at different temperatures [76].

The experimental OCV and the theoretical equilibrium potential are often, erroneously, considered to be equivalent. However, the OCV refers to the measured cell voltage without any external current and drifts with time. With sufficient time, it is often assumed the OCV will eventually relax to the equilibrium potential, but meta-stable states can occur that show no variation over experimental time scales of hours or even days [71, 226, 227]. The true equilibrium potential, as defined in equation (29), is a thermodynamic quantity and is not history-dependent [9, 71]. Experimentally, a hysteresis of the measurable OCV between lithiation and delithiation is observed for Li/graphite half cells [71, 170, 195, 200, 206, 207, 223, 228, 229] as shown in figure 8. Hysteresis is observed even after several hours of relaxation time and for $T > 298$ K, clearly demonstrating that the measured OCV is not a simple function of the thermodynamic ground state. Hysteresis therefore poses an interesting challenge to atomistic modellers.

It was recently shown that (de)-lithiation hysteresis in graphite is intimately connected with disorder in Stage II configurations and appears to be associated with a different carbon stacking pathway in each cycling direction [71]. Notably, energetic barriers to translate between ground state configurations, as determined through climbing image nudged elastic band (CI-NEB) calculations (Methods section 2.1.3), do not explain the hysteresis in graphite. Non-ground state configurations are involved in the delithiation direction. Understanding that behaviour requires the configurational entropy of Li/vacancy arrangements to be quantified, which is explained in more detail in the next section.

3.2.3. Entropy

The internal energy of intercalation electrodes arises largely from electrostatic interactions between the constituents. Those interactions can be well approximated by DFT. An atomistic description of the entropic behaviour of intercalation electrodes, $S(x)$, is also needed to correctly model thermal behaviour at $T > 0$ K. The partial molar entropy, $dS(x)/dx$, is an experimentally accessible quantity, which can be probed by monitoring how the OCV, described in the previous section, varies with temperature (equation (31), cf [71, 91, 93, 100, 169, 170, 230] for further details). $S(x)$ is a sum of configurational, vibrational, and electronic components [169, 225]. For lithium in graphite, the electronic component can be neglected and the vibrational component can be well approximated by assigning a Debye temperature to all of the

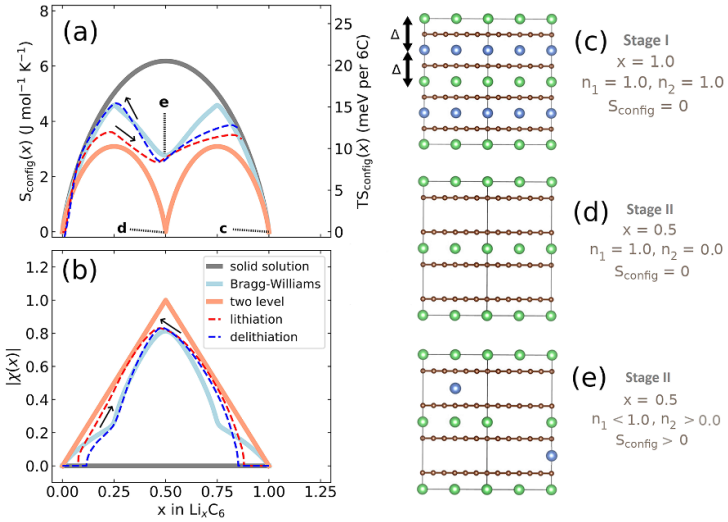

Figure 10. (a) Configurational entropy obtained at $T = 320$ K: *dark grey solid line*: ideal solid solution; *light blue solid line*: Bragg–Williams solution; *orange solid line*: sequential two level solid solution; *red dashed line*: experimental lithiation; *blue dashed line*: experimental delithiation. (b) Order parameter $|\chi|$, as described in the main text, labelled as in (a). In (a), select points (c)–(e) are indicated and schematic representations of the lattice occupations of Li in levels n_1 (green balls) and n_2 (blue balls) are shown on the right. Reproduced from [71]. CC BY 3.0.

vibrational modes [169, 225], or by computing phonon spectra from electronic structure methods [196, 231] (cf section 2.3.4). The quantity that shows the greatest difference with lithium concentration, x, is the configurational entropy of Li/vacancy arrangements, S_{config}. Because of the staging phenomena described in section 3.2.1, S_{config} strongly deviates from ideal solid solution behaviour for Li in graphite.

The partial molar entropy $dS(x)/dx$ is difficult to interpret atomistically and so integration is required to get S_{config}:

$$\int_{x'=0}^{x'=x} \left(\frac{\partial S_{\text{config}}(x')}{\partial x'} \right) dx' = S_{\text{config}}(x) \approx S(x) - S_{\text{vib}}(x), \tag{42}$$

where S_{vib} is the vibrational entropy approximated by Debye temperatures [169, 225]. The integration constant is $S_{\text{config}} = 0$ at $x = 0$, because there can be no Li disorder in pure graphite.

Dashed lines in figure 10(a) denote post-processed experimental data obtained during lithiation and delithiation using equation (42) from [71]. Qualitatively, this shows more configurational Li disorder, i.e. larger entropy, is obtained during delithiation than lithiation. The lithium arrangements can be split into sublattice occupancies n_1 and n_2 arranged in alternate planes, as shown visually in figures 10(c)–(e). Each sublattice occupancy is linked to the degree of lithiation, x, via $x = (n_1 + n_2)/2$.

Solid lines in figures 10(a) and (b) indicate three hypothetical cases. The orange solid line denotes solid solution (random) filling of Li into one of the sublattices for $x < 0.5$, followed by solid solution filling of the other sublattice, resulting in two maxima. Note that S_{config} is zero in Stage II at $x = 0.5$ (cf figure 10(d)). The dark grey line shows the result for an ideal solid solution, if Li were to fill all available sites at random, i.e. $n_1 = n_2$ for all x. The blue solid line is the solution to a Bragg–Williams model [91, 217], assuming only nearest neighbour repulsive pairwise lithium interactions between planes of $\Delta = 75$ meV and no in-plane interactions. That model allows a direct evaluation of the partition function (cf equation (10)) by enumerating through all possible arrangements of Li atoms on the two sublattices for a given x within the canonical ensemble. The out-of-plane Li–Li interactions are treated within a mean field (non-local) approximation to simplify the computation (details and formulae in references [91, 92, 217]).

The Bragg–Williams model produces a behaviour in $S_{\text{config}}(x)$ between that expected for the solid solution and sequential two level filling. At $x = 1$, there is a net repulsion on each Li atom of 2Δ, as represented in figure 10(c). At $x = 0.5$, one of the sublattices becomes preferentially filled, as represented schematically in figure 10(e). In contrast, a perfect Stage II structure as predicted by sequential two level filling (figure 10(d)), would result in $S_{\text{config}}(0.5) = 0$.

These results can be understood within the framework of order parameters [81]. The relevant staging order parameter, $\chi(x) = n_1 - n_2$, is shown in figure 10(b). Formally, $\chi(x)$ takes values between -1 and $+1$, but only the absolute value is meaningful in this case. If $|\chi(x)| = 1$, then only one layer is filled with Li,

representing maximal staging order. If $\chi(x) = 0$, both sublattices are occupied with equal probability, maximising disorder and hence no staging order is observed.

Greater interlayer Li disorder is observed during delithiation below $x = 0.5$. The Li ordering, as described by the order parameter, closely follows the Bragg–Williams model. This is expected if the host lattice remains in a metastable AA stacking. The lithiation behaviour shows a configurational entropy closer to solid solution filling of half the sites, which would be expected in AABB stacking, since only half the interlayers (i.e. those locally adopting AA or BB stacking) provide favourable Li insertion sites. As shown in figure 9(a), this is the ground state stacking configuration for $x < 0.5$.

The wider implication of these results is that the transformations between the stackings in graphite, and possible stacking dynamics in other layered intercalation hosts, deserve more attention. These phase transformations not only create a challenge from a cell diagnosis point-of-view, they could also be partially responsible for mechanical degradation, fracture, unstable interfaces and loss of active material. Phase transformations should be described in a rigorous way in continuum models. It is not sufficient to approximate the guest ions as an ideal solid solution as, for instance, done in the popular DFN-type models.

It is worth noting that the host lattice ordering of graphite obtained in electrochemical conditions is difficult to access from experimental analysis. In-operando x-ray and neutron diffraction experiments allow the interlayer carbon separation to be obtained [189, 195, 200, 204–206]. However, it is extremely difficult to obtain the stacking displacements within each carbon layer, as the superstructure peaks associated with these displacements [197] are weak and obscured by peaks from the current collector [206, 208, 209]. A reason as to why there is still some dispute in the literature regarding the Li-graphite stages of order greater than 2, as highlighted earlier in section 3.2.1, is that these in-plane displacements cannot be completely elucidated. These displacements influence the lithium ordering in each atomic layer, which is even harder to determine than the carbon ordering and is currently not feasible even in neutron diffraction experiments. It is also not possible to determine this information through local probes such as nuclear magnetic resonance (NMR) and Raman scattering [222, 232]. It is only through the combination of atomistic and statistical mechanical models, together with entropy profiling measurements, that the proportion of lithium in the different layers in Stage II configurations could be quantified [71]. With regard to systems other than lithium-graphite, atomistic techniques could enable lithium guest orderings to be quantified by means of order parameters, which, for the reasons explained above, is information inaccessible through experiment alone. Synergies between models of host and guest ion orderings with appropriate experimental characterisation will enable a new generation of modelling tools that can predict these phenomena with greater accuracy [9, 233].

As shown in the next section, orderings in Li-GICs have implications for the dynamics of Li intercalation as well.

3.2.4. Ion diffusion in Li-GIC

Having outlined the use of atomistic techniques to evaluate observable thermodynamic properties of anodes and, in particular, graphite, this section focuses on the computation of bulk dynamic properties by DFT and kMC approaches.

Li diffusivity is similar for stage I and stage II Li-GICs [76], with the probable Li migration pathways for LiC_{6n} illustrated in figure 11 [210]. These pathways were determined from DFT calculations within a CI-NEB approach. Here, Li diffusion across the graphite layers through a carbon hexagon hollow (H) are denoted as the through-plane pathway. The in-plane or two-dimensional Li migration along the crystallographic ab plane occurs either by a bridge (B) migration pathway, where Li passes through a rectangle of carbon atoms of subsequent layers, or a top (T) migration pathway, where Li passes in between two congruent carbon atoms.

Diffusion proceeds in the aforementioned through-plane pathways and in-plane pathways via the Frenkel and vacancy mechanisms, respectively. Thinius *et al* showed that Li diffusion along the crystallographic *c* direction is kinetically prohibited, due to a large activation energy barrier [210]. The calculated activation energy for this migration pathway is extremely high (8.00–8.23 eV), therefore, the Boltzmann probability for diffusion through pristine graphene planes is negligible at $T = 300$ K. It is therefore likely that diffusion in the *c* direction occurs via grain boundaries [216]. In contrast, the activation energy for Li diffusion in the crystallographic ab plane is much lower (0.42–0.52 eV), showing that in Li-GICs, Li diffuses mostly within the intercalation layers [210]. In the literature, DFT-based theoretical investigations provide the same qualitative trends for ion diffusion mechanisms in Li-GICs and the calculated activation barriers vary slightly, but are within the same order of magnitude [215, 216, 234, 235].

In order to gain insights into the Li diffusion process in graphite, far from equilibrium and under fast charging conditions, Garcia *et al* simulated a range of compositions between stage I and IV, i.e. dilute Stage I [211]. Their study determined reduced activation barriers in the in-plane migration pathways (0.2–0.32 eV),

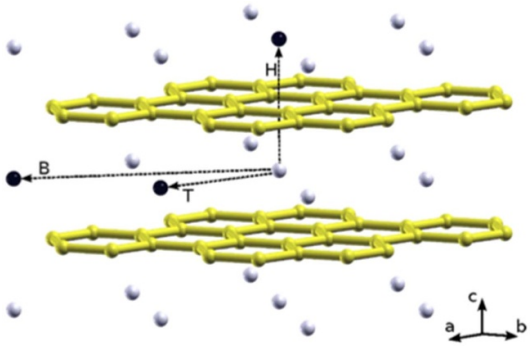

Figure 11. Li migration pathway in LiC_6. In the through-plane pathway, lithium migrates through a carbon hexagon hollow (H) along the crystallographic c direction. The in-plane pathways are denoted as bridge (B) and top (T). Reprinted with permission from [210]. Copyright (2014) American Chemical Society.

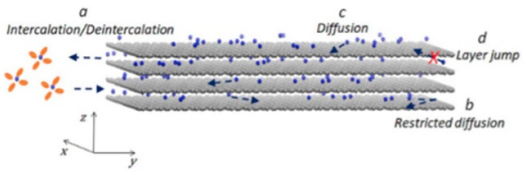

Figure 12. Representation of insertion and diffusion of lithium in graphite in a kMC model. Reproduced from [103]. CC BY NC-ND 4.0.

which is attributed to the presence of a higher number of electrons compared to Li^+ ions, occurring at the very beginning of the lithiation cycle during fast charging conditions. This extra charge increases the interlayer spacing in the diffusion layer and adjacent channels, increasing the Li diffusivity [211]. Ji *et al* investigated the anisotropic strain effects on lithium diffusion in graphite anodes using DFT and kMC simulations [214]. According to their study, the activation energy for Li diffusion in unstrained Li_xC_{6n} is 0.48 eV. The tensile strain along the direction perpendicular to the graphite planes facilitates in-plane Li diffusion by reducing the energy barrier and vice versa [214].

Gavilán-Arriazu *et al* have recently simulated the dynamic properties of lithium intercalation in graphite using kMC [102, 103, 220]. These models considered exchange of Li with the solution on one side of a slab (figure 12), with only interplanar Li transport allowed, based on the diffusion barrier arguments presented above. Energetic barriers for Li exchange into/out of the graphite were calculated assuming Butler–Volmer kinetics, based on experimental exchange current density data. Interplanar diffusion barriers were computed using random walk theory, based on experimental data in the dilute limit. Respective barriers of 0.655 and 0.370 eV for exchange and interplanar diffusion were obtained. This approach enabled the simulation of several different dynamic properties dependent on lithium concentration, x [102, 102], sweep direction [102], and temperature [103], with a few of these highlighted in figure 13. Additionally, the importance of metastable Daumas–Hérold orderings in Stage II configurations [220] and clogging of lithium at the interface [102] leading to slow Li insertion kinetics were identified as important challenges limiting the kinetics of the lithium (de)insertion processes.

Having described modelling of the thermodynamics and bulk Li diffusion in graphite, the following section will focus on another important aspect for a multiscale model: the structure and dynamics of the graphite edges.

3.3. Graphite surfaces and interfaces

3.3.1. Possible graphite surfaces and their stability

As discussed above, investigating the bulk properties of lithium is key to understanding Li intercalation kinetics and (dis)charging rates in graphite. However, Li exchange occurs between the graphite surfaces and the electrolyte, hence a multiscale model needs to include these phenomena. Addressing the surface properties of graphite would improve the understanding of (dis)charging behaviours at graphite anodes and possibly suggest how to enhance the (dis)charging rates.

As shown in figure 14 and section 3.2, graphite consists of multiple stacked graphene layers. One of the exposed surfaces is the basal plane or the (001) surface, which has been widely investigated in both the

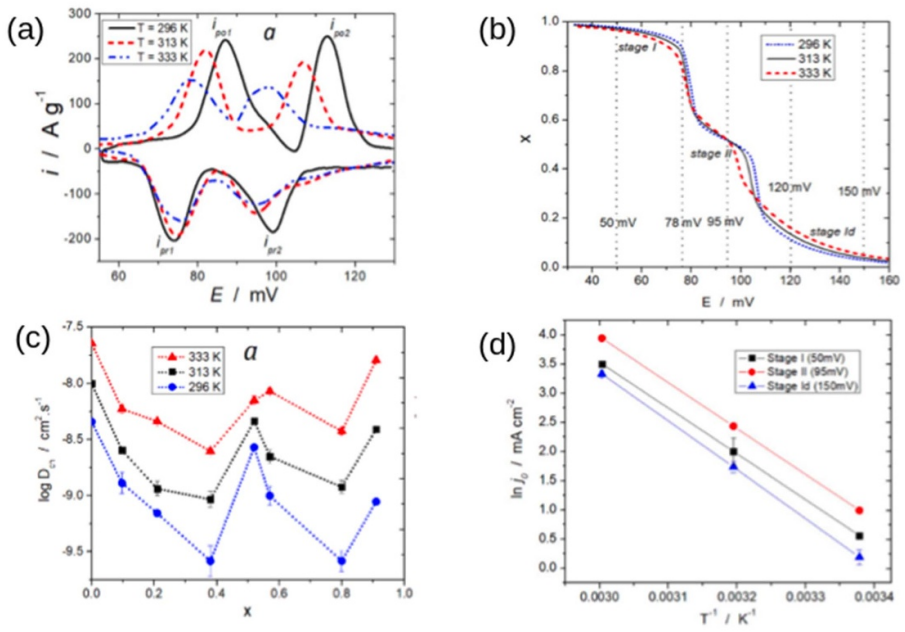

Figure 13. Effect of temperature on the dynamic behaviour of lithium insertion in graphite. (a) Voltammograms, (b) voltage profiles (isotherms), (c) diffusion coefficients, (d) exchange current density. Insertion and diffusion of lithium in graphite in kMC model. Reproduced from [103].

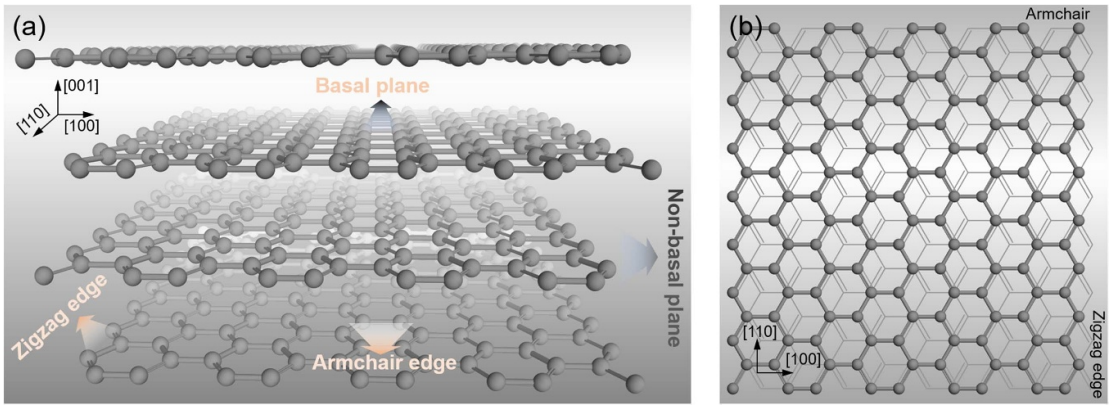

Figure 14. (a) Structures of the basal plane and the non-basal plane of graphite. The latter plane consists of different edges of graphites, such as armchair edge and zigzag edge. (b) Topological geometries of graphite edges.

theoretical and experimental studies [76, 210, 235–237]. In contrast, the non-basal planes attract less attention, due to their complicated edge morphology. Recently, experimental studies characterised the SEI formation and growth along the graphite edges as opposed to the basal plane [238, 239], indicating the importance of the graphite non-basal plane for facilitating Li intercalation.

Thinius *et al* investigated the stability of various low index graphite surface planes including the (001), (110), and (100) planes. The calculations were performed using dispersion corrected DFT approaches [46, 48]. The surface energies of these planes were found to go in the order (001) < (110) < (100) [240], indicating that the (001) surface (the basal plane) is the most energetically favourable. However, this plane does not favour Li intercalation, due to the high diffusion barrier required for Li to go through the carbon hexagon [76, 210], as highlighted in the previous section on ion diffusion in Li-GICs (section 3.2.4). Li intercalation of graphite particles must therefore proceed either via defects in the (001) plane or via the non-basal planes.

The (100) surface consists of nanoribbons with a zigzag edge, whereas the (110) surface adopts an armchair conformation. The relatively unstable surface planes, such as the (100) plane, can be stabilised by various procedures, including chemisorption of oxygen atoms [241]. It was found that the oxygen functional groups not only stabilise the graphite edges, but are also critical for the formation of the SEI layer near the

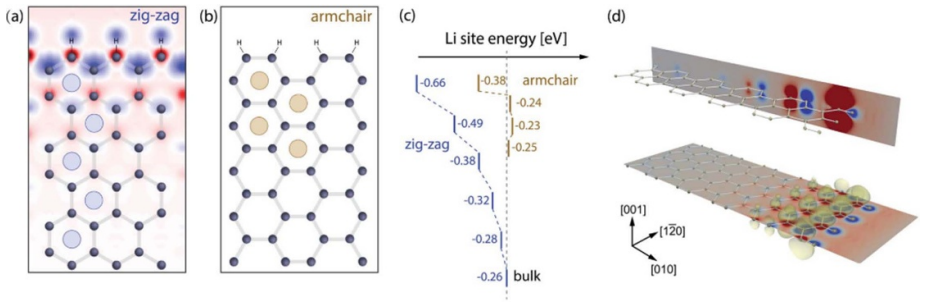

Figure 15. Structures of the zigzag-edged graphite (a) and the armchair-edged graphite (b). (c) shows the energy profile of Li adsorption in edged graphite. (d) is the spin densities of zigzag-edged graphite. The iso-surface value is 0.0002 e Å^{-3}. Reproduced from [70] with permission of The Royal Society of Chemistry.

edge, thereby preventing graphite exfoliation [242]. Investigating those non-basal planes and their effects on Li intercalation are therefore important and are addressed in the following section.

3.3.2. Surface effect on intercalation energy

Understanding the nature of Li intercalation in graphite is important for optimisation of the anode material. As described above, Li intercalation in the bulk of graphite has been widely investigated [76, 210, 235, 236, 243]. Experimental Li diffusivities in graphite have been reported, ranging from 10^{-6}–10^{-14} cm^2 s^{-1} [235, 244–246]. However, DFT calculations [76] based on bulk graphite indicate that Li diffusion coefficients based on the AABB and AA stacked graphite are around 10^{-7} cm^2 s^{-1} and decrease slightly with increasing Li concentration [76]. The variability between reported experimental diffusion coefficients arises from a combination of the staging dynamics and the anisotropy of Li diffusion (through versus into the basal plane). There is also a difference between the surface morphologies of different types of graphite, i.e. the proportion of zigzag and armchair edges and their surface chemical terminations, implying possible differences between the electronic behaviour and charge transfer kinetics dependent on edge morphology and termination. Therefore, investigation beyond the bulk properties of graphite is necessary to optimise the overall rate performance of graphite electrodes. As described in section 3.3, the basal plane is relatively inert towards Li intercalation [216]. The non-basal plane, consisting of different edge morphology, attracts more attention due to observations of Li intercalation and SEI growth [238, 239]. Uthaisar and Barone studied the Li adsorption and diffusion on the edged graphene system using DFT [247]. The graphene edges were found to affect not only Li adsorption but also the diffusion coefficient. Narrower graphite nanoribbons showed faster delithiation behaviour than the larger sized graphene, due to the topological effect of graphene edges. This highlights that an in-depth knowledge of interface effects is needed to understand Li intercalation rate and enable rational optimisation of the battery performance.

From an atomistic perspective, the surface and edge morphology of anode materials were found to have a strong impact on Li binding energies [247, 248]. Through investigating Si nano-structures, Chan and Chelikowsky found that Li has higher binding energies at the bulk site compared to the edge, requiring a higher energy cost of Li migration from the bulk towards the edge [249]. In graphite anode materials, however, Leggesse *et al* reported that the edged graphite systems showed remarkably enhanced Li binding energies and high Li mobility along graphite edges [248]. Peng *et al* recently quantified the edge effects on Li intercalation in graphite [70]. In their work, different edged graphites at dilute Li concentration were comprehensively investigated using DFT calculations. Interestingly, they found the unique topological electronic structures near the edges, particularly near the zigzag edge, induced distinct intercalation energies of Li in graphite. Figure 15(c) shows the Li adsorption energies at the armchair-edged and the zigzag-edged graphite, respectively. The adsorption energy, E_{ads}, is expressed as:

$$E_{ads} = E_{Li|Graphite} - E_{Graphite} - E_{Li}, \tag{43}$$

where $E_{Li|Graphite}$, $E_{Graphite}$, and E_{Li} are the energies of Li adsorption in graphite, the pristine graphite, and one Li in body-centred cubic (bcc) Li metal, respectively. At the armchair edge, from the energy profile (cf figure 15), the adsorption energy of Li is the lowest at the edge site (−0.38 eV). With Li penetrating into the bulk, the adsorption energy decreases rapidly to −0.24 eV at the sub-surface site and becomes −0.26 eV at the bulk site. The topological geometry of the armchair edge promotes Li adsorption relative to the graphite bulk.

At the zigzag edge, the edge effect becomes even stronger, due to the existence of the surface state which consists of C $-$ p_z orbitals emerging from the zigzag edge [250, 251]. Figure 15(c) shows that Li achieves a much lower adsorption energy of -0.66 eV at the zigzag edge site, indicating the strong binding of Li at the edge. The edge effect in the zigzag system is much stronger than that at the armchair edge and additionally penetrates into the bulk, indicated by the gradual decrease in magnitude of the Li adsorption energy from the edge to the bulk.

The zigzag edge displays completely different spin densities contributed by the p_z orbitals perpendicular to the graphene planes, as shown in figures 15(a) and (b) [70, 248, 250, 251]. These spin densities consist of the unpaired electrons accumulating on the edged carbons. The amplitude of this topological surface state gradually diminishes over a few bond distances beneath the surface. It is this surface state that interacts with Li at the zigzag edge and favours its adsorption. In summary, the graphite edges show stronger interactions with Li than those in the bulk. The effect is especially pronounced at the zigzag edge, strongly stabilising Li binding due to the topological surface states.

3.3.3. The surface effect on Li diffusion

As Li obtains higher binding energies at the graphite edge, due to the specific topological structure of graphite edges [70, 248], it is worth examining the impact of those edges on Li diffusion. In bulk graphite, the diffusion barrier of Li jumping from one site to another is around 0.4 eV at the dilute limit [210]. Li, however, exhibits completely different diffusion kinetics at graphite edges in contrast to those in the bulk [70, 248].

Peng *et al* show the energy profile of Li diffusion from the graphite edge towards the bulk at dilute Li concentration, figure 16. In the armchair-edged graphite, Li has to overcome an energy barrier of 0.43 eV to move from site 1 to site 2 and a 0.42 eV barrier to further move from site 2 to site 3. The direct jump from site 1 to site 3 has to overcome an energy barrier of 0.58 eV and is therefore less favourable. In contrast, for bulk diffusion, Li needs to overcome a $\sim$0.43 eV barrier to move to either adjacent site. The higher diffusion barrier at the armchair edge is caused by the compensation of Li adsorption energy at the edge site. At the zigzag edge, Li obtains two different diffusion pathways. Li diffusion from the edge (site 1) to the subsurface (site 3), where the diffusion barrier is 0.48 eV. In contrast, there is only a 0.21 eV activation barrier for Li diffusion along the edge sites (site 1 to site 2), which is much lower. This indicates that Li is extremely mobile at the zigzag edge, which can be verified by the stronger flux connecting the edge sites compared to diffusion towards the bulk (cf figure 16). Due to the surface effect identified at the zigzag edge, Li favours diffusion along the edge direction within the first sub-surface sites, as the diffusion barrier (0.41 eV) is still lower than the barrier to moving Li into the bulk (0.49 eV). Markov chain analysis was conducted in Peng *et al*'s study to examine Li diffusion from the armchair edge and the zigzag edge to a bulk site 20 Å below the edge surface (see figure 16(c)). They demonstrated that Li diffusion from the armchair edge to the bulk site is around one order of magnitude faster than its diffusion from the zigzag edge to the bulk, due to the strong binding of Li at the zigzag edge that generates a deep potential well for Li [70].

On the basis of these studies, it was shown that the graphite edges have strong effects not only on the Li intercalation energies but also on its diffusion kinetics close to the edge [70, 248]. The effect is pronounced at the zigzag edge [242, 252, 253]. Thus much more sluggish (de)intercalation kinetics are expected at that edge, compared to the armchair edge. Strategies including promoting growth of armchair edge over zigzag edge during synthesis of graphite nanomaterials [242], and tuning the edge properties by chemical doping to improve Li diffusion rate towards the bulk could be useful to enhance Li (dis)charging rate for graphite anodes [254–256].

Designing edge-controlled graphite for validating the electronic and electrochemical properties predicted by DFT is still state-of-the-art. Commercial graphite powders contain a distribution of sizes, the proportion of edge types on each particle is dependent on particle size, and it is currently not possible to form graphite with only one type of edge. This makes systematic experimental characterisation to determine the influence of edges difficult [257]. To try to understand these effects Bernardo *et al* studied the effect of hydrogen and oxygen gas etching on graphite materials with a higher incidence of zigzag or armchair edge orientations [242]. The proportion of each edge was quantified by high resolution transmission electron microscopy, with the authors finding that a higher proportion of zigzag edges leads to a less stable SEI. Velický *et al* studied the local electron transfer rate, double layer capacitance, and local density of states of the edge versus the basal plane of graphite in a microdroplet electrochemical cell [252]. This study was feasible owing to the vastly different electronic structure and electron transfer rate constant of the basal plane versus the graphite edges. It has yet to be determined if it is currently feasible to distinguish these properties for the zigzag and armchair edge, in a real electrochemical environment, through such an approach. Even so, the finding that the surface state from the zigzag edge could be a major bottleneck to the Li intercalation rate is a triumph for atomistic modelling that could direct future materials design strategies and experimental characterisation for

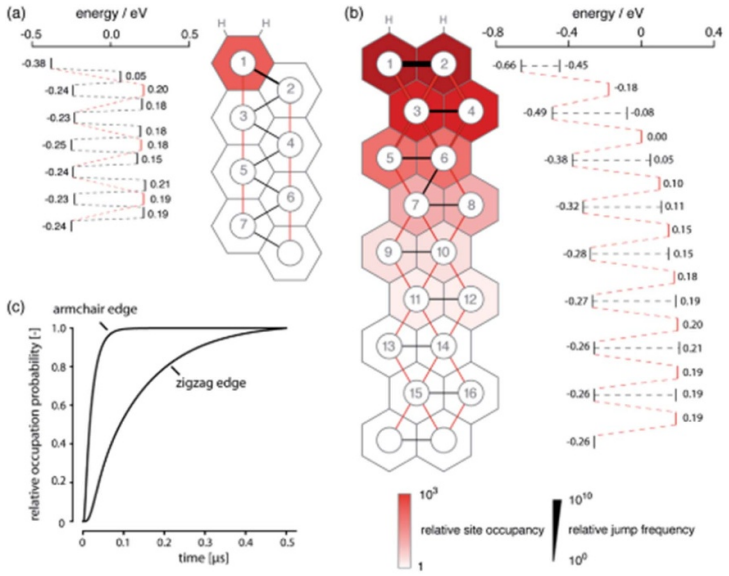

Figure 16. Li diffusion at (a) the armchair-edged and (b) the zigzag-edged graphite. The hexagons indicate lattice sites and the colours show occupancy probability relative to that in the bulk. The width of the lines connecting sites implies the jump frequencies. (c) shows the occupation probability for Li to occupy a site approximately 20 Å below the graphite edge, relative to the steady-state value after being introduced at time zero at the edge. Reproduced from [70] with permission of The Royal Society of Chemistry.

anodes [70, 258]. Moreover, the interplay between edge orientation and nitrogen/boron doping warrants further systematic exploration from both experiment and theory.

These studies can also offer some universal insights for investigating the interface effects of other materials such as the cathode. Prior to Li intercalation into graphite, the Li desolvation process is also an important step affecting the overall (dis)charging rate. However, due to the complicated solid-liquid interface, addressing the graphite interaction with the electrolyte is an extremely challenging aspect for both modelling and experiment, as discussed in the following sections. We discuss the effect of that interface on Li plating and aspects related to the SEI in the following sections.

3.3.4. Li deposition on graphite anodes

Apart from intercalation of Li ions into the graphite anode, Li ions can also deposit on surface of graphite in the form of metallic Li dendrites, which can grow during battery operation and cause internal short-circuits. Several situations for the deposition of Li metal on the graphite anode have been identified, as shown schematically in figure 17 [259]. A 'normal' intercalation mechanism is shown in figure 17(a). When the voltage of the graphite electrode drops below 0 V with respect to Li/Li$^+$, deposition of Li$^+$ ions on the graphite surface, as metallic Li, becomes thermodynamically possible, as shown in figure 17(b). The thermodynamic criterion can be satisfied when the overpotential, η_{int}, is larger than the equilibrium voltage of the stage II to stage I phase transition (∼85 mV). Deposition becomes kinetically feasible when the overpotential for the intercalation reaction (η_{int}) becomes larger than the intercalation voltage (∼85 mV), so that the graphite voltage drops below 0 V with respect to Li/Li$^+$. The overpotential originates from mass transfer limitations in the electrolyte region near the graphite edge, as shown schematically in figure 17(c). Li plating can be triggered upon local salt depletion in the electrolyte, $c_l \rightarrow 0$, if liquid diffusion is slow compared to intercalation. Solid-state diffusion between the graphite edge and the bulk, as shown schematically in figure 17(d), also contributes to this overpotential. Li plating can occur when intercalated Li$^+$ ions saturate the graphite edge ($c \rightarrow 1$) and block further insertion, if diffusion from surface to the bulk is slow compared to Li insertion at the edge. A combination of both effects can result in Li deposition on the graphite surface.

A recent DFT study by Peng *et al* has shown that in a vacuum environment: (1) Li deposition is more favourable near the graphite edges rather on the basal plane, (2) the energy barrier for Li deposition at the zigzag edge (only) increases with the degree of lithiation of the graphite, (3) chemical doping of nitrogen can increase the energy barrier and can possibly suppress the Li deposition on graphite anode on the zigzag edge [258]. More advanced models for DFT simulations in the presence of an electrolyte under applied potential (cf section 2.2.1 and [260]), have the potential to shed more light on the Li deposition phenomenon in experimental conditions.

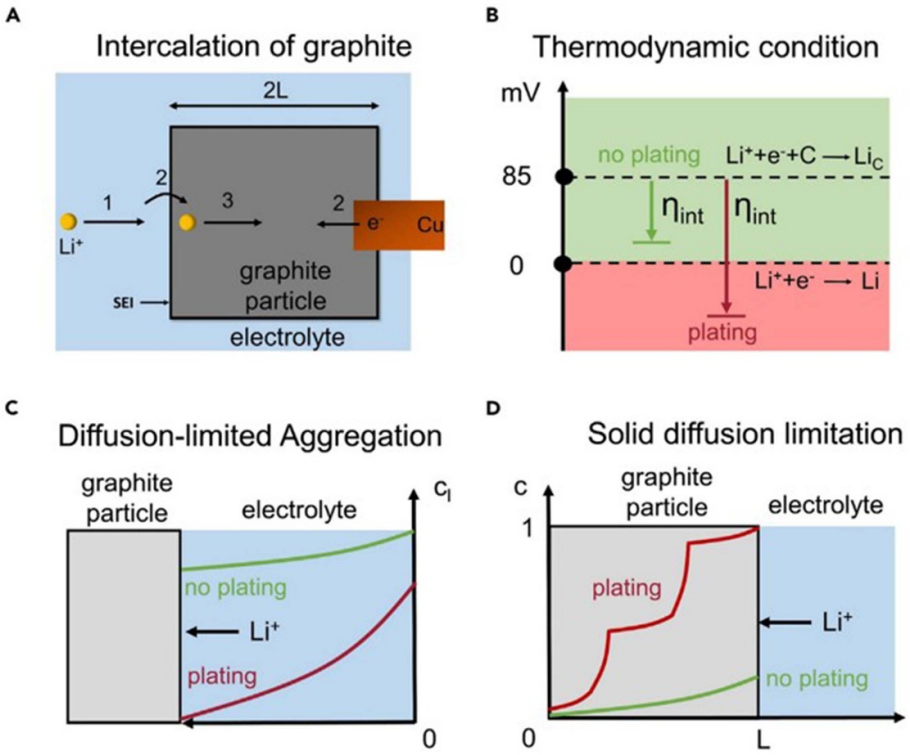

Figure 17. (a) 2D schematic of intercalation of a graphite particle. Three sequential steps take place during charging at the graphite anode: (1) Li^+ transport in electrolyte towards the reaction site; (2) Li^+ intercalation into a graphite particle (including de-solvation and migration through the SEI); and (3) Li^+ solid diffusion within the graphite particle. (b) Thermodynamic criterion for Li plating (cell voltage, $U < 0$ V versus Li/Li^+). The green and red arrows illustrate the required overpotentials to drive the insertion reaction at small current/fast insertion kinetics and large current/slow insertion kinetics. (c) 1D schematic of diffusion-limited aggregation resulting from electrolyte transport limitations. The green and red curves illustrate the Li^+ salt concentration profile in the electrolyte. (d) 1D schematic of solid diffusion-limitation mechanism. The green and red curves illustrate the Li^+ concentration profile in the graphite particle. Reprinted from [259], Copyright (2021), with permission from Elsevier.

3.3.5. Solid-electrolyte interphase

The SEI is an important component of the rechargeable Li-ion battery and is formed from deposition of the decomposition products of the electrolyte and solvent on the anode surface. The SEI allows transport of Li^+ ions but blocks the transfer of electrons, thereby stopping further electrolyte decomposition reactions [261, 262]. Here we discuss aspects of the SEI related to our discussion of Li-ion diffusion energy barrier in bulk and graphite surfaces. A recent comprehensive review on the atomistic modelling of the SEI describes several other aspects of the SEI in detail [16]:

- Electrolyte and solvent reduction mechanisms, including: prediction of the reduction voltage for each solvent and electrolyte species, the effect of the electrolyte solvation structure, the effect of anode surface termination, and the dynamic buildup of the nanometer thick SEI layer.
- Modification of the SEI by electrolyte additives and prediction of new electrolyte additives.
- Correlation of the SEI properties with battery performance, including: the electron insulating properties of the inorganic components in the SEI, the ionic conductivity of the SEI components, Li-ion desolvation at the SEI/electrolyte interface, chemical stability of the SEI components, and mechanisms of SEI growth and battery aging.
- The use of coatings to artificially design the SEI.

One way to describe the SEI is via the implicit continuum models described in section 2.2.1. Applying their DFT + implicit electrolyte model on an armchair edge of 1634-atom graphite slab in contact with a 0.5 M $LiPF_6$ in EC solution, Dziedzic *et al* calculated that a Li atom is 2.34 eV more stable at the graphite edge than in the electrolyte solution [135]. Similarly, Haruyama *et al* found favourable energetics for Li intercalation from the electrolyte solution into the graphite edge [263]. They also studied the variation in energy as a function of Li distance from the graphite edge, as shown in figure 18. In Haruyama *et al*'s model, Li intercalation is accompanied by an electron gain from the external circuit. This was implemented using a grand canonical version of electronic DFT, where the number of electrons in the electrode can change subject

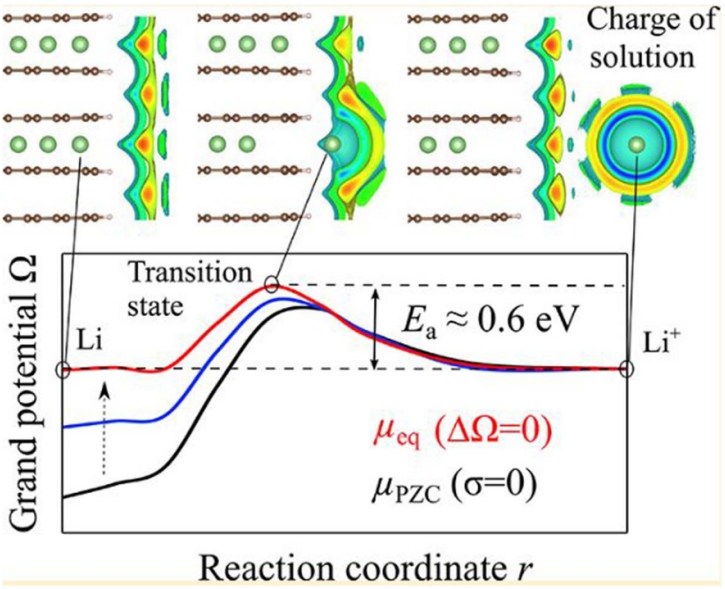

Figure 18. Profiles of grand potential Ω as a function of the Li-position during Li-intercalation process at the interface between graphite edge and an implicit electrolyte solution. The simulation is performed at conditions of constant chemical potential of electrons μ_e (constant electrode potentials similar to experiments). Reprinted with permission from [263]. Copyright (2018) American Chemical Society.

to fixed electrode potential. Correspondingly, the appropriate thermodynamic quantity to represent this ensemble is the grand potential, $\Omega = A - \mu_e N_e$, which is plotted on the y axis for several different constant chemical potentials of electrons, μ_e. Two illustrative cases include: (a) the potential of zero charge, which is the electrochemical potential of a charge-neutral Li-graphite system, and (b) the equilibrium potential (cf sections 2.3.1 and 3.2.2), where the net change in the grand potential for the intercalation reaction becomes zero. Haruyama *et al*'s simulations estimate an energy barrier of around 0.6 eV for Li intercalation into the graphite edge, which is close to the experimental measurements from impedance spectroscopy [264].

Another way to describe the SEI is via explicit consideration of SEI components. Shi *et al* performed a direct calculation of Li-ion transport in the Li_2CO_3 component of the SEI [265], via DFT-based CI-NEB calculations (section 2.1.3). Two mechanisms for Li^+ diffusion were considered, namely, the knock-off and direct hopping mechanisms, which were found to have energy barriers of 0.31 and 0.54 eV respectively, as shown in figure 19. The Li self-diffusion coefficient was calculated to be 1.1×10^{-7} cm^2 s^{-1} and 8.4×10^{-12} cm^2 s^{-1} respectively. Estimating the formation energy of corresponding defects in the lattice of Li_2CO_3 as a function of voltage, the total activation energy barrier for Li-ion diffusion was predicted to be in the 0.67–1.07 eV range for the knock-off mechanism and in the 0.92–1.32 eV range for the direct-hopping mechanism.

The predicted values of the Li-ion diffusion energy barrier by both the implicit and the explicit models described above are significantly higher than that in the bulk of graphite, which is reported to be between 0.2 and 0.5 eV (cf section 3.2.4) [76, 210, 211]. This indicates a limiting role of the SEI in determining overall kinetics of Li-ion diffusion and the overall rate-capability of Li-ion batteries.

3.4. C/Si composities

Use of anode materials capable of electrochemically alloying with lithium could allow higher energy densities than are possible with graphite. In particular, silicon, due to its high gravimetric capacity of 4200 mAh g^{-1}, has achieved tremendous attention as an anode material [266]. Si has a low electrochemical potential 0.37–0.45 V vs. Li/Li^+, which is only ~0.27 V higher than graphite [267]. Si is highly abundant, cost effective and non-toxic [267–269]. While pure Si anode materials are not presently viable, present day anode materials combine a small atomic fraction (typically 5–10 at %) of silicon with graphite to boost the gravimetric capacity of the anode [14]. However, there are certain challenges in understanding the behaviour of Si and C/Si composites that are summarised in this section.

The phase diagram of lithium and silicon shows five crystalline intermetallic Zintl-like phases: $Li_{21}Si_5$, $Li_{13}Si_4$, Li_7Si_3, $Li_{12}Si_7$, and LiSi [270]. However, LiSi is not accessible under electrochemical conditions, since

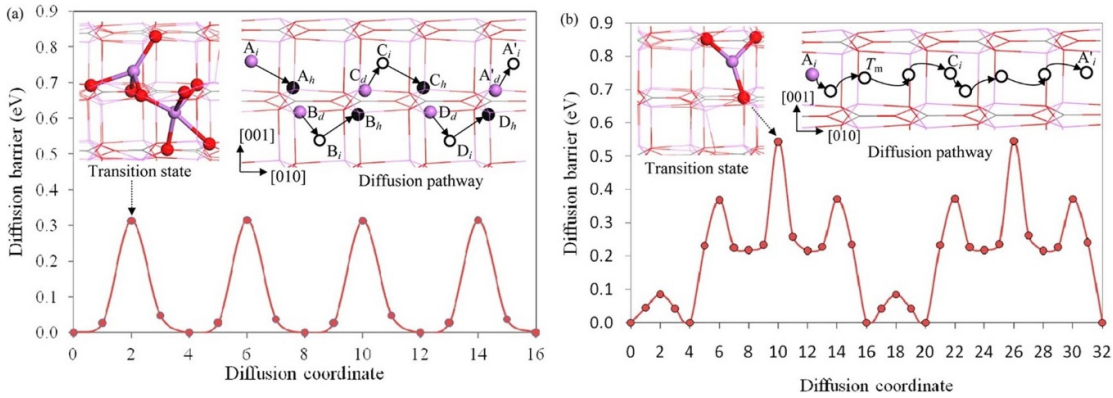

Figure 19. Energy barrier for Li-ion transport in the SEI via (a) knock-off and (b) direct hopping mechanisms. Reprinted with permission from [265]. Copyright (2012) American Chemical Society.

it is synthesised under high pressure, and the stoichiometry of $Li_{21}Si_5$ is disputed, with a mixed $Li_{21}Si_5/Li_{22}Si_5$ phase also proposed [271]. Under electrochemical conditions, metastable phases with compositions $Li_{15}Si_4$ [272] and amorphous Li_xSi_y can be formed [273]. It has been proposed that a different reaction pathway between these phases during lithiation and delithiation contributes to the observed charge/discharge hysteresis in lithium silicides and C/Si composites . In particular, Jiang *et al* found that the crystalline phase $Li_{15}Si_4$ is accessed during lithiation, but the lattice undergoes an amorphisation process during delithiation, with the latter step being rate determining [272]. This limits the utility of ground state DFT calculations for understanding the Li-Si system under operating battery conditions, and is therefore a challenge for MSM.

An additional challenge is the volume expansion. Upon full lithiation, the volume of Si can expand to more than three times its original volume, which means the Si electrodes do not retain their morphology during prolonged cycling or, even worse, some particles become detached from the electrode assembly [267, 269, 274]. This volume expansion/contraction during cycling also leads to severe cracking and degradation of the SEI. It is for mainly these reasons that pure Si anodes are not currently commercially viable and must be combined with graphite. Several strategies have been proposed to change the morphology to mitigate these issues, including development of different Si robust nanostructures (0D or hollow nanoparticles, 1D nanowires, 2D film-like Si, and 3D Si structures) [267], and the development of composites (Si/carbon composites, Si/polymer composites, Si alloys, and Si/metal oxide composites) [14]. While modelling the complex nature of the degradation pathways of the Si, Si-composites and their SEIs is presently out of reach of atomistic methods, these techniques nonetheless emerge as natural tools for high-throughput screening of different promising anode materials [275]. These approaches can also tell experimentalists the most promising part of the parameter space in which to perform more extensive, time consuming, and sometimes costly characterisation.

A more comprehensive overview of the application of mesoscale models to challenging composite systems is presented by Franco *et al*, with the volume averaging approach highlighted perhaps being particularly applicable to Si and C/Si systems [233]. Particularly for carbon anodes in combination with Si or silicon suboxide (SiOx), collectively referred to as C/Si or C/SiO_x, it may presently be necessary to sacrifice some details of the atomic level description to enable these systems to be tractably modelled at either mesoscale or continuum levels. Regarding the dynamic and metastable behaviour described above, kMC would be a natural technique to bridge length scales and include different time scale dynamic events, as explained in a recent review dedicated to this technique [104].

3.5. Outlook and challenges for anodes

Graphite remains the predominant anode material in most Li-ion cells, due to its suitably high capacity of 372 mAh g^{-1}, an operating potential close to 0 V vs. Li/Li^+, and its compatibility with liquid organic electrolytes. Alternative materials that form solid solutions with lithium (including silicides) presently do not have sufficient long term structural stability to be used as the primary anode material, requiring them to be composites with graphite. The development of graphite-based anodes has relied upon not only understanding staging formation in bulk, but also upon the development and understanding of a stable SEI and its implications of that SEI for cell longevity and (de)intercalation rate behaviour.

Advancements in developing ASSBs have resulted in additional research of Li metal anodes, as reviewed by Fang *et al* [276] and Li *et al* [277]. In this section, we have summarised the safety and degradation

challenges caused by lithium plating on graphite anodes. The use of Li metal as the anode for LiBs and ASSBs still face similar issues regarding redeposition of metallic Li as dendrites and consumption of cyclable lithium [276, 277].

Many aspects of modelling the bulk behaviour of lithium (de)insertion graphite are well understood. As shown in this section, challenging aspects like quantifying the Li ion ordering with lithiation fraction can only be obtained by combining experimental observations with atomistic models. However, there are challenges with atomistic modelling in anodes that hinder improvements in capacity, rate performance, safety and durability of the anode itself and, consequently, full Li-ion cells. In addition, there are challenges with transferring insights from atomistic modelling in a scalable form to models on different length and time scales, while maintaining physical integrity. These outstanding challenges are:

- The role of metastable phases in the kinetics of staging behaviour. New theoretical frameworks should be developed to understand the connectivity between different phases and the effect of this on the path dependency of measurable behaviour like the OCV. These distinct pathways also have implications for mechanical degradation and fracture. A promising approach in this direction is the semi-grand canonical framework developed by Van der Ven *et al* describing layered transitions in cathodes [9, 231, 278, 279] that could also be applicable to graphite anodes and other candidate materials like silicides.
- The role of the configurational, vibrational and electronic entropy of lithium insertion. Longer length scales, i.e. continuum models, still assume that the entropy follows an ideal solid solution behaviour. The importance of configurational entropy to the phase transitions of lithium in graphite was highlighted in previous sections [71, 91, 225]. One promising extension would be to use the results from MC calculations to parameterise a phase field model, such as those developed by Bazant [95], Guo *et al* [96] and Bai *et al* [97], with a more realistic Hamiltonian and thus include entropy effects in a rigorous way.
- Regarding dynamics, kMC approaches with an empirical Hamiltonian show promise [102–104, 220], but are limited by the length and time scale of the properties that can currently be modelled. A possible solution would be to develop an ECI Hamiltonian linking with a linear scaling DFT code, such as ONETEP. Parellelisation of the kMC calculations could be achieved by exploiting recently developed graphical processing unit architectures.

Superior models of surface and interface effects are needed. This includes development of a physically rigorous version of the Butler–Volmer equation, which is valid for electron transfer but is conventionally assumed to be valid too for ionic transfer in Li-ion batteries. The current models of the interface are too simplistic or represent an ideal situation instead of dealing with the complex reality of the SEI. A systematic coarse-graining approach involving multi-length- and multi-time-scale physics can help in understanding the complex nature of the SEI and its influence on performance of Li-ion batteries. Controlling and improving the properties of SEI is crucial to improve the overall rate capability of Li-ion batteries, as that interface is the bottleneck for Li-ion diffusion.

Regarding graphite, atomistic modelling can be used to predict systematic modifications to the edge morphology or the use of dopants on the graphite edge [70, 254, 255], or tuning of the interlayer carbon spacing [214] to enable systematic tuning of the rate performance. This approach has the potential to lead to more robust interfaces and strategies to tune the anode voltage and dynamics, thus tuning nucleation barriers and mitigating the risk of lithium plating [258]. In this regard, it should be pointed out that decoupling the rate performance of different graphite edges is still a great challenge from experiment and therefore this finding represents a success for atomistic modelling.

We highlight that there are still outstanding challenges regarding modelling metastable behaviour, volume expansion and degradation in solid solution materials such as silicides. So far, high-throughput atomistic modelling techniques have provided a predictive tool to suggest anode materials that are promising for more extensive experimental characterisation. However, composite materials such as C/Si and C/SiO_x, which are increasingly being used in commercial anodes, are presently challenging to model on the atomistic scale. In this regard, an extension to mesoscale modelling, such as a volume averaged approach as suggested by Franco *et al*, could be a promising way to model challenging materials such as composites, in which each component experiences different degrees of volume expansion [233].

4. Electrolytes

4.1. Introduction

Electrolytes are a medium for the transport of charged ionic species, i.e. Li^+, between the electrodes [280, 281]. While the electrons flow through the outer circuit, an equal ionic current flows through the electrolyte to balance the charge. Electrolytes can be categorised into two groups: liquid and solid, both of

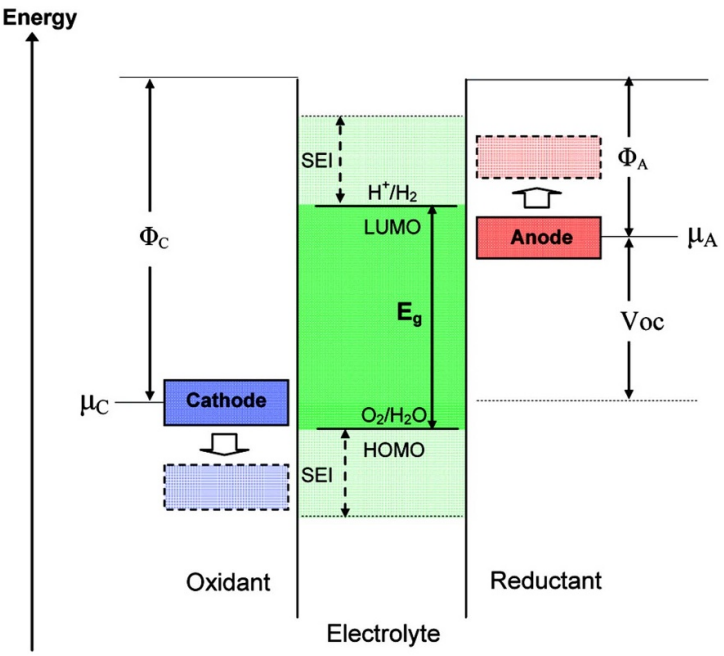

Figure 20. Schematic open circuit energy diagram of an aqueous electrolyte. Φ_A and Φ_C are the anode and cathode work functions. E_g is the electrochemical stability window of the electrolyte. If $\mu_A >$ LUMO and/or $\mu_C <$ HOMO, the electrolyte would be thermodynamically unstable and its usage would require kinetic stability through the formation of a SEI layer. Reprinted with permission from [2]. Copyright (2010) American Chemical Society.

which have their benefits and drawbacks. Liquid electrolytes are currently used in commercial LiBs and offer high conductivities, but have safety concerns [282–284]. Solid electrolytes are a safer alternative that are approaching commercialisation and can potentially reach higher energy densities [285]. There are several key aspects to the design of either liquid or solid electrolytes in LiBs: their electrochemical stability window [2, 286], ionic conductivity [287, 288], electric double layers [280, 289], SEI [290, 291], and safety, which are all discussed in the following sections [292, 293].

4.1.1. Electrochemical stability window

An electrolyte can be safely used within its electrochemical stability window, which defines the voltage range outside of which it can be oxidised or reduced [2]. The electrochemical stability window is schematically depicted in figure 20, showing the electronic energy levels in the electrodes and electrolyte of a battery cell. If the anode electrochemical potential, μ_A, is above the lowest unoccupied molecular orbital (LUMO) of the electrolyte, the electrolyte will be reduced. Conversely, if the cathode electrochemical potential, μ_C, is below the highest occupied MO (HOMO) of the electrolyte, the electrolyte will be oxidised. Therefore, the electrochemical potentials, μ_A and μ_C, should lie within the energy gap, E_g, between the LUMO and the HOMO of the electrolyte, constraining the OCV, V_{oc}, of a battery cell, such that [2]:

$$eV_{oc} = \mu_A - \mu_C \leqslant E_g, \tag{44}$$

where e is the elementary charge, i.e. the magnitude of the charge on an electron.

The energy gap, E_g, for an aqueous electrolyte is ∼1.3 eV, severely limiting the OCV, V_{oc}. In order to obtain a higher OCV, non-aqueous electrolytes with larger E_g have been used in LiBs [2, 292]. A good summary of electrochemical stability windows of different classes of non-aqueous electrolytes including (organic and inorganic) liquids, solids, ionic liquids, polymers and their combinations is presented by Goodenough and Kim [2]. Commonly used organic liquid electrolytes, such as 1 M $LiPF_6$ in 1:1 EC:DMC, have stability windows between ∼1.3–5.0 V, while ionic liquids have stability window between ∼1.0–5.3 V. A desirable property of solid electrolytes is their larger electrochemical stability window (∼0.0–8.0 V), compared to liquid electrolytes [2], allowing them to operate within a larger voltage window and thus increase the energy density of the battery.

4.1.2. Ionic conductivity

High ionic conductivity ($>10^{-4}$ S cm^2) in the electrolyte (liquid or solid) and across the electrode-electrolyte interphase enables a high rate-capability of the overall Li-ion battery [2, 287, 288]. Generally, the ionic conductivity of liquid electrolytes is higher than that of solid electrolytes. However, new classes of solid materials have been found with ionic conductivity surpassing that of liquids (cf section 4.3), known as superionic conductors. The ionic conductivity of commonly used liquid electrolytes is several orders of magnitude higher than that in the bulk of electrodes and the electrode-electrolyte interphase [287].

4.1.3. Electric double layer

During the charging of an electrode in contact with a liquid electrolyte, excess charge develops at the electrode surfaces. This triggers the rearrangement of electrolyte ions in the electrolyte solution, such that counter-electrolyte charges accumulate near the electrode-electrolyte interface, forming an interfacial charge density perturbation, to achieve local electroneutrality at the interface. In the classical system of dilute electrolytes, electroneutrality is achieved by the formation of a monotonically decaying 'double layer' [280]. The double layers in solid electrolytes cannot be directly observed experimentally, so modelling can be used to rationalise their effects. Several models of the electric double layer in electrochemistry exist, such as Helmholtz, Gouy–Chapman, and Gouy–Chapman–Stern [281]. Early models were limited in sophistication: the Helmholtz double layer model suggested charge screening by a plane of counter-charged electrolyte ions near the electrode surface, resembling a capacitor. In contrast, the Gouy–Chapman model screens charge via a diffuse layer of electrolyte ions, decaying monotonically to their bulk concentration value, where the electric potential will fall to zero. The Gouy–Chapman–Stern model accounted for discrepancies encountered by including both a Helmholtz layer of counter charge, as well as a diffuse layer of electrolyte ions, as shown schematically in figure 21(a). These continuum models of electrolyte ions are also being integrated with quantum mechanical methods, such as DFT (cf section 2.2.1). Bhandari *et al* recently implemented such a hybrid quantum-continuum model to achieve electroneutrality in simulations of charged electrochemical interfaces, based on a modified PBE [66].

At the interface between solid electrolytes and electrodes, a similar decay in charge is observed. However, in this case, the charge carrier is the charge vacancy. Maier discuss the theory of this decay in detail [294] and new continuum models continue to be developed for solid electrolytes [295–298]. Swift *et al* present a model for formation of the double layer in solid-solid electrochemical interfaces, based on the Poisson–Fermi–Dirac equation. The resulting space charge layer of point defects in a solid electrolyte material is shown schematically in figure 21(b). However, this study only accounts for the effect of correlations between ions by limiting the concentration of defects in the interfacial layer to be below a certain value.

At higher concentrations, screening of electrodes changes markedly in liquids, with a new regime emerging when the Debye screening length is of roughly equal value to the ionic diameter. In this regime, charge is screened by means of exponentially damped oscillations of counter-ions and co-ions, in an ordered interfacial structure known as overscreening [299]; a structure that has previously been observed experimentally for liquids [300–303]. In 2021, Dean *et al* became the first to propose the existence of a similar oscillatory decay at solid electrolyte grain boundaries [304].

4.1.4. Solid-electrolyte interphase

The 'interface' described above is basically a two-dimensional surface between the electrode and electrolyte. In LiBs, the electrolyte reacts irreversibly and decomposes on the electrode surfaces, leading to the formation of a distinct phase, several nanometres thick, between the electrode and the electrolyte, known as the SEI [290]. The ability to form a stable interphase, which is both ionically conducting and electronically insulating, is an important criterion for the selection of an electrolyte material. The electron insulating property of the SEI is important, to stop further decomposition of the electrolyte on the electrode [2, 292]. High ionic conductivity through the SEI is important, otherwise this can form a bottleneck for the overall rate capability of LiBs [16, 293]. While the SEI was originally discovered in liquid electrolytes, its rate-limiting behaviour is now also observed in ASSBs [291].

The two major classes of electrolyte materials, solid and liquid electrolytes, are discussed separately. We focus on the atomistic modelling of different types of liquid and solid electrolytes and their battery related properties. For the liquid electrolyte section, this includes the bulk structure, diffusion properties, solvation energies, and activity coefficients of different solvents. For the solid electrolyte section, there is a particular emphasis on the ion transport mechanisms, material stability, and the electrode-electrolyte interfaces. Finally, we discuss the individual challenges and outlook for future atomistic modelling of both liquid and solid electrolytes.

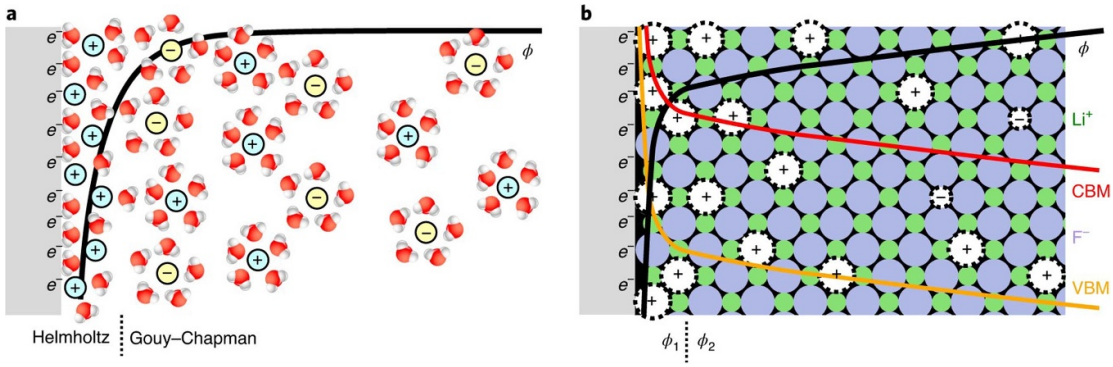

Figure 21. Schematic comparing the double layer formed at the solid–liquid and solid–solid electrochemical interfaces. (a) For the solid–liquid interface, excess electrons on the electrode are balanced by increased density of solvated positive ions in the liquid electrolyte. ϕ is the electrostatic potential and is mediated by the Helmholtz layer, followed by exponential decay in the diffuse layer (described by Gouy–Chapman theory). (b) For the solid–solid interface, excess electrons on the electrode are balanced by increased density of positive point defects in the solid electrolyte. Electronic band bending occurs in the solid electrolyte. ϕ_1 and ϕ_2 are the electrostatic potentials next to and further from the interface. Electronic band-bending is shown via the valence-band maximum (VBM), also known as the HOMO, and conduction-band minimum (CBM), also known as the LUMO. Reproduced from [289]. CC BY 3.0.

4.2. Liquid electrolytes

4.2.1. Introduction to liquid electrolyte materials

The most widely used liquid electrolyte in Li-ion batteries is $LiPF_6$ in a solvent, which is typically a mix of two or more solvents, for example EC, DMC, propylene carbonate (PC), or ethyl methyl carbonate (EMC), in order to achieve the competing objectives of dissolution of a high concentration of salt, low viscosity, and high dielectric constant at typical operational temperatures [22, 194, 292, 293, 305]. Cyclic carbonates (EC, PC) have a higher dielectric constant but also high viscosity, while 'linear' carbonates (DMC, EMC) have low viscosity but also a low dielectric constant. For that reason, mixtures of solvents are often used to optimise performance in a specific application [22, 194, 306]. However, in the last two decades there has been continued innovation in electrolyte mixtures, including ionic liquids [307] and salt in water-based systems [308]. This section will touch on both traditional and emergent electrolyte solvents.

4.2.2. An introduction to modelling liquid electrolytes

The modelling of liquid electrolytes for conventional batteries is a broad and diverse field. Over the past 20–30 years, atomistic modelling has helped to shape the fundamental physics of liquids, determining a new physical basis and validating decades-old pen and paper theories of concentrated electrolytes [309–312]. Here, we focus on the development of liquid electrolyte models and the considerations needed when modelling these materials, before moving on to their applications in measuring different properties.

Atomistic modelling of liquid electrolytes can be broadly separated into *ab initio* and classical (potentials-based) MD modelling (cf section 2.1.6). These are complementary techniques which can be used to aid each other. For example, *ab initio* calculations are able to provide information on the electron distribution, required for parameterising the non-bonded components of force fields used in classical MD. Classical MD can also be used to provide the starting conditions for DFT calculations. *Ab initio* and classical methods can also be combined in quantum mechanics/molecular mechanics studies, where the larger system is treated classically with a smaller sub-region being modelled using *ab initio* methods. For example, a study by Fujie *et al* used the 'Red Moon' method to investigate the formation of the SEI at the metallic electrode [313].

In this section, we first discuss the separate design and use of *ab initio* and classical MD methods, followed by their application to determine properties in the bulk liquid electrolyte. Finally, we discuss the application of atomistic methods to SEI investigations, from the perspective of the liquid electrolyte (complementary to the solid-focused SEI discussion given in section 3.3.5).

4.2.3. Ab initio *modelling of liquid electrolytes*

Ab initio calculations on liquid electrolytes provide critical information that has been used to explain their behaviour in experimental applications. For many years, DFT calculations (cf section 2.1.1) have been used to provide information on the electrochemical stability of solvents [314]. Modelling the electrochemical stability allows more complex effects to be decoupled, which is not possible through experimental techniques, and these models have aided the understanding of the functional form of the LUMO and

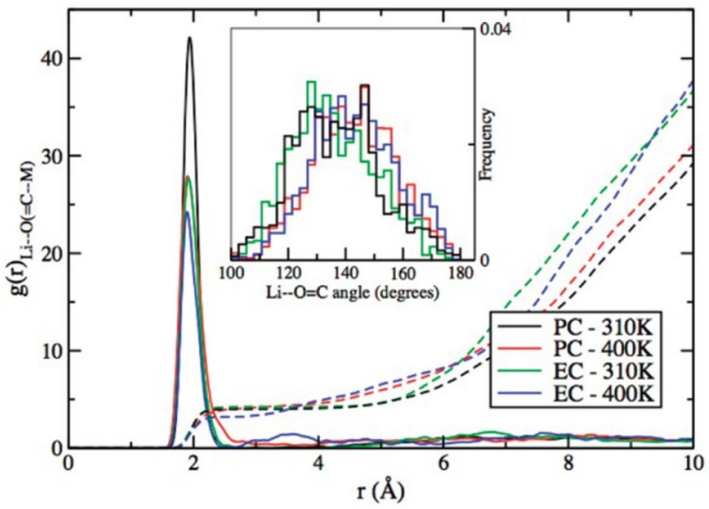

Figure 22. Partial RDF of Li-ion with the carbonyl oxygen of EC and PC along with the partial-density weighted integral (dashed lines) which equals the Li-ion coordination number. In both electrolytes, the Li–O (carbonyl) distance is ∼2 Å and the first-solvation shell of Li-ion has four EC or PC molecules, consistent with the experiments. The inset shows the histogram of the Li–O=C angle. Reprinted with permission from [321]. Copyright (2011) American Chemical Society.

HOMO, opening routes to raise the stability window by design. Computational models were further developed in 2011 when Ong *et al* used a combined MD and DFT approach to model the electrochemical stability window of several ionic liquids with a higher degree of accuracy than previously seen [315]. This methodology has since been widely used in studying the stability of various ions in solution, with many key studies being based on the initial work of Vuilleumier and Spirk [316]. Here, the authors modelled the ionisation of sodium and silver using AIMD, which was later extended to model fluctuations in the coordination shells [317], and then to model copper [318] ions and the redox of molecular species [319]. However, the applicability of any such method is somewhat dependent on the solvent. This point was made clear by Lynden-Bell on the subject of the difficulties of applying Marcus theory to ionic liquids, where long range electrostatic interactions may become important [320]. This type of modelling is important, as single atom events cannot easily be viewed in isolation experimentally, with a temporally and spatially averaged perspective of the system being obtained using most experimental probes. In explicit atomistic simulations, behaviour can be observed at an atomic scale, as shown in further detail in section 4.2.5.

Ab initio modelling using DFT provides a parameter-free approach to simulating the properties of liquid electrolytes. For example, Ganesh *et al* demonstrated the use of AIMD of liquid electrolytes, using the PBE-generalised gradient approximation exchange-correlation functional to calculate the statistical and dynamic properties [321]. They performed simulations of $LiPF_6$ at 310 and 400 K in EC and PC at densities comparable with typical experimental compositions. They observed a spontaneous decomposition of $LiPF_6$ into Li^+ and PF_6^- and a coordination number of 4 for solvated Li^+, similar to experimental observations. The plots of the radial distribution function (RDF) of Li-ion with the carbonyl oxygen of EC and PC are shown in figure 22. The Li–O (carbonyl) near-neighbour distance in PC is found to be ∼1.94 Å at 310 K and ∼1.90 Å at 400 K, quite close to the experimentally measured distance of ∼2.04 Å by time of flight neutron scattering experiments [322]. The Li–O (carbonyl) peak for EC is ∼1.92 Å at 310 K and ∼1.90 Å at 400 K, which is quite close to that for PC. Comparatively, a classical MD simulation predicted a Li–O (carbonyl) peak at ∼1.70 Å [323]. The Li–O=C bond angle distribution is shown in the inset of figure 22. The centre of the distribution for PC is at 140° which is in agreement with the experimentally measured value of 138° [322]. Here, the distribution for EC is predicted to be similar to that for PC. Calculations using classical MD simulation also predict EC and PC to have similar distributions, though at a much higher Li–O=C angle ∼160° for both solvents [323].

Perhaps the most enticing possibility regarding *ab initio* methods at interfaces is to study the liquid-electrode interfacial behavior. The physics of such a study are, however, complex and therefore trade-offs in functional choice and solvent model may need to be made, in order to make calculations feasible. Lespes and Filho used an implicit solvent model to study the interfacial electrochemistry of lithium EC solutions [324].

While AIMD is free from the effects of arbitrary parameters and is highly accurate, a major limitation of this approach is the high computational cost, restricting the reachable time- and length-scales to just tens of

pico-seconds and between hundreds (conventional DFT) and thousands of atoms (linear-scaling DFT approaches, cf section 2.1.2), resulting in inaccuracies and irregularities in the calculations.

When considering the impacts of small length scales, the critical issue is the introduction of spurious long- to medium-range correlations of atoms and molecules. As liquids do not exhibit long-range order, the presence of periodic images that are located at exactly a cell's width in all directions introduces an unphysical correlation. This is observed in the modelling of systematically disordered solids in smaller cells [325]. For example, Zhao *et al* recently revealed that there is a distribution of different, low-symmetry, local motifs in cubic halide perovskites, such as tilting and rotations, which are only observed if you allow for a larger-than-minimal cell size [326]. Beyond truncating the RDF to a shorter distance than is optimal (i.e. half the shortest distance between periodic images), this effect will also introduce (normally small) inaccuracies in thermodynamic and dynamic quantities [85, 327–329]. These inaccuracies are of a particular concern in liquid electrolytes, as the electrostatic interactions between ions gives rise to longer range interactions, even when the Debye length is far smaller than the system size [330].

The short time scales of *ab initio* simulations can, particularly for more viscous liquids, lead to highly non-ergodic (fully-sampled) simulations. When snapshots throughout the whole trajectory are highly correlated [331], this can lead to problems for both dynamic and equilibrium studies.

Often, neither time correlation nor finite size have a significant detrimental effect on the reproducibility of experimental results in *ab initio* studies. However, in specific studies where they need to be avoided, or where a quantum description of a liquid electrolyte provides no significant advantage over a classical description, it is beneficial to turn towards far less computationally expensive potentials-based simulations, allowing larger and longer simulations.

4.2.4. Classical modelling of liquid electrolytes

Classical simulation of liquid electrolytes includes classical force field-based MD (cf section 2.1.6) and the related field of classical MC (cf section 2.1.5). Classical MD, also known in solid-state communities as potentials-based MD, is a broad field which uses many different types of force fields for different studies. The development of force fields for ionic solids is described in section 2.2.2, whereas here we evaluate the force fields used for liquid electrolytes and the considerations for developing them. Historically, force fields for different electrolyte systems have developed at similar paces. Here, we use the example of the development of force fields for ionic liquids.

Electrolyte solvents, from water to molecular solvents and ionic liquids, pose a challenge that is not normally present in the solid-state, specifically the need to model covalent bonding. This is achieved by splitting the potential acting on each atom into bonding and non-bonding contributions. The non-bonding component accounts for the effects of electrostatics, dispersion, and degeneracy pressure; and the bonding component accounts for the effects of covalent bonding. In classical modelling of liquid electrolytes, we are mainly interested in the behaviour within the electrolyte's electrochemical stability window (cf section 4.1). Therefore, the vast majority of classical studies model bonds with unbreakable, harmonic potentials. There are four distinct types of bonded potential [331, 332]: bonds, angles, dihedrals, and improper dihedrals. These can be traced back to the parameterisation of force fields, such as OPLSA-AA [333, 334], and are often parameterised from spectroscopic force constants. There are many ways of defining bonded potential types in available codes [113, 332], though their discussion is beyond the scope of this review. Atoms which are subject to a bonded potential are often wholly, or partially, excluded from non-bonded interactions, though in large molecules, non-bonded intramolecular interactions are important. Alternatively, bonds can be kept rigid using a constraint algorithm [335–337].

When developing force fields, generally, it is the non-bonded force field components, in particular the partial charges on atoms, which are more frequently varied. A common model for liquid electrolytes is the OPLS-AA force field [334]. This is a Lennard-Jones potential-based force field with an additional coulombic term [338–341]. Further developments can be made from this base force field, such as the CP&P force field [333, 342–344], describing a wide range of ionic liquid cations and anions. Some non-bonded parameters, particularly charges, were varied from OPLS-AA. The charges on the individual molecules are obtained from DFT calculations, in this case by use of the charge mapping algorithm CHelpG [333] (though other algorithms may also be used [345–347].)

Electrostatic interactions are important when modelling charged electrolytes, as are the effects of polarisability. Often it is advantageous in a non-polarisable force field to scale the charge on each ion down from a value of 1e [348–350]. This accounts for the effect of polarisability on the strength of electrostatic interactions between ions, which is particularly important for transport properties. However, other force fields have been defined to account directly for polarisability [349]. As described in section 2.2.2, polarisability can be introduced to a force field by the employment of Drude Oscillators (core shell model) [332, 348, 349]. This approach is computationally cheap and is core to the polarisable ionic liquid force field

developed from CL&P by Schröder [348]. A more advanced representation of polarisability can be provided by intrinsically polarisable force fields, normally based on the Fumi-Tosi potential [351]. This method has been used for molten salts [352], ionic liquids [349, 353], and lithium salts in molecular solvents [354–356]. This provides the best description of polarisability in a classical force field, however, there is an associated higher computational cost, and a particular code, such as metalwalls [357]) is often required to implement it.

The development of force fields for metal cations has seen an equal level of discussion and interest. These cations can be slightly easier to model, owing to their relative non-polarisability [349, 358, 359]. They are frequently modelled as Lennard-Jones spheres to match the potential in the prevailing solvent models (SPC and OPLS-AA). For alkali and alkali earth metal cations, a wide range of values of σ (excluded volume) and ε (interaction strength) can be used, as the basic energetics associated with one of these force fields can be recovered for many pairs of sigma and epsilon values. The choice of which pair of parameters to use is normally driven by which property requires the highest degree of accuracy for the targeted study [358]. It is worth noting that many force fields used to modelled the electrolytes of specific interest to us here, were parameterised for aqueous solutions [358].

4.2.5. Bulk structure and landscaping

For structural analysis of liquid electrolytes, analysis of the RDF is the mostly widely used approach. Modelling of structural properties in this capacity provide more information-rich data compared to scattering, especially in complex systems, and is less labour intensive. RDFs can be converted to structure factors by a simple Fourier transform into reciprocal space, allowing for easy comparison with experimental structure factors [350, 360–362], subject to re-scaling for the specific intensities associated with different atoms. This method has been used frequently for a broad array of electrolytes and has seen particular utility for ionic liquids, where the large, inhomogenous ion surface can lead to complex patterns, for which MD can provide explanation. Modelling of this sort of behaviour has been performed for aprotic [363] solvate ionic liquids [350], imidazolium salts [361], lithium carbonate solutions [364], and highly concentrated aqueous solvents [360].

The RDF is closely related to potential of mean force acting on a particle, however, the physical relevance of RDFs goes further than this. The mean force describes the changing potential landscape acting between particles as they approach one another [331]. Information on the potential of mean force is exceptionally challenging to obtain experimentally, which is why modelling techniques are frequently used in colloidal systems, as outlined below, where this information is also of interest [330, 365–370].

The form and gradient of the decay of the RDF towards an asmyptote is crucial when studying the charge screening properties of an electrolyte. These charge screening properties have a particularly prominent effect on electrolyte behaviour when confined [299], for instance, in a nanoporous electrode [371]. Surface force experiments [365] and fluorescence [366] based methods do provide an indirect experimental probe of charge screening. However the form of the decay in the correlations between charges, which can be either damped oscillatory or monotonic, cannot be observed, and both methods are restrictive in the systems that can be studied. Atomistic studies of this decay are able to resolve the form of this decay with a great deal of precision, allowing direct calculation of many body correlations [330, 367, 368]. This provides validation to integral equation theories, which can describe confined electrolytes with greater accuracy [369, 370].

As well as being generated from an RDF, the potential of mean force can be obtained by direct calculation by use of centre of mass pulling, umbrella sampling [332], or running multiple calculations with ions frozen an exact distance apart from one another. When modelling liquid electrolytes, this method is also used to study the approach of ions to an electrode, where the energetics associated with decoordination from the solvent and coordination to the electrode can be modelled. Such information about the energetics of ion approach is not directly accessible experimentally and therefore this allows us to understand the liquid electrode interface more intimately. For instance, in the solvate ionic liquid $[G4(Li)]_+[TFSI]_-$, a lithium sulfur electrolyte, this sort of analysis gives an understanding of the interplay between dechelation and approach to electrode which would not have been observable experimentally, nor explainable with mean field theory [372, 373]. In another example, Sergeev *et al* looked at the approach of oxygen and lithium based species towards electrodes [374]. Here, the authors performed MD simulations of the electrode/electrolyte interfaces of a Li–O_2 cathode with an experimentally relevant potential in 1 M dimethyl sulfoxide solution of $LiPF_6$ salt. They found that oxygen anions are effectively pushed out of the reaction layer, making the second reduction of superoxide anion improbable, indicating the main cause of the electrode surface passivation is the presence of lithium superoxide near the electrode surface. This mechanistic result could not be obtained experimentally due to the number of side reactions; however, the ability of atomistic modelling to simplify the problem allowed for the mechanism to be elucidated. Sergeev *et al* proposes a way to suppress the passivation by shifting the equilibrium $\dot{O}_2^- + Li^+ \rightleftharpoons LiO_2$ to the side of separately solvated ions, for example, by using solvents resulting in lower free energy of the ions [374].

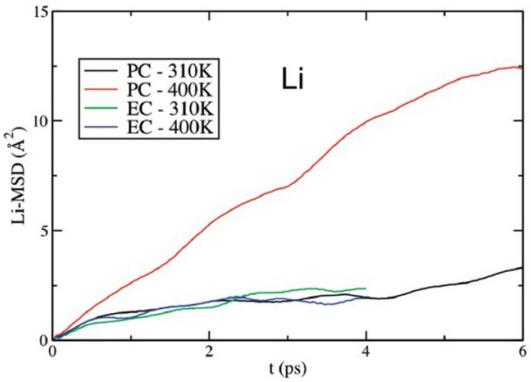

Figure 23. Mean-squared displacement of solvated Li-ion in EC and PC. Reprinted with permission from [321]. Copyright (2011) American Chemical Society.

4.2.6. Li-ion diffusion

Diffusion (cf section 2.3.3) plays a critical role in the operation of liquid electrolytes through its impact on conductivity. However, in liquid electrolytes its impact goes deeper, as the dielectric constant of liquids consists of both dipolar and ionic contributions. These two contributions can be obtained by analysis of the dipole orientation and current auto-correlation functions using the Einstein–Helfand method. For example, Coles *et al* performed this analysis on four liquid electrolytes (three in aqueous solvent and one in a common organic solvent mixture): aqueous solutions of LiCl, NaI, and lithium bistriflimide (LiTFSI), as well as the same LiTFSI salt solvated in an equimolar mixture of dimethoxyethane (DME) and 1,3-dioxolane (DOL) [330]. Here, it was shown that for polar solvents, the dipolar contribution is nearly always dominant, with the current making a small corrective contribution which could feasibly be neglected (particularly for more dilute systems). For ionic liquids, which contain ionic species that can exhibit a net dipole, such as TFSI, both dipolar and ionic contributions would be observed. The effect of molecular ions having simultaneous charges and dipoles was explored by Schröder, who showed that even more thorough treatment may be required to observed the impacts of their interplay [375, 376]. These contributing factors cannot be easily/feasibly disentangled experimentally.

The self-diffusion coefficient can be calculated from the slope of the mean-squared displacement, according to the Stokes–Einstein relation. For example, Ganesh *et al* calculated the mean-squared displacement of solvated Li-ion in EC and PC solvents from AIMD, as shown in figure 23. For PC, the self-diffusion coefficient is calculated to be $\sim 0.7 \times 10^{-9}$ m^2 s^{-1} at 310 K while the experimentally measured value of self-diffusion coefficient at 303 K is $\sim 0.16 \times 10^{-9}$ m^2 s^{-1} [377]. For EC, it is calculated to be $\sim 1.0 \times 10^{-9}$ m^2 s^{-1} at 310 K, while the experimentally measured value of self-diffusion coefficient at 313 K is $\sim 0.21 \times 10^{-9}$ m^2 s^{-1} [377]. At 400 K, the calculated diffusion coefficient for PC increases to $\sim 3.7 \times 10^{-9}$ m^2 s^{-1}, while it remains the same for EC. It is notable here that the Li-ion diffusion in the electrolyte solution is 4–5 orders of magnitude higher than that in the bulk of electrodes, e.g. in the graphite anode (cf section 3.2.4).

Investigation of the diffusion of different ions subject to a field gives a sense of the diffusion rate of specific ions and also an idea of exchange rates of solvent molecules. This information can be obtained using NMR, however, atomistic models can provide more detailed data, as outlined here. For instance, strongly coordinated solvents will have diffusion coefficients closer to the ions they are coordinated to, whereas less strongly coordinated ligands will have diffusion coefficients dissimilar from the coordinating ion [350, 354, 378–380]. Examples of this behaviour can be found in the MD studies of Borodin *et al*, which looked at diffusion in lithium solutions of both the common carbonate [354] and ethylene glycol oligomer solvents [379]. For the common carbonate, MD predictions of the ion and solvent self-diffusion coefficients and conductivity were in good agreement with experiments, with approximately half of the charge transported by charged ion aggregates with the other half carried by free ions [354]. The self-diffusion coefficients and conductivity predicted by MD for the ethylene glycol oligomer solvents were also found to be in good agreement with experimental data. Li^+ transport was found to primarily occur though exchange of $TFSI^-$ anions in the first coordination shell [379]. The 2015 study of Shimizu *et al* investigated a number of different lithium glyme solvate ionic liquids [350]. Here, the authors found that although MD was unable to yield quantitative information about the dynamics of the system, it could provide two important pieces of information: the auto-diffusion coefficients of glyme molecules in pure glyme are much larger than those of glyme molecules in glyme equimolar mixtures at the same temperature; the decrease in the glyme diffusion

coefficients is more pronounced in the Li[Ntf_2] + glyme system than in the Li[NO_3] + glyme mixture [350]. The study of Lesch *et al* used MD to investigate lithium salts dissolved in aprotic ionic liquids [378]. The authors found that the exchange of TFSI anions in and out of the first coordination shell of Li^+ was faster in pyr_{13}-based systems, compared to emim-based systems, and that the Li^+ ion transference number was higher [378]. The atomic scale context provided by atomistic simulation allows for the specific dynamics and atomic scale effects, such as dynamic (de)coordination, which govern diffusion to be observed directly. These behaviours cannot be observed directly in a spatially and globally averaged NMR measurement [350].

In more complex solvents, such as ionic liquids, the nature of the solvent plays a important role too, for instance Borodin and Smith showed the effect of fluorination of ionic liquid cations on diffusion behaviour [380]. This sort of study can be directly compared with pulsed field gradient NMR experiments of battery materials. This was done, for example, when Shimizu *et al* studied a LiTFSI-based solvate ionic liquid, which had been proposed as a solvent for Lithium Sulfur batteries [350]. The authors found the molecular behaviour of solvate ionic liquids to be probed effectively using a combination of MD trajectories and structural/aggregation analysis techniques.

Atomistic simulations are also providing new understanding of the fundamental physics behind non-linear relationships between the electric field and the electrolyte conductivity, known as Onsager's Wein effect [381]. In a recent study of dilute electrolytes and molten salts Lesnicki *et al* [382] performed a direct study of this half century old conundrum, by directly observing the interplay between external fields as well as the correlations between, and clustering of, ions using atomistic modelling and innovative statistical mechanical analysis. This direct observation of liquid structure and dynamics could only be obtained through simulation. Such studies are likely to expand into the study of battery electrolytes in the coming years where this sort of behaviour has a direct effect on conductivity and function. In the above examples of diffusion studies, ion pairing plays a contributing role; in general, any phenomenon originating from ion paring can benefit from investigation by atomistic simulation.

Shimizu *et al*'s work highlights a key advantage of molecular simulation. While the authors utilised both scattering and NMR based experimental probes, neither could provide the same unambiguous detail of the nature and dynamics of ion pairing, on the single atom scale in the liquid, that can be obtained from simulation [350]. More recently, the richness of simulated data sets has allowed for the analysis of liquid structures with deep learning based approaches, providing a more complete picture of electrolytes, their disorder, and complexity [383].

4.2.7. Solvation energies

Solvation energies in electrolytes have been widely studied and, though research focus has been on aqueous solvation of biomolecules, these techniques can also be used to look at solvation of metal ions with organic solvents. Dependent on the exact thermodynamics of the system, the solvation energies of ions may be obtained by a number of methods. Skarmoutsos *et al* combined DFT and MD methods to look at the solvation structures of lithium salts in ternary mixtures of different carbonate solvents and showed that different solvents were found to dominate at different distances from a central lithium cation, observing a particular preference for solvation of lithium by DMC ions over PC and EC, as shown in figure 24. Takeuchi *et al* looked even deeper at the energetics behind the direct contact between cations and anions in solution [385]. The relative stabilities of the mono-, bi-, and tri-dentate coordination structures were assessed with and without solvent, where water, PC, and DMC were found to favour the ion pair (CIP)–solvent contact. Vacant sites of Li^+ cation in CIP are solvated with three carbonyl oxygen atoms of PC and DMC solvent molecules, and the solvation is stronger for the monodentate CIP than for the multidentate [385]. Such detailed analysis is not possible to resolve through experimental techniques.

These are just a few notable studies on solvation energies in liquid electrolytes. A compelling theoretical description of solvation is given by Lazaridis [386].

4.2.8. Activity coefficients of electrolytes

The activity coefficients describe the deviation of actual electrolytes from an ideal mixture of substances [171] and can be calculated using DFT + PBE simulations (cf section 2.1.1) of solutes in electrolyte solutions, as described in section 2.3.2. The experimental value of bulk permittivity of EC is ($\varepsilon^{\infty} = 90.7$) [387] and its surface tension is (0.0506 N m^{-1}) [388]. These values were used by Dziedzic *et al* to calculate the activity coefficient of $LiPF_6$ in EC [135]. The solvent radius was set to $R_k^{\text{solvent}} = 10.5\ a_0$, to approximate the size of an EC molecule, and the isovalue of solute electronic density, (ρ_e^{λ}), is varied to match the experimental activity coefficients. A plot of the computed activity coefficients as a function of the square root of electrolyte concentration is given in figure 25, along with experimental values from Stewart and Newman [389]. Here, we see a good agreement for $\rho_e^{\lambda} = 0.002\ e/a_0^3$. Trends are also plotted from the linearised approximation of PBE, where the solvent radius is reduced to resemble the prediction for point charges from

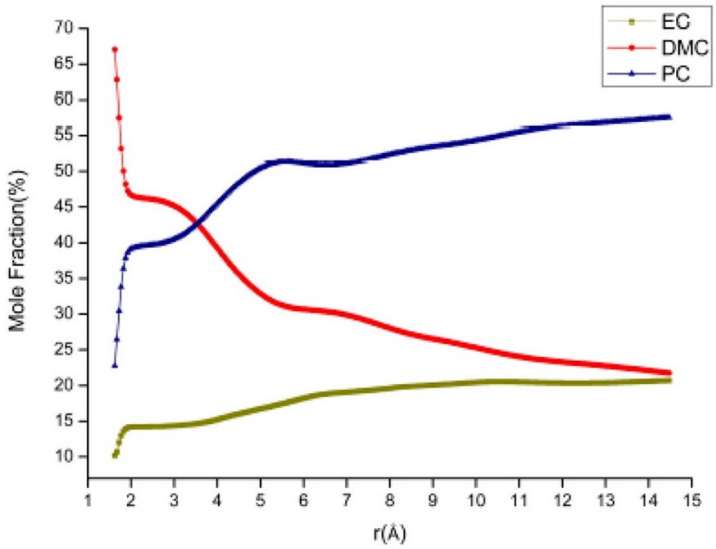

Figure 24. Local mole fractions (%) of EC, PC, and DMC as a function of the distance from the lithium cation in the ternary mixture. Reprinted with permission from [384]. Copyright (2015) American Chemical Society.

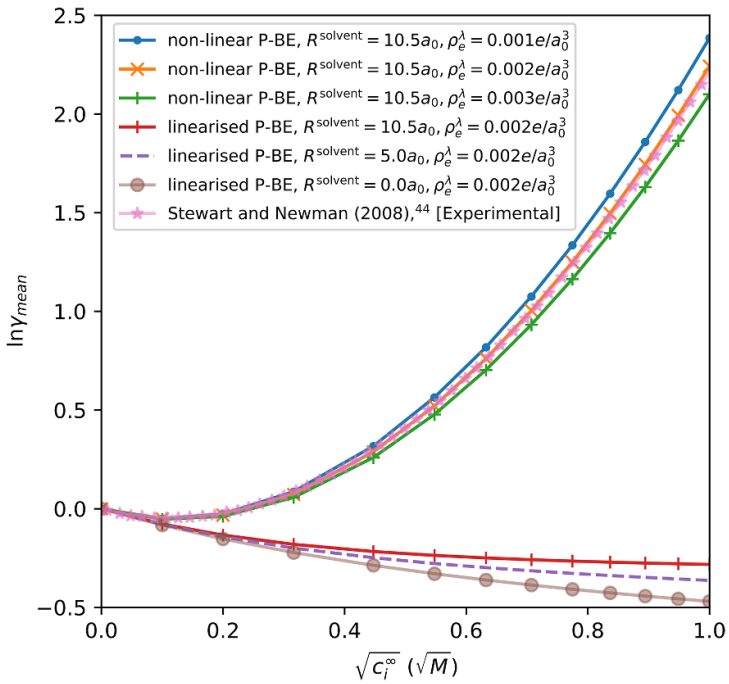

Figure 25. Mean activity coefficients for $LiPF_6$ in EC at $T = 308$ K as a function of concentration and for different values of the atomic electronic density isovalue parameter which determines the extent of the accessibility function. Calculations with the linearised approximation to P-BE are also shown. Reprinted with permission from [135]. Copyright (2020) American Chemical Society.

the Debye-Hückel theory [390]. The thermodynamic factor can be obtained from numerically differentiating these curves. This is a novel technique of calculating activity coefficients and thermodynamic factors from hybrid atomistic-continuum methods.

4.2.9. Interfacial nanostructure of electrolytes

In sections 3.3 and 5.4, the interfaces between solids and liquids from the perspective of the solid have been discussed. However, the interface from the perspective of the liquid is also of interest. The structure of liquid electrolytes at metallic [391] and charged dielectric [365] interfaces will normally extend away from the interfacial region and can be observed prominently for tens of nanometers and, dependent on concentration of the liquid, can either be monotonic or oscillatory, as described in section 4.2. Spectroscopic and surface

methods used to study the liquid–solid interface are often indirect and require specific conditions for analysis (e.g. transparency and smoothness) [392–394], which often constrains the interfaces we can study as well as the detail and conclusiveness of the data obtained. Computational modelling provides a route to direct and data rich understanding of the liquid solid interface. This section will highlight some particular areas of study.

Concentrated electrolytes and ionic liquids both adopt the characteristic overscreening structure at charged interfaces, including electrodes. This structure, comprising oscillations of charge decaying into the bulk, is commonly observed [373, 391]. Modelling these systems requires an appropriate electrode model. While interesting information can be gained from simulating ions at an electrode with a fixed charge, for example in a high throughput study looking at structural changes with electrode surface charge [373], fixed potential boundary conditions will provide a more accurate description of the capacitance [391, 395], interfacial structuring of a liquid electrolyte [373, 396, 397], and the decoordination and dechelation dynamics of coordinated ions [398]. Though we note that, in light of a recent study by Scalfi *et al*, this field continues to evolve as more nuanced classical electrode models are employed, such as the Thomas–Fermi based model proposed by Scalfi *et al* [395].

A wide variety of different electrolytes have been studied using fixed potential electrolytes, from ionic liquids to concentrated electrolyte. Both nanoporous [371, 396, 398, 399] and nanoscopically rough electrode surfaces have been heavily used [400]. A specific example of interest is the work of Borodin and Bedrov, where MD simulations were performed on dilithium ethylene dicarbonate (Li_2EDC) and dilithium butylene dicarbonate (Li_2BDC), in contact with mixed solvent electrolyte (EC:DMC) doped with $LiPF_6$ [401]. In this study, the authors examined the SEI–electrolyte interface and found an increase of EC and $PF6^-$ molecules and a decrease of DMC at the interfacial layer next to the SEI surface, compared to bulk electrolyte concentrations. The activation energies for the Li^+ solvation–desolvation reaction were estimated to be 0.42–0.46 eV for the Li_2EDC–electrolyte and Li_2BDC–electrolyte interfaces.

While the context provided by these methods is useful, more generally the capacitance curves generated by atomistic studies of fixed potential electrodes have frequently been able to replicate experimental results when mean field theory cannot. For instance, Simoncelli *et al* were able to replicate the experimental behaviour, in particular the double layer capacitance, of a nanoporous brine based capacitor, where a variety of mean field models were unsuccessful [402]. Li *et al* were able to show the exact rearrangements of the molecules and ions at a metallic interface which gave rise to the nature of the experimentally and computationally observed relationship between capacitance and voltage of a water in salt electrolyte [397].

4.2.10. Outlook and challenges

Liquid electrolytes will likely remain the most prominent form of commercialised electrolyte for battery applications in the near future. This is partly due to their monopoly in the market and partly due to their low cost, which will continue to drive popularity. Despite the overwhelming success of commercial liquid electrolytes, there is still room for further performance improvements, with several key issues as limiting factors. Liquid electrolytes are known to be limited by narrow electrochemical windows, solvent toxicity, and material flammability/safety concerns. There are two potential avenues for solving these issues:

- Resolving these limitations within the confines of liquid electrolytes: ionic liquids have a large electrochemical window and high thermal stability, and their conductivities are similar to those of conventional organic solvent solutions [307]. However, they are expensive and there are associated safety concerns [282, 283]. A liquid electrolyte alternative to this could be in water-in-salt electrolytes. Water-in-salt electrolytes are a novel class of electrolytes, which inverts the conventional idea of a salt being dissolved in a solvent, with a small amount of water being dissolved in a hygroscopic lithium salt to the point where a liquid is obtained [403, 404], analogous to the high concentration organic electrolyte solutions described by Yamada *et al* [306]. These liquids have the advantage of being comprised solely of a lithium salt and water, which decreases cost and eliminates the toxicity and risk of flammability and thermal runaway traditionally associated with organic solvents. The high concentration of salt also leads to a greatly expanded electrochemical window of 3 V [308] from the 1.23 V value for dilute aqueous solutions. However, the highly concentrated solutions in these electrolytes lead to re-crystallisation of the lithium salt and low conductivity, due to the high viscosity of the liquid [404, 405].
- Replacing liquid electrolytes with solid or soft matter alternatives: despite the success of liquid electrolytes in LiBs, a number of issues have arisen that may prove impractical to address within the grouping of liquids. Organic liquid electrolytes are highly flammable, leading to safety issues, such as thermal runaway, when deployed in portable electronic devices and EVs [17, 18, 406]. These safety issues may have a low frequency of occurrence, but when used often by a large number of people, they become nearly inevitable events, as evidenced by EV and portable device explosions making the news headlines.

The use of liquid electrolytes also limits the compatibility with electrode materials and thereby limits the maximum energy density of a battery [19]. For example, higher energy density lithium sulfur (Li-S) batteries are unstable, due to interactions between the liquid electrolyte and the electrodes [407]. Similarly, Li metal anodes cannot be used with organic liquid electrolyte solvents without additives [408], because of dendrite formation and capacity loss [409, 410]. Due to these concerns, research in recent years has shifted to looking at alternatives, such as solid and soft matter-based electrolytes [26]. Solid electrolytes are discussed in detail in the next section (cf section 4.3) and soft matter electrolytes are discussed in detail by Hallinan and Balsara [411] and Popovic [412].

The design of the electrode-electrolyte interfaces affects the capacity and rate capability in LiBs [290, 293]. Further work to design better interfaces that are compatible with the electrodes, thermodynamically stable, kinetically fast for Li-ion transfer, electronically insulating, and which lead to minimal loss in performance, will be crucial to progress LiB performance [2, 291, 292]. Atomistic modelling can help in this area by analysing the chemical reactions leading to SEI formation and predicting new materials which form a well-structured SEI, conducive to ion transmission [16]. Further details of the formation and function of the SEI at the graphite anode are summarised in section 3.3.5.

Liquid electrolytes are complex substances and are therefore difficult to fully capture in atomistic models. In recent years, computational capacity has expanded, allowing more complex models to be studied. Alongside this, new computational methods have been developed under the open source license, allowing research of these materials to become more accessible [357, 371, 401, 402]. Future advances in computational ability, combined with improved experimental studies, provide a framework for high throughput screening of electrolyte materials.

Developments in expanding the achievable time and length scales of AIMD will allow more complex models to be developed. However, it is still implausible that AIMD will be able to simulate whole electrodes/interfaces/battery cells for long enough time and length periods to achieve full ergodicity (statistical convergence). Therefore, methods which can provide long scale simulations are still needed. In particular, the emerging fields of fitting machine learnt potentials for liquid electrolytes [413–415], and more complex classical models which incorporate polarisability [349, 357] or bond breaking dynamics [416, 417]. This would enable simulations of electron transfer, bond formation, and the effect of ion and solvent polarisability at larger scales and in greater detail.

Atomistic modelling of liquid electrolytes does not necessarily require more computational expense to advance. Exploitation of underused physical methods to model liquid systems at far lower cost has been explored. One such method, classical DFT, has already been applied to model aqueous capacitors [369] and confined ionic liquids [418]. This has the potential to be coupled with electronic DFT (cf section 2.1.1) to model electron transfer [419].

It should be emphasised that, for practical use, the interfaces between the liquid electrolyte and the electrodes are the major limiting factors in terms of performance, stability, and safety. Therefore, advancement through electrolyte design is crucial, where the critical obstacles discussed here could be resolved by the use of novel, solvents, salts, or electrolyte salts. Several articles discuss the challenges of this topic in greater detail [420–422].

4.3. Solid electrolytes

4.3.1. Introduction

Solid electrolytes have attracted considerable attention as an alternative to highly-flammable liquid electrolytes, as they significantly improve device safety and have the potential to improve energy and power densities, while also reducing the cost of synthesis [285, 423–426]. An ideal solid electrolyte material should possess high electronic resistance, high ionic conductivity, outstanding thermal stability, strong electrochemical stability, excellent mechanical strength, and reduced interfacial resistance [427, 428]. There are three different categories of solid electrolytes used in rechargeable batteries [426]: (1) inorganic ceramic electrolytes, (2) organic polymer electrolytes, and (3) composite electrolytes.

Solid electrolytes were discovered by Michael Faraday in the early 1830s through research on the conduction properties of heated solid silver sulfide (Ag_2S) and lead fluoride (PbF_2) [429]. The use of a ceramic-based β-alumina ($Na_2O{\cdot}11Al_2O_3$) in high-temperature sodium-sulfur (Na-S) batteries in the 1960s was considered as a milestone in the development of batteries, enabled by solid electrolytes [430]. In the 1980s, the Zeolite Battery Research Africa (ZEBRA) group developed the 'ZEBRA' batteries using $Na_2O{\cdot}11Al_2O_3$ as the solid electrolyte [431]. So far, the Na-S battery has been commercialised in Japan [432], whereas the ZEBRA battery is currently being developed by the General Electric Corporation in the United States [433].

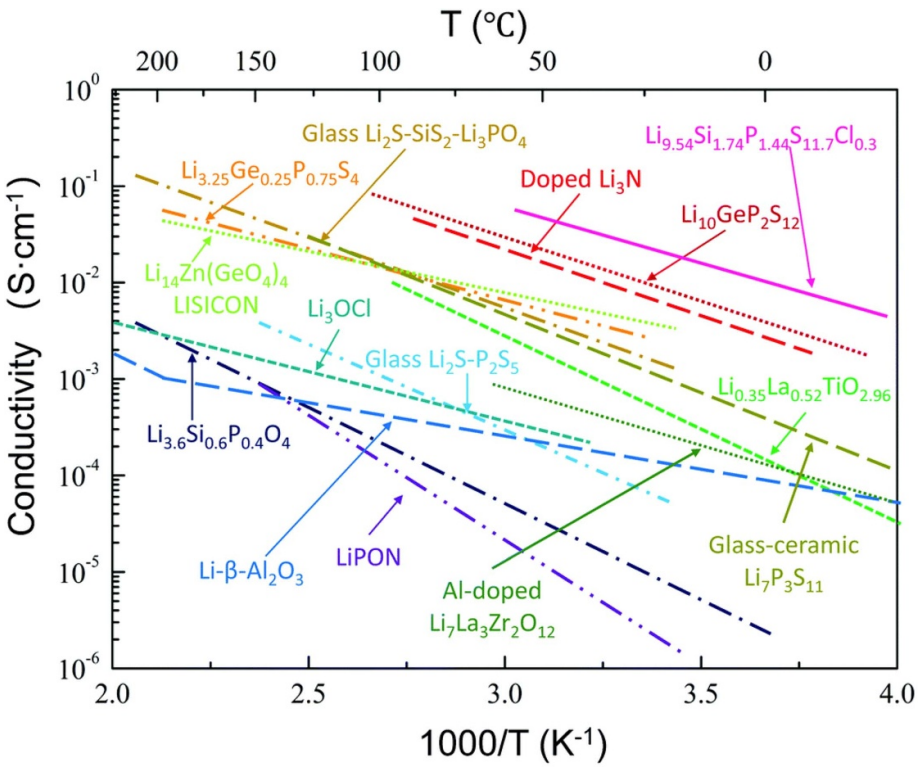

Figure 26. Ion conductivity of several well-known solid lithium ion conductors, including glass and crystalline conductors. Reproduced from [26]. CC BY 3.0.

In 1990, the Oak Ridge National Laboratory synthesised a lithium phosphorus oxynitride (LiPON) material [434, 435], opening up the use of inorganic solid-state electrolytes in LiBs. Since then, a huge number of inorganic, lithium-ion conductive ceramic materials have been developed, including perovskite-type [436], garnet-type oxides [437, 438], garnet-type sulfides [439], lithium super ionic conductor (LISICON) [440], sodium super ionic conductor (NASICON)-like materials [441], lithium-argyrodite materials [442], and Li-rich anti-perovskites [443, 444].

Despite recent advancements in crystalline inorganic electrolytes, they are still brittle and therefore difficult to fit into different battery shapes. Solid-state polymer electrolytes (SSPEs), due to their high flexibility, can fit into any battery shape and present improved safety and stability features compared to crystalline inorganic electrolytes [426]. Since 1980, various high molecular weight, dielectric polymer hosts were investigated for LiBs as high conductivity electrolytes, such as poly(ethylene oxide) [445], polyacrylonitrile [446, 447], PVDF [448–450], poly(methyl methacrylate) [451, 452], and poly(vinylidene fluoride-hexa-fluoropropylene) [453–455].

The ionic conductivities of most polymer electrolytes are significantly lower than those of both oxide solid electrolytes and liquid electrolytes [456]. A possible solution to this limitation is to create composites by integrating nanoscale, highly conductive, inorganic, particulate fillers into the polymer electrolyte material [426]. This enhances the ionic conductivity and improves the mechanical strength and stability of the SSPEs, including the interfacial stability [457]. Here, heterogeneous doping increases the ionic conductivity as a result of increasing interfacial regions between an inert solid phase, such as silica, alumina, or boron oxide particles, and an electrolyte [458]. A wide range of inorganic solid composite electrolytes have previously been studied, based on oxides (Li_2O:Al_2O_3 [459], Li_2O:B_2O_3 [460–462]) hydrides ($LiBH_4$:SiO_2 [463]) halides (LiI:Al_2O_3 [464], LiI:SiO_2 [465], LiF:Al_2O_3 [466]) and sulfides (Li_2S:SiS_2 [467]).

Over the last decade, a limited number of candidates with high ionic conductivities (>1 mS cm^{-1}) have arisen as potential competitors to liquid electrolytes [468–476]. Figure 26 presents the ionic conductivities of most currently known solid electrolytes [26].

In this section, we review atomistic modelling investigations into the structure-property relationships in selected solid-state electrolytes: $Li_{10}GeP_2S_{12}$ (LGPS), lithium argyrodites, and $Li_7La_3Zr_2O_{12}$ (LLZO), belonging to the inorganic solid ceramic electrolyte type, and Li_2O:B_2O_3 materials, belonging to the oxide-based solid composite type. A particular focus is given to the ion transport mechanism in those materials, which is important for reaching high conductivities, a key property of battery materials. Finally, we

take a more detailed look at the interface of solid electrolytes with the electrodes, and discuss the challenges and outlook for future atomistic modelling investigations.

4.3.2. Sulfides

There are a substantial number of computational studies of sulfides which largely relate to a recent emergence of newly discovered crystalline sulfide superionic conductors. Sulfides also tend to have comparatively lower intrinsic electrochemical and chemical stability, which has stimulated interest in understanding the interfacial interactions within batteries [28]. The sulfide group encompasses a range of sulfide-based solid electrolytes, including glass ceramics [477], argyrodites [478], and thio-LISICONs [479]. Some of the most promising solid electrolytes to emerge in recent years include LGPS [288, 480, 481], and the Li-argyrodite (Li_6PS_5X, X = Cl, Br, I) [442, 482–486] families of superionic conductors.

4.3.2.1. LGPS

A study by Kamaya *et al* reports that LGPS can reach high room temperature ionic conductivities of 12 mS cm^{-1}, comparable to that of commercial liquid electrolytes (∼10 mS cm^{-1}) [288]. The authors also determined that diffusion in LGPS is anisotropic, where *c* directional motion is predominant over the *ab* plane, with an overall energy barrier for Li diffusion being 0.24 eV, with later reports measuring 0.22 eV [487]. Using AIMD, Mo *et al* later determined the average direction energy barriers of 0.17 eV along the *c* channel and 0.28 eV in the cross channel (*ab* plane) [481], with Xu *et al* showing the Li migration mechanism is through cooperative motion, instead of the initially determined single hop mechanism [488]. More recently, Adams and Prasada Rao predicted the presence of additional Li sites using MD, which would allow diffusion along the *ab* plane [489]. These sites could change not only the Li occupancies in the *c* channel, but also provide a diffusion mechanism involving the *ab* plane, opening up the possibility of cross-channel diffusion. The presence of these additional sites were later confirmed experimentally using single crystal x-ray diffraction (XRD) [490].

More recently, Bhandari and Bhattacharya also investigated the lithium diffusion dimensionality in LGPS by performing a DFT study of the lithium diffusion energy barrier, using the NEB method [480]. In this study, the authors took into account the fractional occupancies leading to variable *c* channel Li populations, variable chemical environments surrounding Li, and all possible migration mechanisms. The authors found that lithium diffusion is neither purely *c* directional nor purely along the *ab* plane, but there exists a correlated mechanism of motion along $c - ab$ which critically controls the degree of anisotropy of Li diffusion in LGPS. The energy barriers for different mechanisms of Li-diffusion, shown in figure 27, suggest that correlated hopping has the lowest energy barrier. Bhandari and Bhattacharya further performed a statistical average of all diffusion energy barriers, taking into account the formation energy of various Li configurations and predicting an overall energy barrier of 239 meV [480], which is in close agreement with experiments [288]. Thus, the DFT approach not only explained the overall diffusivities and energy barriers, but also gave insight into the underlying mechanism behind the fast Li diffusion in LGPS, resolving the discrepancy about the anisotropy of Li diffusion in this compound, which was insight not possible to obtain only from experiments.

4.3.2.2. Lithium argyrodites

Li_6PS_5X (X = Cl,Br,I), can reportedly reach ionic conductivities of up to 10^{-2} S cm^{-1} [483]. While Li_6PS_5Cl and Li_6PS_5Br exhibit high ionic conductivities of 10^{-3} S cm^{-1} at room temperature, Li_6PS_5I has considerably lower conductivitives of 10^{-6} S cm^{-1} [491]. The difference of three orders of magnitude is surprising, as the identical crystal structures suggest the same Li diffusion pathways exist in all systems. Another intriguing aspect is that the conductivity trend runs counter to other families of solid electrolytes, such as LGPS, where larger, more polarisable and less electronegative anions are linked with increased ionic conductivities [492].

Understanding which properties and mechanisms influence the conductivity is essential to obtaining higher ionic conductivities and improving battery performance. Material stoichiometry, anion/cation disorder, and doping, have all been shown to influence conductivity. Modification of the lithium stoichiometry has been achieved through aliovalent cation substitution on the P sites [482, 493–495] and through anion substitution on the S^{2-}/X^{-} sites [486, 496, 497]. For example, Ge substitution on the P site to give $Li_{6+x}P_{1-x}Ge_xS_5I$ is able to reach conductivities of up to 5.4 mS cm^{-1} [482, 495]. The underlying reasons for increased ionic conductivity through cation/anion doping in lithium argyrodites are not clear, with two competing explanations proposed in the literature. (1) Doping increases anion disorder, resulting in percolating networks of lithium diffusion pathways [498]. (2) Doping increases lithium stoichiometry. The additional lithium is accommodated as ‘interstitials’ which switches on a low-energy concerted diffusion mechanism.

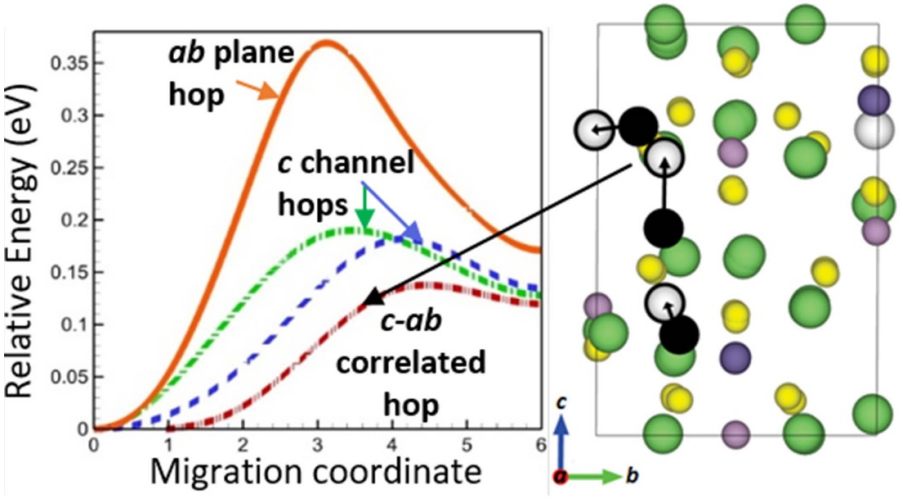

Figure 27. Energy barrier for Li-ion diffusion in the solid electrolyte, $Li_{10}GeP_2S_{12}$ (LGPS), calculated using the NEB method. Reprinted with permission from [480]. Copyright (2016) American Chemical Society.

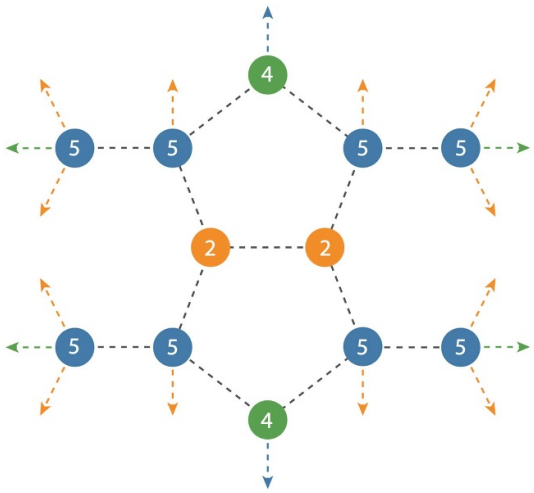

Figure 28. (a) Possible Li diffusion pathways in Li-argyrodites, involving type 2, 4, and 5 tetrahedra for long-range diffusion. Reprinted with permission from [498]. Copyright (2021) American Chemical Society.

The effects of interrelated factors on ionic conductivity is challenging to resolve purely from experiment. In doped Li-argyrodites there are always *both* changes to the host-framework (e.g. disorder on anion sites and/or substitution and disorder on the P sites) and a change in lithium stoichiometry. This is where computational analysis can provide vital insight, allowing deconvolution of coupled properties by modelling non-charge-balanced hypothetical systems to better understand how each of these factors affect ionic conductivity, which is not feasible in experimental systems.

A particularly interesting aspect of the Li-argyrodites is the diffusion topology, comprising of interconnected Li_6S cages, with anions arranged at 4 *a*, 4 *c*, and 16 *e* Wyckoff positions and Li arranged over a tetrahedra, with sites labelled as types 1–5 [499]. Lithium mainly occupies type 5 tetrahedral sites in $x(Li) = 6$ argyrodites, with occupation of non-type 5 sites only recently observed experimentally [493, 500]. Computational studies, however, have previously predicted occupation of non-type 5 sites, showing lithium distributed over tetrahedral types 5, 2, and 4 [483, 498, 501].

Li hopping within these cages, while effectively barrierless, does not contribute to long-range diffusion. In fact, a combination of inter-cage and intra-cage hopping is needed, with occupation of non-type 5 sites and transitions between all adjacent site types, to achieve long-range diffusion. This is shown schematically in figure 28, showing the connectivity between the Li tetrahedral sites. AIMD simulations have shown that cation and anion substitution [442, 493], anion site disorder [498, 500], and lithium concentration [502–504] all influence the ionic conductivity.

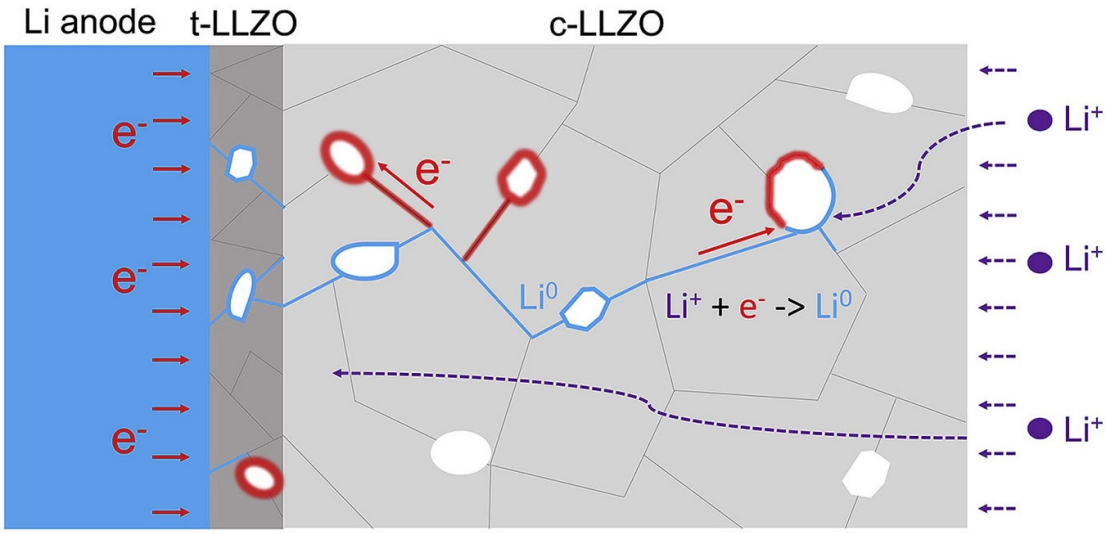

Figure 29. Schematic showing Li metal formation (blue) along grain boundaries and pores, due to electron accumulation (red) combining with Li^+ as they move through the electrolyte. Reprinted from [517], Copyright (2018), with permission from Elsevier.

The influence of anion substituent concentration on conductivity is currently uncertain, with research by De Klerk *et al* determining excess Cl in $Li_5PS_4Cl_2$, resulting in similar conductivities to Li_6PS_5Cl [442], in contrast to research by Yu *et al* and Feng *et al*, who concluded that excess Cl improved Li conductivity [504, 505]. Yu *et al* determined the highest conductivity was produced by $Li_{5.7}PS_{4.7}Cl_{1.3}$ (6.4 mS cm^{-1}) [503, 505], while Feng *et al* determined this to be $Li_{5.3}PS_{4.3}Cl_{1.7}$ (17 mS cm^{-1}) [504]. Feng *et al*, however, presented alternative, or coupled, reasoning for this increased conductivity. Drawing from previous studies [486, 496], they proposed that the increased Cl content amplified the anion disorder in the system, which is the underpinning cause of the higher conductivities.

4.3.3. Oxides

4.3.3.1. LLZO

Cubic $Li_7La_3Zr_2O_{12}$ (c-LLZO) has a high Li-ion conductivity of 10^{-4} S cm^{-1} [506], a high shear modulus of 59 GPa [507], and the largest thermodynamic stability window with reference to lithium metal [24, 508, 509] of current solid electrolyte materials (cf section 4.3.4). However, at low temperatures (<150 °C), c-LLZO is not stable and transitions to the less conductive tetragonal LLZO (t-LLZO) phase [510]. Attempts have been made to retain the more desirable c-LLZO by Al doping on lithium sites, with some success [510, 511].

Lithium dendrite growth has been shown to be a challenge in solid-electrolytes. For LLZO, dendrite growth has caused short circuits in the cells after relatively short periods [512, 513]. Cheng *et al* observed this growth directly and found that the process occurs mostly through grain boundaries [514]. Recently, Kim *et al* confirmed these observations and investigated the use of an interlayer buffer, to restrict Li propagation through grain boundaries [515].

There has been a wide effort to understand dendrite formation through modelling [516–518]. For example, Tian *et al* used DFT to investigate dendrite growth through analysis of c-LLZO and t-LLZO bulk and slab surface energies, via the total density of states [517]. The authors found that t-LLZO forms at the surface of bulk c-LLZO, even with Al-doping [519, 520], and that extra states appear in the band gap for the slab structures, which do not appear in the bulk, potentially allowing electrons to be trapped on the surface of LLZO. Electrons localised primarily around Li^+ and La^{3+} ions on the surface lead to the nucleation of lithium metal, which can result in lithium growth through grain boundaries and pores in the LLZO, eventually forming dendrites [512], as shown in figure 29. This analysis was also conducted on LiPON, where no electron trapping was found to occur, indicating that LiPON could be a suitable coating to prevent dendrite and t-LLZO formation (cf section 4.3.4).

Gao *et al* attributed the dendrite growth mechanism to the under-coordination of Zr present on some of the stable interfaces of LLZO with Li [518], leading to inhomogenous Li depletion, which has been linked to Li metal deposition and dendrite formation [521–525]. It is unclear whether the suggested cause by Gao *et al* is complementary evidence of Tian *et al*'s electron trapping theory or a separate cause of interface dendrite growth. However, the papers do differ on their choice of surface. Tian *et al* used Li and La rich surfaces, which were determined to be more stable by Thompson *et al*, who used DFT to investigate six different LLZO

slabs for the (100) and (110) planes [526]. By contrast, Gao *et al* drew upon results presented in several methods [516, 526, 527] and performed DFT calculations on a wider range of surfaces, finding (100) and (001) surfaces to be the most stable. The findings of these studies agree that Li and La rich surfaces are the most stable. However, Gao *et al* calculated the interface formation energies of the Li-LLZO interfaces using the CALYPSO interface structure prediction method [528] and determined the Zr-rich surfaces to be the most stable at this interface [529]. Experimental observations corroborate these findings, also determining that the formation of Zr-rich surfaces to be a cause of interfacial degradation [524].

Experimental measurements have suggested a non-uniform distribution of current on the surfaces as a possible cause of dendrite growth [522, 530]. Non-uniform current distribution produces random, local spikes in current density for short periods of time, leading to a reduction of Li at these sites. Squires *et al* used DFT to model the electronic conductivity in LLZO to probe the importance of the surface current to dendrite formation [531]. The authors determined that at room temperature, bulk c-LLZO was found to have negligible electron/electron–hole concentrations, indicating that bulk defects are not a significant factor in dendrite growth. However, these models did not account for other forms of defects, such as grain boundary and surface effects.

Understanding Li-ion migration is key to improving battery conductivity. Xu *et al* analysed the Li-ion migration path through LLZO using DFT with the NEB method (cf section 2.1.3) [532]. Two migration paths were observed, depending on Li concentration. Low Li_x ($Li_5La_3Zr_2O_{12}$) led to a higher energy, single hop migration path, whereas higher Li_x ($Li_7La_3Zr_2O_{12}$) led to a lower energy, two hop migration path. Using potentials-based MD (cf section 2.1.6), Burbano *et al* further investigated the Li-ion transport mechanisms by comparing ionic conductivity in t-LLZO and c-LLZO [533]. The authors found that the longer time scale of potentials-based MD allowed the observation of a large sample of diffusion events in both LLZO structural forms. Diffusion events in t-LLZO were less common and involved exactly 8 Li ions, which corresponds to the cyclic movement of Li ions around the 12 octahedral and tetrahedral ring sites in t-LLZO. This cyclic mechanism results in no net long-range diffusion of Li and hampers the ability of t-LLZO to conduct ions. AIMD (cf section 2.1.6) investigations of the transport mechanism in LLZO have also been conducted. However, the shorter time scale led to some key disagreements about the transport mechanism in c-LLZO [533–535].

DFT calculations have determined that Al doping reduces the energy barrier for Li-ions to move between octahedral and tetrahedral sites, increasing the ionic conductivity [536, 537]. More recent work by Bonilla *et al*, using potentials-based MD, supports this conclusion, finding increased conductivity in t-LLZO, due to the Al forcing Li ions into previously inaccessible tetrahedral sites [538]. The authors also found that Al doping in c-LLZO led to a slight decrease in conductivity. They attributed this to the tendency for Al to 'trap' Li ions close to the dopant. Resolving Li-ion migration through LLZO experimental measurement is challenging due to the complexity of the system coupled with the need to observe the processes during active (dis)charge. While high-level experimental measurements regarding conductivity can be made, which provide spatially-averaged information [539], techniques such as x-ray and neutron diffraction struggle to probe at the atomistic level required for investigating Li-ion migration pathways, due to low ^{7}Li scattering intensities [534]. Other experimental techniques, such as pulsed-gradient NMR require high-temperature measurements [540] and electrochemical impedance spectroscopy (EIS) often includes non-Li charge carriers such as protons or electrons [541]. Brugge *et al* used an ion exchange method with focused ion beam secondary ion mass spectrometry to directly observe ion transport occurring through LLZO [541]. The authors noted that the sensitivity of LLZO surfaces to carbon contaminants from the air is problematic and leads to large interfacial resistances [541, 542]. Atomistic modelling does not have the same hindrances stated above and was able to provide a mechanistic pathway to explain the reduced ionic-conductivity of t-LLZO and a thermodynamic description of the effect of Al-doping on ionic conductivity.

4.3.3.2. Oxide nanocomposites

Due to attractive mechanical, electrical, optical, and magnetic properties, nanocomposite oxide materials represent a new generation of advanced materials [458, 460]. They often show enhanced conductivity, compared to single-phase ceramic oxides, making them suitable candidates as electrolytes for future ASSBs. For example, Li_2O:B_2O_3 [460–462] and Li_2O:Al_2O_3 nanocomposites [459] have higher ionic conductivities than nanocrystalline Li_2O, although B_2O_3 and Al_2O_3 are insulators. The ionic conductivity shows a maximum at about 50% of B_2O_3/Al_2O_3 content. This surprising behaviour was attributed to the increased fraction of structurally disordered interfacial regions and the enhanced surface area of the nanosized particles [460]. The oxide nanocomposites contain three types of interfaces, as presented in figure 30(a): interfaces between the ionic conductor grains (green lines), between the insulator grains (black lines), and between the ionic conductor and the insulator grains (red lines). The latter can lead to surprising effects in the

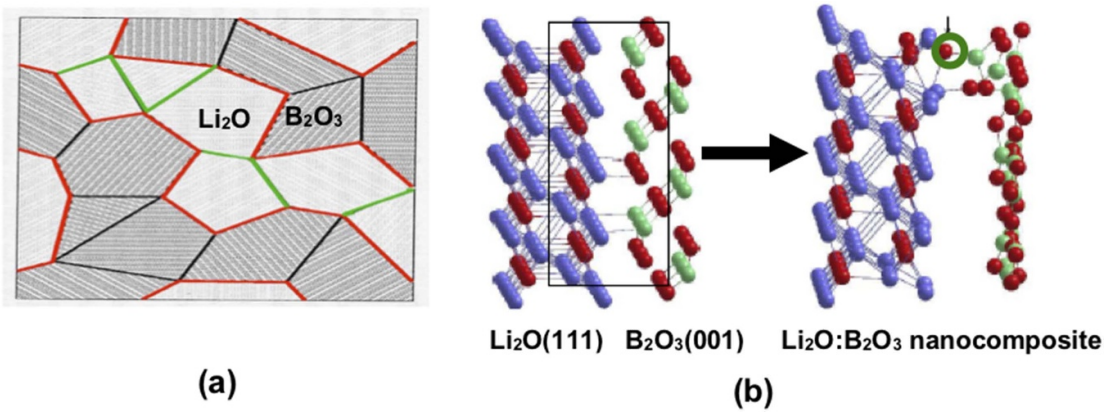

Figure 30. (a) Schematic diagram of Li_2O and B_2O_3 interface (b) atomistic model of Li_2O:B_2O_3 nanocomposite. Reproduced from [543].

conductivity of composite materials. In this case, the highly conducting interface region can act as a bridge between two Li_2O grains not in direct contact with each other, opening up additional paths for Li ions. The conductivity enhancement in the interfacial regions may have different origins, e.g. the formation of space charge layers, an enhanced concentration of dislocations, or defects, or the formation of new phases.

Islam *et al* studied the interface of Li_2O:B_2O_3 nanocomposite, by modelling a combination of two favourable surfaces of Li_2O and B_2O_3 using hydrofluoric acid (HF)/DFT Hybrid approach [543, 544]. After full structural optimisation, it was observed that Li–O bonds are weakened, while B–O bonds are formed simultaneously at the boundary between the two surfaces, figure 30(b). An oxygen atom from the Li_2O surface (marked by a green circle) is pulled from the surface layer towards a neighbouring boron atom of the B_2O_3 surface. This preference of oxygen bonding with B (or Al in Li_2O:Al_2O_3) plays a key role in generating low-coordinated Li. As a consequence of this dislocation, the coordination of a Li atom in the second layer is reduced from four to three.

The defect properties were investigated in the interface region. It was observed that the removal of surface oxygen from Li_2O is responsible for the increased vacancy defect concentration in Li_2O:B_2O_3 (or Li_2O:Al_2O_3) nanocomposite materials. Therefore, the nanocomposites of ionic compounds (containing weakly bound and therefore mobile cations) with highly covalent compounds (with strong metal- or nonmetal-oxygen bonds) are promising candidates for high ionic conductivity. The model calculations showed that the most likely mechanism for Li^+ migration was in a zigzag pathway, rather than in a straight line along a direction parallel to the interface plane.

The average calculated activation energy for Li^+ migration in the Li_2O:B_2O_3 interface (0.28 eV) [543, 544] is similar to the experimental values of bulk Li_2O (0.31 eV) [460], Li_2O:B_2O_3 (0.34 ± 0.04 eV), [462] and Li_2O:Al_2O_3 (0.30 ± 0.02 eV) [459] nanocomposites. According to the defect formation energies, the interface region of Li_2O:B_2O_3 nanocomposites contains higher concentrations of both Li vacancies and Frenkel defects than bulk Li_2O and Li_2O surfaces [543, 544]. Therefore, the experimentally observed enhanced Li mobility in the Li_2O:B_2O_3 interface region is thermodynamically and not kinetically controlled. The models proposed in this study allowed a direct simulation of the defect formation and ion mobility at the atomic scale, without any experimental input. They provide a deep insight into the local bonding situation at the interface of oxide nanocomposites, which is difficult to obtain from experiments. State-of-the-art synchrotron techniques, like hard x-ray photoelectron spectroscopy, could possibly shed light on this challenge [545, 546].

4.3.4. Interface stability

Experimental investigations of solid electrolyte interfaces are often challenging, making atomistic modelling a vital tool [29]. The interfacial stability properties of solid electrolyte materials in contact with an electrode are best described by the electrochemical stability window, defined by Zhu *et al* as the range of voltages under which the interface configuration, a mixture of electrode (Li) and the solid electrolyte, does not undergo a decomposition reaction [508].

Atomistic simulation was able to resolve the characterisation of the electrochemical stability window for a number of SSEs. Cyclic voltammetry experiments had reported no significant SSE degradation in contact with a Li anode for a large (>5 V) voltage range [288, 547, 548]. For example, Kamaya *et al* used cyclic

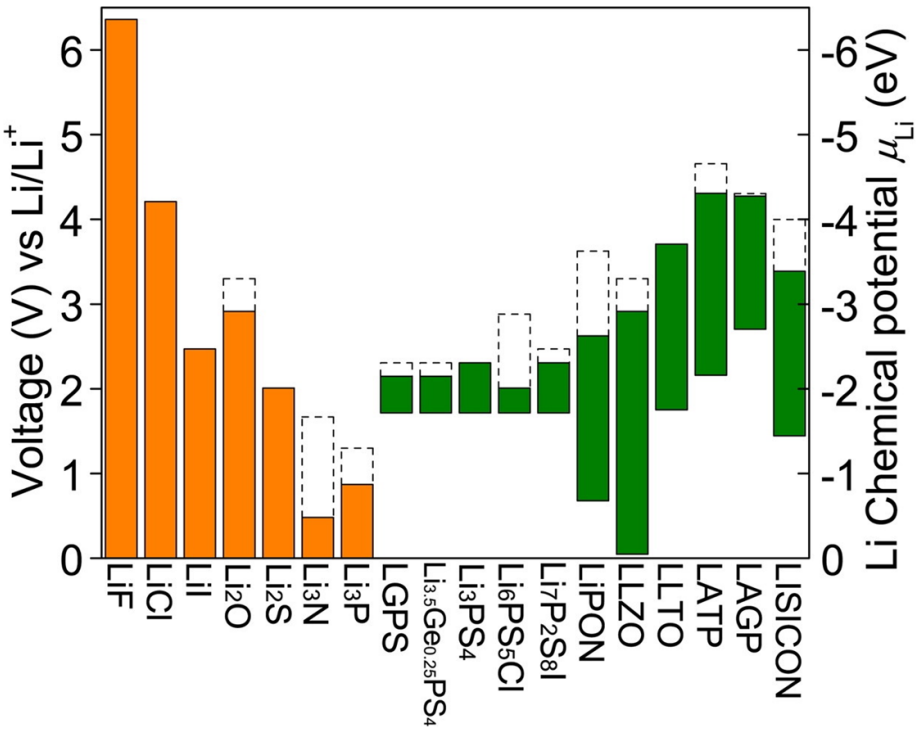

Figure 31. A comparison of the voltage stability windows for a selection of solid electrolytes (green) and the binary compounds that often form upon decomposition of the solid electrolyte (orange). The dashed line represents the oxidation potential to fully delithiate the material. Reprinted with permission from [24]. Copyright (2015) American Chemical Society.

voltammetry to probe the stability of the LGPS/Li interface for a voltage range of −0.5 to 5 V [288]. The authors found no evidence of electrolyte decomposition using this technique, and thus concluded that LGPS has a high electrochemical stability. However, a DFT based investigation by Mo *et al* predicted an electrochemical stability window of 3.6 V for LGPS by simply calculating the band gap of the SSE, rendering an electrochemical stability window >5 V, as indicated by the cyclic voltammetry results, to be unlikely [481]. A more recent DFT study by Zhu *et al*, posits the formation of an interphase layer, and determining the electrochemical stability window for LGPS to be 0.43 V (figure 31) [24]. The authors attribute the apparent contradictory interpretation of the cyclic voltammetry results to the slow kinetics of degradation that occur at SSE/Li interfaces, forming the interphase layer, i.e. there is a large kinetic overpotential for the oxidation and reduction reactions calculated by Zhu *et al* [24]. Cyclic voltammetry is also only able to detect electrochemical degradation processes, in which electrons are transferred. These experiments are unable to detect purely chemical processes (i.e. no electron transfer), which may also occur in parallel with electrochemical processes and lead to erroneous conclusions of 'stability' of solid electrolytes through cyclic voltammetry [508].

A smaller thermodynamic window increases the importance of the interphase layer formation. Zhu *et al* determined that a range of solid electrolytes are unstable with respect to Li metal at low and high voltages, with the exception of LLZO, which appears to be kinetically stabilised at low voltages, due to an unfavourable reduction energy of −0.02 eV per atom. Any potential outside of the thermodynamic stability window results in decomposition into lithium binary compounds, unless otherwise kinetically stabilised. This is problematic for germanium- and titanium-containing compounds, as they form electronically conductive alloys upon decomposition [24]. This renders the passivation process, proposed by Mo *et al* [481, 549], as the cause of cyclic voltammetry overestimates, unlikely as this degradation process would be sustained throughout the bulk cycling, severely limiting the efficacy of these materials as electrolytes [24]. Such degradation can also increase interfacial resistance [550, 551]. Other solid electrolytes face different problems. As explained in section 4.3.3, LLZO forms the far less ionically conductive tetragonal LLZO at the surface. The Li-LiPON and Li-argyrodite interfaces were reported to degrade favourably, forming an ionically conductive and electronically insulating interphase consisting of Li_2O, Li_2S, Li_3P, Li_3N, and LiI [24].

Further study by Zhu *et al* sought to investigate the mechanism behind the degradation/instability at the surface [508]. In order to probe these mechanisms, the authors calculated the chemical and electrochemical stability of several solid electrolytes (LGPS, LLZO, LiPON, NASICON-type, lithium lanthanum titanate

oxide (LLTO)) as well as the equilibrium conditions at the interfaces. Examining the cathode-electrolyte interface, using lithium cobalt oxide (LCO) as the cathode, a similar pattern emerged: oxides were found to be far more stable than their sulfide counterparts. However, LLTO and lithium aluminum titanium phosphate had the best electrochemical stability against LCO.

Studies looking into the interfacial resistance have been conducted [30, 552–554], with the main source of resistance attributed to the electric double layer, which, in liquid electrolytes, consists of a capacitance and diffusion layer (cf section 4.1) [30]. Tateyama *et al* used the CALYPSO method [528, 529] to find low-energy surfaces to probe the interface. The lithium chemical potential of these stable interfaces in the Helmholtz layer, corresponding to the negative of the Li ion vacancy formation energy, was determined. These energies correspond to lithium moving from the electrode to the electrolyte, with the vacant lithium sites becoming a potential source of interfacial resistance. Okuno *et al* use DFT calculations to compare the interfacial resistances of sulfide and oxide based solid electrolytes with LCO cathodes [552]. The Li vacancy formation energy and ion exchange across various interfaces were calculated. It was found that sulfide-based electrolytes had a higher interfacial resistance, due to the presence of more sites with a low vacancy formation energy on the surface. The authors also found the interfacial resistance to be dependent on the orientation of the crystals at the interface. Interfacial resistance is a major impediment to the commercialisation of ASSBs. The cause of this phenomenon has been elucidated through atomistic simulation of the interface and has provided direction to future SSE development.

A study by Lepley and Holzwarth used DFT to investigate the interface energies between the Li electrode and the compounds that make up the interphase layer of the electrolyte [555]. They defined the interface energy as:

$$\gamma_{ab}(\Omega) = \frac{E_{ab}(\Omega, A, n_a, n_b) - n_a E_a - n_b E_b}{A}, \tag{45}$$

where Ω is the interface configuration of atoms, E_{ab} is the energy of the complete system, E_x is the bulk energy per for formula unit and A is the surface energy. Because the interface energy is intensive, calculating larger systems will give a converging value for γ_{ab},

$$\lim_{\Omega_s \to \Omega} [\gamma_{ab}(\Omega_s)] = \gamma_{ab}(\Omega), \tag{46}$$

where Ω_s is the atomic configuration in a sample of the interface volume. Because the exact matching of lattice constants between interfaces is unlikely, a semi-coherent interface is considered, meaning lattice strain needed to be taken into account. Using the lowest overall lattice energy structure and explicitly accounting for the lattice strain, the most probable interfaces could be found. The Li/Li_3PO_4, Li/Li_2O and Li/Li_2S interfaces were found to be stable and the Li/Li_3PS_4 interface was found to be unstable [555].

In response to the apparent poor stability of most solid electrolytes, many studies have attempted to simulate the effect of coating the electrolyte with an oxide layer [517, 556, 557]. As discussed in section 4.3.3, Tian *et al* identified LiPON as a suitable coating material for LLZO, by comparing the bulk and surface density of states [517]. The authors found no extra states on the surface structure, so concluded that no electron trapping would occur (the primary mechanism that they attributed to dendrite formation). Recently, Sang *et al* proposed an artificial interphase layer between the Li anode and the solid electrolyte, composed of a $Li_{3a_b}N_aX_b$ compound, where X is a halide [558]. This material was investigated computationally by screening stable and metastable structures using the USPEX structure prediction software [559, 560]. The dynamic stability of the stable structures was found by analysing the phonon frequency spectrum by using PHONO3PY [180, 561, 562]. The temperature-dependant ionic transport properties were found using AIMD (cf section 2.1.6).

Phase diagrams for various atomic configurations were then constructed using cluster expansion, implemented through the AT-AT (cf section 2.1.4) [80, 563]. Through these various computational techniques, Sang *et al* found that Li_6NCl_3 has the most favourable properties for use with sulfide-based solid electrolytes, such as LGPS [558]. Authors such as Tian *et al* and Sang *et al* have leveraged the knowledge of the electronic structure and thermodynamic stability gained through atomistic simulation to predict viable coatings for the SSE. The versatility of computational methods allows for a greater variety of these materials to be analysed and could provide a means to screen potential SSE coating materials before performing costly and time-consuming experimental investigations [564].

4.3.5. Outlook and challenges

The drive for the development of commercialised ASSBs has been intense, with the EV industry at the forefront of promoting this [23]. Although ASSBs can offer high gravimetric energy density (250 Wh kg^{-1})

and volumetric energy density (700 Wh l^{-1}), along with improved safety over conventional liquid electrolytes, the slow ionic diffusion can impair fast discharge and charge performance. With solid electrolytes intended to replace both the separator and liquid electrolyte in conventional LiBs [565], there are still multiple challenges which need to be overcome for this to be viable. In recent years, there have been breakthroughs in the discovery of new solid electrolytes, such as $Li_{9.54}Si_{1.74}P_{1.44}S_{11.7}Cl_{0.3}$ [566], which exhibit ionic conductivity competitive with that of organic liquid electrolytes. The improved performance of these materials is enabled by interfacial coatings or buffer layers and micro-structure engineering solutions at the electrode/electrolyte interfaces [567].

ASSBs are currently not capable of reliable cycling at current densities >0.6 mA cm^{-2} [424, 568]. The current density and stability is limited by: poor electrode/electrolyte physical contact, leading to particle cracking and interface delamination, formation and propagation of Li dendrites, chemical and electrochemical stability, and high interfacial resistance [424]. There are several critical issues related to the pairing of solid electrolytes with cathode and anode materials, which need to be addressed for long-term battery operation:

- The limited system sizes of atomistic modelling are not sufficient to capture lattice relaxation, which would allow a coherent (completely matched) interface to form. This amplifies the effects of lattice strain in the model, particularly in cases where periodic boundary conditions are used [555]. The lattice strain energy can be calculated and factored into bulk scale calculations, but it is not as accurate as explicitly calculating dislocation defects that naturally relieve lattice strain [569, 570].
- Dendrite formation has been a notable problem for even the most physically robust electrolytes (cf section 4.3.3). Modelling of dendrite formation mechanisms has yielded some contradictory results, due to incomplete models of the interface [516–518]. However, a more detailed understanding requires modelling of larger systems, encompassing the interface and bulk regions of both materials. This incurs a high computational cost not currently reachable through electronic structure methods methods. Further development of the linear-scaling DFT approach (cf section 2.1.2) may allow a more complete, multiscale approach.
- The system size limitations in DFT modelling also hinder the modelling of the full electric double layer, which is also applicable to liquid electrolytes. Comparatively, in solid electrolytes the double layer is less understood. For example, Tateyama *et al* were only able to successfully model the initial capacitance layer at the interface (Helmholtz layer) [30].
- Interfacial resistance presents an interesting challenge, as it can be introduced through multiple mechanisms [554]: electric double layer [30], surface crystal orientation [552], and production issues, such as poor wettability [553]. Strong collaboration between theorists and experimentalists will be needed, in order to make informed improvements to current interfacial structures.

The interface is the primary source of dendrite formation, lattice mismatch, and interfacial resistance in solid electrolytes. The interface also presents opportunities for atomistic modelling, with the growing popularity of coatings that try to address the shortcomings of popular solid electrolytes [29, 515, 571–584]. For example, Tian *et al*'s solution to dendrite growth in LLZO by utilising a LiPON coating [517] (cf section 4.3.3). Understanding how effective coatings are at addressing the aforementioned issues is essential [517, 556, 557]. A very recent review by Kim *et al* presents a detailed insight into the challenges and future prospects of solid-state Li-metal batteries, which we have touched upon here [567].

5. Cathodes

5.1. Introduction

As mentioned in our Introduction (section 1), LiBs became promising applications in 1979 when Goodenough and Mizushima successfully demonstrated $LiCoO_2$ as a cathode [585]. Since then, LiBs have become instrumental in portable electronics, such as mobile phones, and EVs [586–590], largely attributed to their high energy density [287, 425, 430, 591–599]. Due to the high abundance and low material cost, sodium-ion batteries have also received increased attention, especially for grid storage applications [600–604]. Regardless of the application, the discovery of new materials and the optimisation of current chemistries for improved performance is crucial for the next generation of rechargeable batteries. With that in mind, it is known that the energy density of the cathode material is the limiting factor in improving battery performance, thus current research is largely focused on exploring cathode chemistries. These include layered oxides ($LiMO_2$, M = Co,Mn,Ni), spinel oxides (LiM_2O_4), olivine phosphates ($LiFePO_4$), disordered rock-salts, (Li_2MnO_2F), and other compounds, such as silicates [605, 606].

Layered TM oxides ($LiMO_2$, M = Co, Mn, Ni, etc) are commonly considered to be the first generation of cathode materials in commercial LiBs. These materials possess a theoretical specific capacity of 270 mAh g^{-1}. However, their practical capacity is generally limited to below 200 mAh g^{-1} [607]. $LiCoO_2$ held high capacities but the material was problematic due to capacity fading, low abundance, and the high cost of cobalt and geopolitical issues, including ethical concerns, making large scale applications impractical [608]. There is also considerable instability in the $LiCoO_2$ structure, caused by the extraction of Li during cycling, which results in undesirable phase transitions from O3-type to O6-type Li_xCoO_2 and O1-type CoO_2 [609, 610]. Other layered oxides also pose their own challenges, such as Li_xNiO_2 presenting capacity fade and poor safety [611], and $Li_xMn_2O_4$ presenting low capacity [612]. An emerging alternative to solve some of these challenges is using a combination of the TMs. In 2000, Paulsen *et al* presented $Li_{2/3}[Ni_{1/3}Mn_{2/3}]O_2$ [613, 614], with $Li[Ni_xMn_{1-2x}Co_z]O_2$ (NMC) presented by the authors in 2001 [615]. Partially replacing Co in $LiCoO_2$ with Ni and Mn to obtain layered $Li[Ni_xMn_yCo_z]O_2$ [586], where $x+y+z=1$, shows improved electrochemical performance, while also reducing material cost and improving stability [616]. These layered oxides are commonly termed as NMC, with the subsequent numbering relating to the ratio between the cations.

A huge benefit of combining these TMs is the ability to tune the TM composition to optimise aspects including capacity, (dis)charging rate, electrochemical stability, and lifetime, with the potential of reaching capacities >220 mAh g^{-1} [617]. Some NMC compositions are already used commercially, with industry focus shifting from NMC111 to higher Ni containing compositions including NMC442, NMC532, and NMC622 [618]. These compositions, however, still contain 20% or more Co. A great deal of research is working towards reducing the Co content even further, with compositions such as NMC811 ($Li[Ni_{0.8}Mn_{0.1}Co_{0.1}]O_2$) showing promise as future commercial materials for applications, such as in long-range EVs [619]. These Ni-rich NMC compositions are also considered to be the cathode of choice for future all-solid-state LiBs [607].

Recently, research into further improving the capacity of these materials by inserting lithium into the TM cation sites has attracted considerable attention. This has lead to a new generation of cathode materials termed 'Li-rich' or lithium excess. The increased capacities of these materials arises from invoking redox chemistry on both the TM and oxide ions, as opposed to just TM ions in traditional oxide-based intercalation compounds [620–628]. These Li-rich cathodes, including $Li_{1+x}Ni_yCo_zMn_{(1-x-y-z)}O_2$ layered oxide, can reach high capacities of >300 mAh g^{-1}. However, synthesis of these materials has proven to be difficult and work is ongoing to improve synthesis techniques [629].

There has also been growing interest in disordered intercalation structures, especially disordered rock-salt structures. They were initially disregarded as cathodes, as their structure appeared to limit lithium diffusion. However, recent research has shown that lithium diffusion can be facile in some disordered materials, provided that there is enough of a lithium excess to allow the formation of an uninterrupted percolating network of channels involving no face-sharing TM ions [621, 630, 631]. There have been several examples reported, including $Li_{1.2}Ni_{0.33}Ti_{0.33}Mo_{0.13}O_2$ [631], $Li_{1.2}Ti_{0.4}Mn_{0.4}O_2$ [632], $Li_4Mn_2O_5$ [633–635], Li_3NbO_4-based systems [636–638], and oxyfluorides, where some of the anion sites are occupied by F^- rather than O^2-, such as Li_2MnO_2F [639–641], Li_2VO_2F [642–648], and $Li_2Mn_{2/3}Nb_{1/3}O_2F$ [649]. These materials can be difficult to synthesise, however, as Mn-rich 3D TM compounds tend to form ordered phases, such as $LiMnO_2$ or Li_2MnO_3, high energy mechano-chemical ball-milling methods have been utilised to counter this [633, 640, 650]. These materials are able to reach very high energy storage capacities of 300 mAh g^{-1} [651], which is attributed to the ability to perform both cationic and anionic redox [648, 651, 652]. These materials typicallyshow less first cycle hysteresis than other Li-rich compounds, thought to be because the structure already resembles that of the Li-rich materials after they undergo cation disorder on cycling.

Knowledge of the broad structural and electrochemical properties of cathode materials can be obtained from various experimental methods. However, detailed insight into, for example, TM configurations, vibrational and thermal properties, and atomistic diffusion mechanisms, is challenging and, in some cases, not resolvable using experimental techniques. This is where atomistic modelling can provide greater insight. In this section, we explore a range of cathode material properties, using several Li-ion materials, to highlight different properties and the considerations needed to gain the most desirable electrochemical performance. We describe which atomistic modelling methods are used to investigate the discussed properties and the importance of modelling in this context. Using a range of promising cathode materials (layered oxides, spinel oxides, polyanions, and disordered rock-salt oxides and oxyfluorides) to aid in the discussion, we first look at the different cathode crystal structures and the effects of micro-structuring. We then discuss some of the bulk material properties, including ion diffusion, redox and electronic properties, TM ordering, and vibration and thermal properties. Finally, we consider the surfaces and interfaces of these cathode materials, with an outlook to current and future challenges in the atomistic modelling of cathodes.

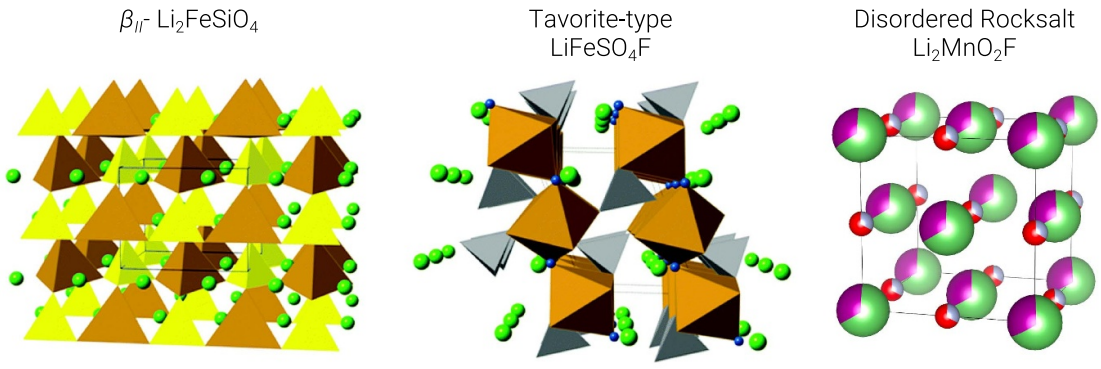

Figure 32. Representative crystal structures of β_{II}-Li_2FeSiO_4, tavorite-type $LiFeSO_4F$, and disordered rock-salt Li_2MnO_2F cathode materials for LiBs. Li^+ ions are shown in green spheres, O in red, Mn in mauve, and F in grey. Fe–O polyhedra are shown in brown, SiO_4 tetrahedra in yellow, and SO_4 tetrahedra in grey.

5.2. Bulk properties

5.2.1. Crystal structure and micro-structure

5.2.1.1. Crystal structure

Cathode materials consist of a range of different crystal structures, with some of the most promising $LiCoO_2$ based materials adopting the α-$NaFeO_2$ structure, with alternating layers of $[CoO_2]^-$ and Li^+. In LiBs, the cathode is a limiting factor, as the amount of lithium that can be reversibly extracted and re-inserted (cycled) directly influences the battery capacity, with the Fermi energy linked to the cell voltage [606]. Thermo-chemical stability and high energy density are also important considerations, with several promising candidates for future battery materials. These include mixed-metal layered oxides (NMC), spinel oxides ($LiMn_2O_4$), polyanion materials($LiFePO_4$ [425, 587, 591, 599], Li_2FeSiO_4 [653–655], $LiFeSO_4F$ [656]), and disordered rock-salt oxides and oxyfluorides (Li_2MnO_2F [639, 648, 651, 652, 657]). The crystal structures of these cathode materials are presented in figures 32 and 33, where these materials are described in more detail.

Some TM oxides are stable in various structural forms, such as LMO, which has been synthesised with layered [658], spinel [659], and rock-salt structures [660]. For intercalation-type cathodes used in LiBs, the structural framework is expected to remain relatively unchanged, with only small changes from lattice expansion/contraction. However, phase transitions can occur during the cycling process. For example, during cycling, a phase transition can occur from the $LiMn_2O_4$ spinel structure to the $LiMnO_2$ rock-salt structure, partially due to oxygen evolution [661]. Phase transitions between layered and spinel structures are also widely observed [662]. For example, Reed *et al* investigated the layered to spinel phase transitions in Li_xMnO_2 using DFT modelling (cf section 2.1.1) [663]. Their investigation determined that partially lithiated layered Li_xMnO_2 transitions to spinel in a two-stage process. Firstly, a large percent of Mn and Li ions quickly occupy tetrahedral sites, to form a meta-stable intermediate. Then, a more complex, coordinated rearrangement of Mn and Li occurs to form spinel. Interestingly, this behaviour is in contrast to Li_xCoO_2 and understanding the reasons for this could prove useful for creating Mn-based cathode materials.

5.2.1.2. Micro-structuring

It is clear that control over bulk structure has an impact on the material's performance, as many properties are dependent on shape and size [664]. The structural and micro-structural properties of a material are also vital to the cycling stability of a cathode. For example, reducing the particle size of $LiFePO_4$ to the nanometre scale is shown to increase the electrochemical performance, compared to equivalent, but larger, particles, by reducing transport path lengths [665–667]. Selective structuring can also provide mechanical benefits, for example, where forces acting on the functional cathode during cycling, as the lattice expands and contracts with lithium intercalation, can cause plastic deformation and extinguish desirable activities. Ledwaba *et al* modelled diffusion-induced stress in layered-spinel LMO composites, revealing structural resilience, enabled by flexing of a porous structure [668]. In this study, Ledwaba *et al* found the yield stress of the bulk material was 11.35 GPa, whilst the nanoporous material subjected to an equivalent strain experienced a stress of 4.32 GPa. In fact, it has been proposed that a β-MnO_2 host should be symmetrically porous and heavily twinned to maximise the cathode's electrochemical properties [669]. Further to this, intergrowing structures of two polymorphs of MnO_2, β-MnO_2 and Ramsdellite-MnO_2 [670], has been shown to enhance cell performance [671], due to reduction in stresses and facile diffusion in more open structure of Ramsdellite-MnO_2.

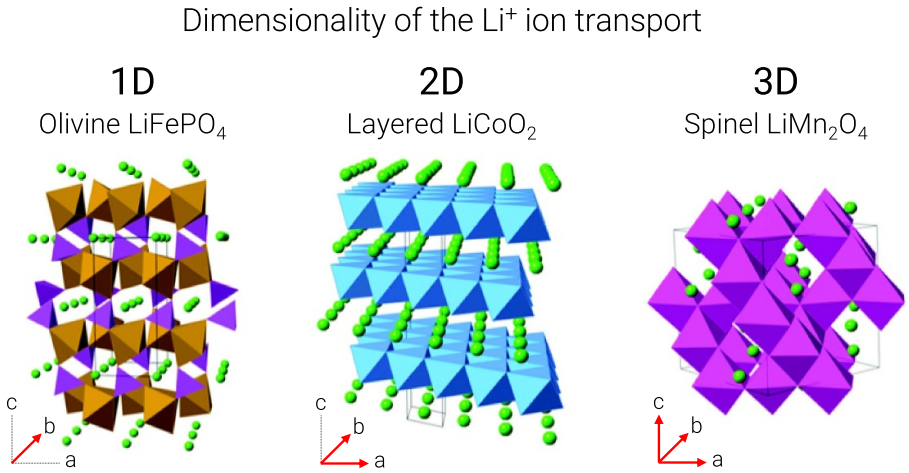

Figure 33. Dimensionality of the Li^+ ion diffusion in $LiFePO_4$, $LiCoO_2$, and $LiMn_2O_4$. Reproduced from [606]. CC BY 3.0.

5.2.2. Lithium-ion diffusion

As discussed in section 2.3.3, Li-ion diffusion coefficients can be calculated using multiple techniques, including AIMD, classical (potentials-based) MD, and MC. Diffusion coefficients, although important experimentally and for parameterising continuum models, are not the only ion transport property of interest on the atomistic scale. Properties such as atomistic diffusion mechanisms, hopping frequencies, and activation energy barriers are all vital to understanding Li-ion transport and (dis)charge rate behaviour. This is of particular interest for investigating the effects of grain-boundaries and interfaces on the migration routes and mechanisms. For example, in $LiCoO_2$, Moriwake *et al* determined that the activation energy, E_a, for Li migration *along* a twin boundary is 0.20 eV, smaller than that in the bulk, while the E_a *across* a twin boundary is 0.4 eV [672]. This demonstrates the influence of grain-boundaries on the kinetic properties.

Computational techniques can provide information regarding a material's diffusion behaviour, which cannot be fully understood through experiments alone. For example, Dixit *et al* compared Li and Na diffusion in $Li_{0.25}FePO_4$ and $Na_{0.25}FePO_4$, respectively, by calculating the potential and free energy diffusion barriers and determining the nuclear quantum effects (NQEs) of the Li ions [673]. Their calculations found that Li diffusion was faster than Na diffusion, which is in agreement with experiments. However, the authors also determined that the NQEs for Li-ions were higher than those for Na-ions and that the quantum behaviour of the Li-ions was unusual. This information would not be possible to resolve using current experimental methods.

The cathode crystal structure determines the available diffusion pathways in the material. DFT calculations [674, 675] and classical MD using a core–shell model [676] show Li_xFePO_4 is an olivine based structure which hosts Li over an interstitial network that has one-dimensional connectivity, i.e. 1-D diffusion, along the *b* lattice vector of the orthorhombic cell [677]. Li_xCoO_2 is a layered compound that accommodates Li ions within octahedral sites forming two-dimensional triangular lattices, resulting in 2D diffusion, along the *b* and *c* lattice vector of the orthorhombic cell [678]. The spinel form of $Li_xMn_2O_4$ has both tetrahedrally and octahedrally coordinated Li interstitial sites, forming a three-dimensional network and resulting in 3D diffusion, along all lattice vectors [679, 680]. These different diffusion pathways can bee seen in figure 33. The 1-D diffusion pathways in Li_xFePO_4 are not actually exactly one dimensional. Although they travel solely along the *b* lattice vector, the pathways themselves are curved, as shown in figure 34, as originally predicted by Islam *et al* using atomistic modelling [676], before later being observed experimentally [681].

Chemical diffusion coefficient of Li in an intercalation compound often has a strong dependence on Li concentration and crystal structure. The combination of DFT cluster expansion Hamiltonians with kMC simulations, as described in sections 2.1.4 and 2.1.5 revealed that the Li diffusion coefficients of TM oxides (and sulfides) are very sensitive to the Li concentration and also to the degree of cation ordering [77, 682–685]. For example, Van der Ven *et al* shows the calculated Li diffusion coefficients for the layered (2D) and spinel (3D) forms of Li_xTiS_2 as a function of Li concentration [9, 682, 683, 685]. This is presented in figure 35, along with the structural images and vacancy mechanisms highlighted. Here it can be seen that not only do the Li diffusion coefficients differ by orders of magnitude, but the shape of the diffusion/Li concentration relation is very different. This shows how the crystal structure, and thus the active diffusion

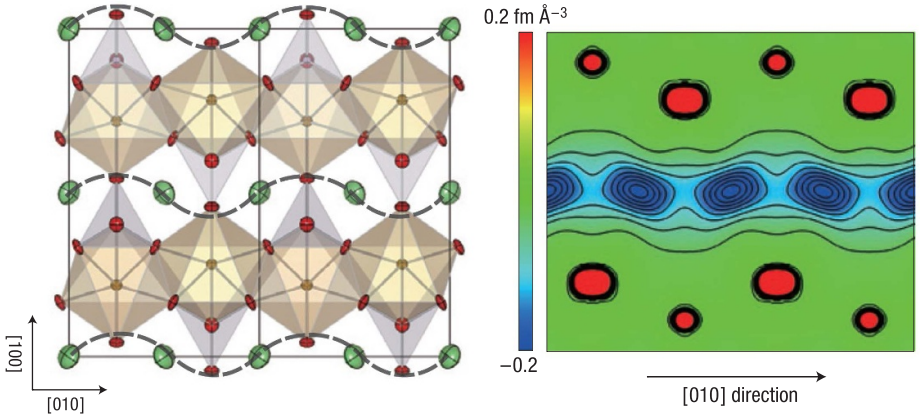

Figure 34. Anisotropic harmonic lithium vibration in $LiFePO_4$. Expected curved one-dimensional continuous chains of lithium motion are drawn as dashed lines to show how the motions of Li atoms evolve from vibrations to diffusion. Two-dimensional contour map sliced on the (001) plane at $z = 0.5$; lithium delocalises along the curved one-dimensional chain along the [010] direction, whereas Fe, P, and O remain near their original positions. Reprinted by permission from Springer Nature Customer Service Centre GmbH: Springer Nature, Nature Materials, [681], © 2008, Nature Publishing Group.

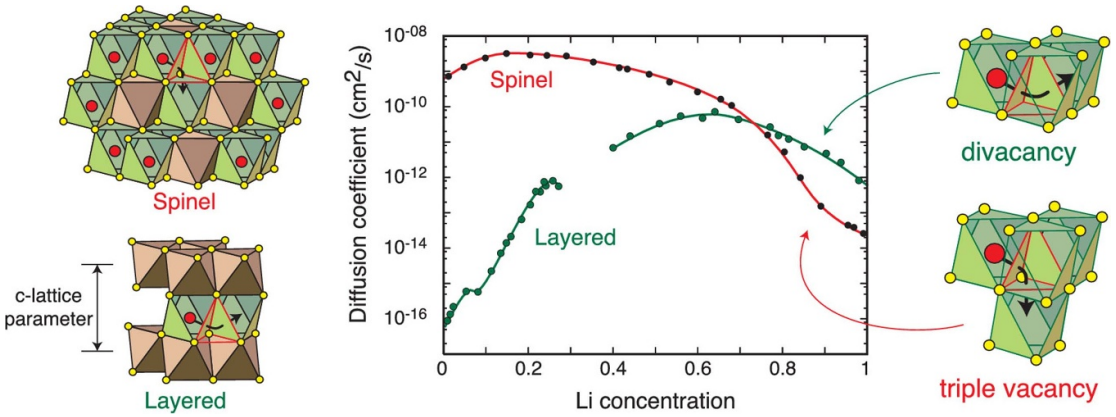

Figure 35. Chemical diffusion coefficient of Li in an intercalation compound often has a strong dependence on Li concentration and crystal structure. Reprinted with permission from [9]. Copyright (2020) American Chemical Society.

pathways, plays a crucial role in determining the concentration dependence of the diffusion coefficients in these materials.

We have already eluded that diffusion is sensitive to the Li-ion concentration. However, the exact relation is through the activation barriers. Early DFT studies [678, 686] of Li_xCoO_2 systems showed that the lithium diffusion was predominately through a divacancy mechanism, when $0 \leqslant x < 1$. However, at infinite vacancy dilutions diffusion is through a single vacancy mechanism [606]. There are two hopping mechanisms at play here; oxygen dumbbell hops and tetrahedral site hops. Oxygen dumbbell hopping occurs when there is a single vacancy and a Li-ion has to travel between two occupied adjacent lithium sites to reach the vacant lithium site. Tetrahedral site hopping occurs when there are divacant or trivacant sites, i.e. when one or both of the adjacent lithium sites are vacant [686]. Oxygen dumbbell hopping has a significantly lower migration barrier energy compared to tetrahedral site hopping, which highlights the sensitivity of the activation barrier to the lithium concentration. Experimental studies of mixed-TM layered oxides, such as $Li(Ni_{0.5}Mn_{0.5})O_2$, have reported site exchange between Li and Ni (∼8%–12%) [687]. DFT has been used to aid in understanding the effects of site–exchange on Li-ion mobility [688, 689]. (De)intercalation of lithium in the material changes the distances between the layers. As Li is removed from the structure, there is a reduced 'barrier' between the oxygen layers which start to repel one another. By calculating the activation energy as a function of the distance between the O layers on either side of the Li layers, a trend between increased O layer separation and lower activation energy is seen [688, 689].

In addition to the crystal structure and available diffusion pathways, doping the cathode material can also influence the material properties, including ion diffusion. NMC cathodes are effectively $LiCoO_2$ doped with Ni and Mn. As previously mentioned in section 5.1, introducing Ni and Mn into the system to form a

mixed-TM layered oxide increases the diffusion/conductivity and electrochemical performance. There are very few detailed computational studies of mixed-TM oxides due to their complexities. An illustration of this is the complexities which arise from TMs, such as Fe, Ni, Co, and Mn, which exhibit localised oxidation states. This can be further complicated, or influenced by, TM ordering. For instance, Lee and Persson investigated the effects of TM disorder on the electrochemical properties of $Li_xNi_{0.5}Mn_{1.5}O_4$ using cluster expansion and MC methods (cf sections 2.1.4 and 2.1.5). The authors determined a correlation between Li vacancy ordering and TM ordering [690]. Hao *et al* found similar evidence for $Li_x(Mn_yNi_{1-y})_2O_4$ [691]. These also have an effect on the diffusion properties of the material. TM ordering in NMC cathodes is discussed in more detail in section 5.2.4. Using experimental techniques, Capsoni *et al* found that doping the cationic sublattice of spinel $LiMn_2O_4$ with as low as 1% Ga^3+ significantly modifies the temperature of the conductivity drop associated with Jahn-Teller (JT) distortion, preventing the transition observed near room temperature [692]. This allows for a wider temperature window for the higher conductivity phase. DFT using GGA or its variant GGA+U (cf section 2.1.1), was also employed to analyse the effect of doping $LiMn_2O_4$ on the JT distortion. In this study, Singh *et al* found that doping with Cr and Mg also suppressed the JT distortion and thus the associated temperature of the conductivity drop [693].

5.2.3. Redox and electronic properties

The cathode operates by the deintercalation of Li^+ on charging, and the reinsertion of Li^+ on discharging. The charge is balanced by the oxidation and reduction of the TM ion, e.g. $LiCo^{3+}O_2 \rightleftharpoons Li_{1-x}Co^{4+}O_2 + xLi^+ + xe^-$. The role of TM redox in LiBs has been well known since the first publications by Goodenough on $LiCoO_2$ as an intercalation electrode in 1980 [585]. Although various classes of compounds have been investigated over the years, the overall mechanism of TM redox is broadly similar. The three major classes of oxide cathodes, (layered [585], polyanion [694], and spinel [695]) all function via a TM redox couple. The specific capacity of most LiB cathode materials is limited by the number of electrons per TM cation that can participate in the redox reaction. However, the recent discovery of oxygen redox reactivity, $O^{2-} \rightarrow (O_2)^{n-}$, in Li-excess cathode materials [620, 622–627, 629, 639, 696–710] has prompted further investigation.

DFT has been pivotal in shedding light on this phenomenon, in conjunction with a range of experimental techniques. DFT can be used to analyse the atomic charge and electronic structure of each ground state, enabling the charge compensation during delithiation to be correctly attributed during simulated charging. Yao *et al* were able to propose a sequence of redox events for delithiation of $Li_4Mn_2O_5$ [634]; first, cationic redox, Mn^{3+}/Mn^{4+}, dominates for $Li_xMn_2O_5$, when $4 \geqslant x > 2$. Then anionic redox, O^{2-}/O^{1-}, dominates for $Li_xMn_2O_5$, when $2 \geqslant x > 1$. Finally, mixed cationic (Mn^{4+}/Mn^{5+}) and anionic (O^{2-}/O^{1-}) redox for $Li_xMn_2O_5$, when $1 \geqslant x \geqslant 0$. Meanwhile, fluorinated materials such as $Li_2Mn_{2/3}Nb_{1/3}O_2F$ [649] and Li_2MnO_2F [639] were found to exhibit some overlap between the redox processes, suggesting that the substitution of O by F favours lower Mn oxidation states, therefore leading to more redox overlap with oxygen. DFT has also been used to establish the band structure for cathode materials, determining which TM orbitals hybridise more with the O(2p) orbitals [699, 711] and to identify hole states [704, 712].

In a combined experimental and computational study, Gent *et al* observed a strong correlation between anion redox, cation migration, and OCV hysteresis in Li-rich layered oxides [624]. Hong *et al* offered an explanation for the strong coupling between anion redox and structural disordering in Li rich layered oxides; they found local stabilisation of short ∼1.8 Å metal-oxygen π bonds and ∼1.4 Å O–O dimers during oxygen redox [713].

Seo *et al* showed that anion redox chemistry is heavily dependent on the anion nearest-neighbour coordination environment [623]. In particular, they described how more Li–O–Li configurations lead to more potentially labile oxygen electrons, resulting in enhanced O redox chemistry, as shown in figure 36. A similar result was found with Li_2MnO_2F; those oxygens coordinated to at least five Li (e.g. OLi_5Mn) in the fully lithiated state were the first to oxidise, whereas those coordinated to three or fewer (e.g. OLi_3Mn_3) did not undergo oxidation at all. This showcased a more continuous variation in the O-redox potential, dependent on the number of Li coordinated to a given O^{2-} ion [639]. Recent computational screening work on layered oxide cathodes using hybrid DFT has reported trends in O-redox activity associated with the electrostatic (Madelung) energy at oxygen sites [714].

Chen and Islam investigated delithiation and kinetic processes in Li_2MnO_3 using hybrid DFT and found that Li extraction is charge-compensated by oxidation of the oxide anion, so that the overall delithiation reaction involves lattice oxygen loss [701]. Localised holes on oxygen (O^-) are formed at the first step but, due to their instability, lead to oxygen dimers (O–O is approximately 1.3 Å) and eventually to the formation of molecular O_2. This then facilitates Mn migration to the octahedral site in the vacant Li layer, leading to a spinel-like structure. DFT has also been used to show the formation of O_2 at high states of charge in Li_2MnO_2F [639] and $Li_{1.2}Ni_{0.13}Co_{0.13}Mn_{0.54}O_2$ [628], agreeing with experimental resonant inelastic x-ray

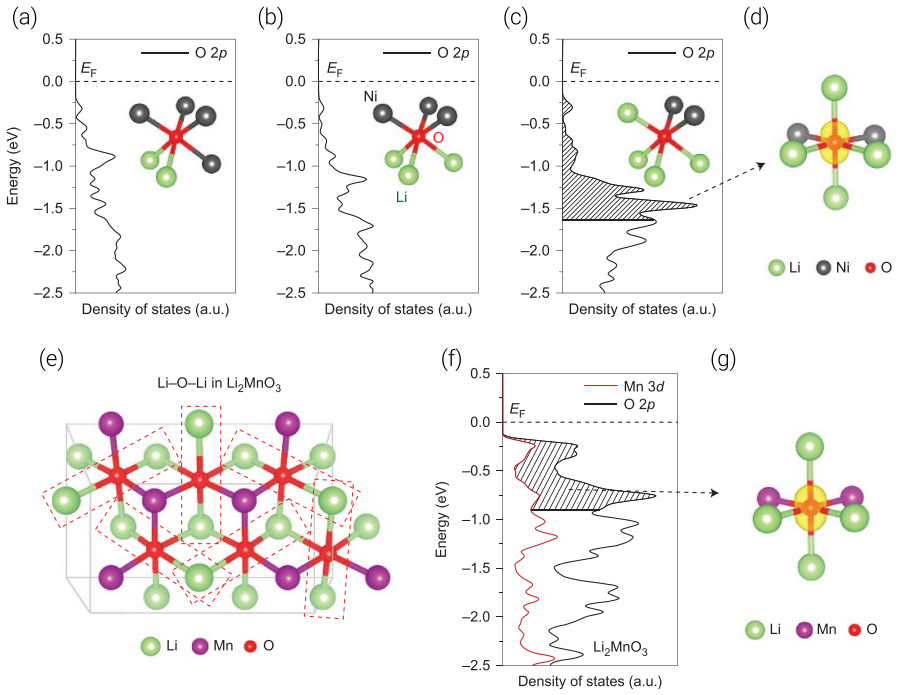

Figure 36. Effect of local atomic environments on the electronic states of O ions in (a)–(d) cation-mixed layered $LiNiO_2$ and (e)–(g) Li_2MnO_3. Cation mixing introduces various local environments around oxygen. Projected density of states (pDOS) of the O 2 *p* orbitals of O atoms in cation-mixed layered $LiNiO_2$ coordinated by (a) two Li and four Ni, (b) three Li and three Ni, and (c) four Li and two Ni. (d) gives the isosurface of the charge density (yellow) around the oxygen coordinated by four Li and two Ni, in the energy range of 0 to −1.64 eV. (e) gives an illustration of Li–O–Li configurations in Li_2MnO_3, with (f) giving the related pDOS of the O 2 *p* orbitals and Mn 3 *d* orbitals, and (g) giving the isosurface of the charge density (yellow) around the oxygen, in the energy range of 0 to −0.9 eV. Reprinted by permission from Springer Nature Customer Service Centre GmbH: Nature Chemistry, Springer Nature, [623], © 2016, Nature Publishing Group.

scattering data, and to report superoxide formation in Li_2VO_2F, in agreement with electron paramagnetic resonance spectroscopy studies [648].

5.2.4. TM ordering in NMC layered oxides

Cation/anion ordering also plays a vital role in the properties/activity of a material, such as the physical and electrochemical properties. A topical illustration of this is the NMC cathode materials, where recent experimental studies show that spin interaction of the TM ions is a major challenge [617, 715]. The varying compositions, charge distributions, and electronegativities of the TMs lead to a mixture of valence states, where Ni can exist as Ni^{2+}, Ni^{3+}, and Ni^{4+}, Co can exist as Co^{3+} and Co^{4+}, and Mn exists as Mn^{4+} [715]. The interactions between these mixed valence states poses a challenge to the identification of ground states. As NMC materials, such as NMC811, emerge as front runners for commercialisation, research into their specific chemistry has become of great interest. Recently, several computational studies have been performed to analyse the influence of TM valence states on the stability and structure-property relationships of NMC materials, which are challenging to resolve experimentally [716–719]. For example, Sun and Zhao analysed 81 NMC compositions using DFT, observing that random arrangements of TMs present similar thermodynamic states [716]. Clusters of random geometries and population were seen, which confirmed that no specific ordering exists at the superlattice scale. This is consistent with previous experiment analysis using x-ray and neutron diffraction characterization on a specific composition of NMC, $Li_{2/3}[Co_xNi_{1/3-x}Mn_{2/3}]O_2$, demonstrating that Co suppresses the superlattice ordering when $x > 1/6$ [720]. The authors also demonstrated, through intensive computational screening, that no long-range ordering exists in the TM layer of NMC. These DFT studies provide fundamental understanding of the physicochemical properties at the intrinsic level of electronic structures and will offer important insight in the selection of NMC materials for enhanced electrochemical performance. It would not be tractable to analyse so many compositions of NMC through experiments.

5.2.5. Vibrational and thermal properties

An important contribution to the thermodynamic properties at finite temperature is the vibrational partition function, which can be evaluated by calculating the material's normal modes of lattice vibrations. A number

of researchers have theoretically addressed the vibrational contribution to the material thermodynamic properties in LiBs, especially in NMC cathodes [181, 182, 721]. There are several works studying cathode materials beyond NMC. Shang *et al* employed DFT phonon calculations with a mixed-space approach to probe the lattice dynamics and finite-temperature thermodynamic properties of olivine structure $LiMPO_4$ (M = Mo, Fe, Co, Ni) [722]. The authors reported that $LiMPO_4$ structures from Mn, Fe, Co, to Ni show increasing zero-point vibrational energy, but a diminishing vibrational contribution to the Gibbs energy, due to the decreasing phonon densities of state at the low frequency region of $LiMPO_4$. Recently, lattice dynamics studies have been expanded to solid electrolytes, aiding in the discovery of lithium fast-ion conductors [723] .

Two major approaches have been developed to compute lattice thermal conductivity; by solving the Boltzmann transport equation (BTE) using anharmonic lattice dynamics and through MD simulations. Puligheddu *et al* compared lattice thermal conductivity values from these two methods and found a satisfactory agreement [724]. The comparison used empirical potentials and took into account the effects of both fourth order phonon scattering and temperature-dependent phonon frequencies, reporting the different effects of quantum and classical statistics.

Using BTE within the relaxation-time approximation, Mattila and Karttunen reported the highly anisotropic lattice thermal conductivities in isotopic $LiCoO_2$, close to the values in Yang *et al*'s work [181, 182], and illustrated the effect of the alkali metal atom by replacing Li by Na [725]. The authors explained this through the significantly shorter phonon lifetimes in $LiCoO_2$. They found that in-plane lattice thermal conductivities in $NaCoO_2$ are ∼0.7 times larger than that in $LiCoO_2$ at room temperature, since the former has significantly longer phonon life times. While Feng *et al* report much lower thermal conductivity values by including four-phonon scattering, using a different functional, the LDA, for exchange and correlation [726]. They also investigated the thermal transport reduction during delithiation (charging) due to reduced phonon velocities and increasing anharmonicity. Furthermore, grain-boundary effects reduced thermal transport and suppressed thermal conductivities in polycrystals are well reproduced when grain sizes were reduced down to several nm in either BTE or MD simulations [155].

The thermal conductivity investigation can be also performed on anodes and many other materials [727, 728]. Recently, a high-throughput study was reported for 37 binary rock-salt and zinc blende material systems, in which the authors highlight the importance of high-order phonon-phonon interactions based on harmonic calculations [729]. Modelling heat transport using DFT calculations is complex but essential due to the difficulties inherent in preparing high-quality samples for experimental measurements.

5.3. Surfaces

Surface structures and morphologies of cathode particles can be difficult to determine using experimental microscopy and spectroscopy methods alone and thus computational investigations can provide vital insights [730]. Due to their synthesis conditions, experimental cathode materials comprise different surface facets, defects, and particle sizes. It is therefore necessary to use model systems to determine which of these effects is more important by studying them in isolation, separating the effects, which is not possible using experimental materials. Both *ab initio* and potentials-based MD have been extensively used to investigate the surfaces and morphologies of layered oxides, spinel oxides, and olivine phosphates, which will be briefly discussed here. These techniques have also been used to investigate cathode materials in sodium-ion batteries, which is covered in more detail in reference [606].

With oxides at the forefront of the battery revolution, it is unsurprising that there have been many DFT and potentials-based MD studies into layered $LiCoO_2$, $LiMn_2O_4$ spinel, MnO_2-type and related materials, looking at properties including the surfaces, nanostructures, and morphologies [731–738]. Surface energies for low-index layered $LiCoO_2$ surfaces, as a function of external Li and O chemical potentials, revealed the (0001) and $(10\bar{1}4)$ surfaces were present for all reasonable values of Li and O chemical potentials, whereas the $(01\bar{1}2)$ surface was only stable under oxidising conditions [731]. Studies into the low-index surface facets of $LiMn_2O_4$ determine the (111) surface to be the most stable. This is due to the site exchange of under-coordinated Mn on the surface, which exhibit a cubo-octahedral type, predominately comprising {111} surfaces [736]. Other studies show that the Mn-terminated (111) surfaces undergo surface reconstruction, indicating instead that the Li-terminated (001) surface has the lowest energy [735].

It has also been shown that electronic spin state transitions occur on the surfaces of stoichiometric $LiCoO_2$. Here Qian *et al* found that the trivalent Co ions at the surface adopt an intermediate spin state if they are square–pyramidally coordinated and a high spin state if they are pseudo-tetrahedrally coordinated. This highlighted the effect of low-coordinated geometries at the particle surface on the Co^{3+}–Co^{4+} redox potential [739]. Hong *et al* investigated the surface properties of $LiCoO_2$ nanoplatelets and their chemical modifications with Al^{3+}, using combined experimental and theoretical approaches [740]. Their models also showed the electronic structures of several $LiCoO_2$ surface facets are different from those of the bulk,

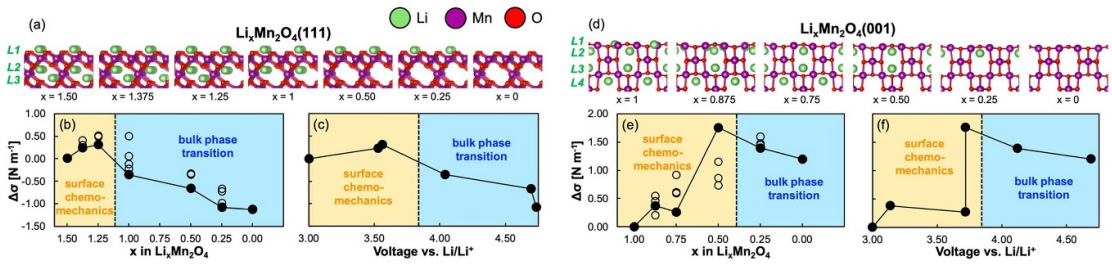

Figure 37. Surface stress evolution upon delithiation of LMO surfaces. Low energy structures of the (a) LMO (111) and (d) LMO (001) surfaces at different Li^+ contents. Differential surface stresses of (b) LMO (111) and (e) LMO (001) as a function of the Li^+ content for various Li^+ configurations. The filled circles in (b), (e) represent the most energetically stable structures for a given stoichiometry. The unfilled circles in (b), (e) denote metastable lithium configurations. Differential surface stresses of (c) LMO (111) and (f) LMO (001) as a function of the cell voltage. The dashed lines correspond to the calculated equilibrium potential of 3.84 V vs Li/Li^+ between LMO and $L_{0.5}MO$. The yellow-shaded regions correspond to surface-dominated mechanics from the near-surface delithiation. The blue-shaded regions correspond to surface phases that are thermodynamically inaccessible because they become stable only at voltages above the equilibrium potential. Reprinted with permission from [746]. Copyright (2020) American Chemical Society.

attributing this to the altered spin states of surface Co^{3+} atoms. The authors found splitting of the Co 3d–O 2p states, which were linked with high-spin-state Co^{3+} at the surface. Partial substitution of Co^{3+} by Al^{3+} was found to increase the ratio of low-spin-state Co^{3+} at the surface, resulting in a distinct change in the intensity ratio of the split Co 3d–O 2p states.

When exposed to certain environmental conditions, $LiCoO_2$ releases Co cations, a known toxicant. Abbaspour-Tamijani *et al* has applied DFT (with different functionals) and thermodynamics modelling to study the $LiCoO_2$ surface transformations [741]. They assessed how the calculated predictions for ion release depend on aspects of the structural surface model. Here, the authors propose a generalised scheme for predicting a threshold pH at which Co release becomes favourable, providing information that could be used to inform macroscopic contaminant fate models. More recently, these authors have furthered this investigation in cation dissolution at the $LiCoO_2$ surface, finding that at a pH of 7%, 16% of surface Co undergoes dissolution [741].

Phase transitions in cathode materials can have negative effects on the desirable properties. However, there are circumstances where use of different structural phases are beneficial. For example, post-modification of Li-rich layered material surfaces to form a spinel $LiMn_2O_4$ membrane, i.e. encapsulating the layered particle, has shown enhanced related rate capability and cycling stability [148, 742, 743]. More significantly, insertion of a spinel component [744] or the formation of platelets [745] on layered-layered composites of NMC cathodes, yields a high specific capacity (∼250 mAh g^{-1}) and can partly correct for voltage fade [148]. Phase transitions can also be a negative consequence of particle surface stress. Warburton *et al* investigated the particle fracturing in $LiMn_2O_4$ caused by stress through the delithiation process [746]. Using DFT, the authors provide a good understanding of the stress buildup at the surface during delithiation, demonstrating that the delithiation of near-surface layers contribute towards the buildup, leading to a $LiMn_2O_4/Li_{0.5}Mn_2O_4$ low-voltage phase transition, figure 37. The authors also investigate if there is an orientation preference, concluding that cracks due to tensile stress buildup are not likely to orient preferentially in the [001] direction, because the stresses act in the plane of the (001) surface [746]. This shows that an in-depth understanding of the electrochemical processes of cathode materials, at the atomistic scale, is urgently needed, especially for more complex chemistries like NMC. A recent study on the NMC surfaces by Liang *et al* looked at the surface segregation and anisotropy using DFT+U calculations [747]. In this study, the authors looked at surface stability, morphology, and elastic anisotropy, all related to the degradation of Li-ion batteries. Ni surface segregation predominantly occurs on the (100), (110), and (104) nonpolar surfaces, showing a tendency to form a rock-salt NiO domain on the surface, due to severe Li–Ni exchange. The findings of this study showed that an uneven deformation is more likely to form in particles which have been synthesised under low oxygen conditions, leading to crack generation and propagation [747].

The surface structures of $LiFePO_4$ exhibit a complex and uneven topology due to the size difference of Li^+, Fe^{2+}, and PO_4^{3-}. The majority of terminating surfaces undergo fairly considerable relaxation, which makes predictions based on rigid terminations unreliable. Although $LiFePO_4$ can be synthesised in multiple morphologies exposing different surfaces [666, 748], studies on the (010) surfaces are particularly interesting. This surface is normal to the most facile pathway for lithium ion conduction [749], reducing the

diffusion path lengths for lithium at the surface, enhancing the electrochemical performance of the cathode. DFT calculation of the diffusion pattern and energy landscape of lithium in $LiFePO_4$ showed that the energy barrier for the Li diffusion along (010) is lower than along the other directions, e.g. (100), indicating that the Li diffusion in $LiFePO_4$ is one dimensional [750]. Understanding processes such as the lithium (de)intercalation on the $LiFePO_4$ (010) surface is important for developing effective approaches for further improving the material's rate performance. Using DFT calculations, Xu *et al* found that the extraction of Li from the surface layer has a significant effect on the work function of the $LiFePO_4$ (010) surface, providing evidence for whether Li atoms are present in the outermost layer of $LiFePO_4$ (010) surface or not [751]. Here, the authors also calculate the redox potential and formation energies for extracting Li from different (010) surface layers. They find that extracting lithium from the outer surface layers has the lowest redox potential and formation energy, indicating that it is energetically favourable to extract Li first from the surface layer. Xu *et al* propose a new method that surface work functions can be used for providing insight into the lithium (de)intercalation on the $LiFePO_4$ (010) surface [751].

Zhang *et al* used a combined experimental and computational (DFT) approach to investigate the preferential cation doping on the surface of $LiFePO_4$ and its effect on properties [752]. The authors found that, for all chosen dopants, there were increased ratios of Fe^{3+}/Fe^{2+} oxidation on the particle surfaces, while the core atoms remained closer to that of the pristine, undoped material. This indicates that the dopants are predominantly pushed to the particle surfaces during phase formation. This disparity in distribution of dopant across the core and surface results in improved conductivities [752]. AIMD simulations with XRD and microscopy experiments on the $LiFePO_4$ cathode show Li-ions migrating along the surface, facilitated by solvent molecules [753]. This work establishes fluid-enhanced surface diffusion as a key factor in tuning phase transformation in anisotropic solids.

5.4. Interfaces

Although the CEI is thinner than the SEI at the anode, it is still quite complex in structure and composition [115, 754]. DFT-based simulations can provide insight into adsorption trends [755], reaction pathways and energetics [756, 757], and migration barriers for Li-ion transfer [758], etc. The electrolyte in a Li-ion battery is typically a Li salt, for example $LiPF_6$ in an organic carbonate solvent, such as EC, PC, diethyl carbonate or DMC. The $LiPF_6$ electrolyte reacts with trace amounts of moisture to form HF [756], which is highly corrosive and reacts with the cathode surface to form fluoride-based products [757]. The organic carbonate solvent also reacts with the cathode surface to form a series of decomposition products [759]. The adsorption of solvent-decomposition and fluoride-based products is the first step in the series of reactions that lead to the formation of the CEI. The decomposition reaction of cyclic organic carbonate solvents proceeds via ring opening, having an energy barrier predicted via CI-NEB calculations (sections 2.1.1 and 2.1.3) to be around 0.62 eV on (100) $LiMn_2O_4$ surfaces [737], over 1 eV on $(10\bar{1}4)$ $LiCoO_2$ surfaces [759], and around 0.29 eV on $(10\bar{1}4)$ Li(Ni,Mn,Co)O_2 surfaces [760]. While experimental studies on the composition of the CEI have shown the presence of both solvent-decomposition and fluoride-based products on most oxide cathodes, such as $LiMn_2O_4$, $LiNiO_2$ $LiCoO_2$ and $LiNi_{0.8}Co_{0.2}O_2$, no solvent reaction or solvent decomposition products are detected on $LiFePO_4$ [754, 761]. Recent calculations of adsorption energies based on DFT have shown that adsorption preference of HF over EC leads to the entire $LiFePO_4$ nano-particle being covered by fluoride-based products, further leading to their dominant presence in the CEI [755]. DFT simulations have also been used to design suitable coatings in order to prevent cathode degradation [757]. These calculations can shortlist effective candidate materials to guide experiments. Thus, atomistic methods can not only provide the necessary insights needed in order to explain experimental observations, but also suggest novel solutions for mitigating cathode degradation.

Apart from the complexity of structure of the CEI, another challenge is understanding Li-ion migration at the CEI, impacting the rate capability of LiBs. Li-ion conductivity in bulk electrolyte is around 1 S cm^{-1} (cf section 4) which is several orders of magnitude higher than that in bulk electrode materials (cf sections 3.2.4 and 5.2.2) (around 10^{-7}–10^{-2} S cm^{-1}) [287, 685]. However, the complex structure of the CEI and uncertainty about the mechanism of Li-ion transfer across it has hindered the understanding of kinetics at the interface. Recent NEB calculations on the $LiFePO_4$ cathode have estimated an energy barrier of 756 meV, for Li to move from a near-surface solvated cluster to a sub-surface vacancy in the $LiFePO_4$ cathode material [758]. Due to preferential adsorption of fluoride on $LiFePO_4$ surfaces [754, 755], the energy barrier has been found to decrease to 410 meV in the presence of fluoride. Nevertheless, the interfacial energy barrier is higher than that in bulk cathode material, which is estimated to be around 270–290 meV [674, 762]. This highlights a rate-limiting behaviour of the interface in the overall Li-ion diffusion process in LiBs. This study motivates further investigation on other cathode electrolyte interfaces, especially with recently developed advanced methods for characterising the interface, as described in section 2.2.1.

5.5. Outlook and challenges for cathodes

Lowering the cost, increasing capacity, and improving the sustainability of battery materials is becoming more critical, as we move towards large-scale deployment of LiBs for applications such as EVs [588]. Here, we highlight some of the outstanding challenges for cathodes and how atomistic modelling can provide insights and suggest solutions.

Ni-rich NMC layered oxides are favourite candidates for cathode materials, due to their high gravimetric and volumetric energy densities [763]. However, these materials have three critical challenges: cycle instability, thermal instability, and air instability. These are all linked with the instability of Ni^{3+} and Ni^{4+} at the surface/interface. Other cathode materials, such as oxyfluorides, have worked towards solving some of these issues, however, there are still outstanding surface and interfacial challenges, for which atomistic modelling is vital:

- In Ni-rich NMC, the unstable Ni^{3+} and Ni^{4+} react aggressively with the electrolyte to form thick CEI layers and cause Ni and Mn dissolution. The dissolute TMs then migrate to the anode and cause electrolyte decomposition, leading to thick SEI layers which limit the battery cyclability [764, 765]. CEI and SEI formation are crucial challenges to be overcome for both conventional and solid-state batteries. Although electrochemical spectroscopic techniques have been used to obtain molecular scale information, further detail, which cannot be resolved using current experimental techniques, is needed to gain more reliable information [766]. For example, deconvoluting impedance components in two-terminal EIS data for materials that have similar time constants, such as solid-state lithium charge transfer in a cell with a graphitized carbon anode and $LiCoO_2$ cathode, is challenging [767]. Half-cell measurements can be used to study the impedance of the two electrodes separately, but these measurements do not fully reflect the processes occurring in a full-cell battery at different states of (dis)charge [768]. Three-electrode cell configurations present a way to potentially disentangle the impedance components from the anode and cathode [767]. However, these measurements are fraught with uncertainties, as the insertion of the reference electrode can fundamentally change the electrochemistry [769, 770]. This is where atomistic modelling is well suited to provide the fundamental understanding of the limiting rate constants in electrochemistry, that can be used to guide further experiments. As available experimental techniques are unable to provide significant insight into the atomistic mechanism of Li-ion transfer at the cathode-electrolyte interface, atomistic modelling is ideally suited to shed light in this area. For example, Bhandari *et al* used DFT to investigate the interfacial Li-ion transfer mechanism at an atomic level, from bulk EC/$LiPF_6$ electrolyte into a $LiFePO_4$ cathode, and provide an estimate on the corresponding energy barrier [758].
- Phase transitions at the surface of cathode materials occur at a high state of charge and affect the surface reactivity, resulting in increased TM dissolution and CEI/SEI formation. The effect of this is rapid capacity fading during cycling [771]. Co-free Li-rich layered oxides, such as $Li[Li_{0.2}Mn_{0.6}Ni_{0.2}]O_2$, are appealing due to their low cost and high capacities (300 mAh g^{-1}) [772, 773]. However, these materials undergo layered to spinel transitions due to low octahedral site stability of Mn^{3+}, leading to voltage decay during cycling and Mn dissolution [774], making these materials challenging to employ as a practical cathode. Atomistic insight into the mechanisms involved in these phase transitions, gained through *ab initio* and potentials-based MD methods, can provide the detail and understanding needed to prevent these phase transitions from occurring.
- Some cathode materials show reversible O-redox, with lower voltage hysteresis and, where O_2 is formed, it reincorporates into the lattice [639]. In contrast, other materials show irreversible O-redox, with O_2 lost from the surface [628, 701, 775], leading to unwanted side reactions with the electrolyte. The formation and potential loss of molecular O_2 is likely to be heavily dependent on local structure. In the case of Li_2MnO_2F, DFT showed that O_2 is formed only in O-Li rich areas, not in O-Mn rich areas [639]. Meanwhile, other oxyfluorides, such as Li_2VO_2F, do not show molecular O_2 formation at all, but instead form superoxides on charging [648].

It is challenging to model disordered systems as, by their very nature, they can have an almost infinite arrangement of atoms. Use of computational techniques, such as cluster expansion, to generate low energy structures of disordered rock-salts, is a promising route to more realistic DFT studies [641].

As discussed in sections 2.2.2 and 4.2.4, more careful considerations of the factors/parameters to include when fitting interatomic potentials for a system is key to improving the quality of research conducted through potentials-based modelling. It is commonplace to reuse potentials from literature sources, without determining how they were fitted, which can lead to inaccuracies in the calculations performed. For example, if the potentials for a cathode material were fitted only to lattice parameters, elastic constants, and the bulk modulus, then the potential would not be accurately representative of the cathode redox properties. If

properties such as the dielectric constant were included, then redox chemistry would be better represented. In effect, interatomic potentials in literature are not necessarily transferable to different types of study. It is not feasible to fit to every material property, however, a broader range of properties, most relevant to the study being conducted, is required. There are tools in development [142, 143, 145, 164] aiming to make this potential fitting process more accessible to atomistic modellers, with the ability to fit to a larger range of parameters. However, there is still a need for improved transparency in the publication of studies using interatomic potentials. Use of machine learning to develop potentials has also shown to be a promising avenue. Deringer *et al* recently published a progress update, showing how machine learning is improving interatomic potentials by 'learning' from electronic-structure data, giving increased accuracy in approximating material properties [776].

In-depth insight into the elemental distribution, electronic structure, and crystalline structure under electrochemical conditions is challenging to achieve experimentally. Atomistic techniques, including DFT and MD, are well suited to provide the insight needed for these properties. However, future research and development of cathode materials will require collaborative efforts, involving the disciplines of chemistry, physics, material science, nanoscience/nanotechnology, and computational modelling/simulation [116].

6. Outlook

In this review, we have introduced the key methods deployed in battery modelling at the atomistic scale (section 2.1) in LiBs and solid-state batteries (ASSBs), which are collectively called lithium batteries. We have summarised progress in this field, covering models for anodes, liquid and solid electrolytes, and cathodes. Outlooks specific to these components are summarised as follows: anodes, in section 3.5; liquid electrolytes, in section 4.2.10; solid electrolytes, in section 4.3.5; and cathodes, in section 5.5.

There are several notable developments in atomistic methods for lithium batteries which need to be addressed. These include development of a semi-grand canonical framework, incorporating order parameters, with initial promising work developed by Van der Ven *et al* [9, 231], the expansion of the linear scaling DFT codes [58, 62, 65], to link up with kMC, the inclusion of entropy effects by parameterising a phase field model (such as those developed by Bazant) [95–97] using results obtained from MC calculations, development of more accurate force field potentials, and parallelisation to speed up MC calculations on longer length scales.

Alongside deepening our understanding of atomic structure and processes, atomistic models can be used to aid the design of new materials with improved capacity, rate capability, and stability. Atomistic modelling approaches have been shown to be strong tools to develop novel nanostructures and composites, understand dynamics and phase behaviour, and could identify novel interfaces to accommodate volume expansion in solid solution materials, such as silicides. Promising areas for future work include tuning the morphology and composition of graphite edges [70, 254, 255] and interlayer spacings [214] to aid intercalation, improved understanding of the phase behaviour and dynamics of silicides as anode materials [272], and investigation of the emerging class of Li-rich cathode materials [626, 627, 629].

We have identified several outstanding challenges for further work. For example, certain anode and cathode materials show pronounced hysteresis between charge and discharge cycles [71, 226, 272, 777–779]. This results in a difference between expected equilibrium potentials from atomic-scale calculations and the experimentally measurable OCV, which creates ambiguity when using the measured OCV in longer length scale models, like control models for BMSs. Future kinetic models must therefore account for metastable behaviour that can persist over experimental time scales of hours or even days [226]. The next generation of models should consider the connectivity between different phase transformations, with the framework developed by Van der Ven *et al* highlighted above being one promising solution that is potentially transferable to a variety of material types.

Flammable liquid electrolyte materials currently dominate the commercial market. Development of safer, non-flammable, electrolyte materials is key to addressing safety concerns and accidents resulting from attempts to confine increasing energy densities into smaller volumes and into geometries that are challenging to thermally manage. More work is needed to investigate potential avenues for resolving these issues, including alternative liquid electrolytes [17, 18, 406], such as water-in-salt electrolytes [403, 404], and replacing liquid electrolytes with solid or soft matter alternatives [23, 567]. Advancements in electrolyte design are crucial, where critical obstacles could be resolved through new novel electrolyte salts and solvents. Development and open source accessibility of atomistic scale models, combined with improved experimental studies, provide a framework for high throughput screening of electrolyte materials [357, 371, 401, 402].

More work is needed to incorporate heterogeneities formed during material synthesis and battery degradation [780–782], such as point defects [89, 93, 289, 531, 718] and grain boundaries [304, 515, 783], into atomistic models and to determine their effect on battery performance. Modelling of the complex

behaviour at interfaces, such as the SEI in LiBs and lattice mismatch in ASSBs, is a prominent challenge which requires further investigation. Atomistic models have already provided insight into particular aspects of degradation, leading to design of more robust materials, but the development of a universal framework for simulating degradation mechanisms and their interactions would be of great benefit and is still beyond current capabilities. In order for such a framework to be truly multiscale, significant work is needed to connect the modelling scales, linking atomistic to continuum modelling and on to longer length scales, such as control models, as well as forming closer links with experiments at all scales.

As we have seen throughout this review, different atomistic modelling approaches can be used individually to gain insight into different aspects and properties of LiB materials, across the wide range of time and length scales encompassing atomistic modelling. When combined into MSM approaches, these techniques can provide a more complete interpretation of the material(s) [10, 11, 233]. A popular approach has been to combine DFT calculations of activation energies of different events, which are then used to implement kMC simulations [104]. DFT calculations of the migration mechanisms and activation barriers of Li-ions have also been combined with classical MD studies of Li-ion diffusion to gain a more complete analysis of the dynamic properties in LiB materials [784, 785]. Quantum mechanical techniques, such as DFT, are also increasing being used to parameterise larger scale techniques, for example classical MD [143–145, 164, 776]. The key consideration when designing MSM approaches is to reproduce the phenomena that dictate the natural behaviour and evolution of the material in given conditions. Thorough reviews, which focus more on the MSM aspect of LiB research, have recently been published by Franco *et al* [233] and Shi *et al* [10]. kMC in particular has been highlighted as a natural technique to bridge length scales, naturally including different time scale dynamic events [104]. In this review, we have instead focused on the individual contributions of atomistic techniques, the understanding of which is key to building MSM approaches. However, the full complexity of composite materials, such as C/Si, may only be accessible by bridging atomistic techniques to MSM such as via phase field methods, volume-averaged approaches, or mesostructurally-resolved models [10, 11, 95, 233].

This review has focused almost entirely on lithium batteries, given that they currently comprise the most technologically advanced rechargeable battery systems that are commercialised at scale. However, atomistic modelling applied to LiBs also improves understanding of batteries that could be based on more environmentally-friendly or Earth-abundant materials, such as sodium. Solid state models of intercalation, applied to LiBs, are directly transferable to other intercalation chemistries. The understanding of interfaces in batteries with other chemistries is even less developed than in LiBs. However, the modelling frameworks highlighted in this review, such as the linear-scaling DFT framework, could also be applied to improve understanding of these interfaces.

Data availability statement

No new data were created or analysed in this study.

Acknowledgments

The authors thank the Faraday Institution (https://faraday.ac.uk/; EP/S003053/1), Grant Number FIRG003, for funding, and Dr Maxim Zyskin for his discussions. We also thank Mr Amir Kosha Amiri for his graphical design expertise in constructing and formatting the figures, as well as Dr Felix Hanke and Dr Victor Milman from BIOVIA for their comments and suggestions.

ORCID iDs

Lucy M Morgan https://orcid.org/0000-0002-6432-3760
Michael P Mercer https://orcid.org/0000-0001-7578-3554
Arihant Bhandari https://orcid.org/0000-0002-2914-9402
Chao Peng https://orcid.org/0000-0003-3099-2808
Mazharul M Islam https://orcid.org/0000-0002-5638-8265
Hui Yang https://orcid.org/0000-0002-7890-5411
Julian Holland https://orcid.org/0000-0001-8959-0112
Samuel W Coles https://orcid.org/0000-0001-9722-5676
Ryan Sharpe https://orcid.org/0000-0002-1337-0209
Aron Walsh https://orcid.org/0000-0001-5460-7033
Benjamin J Morgan https://orcid.org/0000-0002-3056-8233
Denis Kramer https://orcid.org/0000-0003-0605-1047

M Saiful Islam https://orcid.org/0000-0002-8077-6241
Harry E Hoster https://orcid.org/0000-0001-6379-5275
Jacqueline Sophie Edge https://orcid.org/0000-0003-4643-2426
Chris-Kriton Skylaris https://orcid.org/0000-0003-0258-3433

References

[1] Zeng X, Li M, Abd El-Hady D, Alshitari W, Al-Bogami A S, Lu J and Amine K 2019 Commercialization of lithium battery technologies for electric vehicles *Adv. Energy Mater.* **9** 1900161
[2] Goodenough J B and Kim Y 2010 Challenges for rechargeable Li batteries *Chem. Mater.* **22** 587–603
[3] Kubiak P, Cen Z, López C M and Belharouak I 2017 Calendar aging of a 250 kW/500 kWh Li-ion battery deployed for the grid storage application *J. Power Sources* **372** 16–23
[4] Doyle M, Fuller T F and Newman J 1993 Modeling of galvanostatic charge and discharge of the lithium/polymer/insertion cell *J. Electrochem. Soc.* **140** 1526
[5] Fuller T F, Doyle M and Newman J 1994 Simulation and optimization of the dual lithium ion insertion cell *J. Electrochem. Soc.* **141** 1
[6] Fuller T F, Doyle M and Newman J S 4 1994 Relaxation phenomena in lithium-ion-insertion cells *J. Electrochem. Soc.* **141** 982
[7] Doyle M and Newman J 1995 The use of mathematical modeling in the design of lithium/polymer battery systems *Electrochim. Acta* **40** 2191–6
[8] Newman J and Thomas-Alyea K E 2004 *Electrochemical Systems* vol 3 (New York: Wiley)
[9] Van der Ven A, Deng Z, Banerjee S and Ong S P 2020 Rechargeable alkali-ion battery materials: theory and computation *Chem. Rev.* **120** 6977–7019
[10] Shi S, Gao J, Liu Y, Zhao Y, Wu Q, Ju W, Ouyang C and Xiao R 2016 Multi-scale computation methods: their applications in lithium-ion battery research and development *Chin. Phys.* B **25** 018212
[11] Franco A A 2013 Multiscale modelling and numerical simulation of rechargeable lithium ion batteries: concepts, methods and challenges *RSC Adv.* **3** 13027–58
[12] Herbert J M 2021 Dielectric continuum methods for quantum chemistry *Wiley Interdiscip. Rev.-Comput. Mol. Sci.* **11** e1519
[13] Scrosati B 1992 Lithium rocking chair batteries: an old concept? *J. Electrochem. Soc.* **139** 2776–81
[14] Asenbauer J, Eisenmann T, Kuenzel M, Kazzazi A, Chen Z and Bresser D 2020 The success story of graphite as a lithium-ion anode material—fundamentals, remaining challenges and recent developments including silicon (oxide) composites *Sustain. Energy Fuels* **4** 5387–416
[15] Zhang H, Yang Y, Ren D, Wang Li and He X 2021 Graphite as anode materials: fundamental mechanism, recent progress and advances *Energy Storage Mater.* **36** 147–70
[16] Wang A, Kadam S, Li H, Shi S and Qi Y 2018 Review on modeling of the anode solid electrolyte interphase (SEI) for lithium-ion batteries *npj Comput. Mater.* **4** 15
[17] Shepherd K and Siddiqui F 2021 A driverless tesla crashed and burned for four hours, police said, killing two passengers in texas *Washington Post*
[18] Pfrang A, Kriston A, Ruiz V, Lebedeva N and di Persio F 2017 Safety of rechargeable energy storage systems with a focus on Li-ion technology *Emerging Nanotechnologies in Rechargeable Energy Storage Systems* (Amsterdam: Elsevier)
[19] Liu L, Xu J, Wang S, Wu F, Li H and Chen L 2019 Practical evaluation of energy densities for sulfide solid-state batteries *eTransportation* **1** 100010
[20] Galiński M, Lewandowski A and Stępniak I 2006 Ionic liquids as electrolytes *Electrochim. Acta* **51** 5567–80
[21] Wang Y, Meng X, Sun J, Liu Y and Hou L 2020 Recent progress in "water-in-salt" electrolytes toward non-lithium based rechargeable batteries *Front. Chem.* **8** 595
[22] Logan E R and Dahn J R 2020 Electrolyte design for fast-charging li-ion batteries *Trends Chem.* **2** 354–66
[23] Woods L 2021 *Technological Advancements in Solid State Batteries for Electric Vehicles, 2020 Report - Toyota is the Pioneer of Solid-state Battery Research and Development with a Lion's Share of Patent Ownership* (https://www.prnewswire.com/news-releases/technological-advancements-in-solid-state-batteries-for-electric-vehicles-2020-report---toyota-is-the-pioneer-of-solid-state-battery-research-and-development-with-a-lions-share-of-patent-ownership-301218086.html) (Accessed 29 January 2021)
[24] Zhu Y, He X and Mo Y 2015 Origin of outstanding stability in the lithium solid electrolyte materials: insights from thermodynamic analyses based on first-principles calculations *ACS Appl. Mater. Interfaces* **7** 23685–93
[25] Zhang Q, Cao D, Ma Y, Natan A, Aurora P and Zhu H 2019 Sulfide-based solid-state electrolytes: synthesis, stability and potential for all-solid-state batteries *Adv. Mater.* **31** 1901131
[26] Zhang Z *et al* 2018 New horizons for inorganic solid state ion conductors *Energy Environ. Sci.* **11** 1945–76
[27] Gurung A *et al* 2019 A review on strategies addressing interface incompatibilities in inorganic all-solid-state lithium batteries *Sustain. Energy Fuels* **3** 3279–309
[28] Xiao Y, Wang Y, Bo S H, Kim J C, Miara L J and Ceder G 2020 Understanding interface stability in solid-state batteries *Nat. Rev. Mater.* **5** 105–26
[29] Xu L, Tang S, Cheng Y, Wang K, Liang J, Liu C, Cao Y-C, Wei F and Mai L 2018 Interfaces in solid-state lithium batteries *Joule* **2** 1991–2015
[30] Tateyama Y, Gao B, Jalem R and Haruyama J 2019 Theoretical picture of positive electrode–solid electrolyte interface in all-solid-state battery from electrochemistry and semiconductor physics viewpoints *Curr. Opin. Electrochem.* **17** 149–57
[31] Ceder G, Ong S P and Wang Y 2018 Predictive modeling and design rules for solid electrolytes *MRS Bull.* **43** 782–8
[32] Ma Y 2018 Computer simulation of cathode materials for lithium ion and lithium batteries: a review *Energy Environ. Mater.* **1** 148–73
[33] Yan L-M, Su J-M, Sun C and Yue B-H 2014 Review of the first principles calculations and the design of cathode materials for Li-ion batteries *Adv. Manuf.* **2** 358–68
[34] Wang L, Chen B, Ma J, Cui G and Chen L 2018 Reviving lithium cobalt oxide-based lithium secondary batteries-toward a higher energy density *Chem. Soc. Rev.* **47** 6505–602
[35] Maleki Kheimeh Sari H and Li X 2019 Controllable cathode–electrolyte interface of $Li[Ni_{0.8}Co_{0.1}Mn_{0.1}]O_2$ for lithium ion batteries: a review *Adv. Energy Mater.* **9** 1901597

[36] Parr R G and Yang W 1994 *Density-Functional Theory of Atoms and Molecules (Int. Series of Monographs on Chemistry)* (Oxford: Oxford University Press)
[37] Hohenberg P and Kohn W 1964 Inhomogeneous electron gas *Phys. Rev.* **136** B864–71
[38] Kohn W and Sham L J 1965 Self-consistent equations including exchange and correlation effects *Phys. Rev.* **140** A1133–8
[39] Dirac P A M 1930 Note on exchange phenomena in the Thomas atom *Math. Proc. Camb. Phil. Soc.* **26** 376–85
[40] Perdew J P and Wang Y 1992 Accurate and simple analytic representation of the electron-gas correlation energy *Phys. Rev.* B **45** 13244–9
[41] Perdew J P, Burke K and Ernzerhof M 1996 Generalized gradient approximation made simple *Phys. Rev. Lett.* **77** 3865–8
[42] Becke A D 1988 Density-functional exchange-energy approximation with correct asymptotic behavior *Phys. Rev.* A **38** 3098–100
[43] Lee C, Yang W and Parr R G 1988 Development of the Colle-Salvetti correlation-energy formula into a functional of the electron density *Phys. Rev.* B **37** 785–9
[44] Perdew J P, Kurth S, Zupan A and Blaha P 1999 Accurate density functional with correct formal properties: a step beyond the generalized gradient approximation *Phys. Rev. Lett.* **82** 2544
[45] Grimme S 2006 Semiempirical GGA-type density functional constructed with a long-range dispersion correction *J. Comput. Chem.* **27** 1787–99
[46] Grimme S, Antony J, Ehrlich S and Krieg H 2010 A consistent and accurate ab initio parametrization of density functional dispersion correction (DFT-D) for the 94 elements H-Pu *J. Chem. Phys.* **132** 154104
[47] Caldeweyher E, Bannwarth C and Grimme S 2017 Extension of the D3 dispersion coefficient model *J. Chem. Phys.* **147** 034112
[48] Grimme S, Ehrlich S and Goerigk L 2011 Effect of the damping function in dispersion corrected density functional theory *J. Comput. Chem.* **32** 1456–65
[49] Johnson E R and Becke A D 2006 A post-Hartree-Fock model of intermolecular interactions: inclusion of higher-order corrections *J. Chem. Phys.* **124** 174104
[50] Becke A D 1993 Density-functional thermochemistry. III. The role of exact exchange *J. Chem. Phys.* **98** 5648–52
[51] Cramer C J 2013 *Essentials of Computational Chemistry: Theories and Models* (New York: Wiley)
[52] Bredow T and Gerson A R 2000 Effect of exchange and correlation on bulk properties of MgO, NiO and CoO *Phys. Rev.* B **61** 5194–201
[53] Islam M M, Bredow T and Gerson A 2007 Electronic properties of oxygen-deficient and aluminum-doped rutile TiO_2 from first principles *Phys. Rev.* B **76** 045217
[54] Heyd J, Scuseria G E and Ernzerhof M 2003 Hybrid functionals based on a screened Coulomb potential *J. Chem. Phys.* **118** 8207–15
[55] Dudarev S L, Botton G A, Savrasov S Y, Humphreys C J and Sutton A P 1998 Electron-energy-loss spectra and the structural stability of nickel oxide: an LSDA+U study *Phys. Rev.* B **57** 1505–9
[56] Dudarev S L, Liechtenstein A I, Castell M R, Briggs G A D and Sutton A P 1997 Surface states on NiO (100) and the origin of the contrast reversal in atomically resolved scanning tunneling microscope images *Phys. Rev.* B **56** 4900–8
[57] Anisimov V I, Aryasetiawan F and Lichtenstein A I 1997 First-principles calculations of the electronic structure and spectra of strongly correlated systems: the **LDA** + *U* method *J. Phys.: Condens. Matter.* **9** 767–808
[58] Goedecker S 1999 Linear scaling electronic structure methods *Rev. Mod. Phys.* **71** 1085–123
[59] Prodan E and Kohn W 2005 Nearsightedness of electronic matter *Proc. Natl Acad. Sci.* **102** 11635–8
[60] Galli G and Parrinello M 1992 Large scale electronic structure calculations *Phys. Rev. Lett.* **69** 3547–50
[61] Hernández E and Gillan M J 1995 Self-consistent first-principles technique with linear scaling *Phys. Rev.* B **51** 10157–60
[62] Skylaris C K, Haynes P D, Mostofi A A and Payne M C 2005 Introducing ONETEP: linear-scaling density functional simulations on parallel computers *J. Chem. Phys.* **122** 084119
[63] Gillan M J, Bowler D R, Torralba A S and Miyazaki T 2007 Order-*N* first-principles calculations with the conquest code *Comput. Phys. Commun.* **177** 14–18
[64] Mohr S, Ratcliff L E, Genovese L, Caliste D, Boulanger P, Goedecker S and Deutsch T 2015 Accurate and efficient linear scaling DFT calculations with universal applicability *Phys. Chem. Chem. Phys.* **17** 31360–70
[65] Prentice J C A *et al* 2020 The ONETEP linear-scaling density functional theory program *J. Chem. Phys.* **152** 174111
[66] Bhandari A, Anton L, Dziedzic J, Peng C, Kramer D and Skylaris C-K 2020 Electronic structure calculations in electrolyte solutions: methods for neutralization of extended charged interfaces *J. Chem. Phys.* **153** 124101
[67] Jónsson H, Mills G and Jacobsen K W 1998 Nudged elastic band method for finding minimum energy paths of transitions *Classical and Quantum Dynamics in Condensed Phase Simulations* (Pennsylvania State University: Citeseer) 385–404
[68] Henkelman G, Uberuaga B P and Jónsson H 2000 A climbing image nudged elastic band method for finding saddle points and minimum energy paths *J. Chem. Phys.* **113** 9901–4
[69] Henkelman G and Jónsson H 2000 Improved tangent estimate in the nudged elastic band method for finding minimum energy paths and saddle points *J. Chem. Phys.* **113** 9978–85
[70] Peng C, Mercer M P, Skylaris C-K and Kramer D 2020 Lithium intercalation edge effects and doping implications for graphite anodes *J. Mater. Chem.* A **8** 7947–55
[71] Mercer M P, Peng C, Soares C, Hoster H E and Kramer D 2021 Voltage hysteresis during lithiation/delithiation of graphite associated with meta-stable carbon stackings *J. Mater. Chem.* A **9** 492–504
[72] Sanchez J M, Ducastelle F and Gratias D 1984 Generalized cluster description of multicomponent systems *Physica* A **128** 334–50
[73] De Fontaine D 1994 Cluster approach to order-disorder transformations in alloys *Solid State Phys.* **47** 33–176
[74] Blum V and Zunger A 2004 Mixed-basis cluster expansion for thermodynamics of bcc alloys *Phys. Rev.* B **70** 155108
[75] Gallavotti G 2013 *Statistical Mechanics: A Short Treatise* (New York: Springer Science & Business Media)
[76] Persson K, Hinuma Y, Meng Y S, Van der Ven A and Ceder G 2010 Thermodynamic and kinetic properties of the Li-graphite system from first-principles calculations *Phys. Rev.* B **82** 125416
[77] Van der Ven A, Ceder G, Asta M and Tepesch P D 2001 First-principles theory of ionic diffusion with nondilute carriers *Phys. Rev.* B **64** 184307
[78] van de Walle A 2009 Multicomponent multisublattice alloys, nonconfigurational entropy and other additions to the alloy theoretic automated toolkit *Calphad* **33** 266–78
[79] van de Walle A, Asta M D and Ceder G 2002 The alloy theoretic automated toolkit: a user guide *Calphad* **26** 539–53
[80] van de Walle A and Ceder G 2002 Automating first-principles phase diagram calculations *J. Phase Equilib.* **23** 348–59
[81] Natarajan A R, Thomas J C, Puchala B and Van der Ven A 2017 Symmetry-adapted order parameters and free energies for solids undergoing order-disorder phase transitions *Phys. Rev.* B **96** 134204

[82] Pickard C J and Needs R J 2011 *Ab initio* random structure searching *J. Phys.: Condens. Matter.* **23** 053201
[83] Ångqvist M, Muñoz W A, Magnus Rahm J, Fransson E, Durniak C, Rozyczko P, Rod T H and Erhart P 2019 ICET—a Python library for constructing and sampling alloy cluster expansions *Adv. Theory Simul.* **2** 1900015
[84] Chang J H, Kleiven D, Melander M, Akola J, Garcia-Lastra J M and Vegge T 2019 CLEASE: a versatile and user-friendly implementation of cluster expansion method *J. Phys.: Condens. Matter.* **31** 325901
[85] Binder K and Landau D P 2009 *A Guide to Monte-Carlo Simulations in Statistical Physics* 3rd edn (Cambridge: Cambridge University Press)
[86] Lee T D and Yang C N 1952 Statistical theory of equations of state and phase transitions. II. Lattice gas and ising model *Phys. Rev.* **87** 410–9
[87] Mercer M P and Hoster H E 2016 Ultrahigh vacuum and electrocatalysis—the powers of quantitative surface imaging *Nano Energy* **29** 394–413
[88] Oviedo O A, Reinaudi L, Garcia S and Leiva E P M 2015 Underpotential deposition: from fundamentals and theory to applications at the nanoscale *Monographs in Electrochemistry* (Switzerland: Springer International Publishing) (https://doi.org/10.1107/978-3-319-24394-8)
[89] Mercer M P, Finnigan S, Kramer D, Richards D and Hoster H E 2017 The influence of point defects on the entropy profiles of lithium ion battery cathodes: a lattice-gas Monte Carlo study *Electrochim. Acta* **241** 141–52
[90] Kim S-W and Pyun S-I 2001 Thermodynamic and kinetic approaches to lithium intercalation into a $Li_{1-\delta}Mn_2O_4$ electrode using Monte Carlo simulation *Electrochim. Acta* **46** 987–97
[91] Mercer M P, Otero M, Ferrer-Huerta M, Sigal A, Barraco D E, Hoster H E and Leiva E P M 2019 Transitions of lithium occupation in graphite: a physically informed model in the dilute lithium occupation limit supported by electrochemical and thermodynamic measurements *Electrochim. Acta* **324** 134774
[92] Leiva E P M, Perassi E and Barraco D 2017 Shedding light on the entropy change found for the transition stage II → stage I of Li-ion storage in graphite *J. Electrochem. Soc.* **164** A6154–7
[93] Schlueter S, Genieser R, Richards D, Hoster H E and Mercer M P 2018 Quantifying structure dependent responses in Li-ion cells with excess Li spinel cathodes: matching voltage and entropy profiles through mean field models *Phys. Chem. Chem. Phys.* **20** 21417–29
[94] Haftbaradaran H, Song J, Curtin W A and Gao H 2011 Continuum and atomistic models of strongly coupled diffusion, stress and solute concentration *J. Power Sources* **196** 361–70
[95] Bazant M Z 2017 Thermodynamic stability of driven open systems and control of phase separation by electro-autocatalysis *Faraday Discuss.* **199** 423–63
[96] Guo Y, Smith R B, Yu Z, Efetov D K, Wang J, Kim P, Bazant M Z and Brus L E 2016 Li intercalation into graphite: direct optical imaging and Cahn–Hilliard reaction dynamics *J. Phys. Chem. Lett.* **7** 2151–6
[97] Bai P, Cogswell D A and Bazant M Z 2011 Suppression of phase separation in $LiFePO_4$ nanoparticles during battery discharge *Nano Lett.* **11** 4890–6
[98] Metropolis N, Rosenbluth A W, Rosenbluth M N, Teller A H and Teller E 1953 Equation of state calculations by fast computing machines *J. Chem. Phys.* **21** 1087–92
[99] Darling R and Newman J 1999 Dynamic Monte Carlo simulations of diffusion in $Li_yMn_2O_4$ *J. Electrochem. Soc.* **146** 3765–72
[100] Thomas K E and Newman J 2003 Heats of mixing and of entropy in porous insertion electrodes *J. Power Sources* **119–21** 844–9
[101] Zhang X-F, Zhao Y, Patel Y, Zhang T, Liu W-M, Chen M, Offer G J and Yan Y 2017 Potentiometric measurement of entropy change for lithium batteries *Phys. Chem. Chem. Phys.* **19** 9833–42
[102] Gavilán-Arriazu E M, Pinto O A, de Mishima B A L, Barraco D E, Oviedo O A and Leiva E P M 2020 Kinetic Monte Carlo applied to the electrochemical study of the Li-ion graphite system *Electrochim. Acta* **331** 135439
[103] Gavilán-Arriazu E M, Mercer M P, Pinto O A, Oviedo O A, Barraco D E, Hoster H E and Leiva E P M 2020 Effect of temperature on the kinetics of electrochemical insertion of Li-ions into a graphite electrode studied by kinetic Monte Carlo *J. Electrochem. Soc.* **167** 013533
[104] Gavilán-Arriazu E M, Mercer M P, Barraco D E, Hoster H E and Leiva E P M 2021 Kinetic Monte Carlo simulations applied to Li-ion and post Li-ion batteries: a key link in the multi-scale chain *Prog. Energy* **3** 042001
[105] Car R and Parrinello M 1985 Unified approach for molecular dynamics and density-functional theory *Phys. Rev. Lett.* **55** 2471–4
[106] Tuckerman M E and Parrinello M 1994 Integrating the Car–Parrinello equations. I. Basic integration techniques *J. Chem. Phys.* **101** 1302–15
[107] Grossman J C, Schwegler E, Draeger E W, Gygi F and Galli G 2004 Towards an assessment of the accuracy of density functional theory for first principles simulations of water *J. Chem. Phys.* **120** 300–11
[108] Harding J H 1990 Computer simulation of defects in ionic solids *Rep. Prog. Phys.* **53** 1403–66
[109] Buckingham R A 1938 The classical equation of state of gaseous helium, neon and argon *Proc. R. Soc.* A **168** 264–83
[110] Born M and Mayer J 1932 On the lattice theory of ionic crystals *Z. Phys.* **75** 1–18
[111] Mayer J E 1932 Dispersion and polarizability and the van der Waals potential in the alkali halides *J. Chem. Phys.* **1** 270
[112] Todorov I T, Smith W, Trachenko K and Dove M T 2006 Dl_poly_3: new dimensions in molecular dynamics simulations via massive parallelism *J. Mater. Chem.* **16** 1911–8
[113] Plimpton S 1995 Fast parallel algorithms for short-range molecular dynamics *J. Comput. Phys.* **117** 1–19
[114] Gale J D 1997 GULP: a computer program for the symmetry-adapted simulation of solids *J. Chem. Soc. Faraday Trans.* **93** 629–37
[115] Gauthier M *et al* 2015 The electrode-electrolyte interface in Li-ion batteries: current understanding and new insights *J. Phys. Chem. Lett.* **6** 4653–72
[116] Yu X and Manthiram A 2018 Electrode–electrolyte interfaces in lithium-based batteries *Energy Environ. Sci.* **11** 527–43
[117] Jinnouchi R, Kodama K and Morimoto Y 2018 Electronic structure calculations on electrolyte–electrode interfaces: successes and limitations *Curr. Opin. Electrochem.* **8** 103–9
[118] Hansen M H and Rossmeisl J 2016 PH in grand canonical statistics of an electrochemical interface *J. Phys. Chem.* C **120** 29135–43
[119] Sakong S, Naderian M, Mathew K, Hennig R G and Groß A 2015 Density functional theory study of the electrochemical interface between a Pt electrode and an aqueous electrolyte using an implicit solvent method *J. Chem. Phys.* **142** 234107
[120] Skyner R E, McDonagh J L, Groom C R, Van Mourik T and Mitchell J B O 2015 A review of methods for the calculation of solution free energies and the modelling of systems in solution *Phys. Chem. Chem. Phys.* **17** 6174–91
[121] Kang J, Wei S H, Zhu K and Kim Y H 2011 First-principles theory of electrochemical capacitance of nanostructured materials: dipole-assisted subsurface intercalation of lithium in pseudocapacitive TiO_2 anatase nanosheets *J. Phys. Chem.* C **115** 4909–15

[122] Dufils T, Jeanmairet G, Rotenberg B, Sprik M and Salanne M 2019 Simulating electrochemical systems by combining the finite field method with a constant potential electrode *Phys. Rev. Lett.* **123** 195501
[123] Jorn R, Kumar R, Abraham D P and Voth G A 2013 Atomistic modeling of the electrode-electrolyte interface in Li-ion energy storage systems: electrolyte structuring *J. Phys. Chem.* C **117** 3747–61
[124] Zhang C, Sayer T, Hutter J and Sprik M 2020 Modelling electrochemical systems with finite field molecular dynamics *J. Phys. Energy* **2** 032005
[125] Cramer C J and Truhlar D G 1999 Implicit solvation models: equilibria, structure, spectra and dynamics *Chem. Rev.* **99** 2161–200
[126] Tomasi J, Mennucci B and Cammi R 2005 Quantum mechanical continuum solvation models *Chem. Rev.* **105** 2999–3093
[127] Grochowski P and Trylska J 2008 Continuum molecular electrostatics, salt effects and counterion binding—a review of the Poisson–Boltzmann theory and its modifications *Biopolymers* **89** 93–113
[128] Jinnouchi R and Anderson A B 2008 Electronic structure calculations of liquid-solid interfaces: combination of density functional theory and modified Poisson–Boltzmann theory *Phys. Rev.* B **77** 245417
[129] Gunceler D, Letchworth-Weaver K, Sundararaman R, Schwarz K A and Arias T A 2013 The importance of nonlinear fluid response in joint density-functional theory studies of battery systems *Modelling Simul. Mater. Sci. Eng.* **21** 074005
[130] Ringe S, Oberhofer H, Hille C, Matera S and Reuter K 2016 Function-space-based solution scheme for the size-modified Poisson–Boltzmann equation in full-potential DFT *J. Chem. Theory Comput.* **12** 4052–66
[131] Nattino F, Truscott M, Marzari N and Andreussi O 2019 Continuum models of the electrochemical diffuse layer in electronic-structure calculations *J. Chem. Phys.* **150** 41722
[132] Melander M M, Kuisma M J, Christensen T E K and Honkala K 2019 Grand-canonical approach to density functional theory of electrocatalytic systems: thermodynamics of solid-liquid interfaces at constant ion and electrode potentials *J. Chem. Phys.* **150** 041706
[133] Stein C J, Herbert J M and Head-Gordon M 2019 The Poisson–Boltzmann model for implicit solvation of electrolyte solutions: quantum chemical implementation and assessment via Sechenov coefficients *J. Chem. Phys.* **151** 224111
[134] Womack J C, Anton L, Dziedzic J, Hasnip P J, Probert M I J and Skylaris C K 2018 DL-MG: a parallel multigrid Poisson and Poisson–Boltzmann solver for electronic structure calculations in vacuum and solution *J. Chem. Theory Comput.* **14** 1412–32
[135] Dziedzic J, Bhandari A, Anton L, Peng C, Womack J C, Famili M, Kramer D and Skylaris C-K 2020 A practical approach to large scale electronic structure calculations in electrolyte solutions via continuum-embedded linear-scaling DFT *J. Phys. Chem.* C **124** 7860–72
[136] Andreussi O, Dabo I and Marzari N 2012 Revised self-consistent continuum solvation in electronic-structure calculations *J. Chem. Phys.* **136** 064102
[137] Fisicaro G, Genovese L, Andreussi O, Mandal S, Nair N N, Marzari N and Goedecker S 2017 Soft-sphere continuum solvation in electronic-structure calculations *J. Chem. Theory Comput.* **13** 3829–45
[138] Sundararaman R, Letchworth-Weaver K and Schwarz K A 2018 Improving accuracy of electrochemical capacitance and solvation energetics in first-principles calculations *J. Chem. Phys.* **148** 144105
[139] Dziedzic J, Helal H H, Skylaris C K, Mostofi A A and Payne M C 2011 Minimal parameter implicit solvent model for *ab initio* electronic-structure calculations *Europhys. Lett.* **95** 043001
[140] Jones J E 1924 On the determination of molecular fields.—II. From the equation of state of a gas *Proc. R. Soc.* A **106** 463–77
[141] Gale J D 1996 Gulp fitting (available at: https://gulp.curtin.edu.au/local/docs/gulp/gulp_31_manual/gulpnode38.html)
[142] Gale J D 1996 Empirical potential derivation for ionic materials *Phil. Mag.* B **73** 3–19
[143] Stukowski A, Fransson E, Mock M and Erhart P 2017 Atomicrex—a general purpose tool for the construction of atomic interaction models *Modelling Simul. Mater. Sci. Eng.* **25** 055003
[144] Ostrouchov C 2018 dftfit (available at: https://chrisostrouchov.com/dftfit)
[145] Wen M, Li J, Brommer P, Elliott R S, Sethna J P and Tadmor E B 2017 A KIM-compliant *potfit* for fitting sloppy interatomic potentials: application to the EDIP model for silicon *Modelling Simul. Mater. Sci. Eng.* **25** 014001
[146] Wen M, Li J, Brommer P, Elliott R S, Sethna J P and Tadmor E B 2019 potfit (available at: www.potfit.net/wiki/doku.php)
[147] Lewis G V and Catlow C R A 1985 Potential models for ionic oxides *J. Phys. C: Solid State Phys.* **18** 1149–61
[148] Ledwaba R S, Sayle D C and Ngoepe P E 2020 Atomistic simulation and characterization of spinel $Li_{1+x}Mn_2O_4$ ($0 \leqslant x \leqslant 1$) nanoparticles *ACS Appl. Energy Mater.* **3** 1429–38
[149] Sayle T X T, Richard C, Catlow A, Regina Maphanga R, Ngoepe P E and Sayle D C 2005 Generating MnO_2 nanoparticles using simulated amorphization and recrystallization *J. Am. Chem. Soc.* **127** 12828–37
[150] Dawson J A and Tanaka I 2014 Oxygen vacancy formation and reduction properties of β-MnO_2 grain boundaries and the potential for high electrochemical performance *ACS Appl. Mater. Interfaces* **6** 17776–84
[151] Hart F X and Bates J B 1998 Lattice model calculation of the strain energy density and other properties of crystalline $LiCoO_2$ *J. Appl. Phys.* **83** 7560–6
[152] Fisher C A J, Saiful Islam M and Moriwake H 2010 Atomic level investigations of lithium ion battery cathode materials *J. Phys. Soc. Japan* **79** 59–64
[153] Ammundsen B, Burns G R, Saiful Islam M, Kanoh H and Rozière J 1999 Lattice dynamics and vibrational spectra of lithium manganese oxides: a computer simulation and spectroscopic study *J. Phys. Chem.* B **103** 5175–80
[154] Kerisit S, Chaka A M, Droubay T C and Ilton E S 2014 Shell model for atomistic simulation of lithium diffusion in mixed Mn/Ti oxides *J. Phys. Chem.* C **118** 24231–9
[155] He J, Zhang L and Liu L 2019 Thermal transport in monocrystalline and polycrystalline lithium cobalt oxide *Phys. Chem. Chem. Phys.* **21** 12192–200
[156] Lee S and Park S S 2012 Atomistic simulation study of mixed-metal oxide ($LiNi_{1/3}Co_{1/3}Mn_{1/3}O_2$) cathode material for lithium ion battery *J. Phys. Chem.* C **116** 6484–9
[157] Lindan P J D and Gillan M J 1993 Shell-model molecular dynamics simulation of superionic conduction in CaF2 *J. Phys.: Condens. Matter.* **5** 1019–30
[158] Mitchell P J and Fincham D 1993 Shell model simulations by adiabatic dynamics *J. Phys.: Condens. Matter.* **5** 1031–8
[159] Wang B and Cormack A N 2014 Molecular dynamics simulations of Mg-doped beta$''$-alumina with potential models fitted for accurate structural response to thermal vibrations *Solid State Ion.* **263** 9–14
[160] Escribano B, Lozano A, Radivojević T, Fernández-Pendás M, Carrasco J and Akhmatskaya E 2017 Enhancing sampling in atomistic simulations of solid-state materials for batteries: a focus on olivine $NaFePO_4$ *Theor. Chem. Acc.* **136** 43
[161] Lee S and Park S S 2013 Lithium transition metal fluorophosphates (Li_2CoPO_4F and Li_2NiPO_4F) as cathode materials for lithium ion battery from atomistic simulation *J. Solid State Chem.* **204** 329–34

[162] Dai J, Chen Q, Glossmann T and Lai W 2019 Comparison of interatomic potential models on the molecular dynamics simulation of fast-ion conductors: a case study of a Li garnet oxide $Li_7La_3Zr_2O_{12}$ *Comput. Mater. Sci.* **162** 333–9
[163] Pedone A, Malavasi G, Cristina Menziani M, Cormack A N and Segre U 2006 A new self-consistent empirical interatomic potential model for oxides, silicates and silica-based glasses *J. Phys. Chem.* B **110** 11780–95
[164] Morgan L M, Morgan B, Clarke M and O'Rourke C 2021 *PopOff: POtential Parameter Optimisation for Force-Fields* (available at: https://doi.org/10.5281/zenodo.4773795)
[165] Fisher C A J, Hart Prieto V M and Saiful Islam M 2008 Lithium battery materials $LiMPO_4$ (M = Mn, Fe, Co and Ni): insights into defect association, transport mechanisms and doping behavior *Chem. Mater.* **20** 5907–15
[166] Urban A, Seo D-H and Ceder G 2016 Computational understanding of Li-ion batteries *npj Comput. Mater.* **2** 16002
[167] Ceder G and Van der Ven A 1999 Phase diagrams of lithium transition metal oxides: investigations from first principles *Electrochim. Acta* **45** 131–50
[168] Van Der Ven A, Marianetti C, Morgan D and Ceder G 2000 Phase transformations and volume changes in spinel $Li_xMn_2O_4$ *Solid State Ion.* **135** 21–32
[169] Reynier Y, Graetz J, Swan-Wood T, Rez P, Yazami R and Fultz B 2004 Entropy of Li intercalation in Li_xCoO_2 *Phys. Rev.* B **70** 174304
[170] Yazami R and Reynier Y 2006 Thermodynamics and crystal structure anomalies in lithium-intercalated graphite *J. Power Sources* **153** 312–8
[171] Atkins P W and De Paula J 2014 *Atkins' Physical Chemistry* 9th edn (Oxford: Oxford University Press)
[172] Heitjans P and Kärger J 2006 *Diffusion in Condensed Matter: Methods, Materials, Models* (Berlin: Springer Science & Business Media)
[173] Heumann T 2013 *Diffusion in Metallen: Grundlagen, Theorie, Vorgänge in Reinmetallen und Legierungen* vol 10 (Berlin: Springer)
[174] Crank J 1979 *The Mathematics of Diffusion* (Oxford: Oxford University Press)
[175] Einstein A 1905 The presumed movement of suspended particles in static fluids *Ann. Phys., Lpz.* **17** 549–60
[176] Von Smoluchowski M 1906 Zur kinetischen theorie der brownschen molekularbewegung und der suspensionen *Ann. Phys., Lpz.* **326** 756–80
[177] Ladd A J C, Moran B and Hoover W G 1986 Lattice thermal conductivity: a comparison of molecular dynamics and anharmonic lattice dynamics *Phys. Rev.* B **34** 5058
[178] Turney J E, Landry E S, McGaughey A J H and Amon C H 2009 Predicting phonon properties and thermal conductivity from anharmonic lattice dynamics calculations and molecular dynamics simulations *Phys. Rev.* B **79** 064301
[179] Seko A, Togo A, Hayashi H, Tsuda K, Chaput L and Tanaka I 2015 Prediction of low-thermal-conductivity compounds with first-principles anharmonic lattice-dynamics calculations and Bayesian optimization *Phys. Rev. Lett.* **115** 205901
[180] Togo A, Chaput L and Tanaka I 2015 Distributions of phonon lifetimes in Brillouin zones *Phys. Rev.* B **91** 094306
[181] Yang H, Yang J-yue, Savory C N, Skelton J M, Morgan B J, Scanlon D O and Walsh A 2019 Highly anisotropic thermal transport in $LiCoO_2$ *J. Phys. Chem. Lett.* **10** 5552–6
[182] Yang H, Savory C N, Morgan B J, Scanlon D O, Skelton J M and Walsh A 2020 Chemical trends in the lattice thermal conductivity of Li(Ni, Mn, Co)O_2 (NMC) battery cathodes *Chem. Mater.* **32** 7542–50
[183] Tadano T, Gohda Y and Tsuneyuki S 2014 Anharmonic force constants extracted from first-principles molecular dynamics: applications to heat transfer simulations *J. Phys.: Condens. Matter.* **26** 225402
[184] Li W, Carrete J, Katcho N A and Mingo N 2014 ShengBTE: a solver of the Boltzmann transport equation for phonons *Comput. Phys. Commun.* **185** 1747–58
[185] Vetter J *et al* 2005 Ageing mechanisms in lithium-ion batteries *J. Power Sources* **147** 269–81
[186] Agubra V and Fergus J 2013 Lithium ion battery anode aging mechanisms *Materials* **6** 1310–25
[187] Yang X-G, Leng Y, Zhang G, Ge S and Wang C-Y 2017 Modeling of lithium plating induced aging of lithium-ion batteries: transition from linear to nonlinear aging *J. Power Sources* **360** 28–40
[188] Guerard D and Herold A 1975 Intercalation of lithium into graphite and other carbons *Carbon* **13** 337–45
[189] Woo K C, Kamitakahara W A, DiVincenzo D P, Robinson D S, Mertwoy H, Milliken J W and Fischer J E 1983 Effect of in-plane density on the structural and elastic properties of graphite intercalation compounds *Phys. Rev. Lett.* **50** 182–5
[190] Basu S, Zeller C, Flanders P J, Fuerst C D, Johnson W D and Fischer J E 1979 Synthesis and properties of lithium-graphite intercalation compounds *Mater. Sci. Eng.* **38** 275–83
[191] Besenhard J O 1976 The electrochemical preparation and properties of ionic alkali metal-and NR4-graphite intercalation compounds in organic electrolytes *Carbon* **14** 111–5
[192] Yazami R and Touzain P 1983 A reversible graphite-lithium negative electrode for electrochemical generators *J. Power Sources* **9** 365–71
[193] Fong R, von Sacken U and Dahn J R 1990 Studies of lithium intercalation into carbons using nonaqueous electrochemical cells *J. Electrochem. Soc.* **137** 2009–13
[194] Tarascon J M and Guyomard D 1993 The $Li_{1+x}Mn_2O_4$/C rocking-chair system: a review *Electrochim. Acta* **38** 1221–31
[195] Dahn J R 1991 Phase diagram of Li_xC_6 *Phys. Rev.* B **44** 9170–7
[196] Hazrati E, de Wijs G A and Brocks G 2014 Li intercalation in graphite: a van der Waals density-functional study *Phys. Rev.* B **90** 155448
[197] Konar S, Häusserman U and Svensson G 2015 Intercalation compounds from LiH and graphite: relative stability of metastable stages and thermodynamic stability of dilute stage I_d *Chem. Mater.* **27** 2566–75
[198] Shi H, Barker J, Saídi M Y and Koksbang R 1996 Structure and lithium intercalation properties of synthetic and natural graphite *J. Electrochem. Soc.* **143** 3466–72
[199] Sethuraman V A, Hardwick L J, Srinivasan V and Kostecki R 2010 Surface structural disordering in graphite upon lithium intercalation/deintercalation *J. Power Sources* **195** 3655–60
[200] Ohzuku T 1993 Formation of lithium-graphite intercalation compounds in nonaqueous electrolytes and their application as a negative electrode for a lithium ion (shuttlecock) cell *J. Electrochem. Soc.* **140** 2490
[201] He H, Huang C, Luo C-W, Liu J-J and Chao Z-S 2013 Dynamic study of Li intercalation into graphite by *in situ* high energy synchrotron XRD *Electrochim. Acta* **92** 148–52
[202] Trucano P and Chen R 1975 Structure of graphite by neutron diffraction *Nature* **258** 136–7
[203] Okamoto H 1989 The C–Li (carbon-lithium) system *Bull. Alloy Phase Diagr.* **10** 69–72
[204] Billaud D, Henry F X, Lelaurain M and Willmann P 1996 Revisited structures of dense and dilute stage II lithium-graphite intercalation compounds *J. Phys. Chem. Solids* **57** 775–81

[205] Billaud D and Henry F X 2002 Structural studies of the stage III lithium-graphite intercalation compound *Solid State Commun.* **124** 299–304
[206] Didier C, Pang W K, Guo Z, Schmid S and Peterson V K 2020 Phase evolution and intermittent disorder in electrochemically lithiated graphite determined using in operando neutron diffraction *Chem. Mater.* **32** 2518–31
[207] Zheng T, Reimers J N and Dahn J R 1995 Effect of turbostratic disorder in graphitic carbon hosts on the intercalation of lithium *Phys. Rev.* B **51** 734–41
[208] Senyshyn A, Dolotko O, Muhlbauer M J, Nikolowski K, Fuess H and Ehrenberg H 2013 Lithium intercalation into graphitic carbons revisited: experimental evidence for twisted bilayer behavior *J. Electrochem. Soc.* **160** A3198–205
[209] Taminato S *et al* 2016 Real-time observations of lithium battery reactions—operando neutron diffraction analysis during practical operation *Sci. Rep.* **6** 28843
[210] Thinius S, Islam M M, Heitjans P and Bredow T 2014 Theoretical study of Li migration in lithium–graphite intercalation compounds with dispersion-corrected DFT methods *J. Phys. Chem.* C **118** 2273–80
[211] Garcia J C, Bloom I, Johnson C, Dees D and Iddir H 2020 Graphite lithiation under fast charging conditions: atomistic modeling insights *J. Phys. Chem.* C **124** 8162–9
[212] Olsson E, Cottom J, Au H, Guo Z, Jensen A C S, Alptekin H, Drew A J, Titirici M-M and Cai Q 2020 Elucidating the effect of planar graphitic layers and cylindrical pores on the storage and diffusion of Li, Na and K in carbon materials *Adv. Funct. Mater.* **30** 1908209
[213] Lenchuk O, Adelhelm P and Mollenhauer D 2019 Comparative study of density functionals for the description of lithium-graphite intercalation compounds *J. Comput. Chem.* **40** 2400–12
[214] Ji X, Wang Y and Zhang J 2018 Understanding the anisotropic strain effects on lithium diffusion in graphite anodes: a first-principles study *Physica* B **539** 66–71
[215] Wang Z, Ratvik A P, Grande T and Selbach S M 2015 Diffusion of alkali metals in the first stage graphite intercalation compounds by vdW-DFT calculations *RSC Adv.* **5** 15985–92
[216] Persson K, Sethuraman V A, Hardwick L J, Hinuma Y, Meng Y S, Van Der Ven A, Srinivasan V, Kostecki R and Ceder G 2010 Lithium diffusion in graphitic carbon *J. Phys. Chem. Lett.* **1** 1176–80
[217] Otero M, Sigal A, Perassi E M, Barraco D and Leiva E P M 2017 Statistical mechanical modeling of the transition stage II → stage I of Li-ion storage in graphite. *A priori* vs induced heterogeneity *Electrochim. Acta* **245** 569–74
[218] Gavilán-Arriazu E M, Pinto O A, López de Mishima B A, Leiva E P M and Oviedo O A 2018 Grand canonical Monte Carlo study of Li intercalation into graphite *J. Electrochem. Soc.* **165** A2019–25
[219] Gavilán Arriazu E M, López de Mishima B A, Oviedo O A, Leiva E P M and Pinto O A 2017 Criticality of the phase transition on stage two in a lattice-gas model of a graphite anode in a lithium-ion battery *Phys. Chem. Chem. Phys.* **19** 23138–45
[220] Gavilán-Arriazu E M, Pinto O A, López de Mishima B A, Barraco D E, Oviedo O A and Leiva E P M 2018 The kinetic origin of the Daumas-Hérold model for the Li-ion/graphite intercalation system *Electrochem. Commun.* **93** 133–7
[221] Plett G L 2004 Extended Kalman filtering for battery management systems of LiPB-based HEV battery packs: part 2. Modeling and identification *J. Power Sources* **134** 262–76
[222] Sole C, Drewett N E and Hardwick L J 2014 *In situ* Raman study of lithium-ion intercalation into microcrystalline graphite *Faraday Discuss.* **172** 223–37
[223] Allart D, Montaru M and Gualous H 2018 Model of lithium intercalation into graphite by potentiometric analysis with equilibrium and entropy change curves of graphite electrode *J. Electrochem. Soc.* **165** A380–7
[224] Markevich E, Levi M D and Aurbach D 2005 New insight into studies of the cycling performance of li-graphite electrodes *J. Electrochem. Soc.* **152** A778
[225] Reynier Y, Yazami R and Fultz B 2003 The entropy and enthalpy of lithium intercalation into graphite *J. Power Sources* **119–21** 850–5
[226] Liu H, Strobridge F C, Borkiewicz O J, Wiaderek K M, Chapman K W, Chupas P J and Grey C P 2014 Capturing metastable structures during high-rate cycling of $LiFePO_4$ nanoparticle electrodes *Science* **344** 1252817-1–7
[227] Orikasa Y *et al* 2013 Direct observation of a metastable crystal phase of Li_xFePO_4 under electrochemical phase transition *J. Am. Chem. Soc.* **135** 5497–500
[228] Gallagher K G, Dees D W, Jansen A N, Abraham D P and Kang S-H 2012 A volume averaged approach to the numerical modeling of phase-transition intercalation electrodes presented for Li_xC_6 *J. Electrochem. Soc.* **159** A2029–37
[229] Grimsmann F, Gerbert T, Brauchle F, Gruhle A, Parisi J and Knipper M 2018 Hysteresis and current dependence of the graphite anode color in a lithium-ion cell and analysis of lithium plating at the cell edge *J. Energy Storage* **15** 17–22
[230] Osswald P J, del Rosario M, Garche J, Jossen A and Hoster H E 2015 Fast and accurate measurement of entropy profiles of commercial lithium-ion cells *Electrochim. Acta* **177** 270–6
[231] Van der Ven A, Thomas J C, Puchala B and Natarajan A R 2018 First-principles statistical mechanics of multicomponent crystals *Annu. Rev. Mater. Res.* **48** 27–55
[232] Lorie Lopez J L, Grandinetti P J and Co A C 2018 Enhancing the real-time detection of phase changes in lithium–graphite intercalated compounds through derivative operando (dOp) NMR cyclic voltammetry *J. Mater. Chem.* A **6** 231–43
[233] Franco A A, Rucci A, Brandell D, Frayret C, Gaberscek M, Jankowski P and Johansson P 2019 Boosting rechargeable batteries R&D by multiscale modeling: myth or reality? *Chem. Rev.* **119** 4569–627
[234] Imai Y and Watanabe A 2007 Energetic evaluation of possible stacking structures of Li-intercalation in graphite using a first-principle pseudopotential calculation *J. Alloys Compd.* **439** 258–67
[235] Toyoura K, Koyama Y, Kuwabara A and Tanaka I 2010 Effects of off-stoichiometry of LiC_6 on the lithium diffusion mechanism and diffusivity by first principles calculations *J. Phys. Chem.* C **114** 2375–9
[236] Yao F, Gunes F, Ta H Q, Lee S Mi, Chae S J, Sheem K Y, Cojocaru C S, Xie S S and Lee Y H 2012 Diffusion mechanism of lithium ion through basal plane of layered graphene *J. Am. Chem. Soc.* **134** 8646–54
[237] NuLi Y, Yang J and Jiang Z 2006 Intercalation of lithium ions into bulk and powder highly oriented pyrolytic graphite *J. Phys. Chem. Solids* **67** 882–6
[238] Liu T *et al* 2019 *In situ* quantification of interphasial chemistry in Li-ion battery *Nat. Nanotechnol.* **14** 50–56
[239] Zhang Z, Smith K, Jervis R, Shearing P R, Miller T S and Brett D J L 2020 Operando electrochemical atomic force microscopy of solid–electrolyte interphase formation on graphite anodes: the evolution of SEI morphology and mechanical properties *ACS Appl. Mater. Interfaces* **12** 35132–41
[240] Thinius S, Islam M M and Bredow T 2016 Reconstruction of low-index graphite surfaces *Surf. Sci.* **649** 60–65

[241] Larciprete R, Lacovig P, Gardonio S, Baraldi A and Lizzit S 2012 Atomic oxygen on graphite: chemical characterization and thermal reduction *J. Phys. Chem.* C **116** 9900–8
[242] Bernardo P, Le Meins J-M, Vidal L, Dentzer J, Gadiou R, Märkle W, Novák P, Spahr M E and Vix-Guterl C 2015 Influence of graphite edge crystallographic orientation on the first lithium intercalation in Li-ion battery *Carbon* **91** 458–67
[243] Toyoura K, Koyama Y, Kuwabara A, Oba F and Tanaka I 2008 First-principles approach to chemical diffusion of lithium atoms in a graphite intercalation compound *Phys. Rev.* B **78** 214303
[244] Takami N, Satoh A, Hara M and Ohsaki T 1995 Structural and kinetic characterization of lithium intercalation into carbon anodes for secondary lithium batteries *J. Electrochem. Soc.* **142** 371
[245] Yang H, Bang H J and Prakash J 2004 Evaluation of electrochemical interface area and lithium diffusion coefficient for a composite graphite anode *J. Electrochem. Soc.* **151** A1247
[246] Yu P, Popov B N, Ritter J A and White R E 1999 Determination of the lithium ion diffusion coefficient in graphite *J. Electrochem. Soc.* **146** 8
[247] Uthaisar C and Barone V 2010 Edge effects on the characteristics of Li diffusion in graphene *Nano Lett.* **10** 2838–42
[248] Leggesse E G, Chen C-L and Jiang J-C 2016 Lithium diffusion in graphene and graphite: effect of edge morphology *Carbon* **103** 209–16
[249] Chan T-L and Chelikowsky J R 2010 Controlling diffusion of lithium in silicon nanostructures *Nano Lett.* **10** 821–5
[250] Fujita M, Wakabayashi K, Nakada K and Kusakabe K 1996 Peculiar localized state at zigzag graphite edge *J. Phys. Soc. Japan* **65** 1920–3
[251] Lee H, Son Y-W, Park N, Han S and Yu J 2005 Magnetic ordering at the edges of graphitic fragments: magnetic tail interactions between the edge-localized states *Phys. Rev.* B **72** 174431
[252] Velický M, Toth P S, Woods C R, Novoselov K S and Dryfe R A W 2019 Electrochemistry of the basal plane versus edge plane of graphite revisited *J. Phys. Chem.* C **123** 11677–85
[253] Gerischer H 1985 An interpretation of the double layer capacity of graphite electrodes in relation to the density of states at the Fermi level *J. Phys. Chem.* **89** 4249–51
[254] Weydanz W J, Way B M, Van Buuren T and Dahn J R 1994 Behavior of nitrogen-substituted carbon (N_zC_{1-z}) in Li/Li $(N_zC{+}1-z)_6$ cells *J. Electrochem. Soc.* **141** 900
[255] Way B M and Dahn J R 1994 The effect of boron substitution in carbon on the intercalation of lithium in $Li_x(B_zC_{1-z})_6$ *J. Electrochem. Soc.* **141** 907
[256] Endo M, Hayashi T, Hong S-H, Enoki T and Dresselhaus M S 2001 Scanning tunneling microscope study of boron-doped highly oriented pyrolytic graphite *J. Appl. Phys.* **90** 5670–4
[257] Ishii T, Kaburagi Y, Yoshida A, Hishiyama Y, Oka H, Setoyama N, Ozaki J I and Kyotani T 2017 Analyses of trace amounts of edge sites in natural graphite, synthetic graphite and high-temperature treated coke for the understanding of their carbon molecular structures *Carbon* **125** 146–55
[258] Peng C, Bhandari A, Dziedzic J, Owen J R, Skylaris C-K and Kramer D 2021 Mechanism of Li nucleation at graphite anodes and mitigation strategies *J. Mater. Chem.* A **9** 16798–804
[259] Gao T *et al* 2021 Interplay of lithium intercalation and plating on a single graphite particle *Joule* **5** 393–414
[260] Bhandari A, Peng C, Dziedzic J, Anton L, Owen J R, Kramer D and Skylaris C K 2021 Electrochemistry from first-principles in the grand canonical ensemble *J. Chem. Phys.* **155** 024114
[261] Winter M 2009 The solid electrolyte interphase–the most important and the least understood solid electrolyte in rechargeable Li batteries *Z. Phys. Chem.* **223** 1395–406
[262] Verma P, Maire P and Novák P 2010 A review of the features and analyses of the solid electrolyte interphase in Li-ion batteries *Electrochim. Acta* **55** 6332–41
[263] Haruyama J, Ikeshoji T and Otani M 2018 Analysis of lithium insertion/desorption reaction at interfaces between graphite electrodes and electrolyte solution using density functional + implicit solvation theory *J. Phys. Chem.* C **122** 9804–10
[264] Yamada Y, Iriyama Y, Abe T and Ogumi Z 2009 Kinetics of lithium ion transfer at the interface between graphite and liquid electrolytes: effects of solvent and surface film *Langmuir* **25** 12766–70
[265] Shi S, Lu P, Liu Z, Qi Y, Hector L G, Li H and Harris S J 2012 Direct calculation of Li-ion transport in the solid electrolyte interphase *J. Am. Chem. Soc.* **134** 15476–87
[266] Larcher D, Beattie S, Morcrette M, Edstroem K, Jumas J-C and Tarascon J-M 2007 Recent findings and prospects in the field of pure metals as negative electrodes for Li-ion batteries *J. Mater. Chem.* **17** 3759–72
[267] Feng K, Li M, Liu W, Kashkooli A G, Xiao X, Cai M and Chen Z 2018 Silicon-based anodes for lithium-ion batteries: from fundamentals to practical applications *Small* **14** 1702737
[268] Nitta N and Yushin G 2014 High-capacity anode materials for lithium-ion batteries: choice of elements and structures for active particles *Part. Part. Syst. Charact.* **31** 317–36
[269] Wagner N P, Tron A, Tolchard J R, Noia G and Bellmann M P 2019 Silicon anodes for lithium-ion batteries produced from recovered kerf powders *J. Power Sources* **414** 486–94
[270] Okamoto H 1990 The Li–Si (lithium-silicon) system *Bull. Alloy Phase Diagr.* **11** 306–12
[271] Gruber T, Thomas D, Röder C, Mertens F and Kortus J 2013 Raman spectroscopic studies of Li_xSi_y compounds *J. Raman Spectrosc.* **44** 934–8
[272] Jiang Y, Offer G, Jiang J, Marinescu M and Wang H 2020 Voltage hysteresis model for silicon electrodes for lithium ion batteries, including multi-step phase transformations, crystallization and amorphization *J. Electrochem. Soc.* **167** 130533
[273] Kuhn A, Sreeraj P, Pöttgen R, Wiemhöfer H-D, Wilkening M and Heitjans P 2011 Li ion diffusion in the anode material $Li_{12}Si_7$: ultrafast quasi-1D diffusion and two distinct fast 3D jump processes separately revealed by ^{7}Li NMR relaxometry *J. Am. Chem. Soc.* **133** 11018–21
[274] Wang D, Gao M, Pan H, Wang J and Liu Y 2014 High performance amorphous-Si@SiOx/C composite anode materials for Li-ion batteries derived from ball-milling and *in situ* carbonization *J. Power Sources* **256** 190–9
[275] Kirklin S, Meredig B and Wolverton C 2013 High-throughput computational screening of new Li-ion battery anode materials *Adv. Energy Mater.* **3** 252–62
[276] Fang C, Wang X and Meng Y S 2019 Key issues hindering a practical lithium-metal anode *Trends Chem.* **1** 152–8
[277] Li S, Jiang M, Xie Y, Xu H, Jia J and Li J 2018 Developing high-performance lithium metal anode in liquid electrolytes: challenges and progress *Adv. Mater.* **30** 1706375
[278] Radin M D, Alvarado J, Shirley Meng Y and Van der Ven A 2017 Role of crystal symmetry in the reversibility of stacking–sequence changes in layered intercalation electrodes *Nano Lett.* **17** 7789–95

[279] Vinckevičiūtė J, Radin M D and Van der Ven A 2016 Stacking-sequence changes and Na ordering in layered intercalation materials *Chem. Mater.* **28** 8640–50
[280] Schmickler W and Santos E 2010 *Interfacial Electrochemistry* 2nd edn (Berlin: Springer)
[281] Bard A J and Faulkner L R 2010 *Electrochemical Methods: Fundamentals and Applications* 2nd edn (New York: Wiley)
[282] Kralisch D, Stark A, Körsten S, Kreisel Gunter and Ondruschka B 2005 Energetic, environmental and economic balances: spice up your ionic liquid research efficiency *Green Chem.* **7** 301–9
[283] Smiglak M *et al* 2006 Combustible ionic liquids by design: is laboratory safety another ionic liquid myth? *Chem. Commun.* 24 2554–6
[284] Ding F *et al* 2013 Effects of carbonate solvents and lithium salts on morphology and coulombic efficiency of lithium electrode *J. Electrochem. Soc.* **160** A1894
[285] Janek J and Zeier W G 2016 A solid future for battery development *Nat. Energy* **1** 16141
[286] Kazemiabnavi S, Zhang Z, Thornton K and Banerjee S 2016 Electrochemical stability window of imidazolium-based ionic liquids as electrolytes for lithium batteries *J. Phys. Chem.* B **120** 5691–702
[287] Park M, Zhang X, Chung M, Less G B and Sastry A M 2010 A review of conduction phenomena in Li-ion batteries *J. Power Sources* **195** 7904–29
[288] Kamaya N *et al* 2011 A lithium superionic conductor *Nat. Mater.* **10** 682–6
[289] Swift M W, Swift J W and Qi Y 2021 Modeling the electrical double layer at solid-state electrochemical interfaces *Nat. Comput. Sci.* **1** 212–20
[290] Xu K and von Cresce A 2011 Interfacing electrolytes with electrodes in Li ion batteries *J. Mater. Chem.* **21** 9849
[291] Yu C, Ganapathy S, van Eck E R H, Wang H, Basak S, Li Z and Wagemaker M 2017 Accessing the bottleneck in all-solid state batteries, lithium-ion transport over the solid-electrolyte-electrode interface *Nat. Commun.* **8** 1086
[292] Xu K 2004 Nonaqueous liquid electrolytes for lithium-based rechargeable batteries *Chem. Rev.* **104** 4303–418
[293] Xu K 2014 Electrolytes and interphases in Li-ion batteries and beyond *Chem. Rev.* **114** 11503–618
[294] Maier J 1995 Ionic conduction in space charge regions *Prog. Sol. Stat. Chem.* **23** 171–263
[295] Mebane D S 2015 A variational approach to surface cation segregation in mixed conducting perovskites *Comput. Mater. Sci.* **103** 231–6
[296] Mebane D S and De Souza R A 2015 A generalised space-charge theory for extended defects in oxygen-ion conducting electrolytes: from dilute to concentrated solid solutions *Energy Environ. Sci.* **8** 2935–40
[297] Tong X, Mebane D S and De Souza R A 2020 Analyzing the grain-boundary resistance of oxide-ion conducting electrolytes: Poisson–Cahn vs Poisson–Boltzmann theories *J. Am. Ceram. Soc.* **103** 5–22
[298] Lund J, Vikrant K S N, Bishop C M, Rheinheimer W and García R E 2021 Thermodynamically consistent variational principles for charged interfaces *Acta Mater.* **205** 116525
[299] Bazant M Z, Storey B D and Kornyshev A A 2011 Double layer in ionic liquids: overscreening versus crowding *Phys. Rev. Lett.* **106** 046102
[300] Perkin S 2012 Ionic liquids in confined geometries *Phys. Chem. Chem. Phys.* **14** 5052–62
[301] Groves T S, Perez-Martinez C S, Lhermerout R and Perkin S 2021 Surface forces and structure in a water-in-salt electrolyte *J. Phys. Chem. Lett.* **12** 1702–7
[302] Bowers J, Vergara-Gutierrez M C and Webster J R P 2004 Surface ordering of amphiphilic ionic liquids *Langmuir* **20** 309–12
[303] Sloutskin E, Ocko B M, Tamam L, Kuzmenko I, Gog T and Deutsch M 2005 Surface layering in ionic liquids: an x-ray reflectivity study *J. Am. Chem. Soc.* **127** 7796–804
[304] Dean J M, Coles S W, Saunders W R, McCluskey A R, Wolf M J, Walker A B and Morgan B J 2021 Overscreening and underscreening in solid-electrolyte grain boundary space-charge layers *Phys. Rev. Lett.* **127** 135502
[305] Valøen L O and Reimers J N 2005 Transport properties of $LiPF_6$-based Li-ion battery electrolytes *J. Electrochem. Soc.* **152** A882
[306] Yamada Y, Yaegashi M, Abe T and Yamada A 2013 A superconcentrated ether electrolyte for fast-charging Li-ion batteries *Chem. Commun.* **49** 11194
[307] MacFarlane D R *et al* 2014 Energy applications of ionic liquids *Energy Environ. Sci.* **7** 232–50
[308] Suo L *et al* 2016 Advanced high-voltage aqueous lithium-ion battery enabled by "water-in-bisalt" electrolyte *Angew. Chem., Int. Ed. Engl.* **128** 7252–7
[309] Qian J, Henderson W A, Xu W, Bhattacharya P, Engelhard M, Borodin O and Zhang J-G 2015 High rate and stable cycling of lithium metal anode *Nat. Commun.* **6** 1–9
[310] Kim H *et al* 2015 *In situ* formation of protective coatings on sulfur cathodes in lithium batteries with LiFSI-based organic electrolytes *Adv. Energy Mater.* **5** 1401792
[311] Zhou X, Zhou J and Yin Y 2009 Atomistic modeling in study of polymer electrolyte fuel cells–a review *Modeling and Diagnostics of Polymer Electrolyte Fuel Cells* (Berlin: Springer) pp 307–80
[312] Enderby J E and Neilson G W 1981 The structure of electrolyte solutions *Rep. Prog. Phys.* **44** 593
[313] Fujie T, Takenaka N, Suzuki Y and Nagaoka M 2018 Red moon methodology compatible with quantum mechanics/molecular mechanics framework: application to solid electrolyte interphase film formation in lithium-ion battery system *J. Chem. Phys.* **149** 044113
[314] Koch V R, Dominey L A, Nanjundiah C and Ondrechen M J 1996 The intrinsic anodic stability of several anions comprising solvent-free ionic liquids *J. Electrochem. Soc.* **143** 798–803
[315] Ong S P, Andreussi O, Wu Y, Marzari N and Ceder G 2011 Electrochemical windows of room-temperature ionic liquids from molecular dynamics and density functional theory calculations *Chem. Mater.* **23** 2979–86
[316] Vuilleumier R and Sprik M 2001 Electronic properties of hard and soft ions in solution: aqueous Na^+ and Ag^+ compared *J. Chem. Phys.* **115** 3454–68
[317] Blumberger J, Tavernelli I, Klein M L and Sprik M 2006 Diabatic free energy curves and coordination fluctuations for the aqueous Ag^+/Ag^{2+} redox couple: a biased born-oppenheimer molecular dynamics investigation *J. Chem. Phys.* **124** 064507
[318] Blumberger J, Bernasconi L, Tavernelli I, Vuilleumier R and Sprik M 2004 Electronic structure and solvation of copper and silver ions: a theoretical picture of a model aqueous redox reaction *J. Am. Chem. Soc.* **126** 3928–38
[319] VandeVondele J, Sulpizi M and Sprik M 2006 From solvent fluctuations to quantitative redox properties of quinones in methanol and acetonitrile *Angew. Chem., Int. Ed. Engl.* **118** 1970–2
[320] Lynden-Bell R M 2007 Can Marcus theory be applied to redox processes in ionic liquids? A comparative simulation study of dimethylimidazolium liquids and acetonitrile *J. Phys. Chem.* B **111** 10800–6

[321] Ganesh P, Jiang D-E and Kent P R C 2011 Accurate static and dynamic properties of liquid electrolytes for Li-ion batteries from *ab initio* molecular dynamics *J. Phys. Chem.* B **115** 3085–90
[322] Kameda Y, Umebayashi Y, Takeuchi M, Wahab M A, Fukuda S, Ishiguro S I, Sasaki M, Amo Y and Usuki T 2007 Solvation structure of Li^+ in concentrated $LiPF_6$-propylene carbonate solutions *J. Phys. Chem.* B **111** 6104–9
[323] Soetens J-C, Millot C and Maigret B 1998 Molecular dynamics simulation of $Li^+BF_4^-$ in ethylene carbonate, propylene carbonate and dimethyl carbonate solvents *J. Phys. Chem.* A **102** 1055–61
[324] Lespes N and Filhol J-S 2015 Using implicit solvent in *ab initio* electrochemical modeling: investigating Li^+/Li electrochemistry at a Li/solvent interface *J. Chem. Theory Comput.* **11** 3375–82
[325] Morgan B J and Watson G W 2011 Role of lithium ordering in the Li_xTiO_2 anatase → titanate phase transition *J. Phys. Chem. Lett.* **2** 1657–61
[326] Zhao X-G, Dalpian G M, Wang Z and Zunger A 2020 Polymorphous nature of cubic halide perovskites *Phys. Rev.* B **101** 155137
[327] Yeh I-C and Hummer G 2004 System-size dependence of diffusion coefficients and viscosities from molecular dynamics simulations with periodic boundary conditions *J. Phys. Chem.* B **108** 15873–9
[328] Botan A, Marry V and Rotenberg B 2015 Diffusion in bulk liquids: finite-size effects in anisotropic systems *Mol. Phys.* **113** 2674–9
[329] Horbach J, Kob W, Binder K and Angell C A 1996 Finite size effects in simulations of glass dynamics *Phys. Rev.* E **54** R5897–900
[330] Coles S W, Park C, Nikam R, Kanduč M, Dzubiella J and Rotenberg B 2020 Correlation length in concentrated electrolytes: insights from all-atom molecular dynamics simulations *J. Phys. Chem.* B **124** 1778–86
[331] Frenkel D and Smit B 2002 *Understanding Molecular Simulation* (New York: Academic)
[332] Lindahl A and van der Spoel H 2021 *GROMACS 2021 Manual* (https://doi.org/10.5281/zenodo.4457591)
[333] Canongia Lopes J N and Pádua A A H 2012 CL&P: a generic and systematic force field for ionic liquids modeling *Theor. Chem. Acc.* **131** 1129
[334] Jorgensen W L, Maxwell D S and Tirado-Rives J 1996 Development and testing of the OPLS all-atom force field on conformational energetics and properties of organic liquids *J. Am. Chem. Soc.* **118** 11225–36
[335] Hess B, Bekker H, Berendsen H J C and Fraaije J G E M 1997 LINCS: a linear constraint solver for molecular simulations *J. Comput. Chem.* **18** 1463–72
[336] Ryckaert J-P, Ciccotti G and Berendsen H J C 1977 Numerical integration of the cartesian equations of motion of a system with constraints: molecular dynamics of n-alkanes *J. Comput. Phys.* **23** 327–41
[337] Andersen H C 1983 Rattle: a "velocity" version of the shake algorithm for molecular dynamics calculations *J. Comput. Phys.* **52** 24–34
[338] Ewald P P 1921 Die berechnung optischer und elektrostatischer gitterpotentiale *Ann. Phys., Lpz.* **369** 253–87
[339] Darden T, York D and Pedersen L 1993 Particle mesh Ewald: an $N \cdot \log(N)$ method for Ewald sums in large systems *J. Chem. Phys.* **98** 10089–92
[340] Deserno M and Holm C 1998 How to mesh up Ewald sums. II. An accurate error estimate for the particle–particle–particle-mesh algorithm *J. Chem. Phys.* **109** 7694–701
[341] Yeh I-C and Berkowitz M L 1999 Ewald summation for systems with slab geometry *J. Chem. Phys.* **111** 3155–62
[342] Canongia Lopes J N, Deschamps J and Pádua A A H 2004 Modeling ionic liquids using a systematic all-atom force field *J. Phys. Chem.* B **108** 2038–47
[343] Canongia Lopes J N and Pádua A A H 2004 Molecular force field for ionic liquids composed of triflate or bistriflylimide anions *J. Phys. Chem.* B **108** 16893–8
[344] Canongia Lopes J N and Pádua A A H 2006 Molecular force field for ionic liquids III: imidazolium, pyridinium and phosphonium cations; chloride, bromide and dicyanamide anions *J. Phys. Chem.* B **110** 19586–92
[345] Spackman M A 1996 Potential derived charges using a geodesic point selection scheme *J. Comput. Chem.* **17** 1–18
[346] Breneman C M and Wiberg K B 1990 Determining atom-centered monopoles from molecular electrostatic potentials. The need for high sampling density in formamide conformational analysis *J. Comput. Chem.* **11** 361–73
[347] Chandra Singh U and Kollman P A 1984 An approach to computing electrostatic charges for molecules *J. Comput. Chem.* **5** 129–45
[348] Schröder C 2012 Comparing reduced partial charge models with polarizable simulations of ionic liquids *Phys. Chem. Chem. Phys.* **14** 3089–102
[349] Schröder C, Lyons A and Rick S W 2020 Polarizable MD simulations of ionic liquids: how does additional charge transfer change the dynamics? *Phys. Chem. Chem. Phys.* **22** 467–77
[350] Shimizu K *et al* 2015 Structural and aggregate analyses of (Li salt + glyme) mixtures: the complex nature of solvate ionic liquids *Phys. Chem. Chem. Phys.* **17** 22321–35
[351] Sangster M J L and Dixon M 1976 Interionic potentials in alkali halides and their use in simulations of the molten salts *Adv. Phys.* **25** 247–342
[352] Madden P A and Wilson M 1996 "Covalent" effects in "ionic" systems *Chem. Soc. Rev.* **25** 339–50
[353] Borodin O 2009 Polarizable force field development and molecular dynamics simulations of ionic liquids *J. Phys. Chem.* B **113** 11463–78
[354] Borodin O and Smith G D 2006 LiTFSI structure and transport in ethylene carbonate from molecular dynamics simulations *J. Phys. Chem.* B **110** 4971–7
[355] Bedrov D, Piquemal J-P, Borodin O, MacKerell A D, Roux B and Schröder C 2019 Molecular dynamics simulations of ionic liquids and electrolytes using polarizable force fields *Chem. Rev.* **119** 7940–95
[356] Bedrov D, Borodin O, Li Z and Smith G D 2010 Influence of polarization on structural, thermodynamic and dynamic properties of ionic liquids obtained from molecular dynamics simulations *J. Phys. Chem.* B **114** 4984–97
[357] Marin-Laflèche A *et al* 2020 MetalWalls: a classical molecular dynamics software dedicated to the simulation of electrochemical systems *J. Open Source Softw.* **5** 2373
[358] Mamatkulov S, Fyta M and Netz R R 2013 Force fields for divalent cations based on single-ion and ion-pair properties *J. Chem. Phys.* **138** 024505
[359] Mamatkulov S and Schwierz N 2018 Force fields for monovalent and divalent metal cations in TIP3P water based on thermodynamic and kinetic properties *J. Chem. Phys.* **148** 074504
[360] Pethes I 2017 A comparison of classical interatomic potentials applied to highly concentrated aqueous lithium chloride solutions *J. Mol. Liq.* **242** 845–58
[361] Hanke C G, Price S L and Lynden-Bell R M 2001 Intermolecular potentials for simulations of liquid imidazolium salts *Mol. Phys.* **99** 801–9

[362] Tsuzuki S, Shinoda W, Saito H, Mikami M, Tokuda H and Watanabe M 2009 Molecular dynamics simulations of ionic liquids: cation and anion dependence of self-diffusion coefficients of ions *J. Phys. Chem.* B **113** 10641–9
[363] Migliorati V, Serva A, Aquilanti G, Olivi L, Pascarelli S, Mathon O and D'Angelo P 2015 Combining EXAFS spectroscopy and molecular dynamics simulations to understand the structural and dynamic properties of an imidazolium iodide ionic liquid *Phys. Chem. Chem. Phys.* **17** 2464–74
[364] Chaudhari M I, Muralidharan A, Pratt L R and Rempe S B 2018 Assessment of simple models for molecular simulation of ethylene carbonate and propylene carbonate as solvents for electrolyte solutions *Top. Curr. Chem.* **376** 376
[365] Smith A M, Lee A A and Perkin S 2016 The electrostatic screening length in concentrated electrolytes increases with concentration *J. Phys. Chem. Lett.* **7** 2157–63
[366] Gaddam P and Ducker W 2019 Electrostatic screening length in concentrated salt solutions *Langmuir* **35** 5719–27
[367] Zeman J, Kondrat S and Holm C 2020 Bulk ionic screening lengths from extremely large-scale molecular dynamics simulations *Chem. Commun.* **56** 15635–8
[368] Krucker-Velasquez E and Swan J W 2021 Underscreening and hidden ion structures in large scale simulations of concentrated electrolytes *J. Chem. Phys.* **155** 134903
[369] Jeanmairet G, Rotenberg B, Borgis D and Salanne M 2019 Study of a water-graphene capacitor with molecular density functional theory *J. Chem. Phys.* **151** 124111
[370] Cats P, Evans R, Härtel A and van Roij R 2021 Primitive model electrolytes in the near and far field: decay lengths from DFT and simulations *J. Chem. Phys.* **154** 124504
[371] Merlet C, Péan C, Rotenberg B, Madden P A, Daffos B, Taberna P-L, Simon P and Salanne M 2013 Highly confined ions store charge more efficiently in supercapacitors *Nat. Commun.* **4** 2701
[372] Coles S W, Mishin M, Perkin S, Fedorov M V and Ivaništšev V B 2017 The nanostructure of a lithium glyme solvate ionic liquid at electrified interfaces *Phys. Chem. Chem. Phys.* **19** 11004–10
[373] Coles S W and Ivaništšev V B 2019 Simulation of a solvate ionic liquid at a polarizable electrode with a constant potential *J. Phys. Chem.* C **123** 3935–43
[374] Sergeev A V, Chertovich A V, Itkis D M, Sen A, Gross A and Khokhlov A R 2017 Electrode/electrolyte interface in the Li–O_2 battery: insight from molecular dynamics study *J. Phys. Chem.* C **121** 14463–9
[375] Schröder C 2011 Collective translational motions and cage relaxations in molecular ionic liquids *J. Chem. Phys.* **135** 024502
[376] Schröder C and Steinhauser O 2009 On the dielectric conductivity of molecular ionic liquids *J. Chem. Phys.* **131** 114504
[377] Hayamizu K, Aihara Y, Arai S and Martinez C G 1999 Pulse-gradient spin-echo ^{1}H, ^{7}Li and ^{19}F NMR diffusion and ionic conductivity measurements of 14 organic electrolytes containing $LiN(SO_2CF_3)_2$ *J. Phys. Chem.* B **103** 519–24
[378] Lesch V, Li Z, Bedrov D, Borodin O and Heuer A 2015 The influence of cations on lithium ion coordination and transport in ionic liquid electrolytes: a MD simulation study *Phys. Chem. Chem. Phys.* **18** 382–92
[379] Borodin O, Smith G D and Henderson W 2006 Li^+ cation environment, transport and mechanical properties of the LiTFSI doped *N*-methyl-*N*-alkylpyrrolidinium$^+$TFSI$^-$ ionic liquids *J. Phys. Chem.* B **110** 16879–86
[380] Borodin O and Smith G D 2007 Li^+ transport mechanism in oligo(ethylene oxide)s compared to carbonates *J. Solut. Chem.* **36** 803–13
[381] Onsager L and Kim S K 1957 Wien effect in simple strong electrolytes *J. Phys. Chem.* **61** 198–215
[382] Lesnicki D, Gao C Y, Rotenberg B and Limmer D T 2020 Field-dependent ionic conductivities from generalized fluctuation-dissipation relations *Phys. Rev. Lett.* **124** 206001
[383] Jones P, Coupette F, Härtel A and Lee A A 2021 Bayesian unsupervised learning reveals hidden structure in concentrated electrolytes *J. Chem. Phys.* **154** 134902
[384] Skarmoutsos I, Ponnuchamy V, Vetere V and Mossa S 2015 Li^+ solvation in pure, binary and ternary mixtures of organic carbonate electrolytes *J. Phys. Chem.* C **119** 4502–15
[385] Takeuchi M, Matubayasi N, Kameda Y, Minofar B, Ishiguro S I and Umebayashi Y 2012 Free-energy and structural analysis of ion solvation and contact ion-pair formation of Li^+ with BF_4^- and PF_6^- in water and carbonate solvents *J. Phys. Chem.* B **116** 6476–87
[386] Lazaridis T 1998 Inhomogeneous fluid approach to solvation thermodynamics. 1. Theory *J. Phys. Chem.* B **102** 3531–41
[387] Hall D S, Self J and Dahn J R 2015 Dielectric constants for quantum chemistry and Li-ion batteries: solvent blends of ethylene carbonate and ethyl methyl carbonate *J. Phys. Chem.* C **119** 22322–30
[388] Naejus R, Damas C, Lemordant D, Coudert R and Willmann P 2002 Excess thermodynamic properties of the ethylene carbonate-trifluoroethyl methyl carbonate and propylene carbonate-trifluoroethyl methyl carbonate systems at T = (298.15 or 315.15) K *J. Chem. Thermodyn.* **34** 795–806
[389] Stewart S and Newman J 2008 Measuring the salt activity coefficient in lithium-battery electrolytes *J. Electrochem. Soc.* **155** 458–63
[390] Debye P and Hückel E 1923 On the theory of electrolytes. II. Limiting law for electric conductivity *Phys. Z.* **24** 305–25
[391] Merlet C, Péan C, Rotenberg B, Madden P A, Simon P and Salanne M 2013 Simulating supercapacitors: can we model electrodes as constant charge surfaces? *J. Phys. Chem. Lett.* **4** 264–8
[392] Chowdhury A U, Muralidharan N, Daniel C, Amin R and Belharouak I 2021 Probing the electrolyte/electrode interface with vibrational sum frequency generation spectroscopy: a review *J. Power Sources* **506** 230173
[393] Zhang Z, Said S, Smith K, Jervis R, Howard C A, Shearing P R, Brett D J L and Miller T S 2021 Characterizing batteries by *in situ* electrochemical atomic force microscopy: a critical review *Adv. Energy Mater.* **n/a** 2101518
[394] Perkin S *et al* 2006 Forces between mica surfaces, prepared in different ways, across aqueous and nonaqueous liquids confined to molecularly thin films *Langmuir* **22** 6142–52
[395] Scalfi L, Dufils T, Reeves K G, Rotenberg B and Salanne M 2020 A semiclassical Thomas–Fermi model to tune the metallicity of electrodes in molecular simulations *J. Chem. Phys.* **153** 174704
[396] Vatamanu J and Borodin O 2017 Ramifications of water-in-salt interfacial structure at charged electrodes for electrolyte electrochemical stability *J. Phys. Chem. Lett.* **8** 4362–7
[397] Li Z, Jeanmairet G, Méndez-Morales T, Rotenberg B and Salanne M 2018 Capacitive performance of water-in-salt electrolytes in supercapacitors: a simulation study *J. Phys. Chem.* C **122** 23917–24
[398] Vatamanu J, Borodin O and Smith G D 2009 Molecular dynamics simulations of atomically flat and nanoporous electrodes with a molten salt electrolyte *Phys. Chem. Chem. Phys.* **12** 170–82
[399] Merlet C, Rotenberg B, Madden P A, Taberna P-L, Simon P, Gogotsi Y and Salanne M 2012 On the molecular origin of supercapacitance in nanoporous carbon electrodes *Nat. Mater.* **11** 306–10
[400] Vatamanu J, Cao L, Borodin O, Bedrov D and Smith G D 2011 On the influence of surface topography on the electric double layer structure and differential capacitance of graphite/ionic liquid interfaces *J. Phys. Chem. Lett.* **2** 2267–72

[401] Borodin O and Bedrov D 2014 Interfacial structure and dynamics of the lithium alkyl dicarbonate SEI components in contact with the lithium battery electrolyte *J. Phys. Chem.* C **118** 18362–71
[402] Simoncelli M, Ganfoud N, Sene A, Haefele M, Daffos B, Taberna P-L, Salanne M, Simon P and Rotenberg B 2018 Blue energy and desalination with nanoporous carbon electrodes: capacitance from molecular simulations to continuous models *Phys. Rev.* X **8** 021024
[403] Suo L, Borodin O, Gao T, Olguin M, Ho J, Fan X, Luo C, Wang C and Xu K 2015 "Water-in-salt" electrolyte enables high-voltage aqueous lithium-ion chemistries *Science* **350** 938–43
[404] Chen M, Feng G and Qiao R 2020 Water-in-salt electrolytes: an interfacial perspective *Curr. Opin. Colloid Interface Sci.* **47** 99–110
[405] Li Z *et al* 2019 Transport properties of Li-TFSI water-in-salt electrolytes *J. Phys. Chem.* B **123** 10514–21
[406] McCurry J 2017 Samsung blames two separate battery faults for galaxy note 7 fires (available at: www.theguardian.com/technology/2017/jan/23/samsung-blames-faulty-batteries-for-causing-galaxy-note-7-fires)
[407] Zhang S S 2013 Liquid electrolyte lithium/sulfur battery: fundamental chemistry, problems and solutions *J. Power Sources* **231** 153–62
[408] Wu X, Pan K, Jia M, Ren Y, He H, Zhang L and Zhang S 2019 Electrolyte for lithium protection: from liquid to solid *Green Energy Environ.* **4** 360–74
[409] Kushima A, So K P, Su C, Bai P, Kuriyama N, Maebashi T, Fujiwara Y, Bazant M Z and Li J 2017 Liquid cell transmission electron microscopy observation of lithium metal growth and dissolution: root growth, dead lithium and lithium flotsams *Nano Energy* **32** 271–9
[410] Lin D, Liu Y, Li Y, Li Y, Pei A, Xie J, Huang W and Cui Y 2019 Fast galvanic lithium corrosion involving a Kirkendall-type mechanism *Nat. Chem.* **11** 382–9
[411] Hallinan D T Jr and Balsara N P 2013 Polymer electrolytes *Annu. Rev. Mater. Res.* **43** 503–25
[412] Popovic J 2011 Chemistry of soft matter battery electrolytes *Encyclopedia of Inorganic and Bioinorganic Chemistry* (New York: Wiley) pp 1–11
[413] Shao Y, Knijff L, Dietrich F M, Hermansson K and Zhang C 2021 Modelling bulk electrolytes and electrolyte interfaces with atomistic machine learning *Batter. Supercaps* **4** 585–95
[414] Hellström M and Behler J 2016 Concentration-dependent proton transfer mechanisms in aqueous NaOH solutions: from acceptor-driven to donor-driven and back *J. Phys. Chem. Lett.* **7** 3302–6
[415] Tovey S, Krishnamoorthy A N, Sivaraman G, Guo J, Benmore C, Heuer A and Holm C 2020 DFT accurate interatomic potential for molten NaCl from machine learning *J. Phys. Chem.* C **124** 25760–8
[416] Fedkin M V *et al* 2019 Development of the ReaxFF methodology for electrolyte–water systems *J. Phys. Chem.* A **123** 2125–41
[417] Hossain Md J, Pawar G, Liaw B, Gering K L, Dufek E J and van Duin A C T 2020 Lithium-electrolyte solvation and reaction in the electrolyte of a lithium ion battery: a ReaxFF reactive force field study *J. Chem. Phys.* **152** 184301
[418] Forsman J, Woodward C E and Trulsson M 2011 A classical density functional theory of ionic liquids *J. Phys. Chem.* B **115** 4606–12
[419] Jeanmairet G, Rotenberg B, Levesque M, Borgis D and Salanne M 2019 A molecular density functional theory approach to electron transfer reactions *Chem. Sci.* **10** 2130–43
[420] Jie Y, Ren X, Cao R, Cai W and Jiao S 2020 Advanced liquid electrolytes for rechargeable Li metal batteries *Adv. Funct. Mater.* **30** 1910777
[421] Francis C F J, Kyratzis I L and Best A S 2020 Lithium-ion battery separators for ionic-liquid electrolytes: a review *Adv. Mater.* **32** 1904205
[422] Xiong S, Regula M, Wang D and Song J 2018 Toward better lithium–sulfur batteries: functional non-aqueous liquid electrolytes *Electrochem. Energy Rev.* **1** 388–402
[423] Culver S P, Koerver R, Krauskopf T and Zeier W G 2018 Designing ionic conductors: the interplay between structural phenomena and interfaces in thiophosphate-based solid-state batteries *Chem. Mater.* **30** 4179–92
[424] Famprikis T, Canepa P, Dawson J A, Saiful Islam M and Masquelier C 2019 Fundamentals of inorganic solid-state electrolytes for batteries *Nat. Mater.* **18** 1278–91
[425] Goodenough J B and Park K-S 2013 The Li-ion rechargeable battery: a perspective *J. Am. Chem. Soc.* **135** 1167–76
[426] Dirican M, Yan C, Zhu P and Zhang X 2019 Composite solid electrolytes for all-solid-state lithium batteries *Mater. Sci. Eng.* R **136** 27–46
[427] Han L *et al* 2020 Recent developments and challenges in hybrid solid electrolytes for lithium-ion batteries *Front. Energy Res.* **8** 202
[428] Manthiram A, Yu X and Wang S 2017 Lithium battery chemistries enabled by solid-state electrolytes *Nat. Rev. Mater.* **2** 16103
[429] Faraday M 1833 IV. Experimental researches in electricity—third series *Phil. Trans. R. Soc.* **123** 23–54
[430] Armand M and Tarascon J-M 2008 Building better batteries *Nature* **451** 652–7
[431] Sudworth J L 2001 The sodium/nickel chloride (ZEBRA) battery *J. Power Sources* **100** 149–63
[432] Oshima T, Kajita M and Okuno A 2004 Development of sodium-sulfur batteries *Int. J. Appl. Ceram. Technol.* **1** 269–76
[433] Capasso C and Veneri O 2014 Experimental analysis of a zebra battery based propulsion system for urban bus under dynamic conditions *Energy Proc.* **61** 1138–41
[434] Dudney N J, Bates J B, Zuhr R A, Luck C F and Robertson J D 1992 Sputtering of lithium compounds for preparation of electrolyte thin films *Solid State Ion.* **53** 655–61
[435] Bates J B, Dudney N J, Gruzalski G R, Zuhr R A, Choudhury A, Luck C F and Robertson J D 1992 Electrical properties of amorphous lithium electrolyte thin films *Solid State Ion.* **53** 647–54
[436] Inaguma Y, Liquan C, Itoh M, Nakamura T, Uchida T, Ikuta H and Wakihara M 1993 High ionic conductivity in lithium lanthanum titanate *Solid State Commun.* **86** 689–93
[437] Kasper H M 1969 Series of rare earth garnets $Ln_3^{3+}M_2Li_3^{+}O_{12}$ (M = Te, W) *Inorg. Chem.* **8** 1000–2
[438] Mazza D 1988 Remarks on a ternary phase in the La_2O_3□Me_2O_5□Li_2O system (Me = Nb, Ta) *Mater. Lett.* **7** 205–7
[439] Kennedy J H, Sahami S, Shea S W and Zhang Z 1986 Preparation and conductivity measurements of SiS_2□Li_2S glasses doped with LiBr and LiCl *Solid State Ion.* **18** 368–71
[440] Ivanov-Shits A K and Sigaryov S E 1988 Ionic conductivity in LISICON-type materials *Solid State Ion.* **27** 89–100
[441] Lang B, Ziebarth B and Elsässer C 2015 Lithium ion conduction in $LiTi_2(PO_4)_3$ and related compounds based on the NASICON structure: a first-principles study *Chem. Mater.* **27** 5040–8
[442] De Klerk N J J, Rosłoń I and Wagemaker M 2016 Diffusion mechanism of Li argyrodite solid electrolytes for Li-ion batteries and prediction of optimized halogen doping: the effect of Li vacancies, halogens and halogen disorder *Chem. Mater.* **28** 7955–63
[443] Dawson J A, Attari T S, Chen H, Emge S P, Johnston K E and Saiful Islam M 2018 Elucidating lithium-ion and proton dynamics in anti-perovskite solid electrolytes *Energy Environ. Sci.* **11** 2993–3002

[444] Ahiavi E, Dawson J A, Kudu U, Courty M, Saiful Islam M, Clemens O, Masquelier C and Famprikis T 2020 Mechanochemical synthesis and ion transport properties of Na_3OX (X = Cl, Br, I and BH_4) antiperovskite solid electrolytes *J. Power Sources* **471** 228489
[445] Fenton D E 1973 Complexes of alkali metal ions with poly (ethylene oxide) *Polymer* **14** 589
[446] Abraham K M and Alamgir M 1990 Li^+-conductive solid polymer electrolytes with liquid-like conductivity *J. Electrochem. Soc* **137** 1657
[447] Dautzenberg G, Croce F, Passerini S and Scrosati B 1994 Characterization of PAN-based gel electrolytes. Electrochemical stability and lithium cyclability *Chem. Mater.* **6** 538–42
[448] Arcella V, Sanguineti A, Quartarone E and Mustarelli P 1999 Vinylidenefluoride–hexafluoropropylene copolymers as hybrid electrolyte components for lithium batteries *J. Power Sources* **81** 790–4
[449] Kataoka H, Saito Y, Sakai T, Quartarone E and Mustarelli P 2000 Conduction mechanisms of PVDF-type gel polymer electrolytes of lithium prepared by a phase inversion process *J. Phys. Chem.* B **104** 11460–4
[450] Li W, Zhu Z, Shen W, Tang J, Yang G and Xu Z 2016 A novel PVdF-based composite gel polymer electrolyte doped with ionomer modified graphene oxide *RSC Adv.* **6** 97338–45
[451] Appetecchi G B, Croce F and Scrosati B 1995 Kinetics and stability of the lithium electrode in poly (methylmethacrylate)-based gel electrolytes *Electrochim. Acta* **40** 991–7
[452] Bohnke O, Frand G, Rezrazi M, Rousselot C and Truche C 1993 Fast ion transport in new lithium electrolytes gelled with PMMA. 1. Influence of polymer concentration *Solid State Ion.* **66** 97–104
[453] Abbrent S, Plestil J, Hlavata D, Lindgren J, Tegenfeldt J and Wendsjö Å 2001 Crystallinity and morphology of PVdF–HFP-based gel electrolytes *Polymer* **42** 1407–16
[454] Park M-S, Hyun S-H, Nam S-C and Cho S B 2008 Performance evaluation of printed $LiCoO_2$ cathodes with PVdF-HFP gel electrolyte for lithium ion microbatteries *Electrochim. Acta* **53** 5523–7
[455] Yang C-C, Lian Z-Y, Lin S J, Shih J-Y and Chen W-H 2014 Preparation and application of PVdF-HFP composite polymer electrolytes in $LiNi_{0.5}Co_{0.2}Mn_{0.3}O_2$ lithium-polymer batteries *Electrochim. Acta* **134** 258–65
[456] Zhou W, Wang S, Li Y, Xin S, Manthiram A and Goodenough J B 2016 Plating a dendrite-free lithium anode with a polymer/ceramic/polymer sandwich electrolyte *J. Am. Chem. Soc.* **138** 9385–8
[457] Zhang T, He W, Zhang W, Wang T, Li P, Sun Z and Yu X 2020 Designing composite solid-state electrolytes for high performance lithium ion or lithium metal batteries *Chem. Sci.* **11** 8686–707
[458] Uvarov N F 2011 Composite solid electrolytes: recent advances and design strategies *J. Solid State Electrochem.* **15** 367–89
[459] Wilkening M, Indris S and Heitjans P 2003 Heterogeneous lithium diffusion in nanocrystalline Li_2O:Al_2O_3 composites *Phys. Chem. Chem. Phys.* **5** 2225–31
[460] Heitjans P and Indris S 2003 Diffusion and ionic conduction in nanocrystalline ceramics *J. Phys.: Condens. Matter.* **15** R1257–89
[461] Indris S, Heitjans P, Eduardo Roman H and Bunde A 2000 Nanocrystalline versus microcrystalline Li_2O:B_2O_3 composites: anomalous ionic conductivities and percolation theory *Phys. Rev. Lett.* **84** 2889–92
[462] Indris S and Heitjans P 2002 Heterogeneous ^{7}Li NMR relaxation in nanocrystalline Li_2O:B_2O_3 composites *J. Non-Cryst. Solids* **307–310** 555–64
[463] Blanchard D, Nale A, Sveinbjörnsson D, Eggenhuisen T M, Verkuijlen M H W, Vegge T, Kentgens A P M and de Jongh P E 2015 Nanoconfined $Libh_4$ as a fast lithium ion conductor *Adv. Funct. Mater.* **25** 184–92
[464] Liang C C 1973 Conduction characteristics of the lithium iodide-aluminum oxide solid electrolytes *J. Electrochem. Soc.* **120** 1289
[465] Phipps J B and Whitmore D H 1983 Ion transport in $LiISiO_2$ composites *Solid State Ion.* **9** 123–30
[466] Uvarov N F, Isupov V P, Sharma V and Shukla A K 1992 Effect of morphology and particle size on the ionic conductivities of composite solid electrolytes *Solid State Ion.* **51** 41–52
[467] Pradel A and Ribes M 1986 Electrical properties of lithium conductive silicon sulfide glasses prepared by twin roller quenching *Solid State Ion.* **18** 351–5
[468] Kanno R 2000 Synthesis of a new lithium ionic conductor, thio-LISICON–lithium germanium sulfide system *Solid State Ion.* **130** 97–104
[469] Murayama M 2002 Synthesis of new lithium ionic conductor thio-LISICON–lithium silicon sulfides system *J. Solid State Chem.* **168** 140–8
[470] Murayama M, Sonoyama N, Yamada A and Kanno R 2004 Material design of new lithium ionic conductor, thio-LISICON, in the Li_2S–P_2S_5 system *Solid State Ion.* **170** 173–80
[471] Minafra N, Culver S P, Li C, Senyshyn A and Zeier W G 2019 Influence of the lithium substructure on the diffusion pathways and transport properties of the thio-LISICON $Li_4Ge_{1-x}Sn_xS_4$ *Chem. Mater.* **31** 3794–802
[472] Bron P, Johansson S, Zick K, auf der Günne J S, Dehnen S and Roling B 2013 $Li_{10}SnP_2S_{12}$: an affordable lithium superionic conductor *J. Am. Chem. Soc.* **135** 15694–7
[473] Whiteley J M, Woo J H, Hu E, Nam K-W and Lee S-H 2014 Empowering the lithium metal battery through a silicon-based superionic conductor *J. Electrochem. Soc.* **161** A1812–17
[474] Huang W, Yoshino K, Hori S, Suzuki K, Yonemura M, Hirayama M and Kanno R 2019 Superionic lithium conductor with a cubic argyrodite-type structure in the Li–Al–Si–S system *J. Solid State Chem.* **270** 487–92
[475] Yamane H, Shibata M, Shimane Y, Junke T, Seino Y, Adams S, Minami K, Hayashi A and Tatsumisago M 2007 Crystal structure of a superionic conductor, $Li_{73}s_{11}$ *Solid State Ion.* **178** 1163–7
[476] Homma K, Yonemura M, Kobayashi T, Nagao M, Hirayama M and Kanno R 2011 Crystal structure and phase transitions of the lithium ionic conductor Li_3PS_4 *Solid State Ion.* **182** 53–58
[477] Minami T, Hayashi A and Tatsumisago M 2006 Recent progress of glass and glass-ceramics as solid electrolytes for lithium secondary batteries *Solid State Ion.* **177** 2715–20
[478] Bai X, Duan Y, Zhuang W, Yang R and Wang J 2020 Research progress in Li-argyrodite-based solid-state electrolytes *J. Mater. Chem.* A **8** 25663–86
[479] Minafra N, Hogrefe K, Barbon F, Helm B, Li C, Wilkening H M R and Zeier W G 2021 Two-dimensional substitution: toward a better understanding of the structure–transport correlations in the Li-superionic thio-LISICONs *Chem. Mater.* **33** 727–40
[480] Bhandari A and Bhattacharya J 2016 Origin of fast ion conduction in $Li_{10}GeP_2S_{12}$, a superionic conductor *J. Phys. Chem.* C **120** 29002–10
[481] Mo Y, Ong S P and Ceder G 2012 First principles study of the $Li_{10}GeP_2S_{12}$ lithium super ionic conductor material *Chem. Mater.* **24** 15–17

[482] Kraft M A et al 2018 Inducing high ionic conductivity in the lithium superionic argyrodites $Li_{6+x}P_{1-x}Ge_xS_5I$ for all-solid-state batteries J. Am. Chem. Soc. 140 16330–9
[483] Deiseroth H-J, Kong S-T, Eckert H, Vannahme J, Reiner C, Zaiß T and Schlosser M 2008 Li_6PS_5X: a class of crystalline Li-rich solids with an unusually high Li^+ mobility Angew. Chem., Int. Ed. Engl. 47 755–8
[484] Kraft M A et al 2017 Influence of lattice polarizability on the ionic conductivity in the lithium superionic argyrodites Li_6PS_5X (X= Cl, Br, I) J. Am. Chem. Soc. 139 10909–18
[485] Minafra N, Culver S P, Krauskopf T, Senyshyn A and Zeier W G 2018 Effect of Si substitution on the structural and transport properties of superionic Li-argyrodites J. Mater. Chem. A 6 645–51
[486] Adeli P, David Bazak J, Park K H, Kochetkov I, Huq A, Goward G R and Nazar L F 2019 Boosting solid-state diffusivity and conductivity in lithium superionic argyrodites by halide substitution Angew. Chem., Int. Ed. Engl. 58 8681–6
[487] Kuhn A, Duppel V and Lotsch B V 2013 Tetragonal $Li_{10}GeP_2S_{12}$—exploring the Li ion dynamics in LGPS Li electrolytes Energy Environ. Sci. 6 3548–52
[488] Xu M, Ding J and Ma E 2012 One-dimensional stringlike cooperative migration of lithium ions in an ultrafast ionic conductor Appl. Phys. Lett. 101 031901
[489] Adams S and Prasada Rao R 2012 Structural requirements for fast lithium ion migration in $Li_{10}GeP_2S_{12}$ J. Mater. Chem. 22 7687
[490] Kuhn A, Köhler J and Lotsch B V 2013 Single-crystal x-ray structure analysis of the superionic conductor $Li_{10}GeP_2S_{12}$ Phys. Chem. Chem. Phys. 15 11620–2
[491] Zhou L, Minafra N, Zeier W G and Nazar L F 2021 Innovative approaches to Li-argyrodite solid electrolytes for all-solid-state lithium batteries Acc. Chem. Res. 54 2717–28
[492] Bachman J C et al 2016 Inorganic solid-state electrolytes for lithium batteries: mechanisms and properties governing ion conduction Chem. Rev. 116 140–62
[493] Ohno S, Helm B, Fuchs T, Dewald G, Kraft M A, Culver S P, Senyshyn A and Zeier W G 2019 Further evidence for energy landscape flattening in the superionic argyrodites $Li_{6+x}P_{1-x}M_xS_5I$ (M = Si, Ge, Sn) Chem. Mater. 31 4936–44
[494] Zhao F et al 2020 A versatile Sn-substituted argyrodite sulfide electrolyte for all-solid-state Li metal batteries Adv. Energy Mater. 10 1903422
[495] Zhou L, Assoud A, Zhang Q, Wu X and Nazar L F 2019 New family of argyrodite thioantimonate lithium superionic conductors J. Am. Chem. Soc. 141 19002–13
[496] Zhou L, Park K-H, Sun X, Lalère F, Adermann T, Hartmann P and Nazar L F 2019 Solvent-engineered design of argyrodite Li_6PS_5X (X = Cl, Br, I) solid electrolytes with high ionic conductivity ACS Energy Lett. 4 265–70
[497] Wang P, Liu H, Patel S, Feng X, Chien P-H, Wang Y and Hu Y-Y 2020 Fast ion conduction and its origin in $Li_{6-x}PS_{5-x}Br_{1+x}$ Chem. Mater. 32 3833–40
[498] Morgan B J 2021 Mechanistic origin of superionic lithium diffusion in anion-disordered Li_6PS_5X argyrodites Chem. Mater. 33 2004–18
[499] Kuhs W F, Nitsche R and Scheunemann K 1979 The argyrodites—a new family of tetrahedrally close-packed structures Mater. Res. Bull. 14 241–8
[500] Gautam A, Sadowski M, Ghidiu M, Minafra N, Senyshyn A, Albe K and Zeier W G 2021 Engineering the site-disorder and lithium distribution in the lithium superionic argyrodite Li_6PS_5Br Adv. Energy Mater. 11 2003369
[501] Minafra N, Kraft M, Bernges T, Li C, Schlem R, Morgan B and Zeier W 2020 On the local charge inhomogeneity and lithium distribution in the superionic argyrodites Li_6PS_5X (X = Cl, Br, I) Inorganic Chemistry 59 11009–19
[502] Deng Z, Zhu Z, Chu I-H and Ong S P 2017 Data-driven first-principles methods for the study and design of alkali superionic conductors Chem. Mater. 29 281–8
[503] Yu C et al 2020 Superionic conductivity in lithium argyrodite solid-state electrolyte by controlled Cl-doping Nano Energy 69 104396
[504] Feng X, Chien P-H, Wang Y, Patel S, Wang P, Liu H, Immediato-Scuotto M and Hu Y-Y 2020 Enhanced ion conduction by enforcing structural disorder in Li-deficient argyrodites $Li_{6-x}PS_{5-x}Cl_{1+x}$ Energy Storage Mater. 30 67–73
[505] Yu C, Hageman J, Ganapathy S, van Eijck L, Zhang L, Adair K R, Sun X and Wagemaker M 2019 Tailoring Li_6PS_5Br ionic conductivity and understanding of its role in cathode mixtures for high performance all-solid-state Li–S batteries J. Mater. Chem. A 7 10412–21
[506] Murugan R, Thangadurai V and Weppner W 2007 Fast lithium ion conduction in garnet-type $Li_7La_3Zr_2O_12$ Angew. Chem., Int. Ed. Engl. 46 7778–81
[507] Ni J E, Case E D, Sakamoto J S, Rangasamy E and Wolfenstine J B 2012 Room temperature elastic moduli and Vickers hardness of hot-pressed LLZO cubic garnet J. Mater. Sci. 47 7978–85
[508] Zhu Y, He X and Mo Y 2016 First principles study on electrochemical and chemical stability of solid electrolyte-electrode interfaces in all-solid-state Li-ion batteries J. Mater. Chem. A 4 3253–66
[509] Binninger T, Marcolongo A, Mottet M, Weber V and Laino T 2020 Comparison of computational methods for the electrochemical stability window of solid-state electrolyte materials J. Mater. Chem. A 8 1347–59
[510] Geiger C A et al 2011 Crystal chemistry and stability of "$Li_7La_3Zr_2O_{12}$" garnet: a fast lithium-ion conductor Inorg. Chem. 50 1089–97
[511] Rangasamy E, Wolfenstine J and Sakamoto J 2012 The role of Al and Li concentration on the formation of cubic garnet solid electrolyte of nominal composition $Li_7La_3Zr_2O_{12}$ Solid State Ion. 206 28–32
[512] Ren Y, Shen Y, Lin Y and Nan C W 2015 Direct observation of lithium dendrites inside garnet-type lithium-ion solid electrolyte Electrochem. Commun. 57 27–30
[513] Sudo R, Nakata Y, Ishiguro K, Matsui M, Hirano A, Takeda Y, Yamamoto O and Imanishi N 2014 Interface behavior between garnet-type lithium-conducting solid electrolyte and lithium metal Solid State Ion. 262 151–4
[514] Cheng E J, Sharafi A and Sakamoto J 2017 Intergranular Li metal propagation through polycrystalline $Li_{6.25}Al_{0.25}La_3Zr_2O_{12}$ ceramic electrolyte Electrochim. Acta 223 85–91
[515] Kim S et al 2020 The role of interlayer chemistry in Li-metal growth through a garnet-type solid electrolyte Adv. Energy Mater. 10 1903993
[516] Canepa P, Dawson J A, Sai Gautam G, Statham J M, Parker S C and Saiful Islam M 2018 Particle morphology and lithium segregation to surfaces of the $Li_7La_3Zr_2O_{12}$ solid electrolyte Chem. Mater. 30 3019–27
[517] Tian H K, Xu B and Qi Y 2018 Computational study of lithium nucleation tendency in $Li_7La_3Zr_2O_{12}$ (LLZO) and rational design of interlayer materials to prevent lithium dendrites J. Power Sources 392 79–86

[518] Gao B, Jalem R and Tateyama Y 2020 Surface-dependent stability of the interface between garnet $Li_7La_3Zr_2O_{12}$ and the Li metal in the all-solid-state battery from first-principles calculations *ACS Appl. Mater. Interfaces* **12** 16350–8
[519] Ma C *et al* 2016 Interfacial stability of Li metal–solid electrolyte elucidated via *in situ* electron microscopy *Nano Lett.* **16** 7030–6
[520] Rettenwander D, Wagner R, Reyer A, Bonta M, Cheng L, Doeff M M, Limbeck A, Wilkening M and Amthauer G 2018 Interface instability of Fe-stabilized $Li_7La_3Zr_2O_{12}$ versus Li metal *J. Phys. Chem.* C **122** 3780–5
[521] Shen F, Dixit M B, Xiao X and Hatzell K B 2018 Effect of pore connectivity on Li dendrite propagation within LLZO electrolytes observed with synchrotron x-ray tomography *ACS Energy Lett.* **3** 1056–61
[522] Aguesse F, Manalastas W, Buannic L, Del Amo J M L, Singh G, Llordés A and Kilner J 2017 Investigating the dendritic growth during full cell cycling of garnet electrolyte in direct contact with Li metal *ACS Appl. Mater. Interfaces* **9** 3808–16
[523] Krauskopf T, Hartmann H, Zeier W G and Janek J 2019 Toward a fundamental understanding of the lithium metal anode in solid-state batteries—an electrochemo-mechanical study on the garnet-type solid electrolyte $Li_{6.25}Al_{0.25}La_3Zr_2O_{12}$ *ACS Appl. Mater. Interfaces* **11** 14463–77
[524] Zhu Y *et al* 2019 Dopant-dependent stability of garnet solid electrolyte interfaces with lithium metal *Adv. Energy Mater.* **9** 1803440
[525] Tsai C-L, Roddatis V, Chandran C V, Ma Q, Uhlenbruck S, Bram M, Heitjans P and Guillon O 2016 $Li_7La_3Zr_2O_{12}$ interface modification for Li dendrite prevention *ACS Appl. Mater. Interfaces* **8** 10617–26
[526] Thompson T *et al* 2017 Electrochemical window of the Li-ion solid electrolyte $Li_7La_3Zr_2O_{12}$ *ACS Energy Lett.* **2** 462–8
[527] Yu S, Schmidt R D, Garcia-Mendez R, Herbert E, Dudney N J, Wolfenstine J B, Sakamoto J and Siegel D J 2016 Elastic properties of the solid electrolyte $Li_7La_3Zr_2O_{12}$ (LLZO) *Chem. Mater.* **28** 197–206
[528] Wang Y, Lv J, Zhu Li and Ma Y 2012 CALYPSO: a method for crystal structure prediction *Comput. Phys. Commun.* **183** 2063–70
[529] Gao B, Gao P, Lu S, Lv J, Wang Y and Ma Y 2019 Interface structure prediction via CALYPSO method *Sci. Bull.* **64** 301–9
[530] Han F *et al* 2019 High electronic conductivity as the origin of lithium dendrite formation within solid electrolytes *Nat. Energy* **4** 187–96
[531] Squires A, Davies D, Kim S, Scanlon D, Walsh A and Morgan B 2020 Low electronic conductivity of $Li_7La_3Zr_2O_{12}$ (LLZO) solid electrolytes from first principles *ChemRxiv Preprint* (https://doi.org/10.26434/chemrxiv.13154297.v1)
[532] Xu M, Park M S, Lee J M, Kim T Y, Park Y S and Ma E 2012 Mechanisms of Li^+ transport in garnet-type cubic $Li_{3+x}La_3M_2O_{12}$ (M= Te, Nb, Zr) *Phys. Rev.* B **85** 052301
[533] Burbano M, Carlier D, Boucher F, Morgan B J and Salanne M 2016 Sparse cyclic excitations explain the low ionic conductivity of stoichiometric $Li_7La_3Zr_2O_{12}$ *Phys. Rev. Lett.* **116** 135901
[534] Meier K, Laino T and Curioni A 2014 Solid-state electrolytes: revealing the mechanisms of Li-ion conduction in tetragonal and cubic LLZO by first-principles calculations *J. Phys. Chem.* C **118** 6668–79
[535] Jalem R, Yamamoto Y, Shiiba H, Nakayama M, Munakata H, Kasuga T and Kanamura K 2013 Concerted migration mechanism in the Li ion dynamics of garnet-type $Li_7La_3Zr_2O_12$ *Chem. Mater.* **25** 425–30
[536] Rettenwander D, Blaha P, Laskowski R, Schwarz K, Bottke P, Wilkening M, Geiger C A and Amthauer G 2014 DFT study of the role of Al^{3+} in the fast ion-conductor $Li_{7-3x}Al_{3+x}La_3Zr_2O_{12}$ garnet *Chem. Mater.* **26** 2617–23
[537] Rettenwander D *et al* 2016 Structural and electrochemical consequences of Al and Ga cosubstitution in $Li_7La_3Zr_2O_{12}$ solid electrolytes *Chem. Mater.* **28** 2384–92
[538] Bonilla M R, García Daza F A, Carrasco J and Akhmatskaya E 2019 Exploring Li-ion conductivity in cubic, tetragonal and mixed-phase al-substituted $Li_7La_3Zr_2O_{12}$ using atomistic simulations and effective medium theory *Acta Mater.* **175** 426–35
[539] Awaka J, Kijima N, Hayakawa H and Akimoto J 2009 Synthesis and structure analysis of tetragonal $Li_7La_3Zr_2O_{12}$ with the garnet-related type structure *J. Solid State Chem.* **182** 2046–52
[540] Hayamizu K, Seki S and Haishi T 2017 Lithium ion micrometer diffusion in a garnet-type cubic $Li_7La_3Zr_2O_{12}$ (LLZO) studied using ^{7}Li NMR spectroscopy *J. Chem. Phys.* **146** 024701
[541] Brugge R H, Chater R J, Kilner J A and Aguadero A 2021 Experimental determination of Li diffusivity in LLZO using isotopic exchange and FIB-SIMS *J. Phys. Energy* **3** 034001
[542] Sharafi A *et al* 2017 Impact of air exposure and surface chemistry on Li-$Li_7La_3Zr_2O_{12}$ interfacial resistance *J. Mater. Chem.* A **5** 13475–87
[543] Islam M M, Bredow T and Heitjans P 2012 The ionic conductivity in lithium-boron oxide materials and its relation to structural, electronic and defect properties: insights from theory *J. Phys.: Condens. Matter.* **24** 203201
[544] Islam M M, Bredow T, Indris S and Heitjans P 2007 Enhanced conductivity at the interface of Li_2O:B_2O_3 nanocomposites: atomistic models *Phys. Rev. Lett.* **99** 145502
[545] Baggio B F and Grunder Y 2021 *In situ* x-ray techniques for electrochemical interfaces *Annu. Rev. Anal. Chem.* **14** 87–107
[546] Claessen R, Sing M, Paul M, Berner G, Wetscherek A, Müller A and Drube W 2009 Hard x-ray photoelectron spectroscopy of oxide hybrid and heterostructures: a new method for the study of buried interfaces *New J. Phys.* **11** 125007
[547] Thangadurai V and Weppner W 2005 $Li_6ALa_2Ta_2O_{12}$ (A = Sr, Ba): novel garnet-like oxides for fast lithium ion conduction *Adv. Funct. Mater.* **15** 107–12
[548] Liu Z *et al* 2013 Anomalous high ionic conductivity of nanoporous β-Li 3 PS 4 *J. Am. Chem. Soc.* **135** 975–8
[549] Kobayashi T, Yamada A and Kanno R 2008 Interfacial reactions at electrode/electrolyte boundary in all solid-state lithium battery using inorganic solid electrolyte, thio-LISICON *Electrochim. Acta* **53** 5045–50
[550] Takada K, Ohta N, Zhang L, Fukuda K, Sakaguchi I, Ma R, Osada M and Sasaki T 2008 Interfacial modification for high-power solid-state lithium batteries *Solid State Ion.* **179** 1333–7
[551] Sakuda A, Hayashi A and Tatsumisago M 2010 Interfacial observation between $LiCoO_2$ electrode and Li_2S-P_2S_5 solid electrolytes of all-solid-state lithium secondary batteries using transmission electron microscopy *Chem. Mater.* **22** 949–56
[552] Okuno Y, Haruyama J and Tateyama Y 2020 Comparative study on sulfide and oxide electrolyte interfaces with cathodes in all-solid-state battery via first-principles calculations *ACS Appl. Energy Mater.* **3** 11061–72
[553] Sharafi A, Kazyak E, Davis A L, Yu S, Thompson T, Siegel D J, Dasgupta N P and Sakamoto J 2017 Surface chemistry mechanism of ultra-low interfacial resistance in the solid-state electrolyte $Li_7La_3Zr_2O_{12}$ *Chem. Mater.* **29** 7961–8
[554] Jiang Z, Han Q, Wang S and Wang H 2019 Reducing the interfacial resistance in all-solid-state lithium batteries based on oxide ceramic electrolytes *ChemElectroChem* **6** 2970–83
[555] Lepley N D and Holzwarth N A W 2015 Modeling interfaces between solids: application to Li battery materials *Phys. Rev.* B **92** 214201
[556] Zhang Y Q, Tian Y, Xiao Y, Miara L J, Aihara Y, Tsujimura T, Shi T, Scott M C and Ceder G 2020 Direct visualization of the interfacial degradation of cathode coatings in solid state batteries: a combined experimental and computational study *Adv. Energy Mater.* **10** 1903778

[557] Xiao Y, Miara L J, Wang Y and Ceder G 2019 Computational screening of cathode coatings for solid-state batteries *Joule* **3** 1252–75
[558] Sang J, Yu Y, Wang Z and Shao G 2020 Theoretical formulation of $Li_{3a+b}N_aX_b$ (X = halogen) as a potential artificial solid electrolyte interphase (ASEI) to protect the Li anode *Phys. Chem. Chem. Phys.* **22** 12918–28
[559] Glass C W, Oganov A R and Hansen N 2006 USPEX-evolutionary crystal structure prediction *Comput. Phys. Commun.* **175** 713–20
[560] Oganov A R and Glass C W 2006 Crystal structure prediction using *ab initio* evolutionary techniques: principles and applications *J. Chem. Phys.* **124** 244704
[561] Parlinski K, Li Z Q and Kawazoe Y 1997 First-principles determination of the soft mode in cubic ZrO_2 *Phys. Rev. Lett.* **78** 4063–6
[562] Togo A, Oba F and Tanaka I 2008 First-principles calculations of the ferroelastic transition between rutile-type and $CaCl_2$-type SiO_2 at high pressures *Phys. Rev.* B **78** 134106
[563] Hart G L W and Forcade R W 2008 Algorithm for generating derivative structures *Phys. Rev.* B **77** 224115
[564] Sang L, Kissoon N and Wen F 2021 Characterizations of dynamic interfaces in all-solid lithium batteries *J. Power Sources* **506** 229871
[565] Schnell J, Knörzer H, Imbsweiler A J and Reinhart G 2020 Solid versus liquid–a bottom-up calculation model to analyze the manufacturing cost of future high-energy batteries *Energy Technol.* **8** 1901237
[566] Kato Y, Hori S, Saito T, Suzuki K, Hirayama M, Mitsui A, Yonemura M, Iba H and Kanno R 2016 High-power all-solid-state batteries using sulfide superionic conductors *Nat. Energy* **1** 16030
[567] Kim K J, Balaish M, Wadaguchi M, Kong L and Rupp J L M 2021 Solid-state Li–metal batteries: challenges and horizons of oxide and sulfide solid electrolytes and their interfaces *Adv. Energy Mater.* **11** 2002689
[568] Albertus P, Babinec S, Litzelman S and Newman A 2018 Status and challenges in enabling the lithium metal electrode for high-energy and low-cost rechargeable batteries *Nat. Energy* **3** 16–21
[569] Rodney D, Ventelon L, Clouet E, Pizzagalli L and Willaime F 2017 *Ab initio* modeling of dislocation core properties in metals and semiconductors *Acta Mater.* **124** 633–59
[570] Clouet E 2020 *Ab Initio Models of Dislocations* Handbook of Materials Modeling (Berlin: Springer International Publishing) (https://doi.org/10.1007/978-3-319-42913-7_22-1)
[571] Chen H, Liu Q Y, Jing M X, Chen F, Yuan W Y, Ju B W, Tu F Y, Shen X Q and Qin S B 2020 Improved interface stability and room-temperature performance of solid-state lithium batteries by integrating cathode/electrolyte and graphite coating *ACS Appl. Mater. Interfaces* **12** 15120–7
[572] Ito Y, Yamakawa S, Hayashi A and Tatsumisago M 2017 Effects of the microstructure of solid-electrolyte-coated $LiCoO_2$ on its discharge properties in all-solid-state lithium batteries *J. Mater. Chem.* A **5** 10658–68
[573] Yin Y, Jiang C-S, Guthrey H, Xiao C, Seitzman N, Ban C and Al-Jassim M 2020 Improved stability and cyclability of ceramic solid electrolyte by coating polymer *J. Electrochem. Soc.* **167** 020519
[574] Ji X, Hou S, Wang P, He X, Piao N, Chen J, Fan X and Wang C 2020 Solid-state electrolyte design for lithium dendrite suppression *Adv. Mater.* **32** 2002741
[575] Li H, Lian F, Meng N, Xiong C, Wu N, Xu B and Li Y 2021 Constructing electronic and ionic dual conductive polymeric interface in the cathode for high-energy-density solid-state batteries *Adv. Funct. Mater.* **31** 2008487
[576] Yi J, He P, Liu H, Ni H, Bai Z and Fan Li Z 2021 Manipulating interfacial stability of $LiNi_{0.5}Co_{0.3}Mn_{0.2}O_2$ cathode with sulfide electrolyte by nanosized LLTO coating to achieve high-performance all-solid-state lithium batteries *J. Energy Chem.* **52** 202–9
[577] Dai H *et al* 2021 A review of modification methods of solid electrolytes for all-solid-state sodium-ion batteries *Energy Technol.* **9** 2000682
[578] Pan X *et al* 2020 High voltage stable polyoxalate catholyte with cathode coating for all-solid-state Li-metal/NMC622 batteries *Adv. Energy Mater.* **10** 2002416
[579] Jing M X, Yuan W Y, Shen X Q, Zhang L K, Yang H, Liu Q Y, Chen F, Liu M Q and Ji Y S 2020 Highly efficient interface modification between poly(propylene carbonate)-based solid electrolytes and a lithium anode by facile graphite coating *ACS Sustain. Chem. Eng.* **8** 17106–15
[580] Wang C, Sun X, Yang Li, Song D, Wu Y, Ohsaka T, Matsumoto F and Wu J 2021 *In situ* ion-conducting protective layer strategy to stable lithium metal anode for all-solid-state sulfide-based lithium metal batteries *Adv. Mater. Interfaces* **8** 2001698
[581] Zhao F *et al* 2020 Tuning bifunctional interface for advanced sulfide-based all-solid-state batteries *Energy Storage Mater.* **33** 139–46
[582] Zhao B *et al* 2021 Interfacial modification enabled room temperature solid-state lithium–metal batteries *Ionics* **27** 1569–78
[583] Liang J *et al* 2020 Stabilizing and understanding the interface between nickel-rich cathode and PEO-based electrolyte by lithium niobium oxide coating for high-performance all-solid-state batteries *Nano Energy* **78** 105107
[584] Zhang Q, Bruck A M, Stavola A M, Liang W, Aurora P and Gallaway J W 2020 Enhanced electrochemical stability of sulfide-based $LiNi_{0.8}Mn_{0.1}Co_{0.1}O_2$ all-solid-state batteries by Ti surface doping *Batteries Supercaps* **4** 529–35
[585] Mizushima K, Jones P C, Wiseman P J and Goodenough J B 1980 Li_xCoO_2 ($0 < x < -1$): a new cathode material for batteries of high energy density *Mater. Res. Bull.* **15** 783–9
[586] Rozier P and Tarascon J M 2015 Li-rich layered oxide cathodes for next-generation Li-ion batteries: chances and challenges *J. Electrochem. Soc.* **162** A2490
[587] Stanley Whittingham M 2008 Materials challenges facing electrical energy storage *MRS Bull.* **33** 411–9
[588] Dunn B, Kamath H and Tarascon J-M 2011 Electrical energy storage for the grid: a battery of choices *Science* **334** 928–35
[589] Liu J *et al* 2013 Materials science and materials chemistry for large scale electrochemical energy storage: from transportation to electrical grid *Adv. Funct. Mater.* **23** 929–46
[590] Rosa Palacin M 2009 Recent advances in rechargeable battery materials: a chemist's perspective *Chem. Soc. Rev.* **38** 2565–75
[591] Masquelier C and Croguennec L 2013 Polyanionic (phosphates, silicates, sulfates) frameworks as electrode materials for rechargeable Li (or Na) batteries *Chem. Rev.* **113** 6552–91
[592] Bruce P G, Freunberger S A, Hardwick L J and Tarascon J-M 2012 Li–O_2 and Li–S batteries with high energy storage *Nat. Mater.* **11** 19
[593] Scrosati B, Hassoun J and Sun Y-K 2011 Lithium-ion batteries. A look into the future *Energy Environ. Sci.* **4** 3287–95
[594] Etacheri V, Marom R, Elazari R, Salitra G and Aurbach D 2011 Challenges in the development of advanced Li-ion batteries: a review *Energy Environ. Sci.* **4** 3243–62
[595] Takada K 2013 Progress and prospective of solid-state lithium batteries *Acta Mater.* **61** 759–70
[596] Fergus J W 2010 Recent developments in cathode materials for lithium ion batteries *J. Power Sources* **195** 939–54

[597] Ellis B L, Lee K T and Nazar L F 2010 Positive electrode materials for Li-ion and Li-batteries *Chem. Mater.* **22** 691–714
[598] He P *et al* 2012 Layered lithium transition metal oxide cathodes towards high energy lithium-ion batteries *J. Mater. Chem.* **22** 3680–95
[599] Zaghib K, Guerfi A, Hovington P, Vijh A, Trudeau M, Mauger A, Goodenough J B and Julien C M 2013 Review and analysis of nanostructured olivine-based lithium recheargeable batteries: status and trends *J. Power Sources* **232** 357–69
[600] Ellis B L and Nazar L F 2012 Sodium and sodium-ion energy storage batteries *Curr. Opin. Solid State Mater. Sci.* **16** 168–77
[601] Kim S-W, Seo D-H, Ma X, Ceder G and Kang K 2012 Electrode materials for rechargeable sodium-ion batteries: potential alternatives to current lithium-ion batteries *Adv. Energy Mater.* **2** 710–21
[602] Palomares V, Serras P, Villaluenga I, Hueso K B, Carretero-González J and Rojo T 2012 Na-ion batteries, recent advances and present challenges to become low cost energy storage systems *Energy Environ. Sci.* **5** 5884–901
[603] Fergus J W 2012 Ion transport in sodium ion conducting solid electrolytes *Solid State Ion.* **227** 102–12
[604] Yabuuchi N, Kajiyama M, Iwatate J, Nishikawa H, Hitomi S, Okuyama R, Usui R, Yamada Y and Komaba S 2012 P2-type $Na_x[Fe_{1/2}Mn_{1/2}]O_2$ made from earth-abundant elements for rechargeable Na batteries *Nat. Mater.* **11** 512–7
[605] Daniel C, Mohanty D, Li J and Wood D L 2014 Cathode materials review *AIP Conf. Proc.* **1597** 26–43
[606] Saiful Islam M and Fisher C A J 2014 Lithium and sodium battery cathode materials: computational insights into voltage, diffusion and nanostructural properties *Chem. Soc. Rev.* **43** 185–204
[607] Myung S-T, Maglia F, Park K-J, Yoon C S, Lamp P, Kim S-J and Sun Y-K 2017 Nickel-rich layered cathode materials for automotive lithium-ion batteries: achievements and perspectives *ACS Energy Lett.* **2** 196–223
[608] Mo J Y and Jeon W 2018 The impact of electric vehicle demand and battery recycling on price dynamics of lithium-ion battery cathode materials: a vector error correction model (VECM) analysis *Sustainability* **10** 2870
[609] Goonetilleke D, Sharma N, Pang W K, Peterson V K, Petibon R, Li J and Dahn J R 2018 Structural evolution and high-voltage structural stability of $Li(Ni_xMn_yCo_z)O_2$ electrodes *Chem. Mater.* **31** 376–86
[610] Chen Z, Lu Z and Dahn J R 2002 Staging phase transitions in Li_xCoO_2 *J. Electrochem. Soc.* **149** A1604
[611] Min K, Kim K, Jung C, Seo S-W, Song Y Y, Lee H S, Shin J and Cho E 2016 A comparative study of structural changes in lithium nickel cobalt manganese oxide as a function of Ni content during delithiation process *J. Power Sources* **315** 111–9
[612] Tian Z, Yu H, Zhang Z and Xu X 2018 Performance improvements of cobalt oxide cathodes for rechargeable lithium batteries *ChemBioEng Rev.* **5** 111–8
[613] Paulsen J M, Thomas C L and Dahn J R 2000 O_2 structure $Li_{2/3}[Ni_{1/3}Mn_{2/3}]O_2$: a new layered cathode material for rechargeable lithium batteries. I. Electrochemical properties *J. Electrochem. Soc.* **147** 861
[614] Paulsen J M and Dahn J R 2000 O_2-type $Li_{2/3}[Ni_{1/3}Mn_{2/3}]O_2$: a new layered cathode material for rechargeable lithium batteries. II. Structure, composition and properties *J. Electrochem. Soc.* **147** 2478
[615] Lu Z, MacNeil D D and Dahn J R 2001 Layered $Li[Ni_xCo_{1-2x}Mn_x]O_2$ cathode materials for lithium-ion batteries *Electrochem. Solid-State Lett.* **4** A200
[616] Ohzuku T and Makimura Y 2001 Layered lithium insertion material of $LiNi_{1/2}Mn_{1/2}O_2$: a possible alternative to $LiCoO_2$ for advanced lithium-ion batteries *Chem. Lett.* **30** 744–5
[617] Duan Y, Yang L, Zhang M-J, Chen Z, Bai J, Amine K, Pan F and Wang F 2019 Insights into Li/Ni ordering and surface reconstruction during synthesis of Ni-rich layered oxides *J. Mater. Chem.* A **7** 513–9
[618] Zhang N, Li J, Li H, Liu A, Huang Q, Ma L, Li Y and Dahn J R 2018 Structural, electrochemical and thermal properties of nickel-rich $LiNi_xMn_yCo_zO_2$ materials *Chem. Mater.* **30** 8852–60
[619] Azevedo M, Campagnol N, Hagenbruch T, Hoffman K, Lala A and Ramsbottom O 2018 Metals and mining (available at: www.mckinsey.com/industries/metals-and-mining/our-insights/lithium-and-cobalt-a-tale-of-two-commodities)
[620] Sathiya M *et al* 2013 Reversible anionic redox chemistry in high-capacity layered-oxide electrodes *Nat. Mater.* **12** 827–35
[621] Lee J, Urban A, Li X, Su D, Hautier G and Ceder G 2014 Unlocking the potential of cation-disordered oxides for rechargeable lithium batteries *Science* **343** 519–22
[622] Oishi M, Yogi C, Watanabe I, Ohta T, Orikasa Y, Uchimoto Y and Ogumi Z 2015 Direct observation of reversible charge compensation by oxygen ion in Li-rich manganese layered oxide positive electrode material, $Li_{1.16}Ni_{0.15}Co_{0.19}Mn_{0.50}O_2$ *J. Power Sources* **276** 89–94
[623] Seo D-H, Lee J, Urban A, Malik R, Kang S and Ceder G 2016 The structural and chemical origin of the oxygen redox activity in layered and cation-disordered Li-excess cathode materials *Nat. Chem.* **8** 692–7
[624] Gent W E *et al* 2017 Coupling between oxygen redox and cation migration explains unusual electrochemistry in lithium-rich layered oxides *Nat. Commun.* **8** 2091
[625] Assat G and Tarascon J-M 2018 Fundamental understanding and practical challenges of anionic redox activity in Li-ion batteries *Nat. Energy* **3** 373–86
[626] Naylor A J *et al* 2019 Depth-dependent oxygen redox activity in lithium-rich layered oxide cathodes *J. Mater. Chem.* A **7** 25355–68
[627] House R A *et al* 2020 Superstructure control of first-cycle voltage hysteresis in oxygen-redox cathodes *Nature* **577** 502–8
[628] House R A *et al* 2020 First-cycle voltage hysteresis in Li-rich 3D cathodes associated with molecular O_2 trapped in the bulk *Nat. Energy* **5** 777–85
[629] Hy S, Liu H, Zhang M, Qian D, Hwang B-J and Meng Y S 2016 Performance and design considerations for lithium excess layered oxide positive electrode materials for lithium ion batteries *Energy Environ. Sci.* **9** 1931–54
[630] Urban A, Lee J and Ceder G 2014 The configurational space of rocksalt-type oxides for high-capacity lithium battery electrodes *Adv. Energy Mater.* **4** 1400478
[631] Lee J, Seo D-H, Balasubramanian M, Twu N, Li X and Ceder G 2015 A new class of high capacity cation-disordered oxides for rechargeable lithium batteries: Li–Ni–Ti–Mo oxides *Energy Environ. Sci.* **8** 3255–65
[632] Yabuuchi N *et al* 2016 Origin of stabilization and destabilization in solid-state redox reaction of oxide ions for lithium-ion batteries *Nat. Commun.* **7** 13814
[633] Freire M, Kosova N V, Jordy C, Chateigner D, Lebedev O I, Maignan A and Pralong V 2016 A new active Li–Mn–O compound for high energy density Li-ion batteries *Nat. Mater.* **15** 173–7
[634] Yao Z, Kim S, He J, Hegde V I and Wolverton C 2018 Interplay of cation and anion redox in $Li_4Mn_2O_5$ cathode material and prediction of improved $Li_4(Mn, M)_2O_5$ electrodes for li-ion batteries *Sci. Adv.* **4** eaao6754
[635] Bhandari A, Jindal P and Bhattacharya J 2019 Discovery of new ground state structures for $Li_4Mn_2O_5$ and V_2O_5 from first principles *Comput. Mater. Sci.* **159** 454–9
[636] Nakajima M and Yabuuchi N 2017 Lithium-excess cation-disordered rocksalt-type oxide with nanoscale phase segregation: $Li_{1.25}Nb_{0.25}V_{0.5}O_2$ *Chem. Mater.* **29** 6927–35

[637] Yabuuchi N et al 2015 High-capacity electrode materials for rechargeable lithium batteries: Li_3NbO_4-based system with cation-disordered rocksalt structure *Proc. Natl Acad. Sci.* **112** 7650–5
[638] Wang R, Li X, Liu L, Lee J, Seo D-H, Bo S-H, Urban A and Ceder G 2015 A disordered rock-salt Li-excess cathode material with high capacity and substantial oxygen redox activity: $Li_{1.25}Nb_{0.25}Mn_{0.5}O_2$ *Electrochem. Commun.* **60** 70–73
[639] Sharpe R et al 2020 Redox chemistry and the role of trapped molecular O_2 in Li-rich disordered rocksalt oxyfluoride cathodes *J. Am. Chem. Soc.* **142** 21799–809
[640] House R A et al 2018 Lithium manganese oxyfluoride as a new cathode material exhibiting oxygen redox *Energy Environ. Sci.* **11** 926–32
[641] Lun Z et al 2020 Design principles for high-capacity Mn-based cation-disordered rocksalt cathodes *Chem* **6** 153–68
[642] Chen R, Ren S, Yavuz M, Guda A A, Shapovalov V, Witter R, Fichtner M and Hahn H 2015 Li^+ intercalation in isostructural Li_2VO_3 and Li_2VO_2F with O^{2-} and mixed O^{2-}/F^- anions *Phys. Chem. Chem. Phys.* **17** 17288–95
[643] Chen R, Ren S, Knapp M, Wang Di, Witter R, Fichtner M and Hahn H 2015 Disordered lithium-rich oxyfluoride as a stable host for enhanced Li^+ intercalation storage *Adv. Energy Mater.* **5** 1401814
[644] Baur C et al 2019 Improved cycling stability in high-capacity Li-rich vanadium containing disordered rock salt oxyfluoride cathodes *J. Mater. Chem.* A **7** 21244–53
[645] Cambaz M A et al 2019 Suppressing dissolution of vanadium from cation-disordered $Li_{2-x}VO_2F$ via a concentrated electrolyte approach *Chem. Mater.* **31** 7941–50
[646] Baur C, Lacatusu M-E, Fichtner M and Johnsen R E 2020 Insights into structural transformations in the local structure of Li_2VO_2F using operando x-ray diffraction and total scattering: amorphization and recrystallization *ACS Appl. Mater. Interfaces* **12** 27010–6
[647] Källquist I, Naylor A J, Baur C, Chable J, Kullgren J, Fichtner M, Edström K, Brandell D and Hahlin M 2019 Degradation mechanisms in Li_2VO_2F Li-rich disordered rock-salt cathodes *Chem. Mater.* **31** 6084–96
[648] Chang J H et al 2020 Superoxide formation in Li_2VO_2F cathode material—a combined computational and experimental investigation of anionic redox activity *J. Mater. Chem.* A **8** 16551–9
[649] Lee J et al 2018 Reversible Mn^{2+}/Mn^{4+} double redox in lithium-excess cathode materials *Nature* **556** 185–90
[650] Freire M, Lebedev O I, Maignan A, Jordy C and Pralong V 2017 Nanostructured Li_2MnO_3: a disordered rock salt type structure for high energy density Li ion batteries *J. Mater. Chem.* A **5** 21898–902
[651] Jacquet Q, Iadecola A, Saubanere M, Li H, Berg E J, Rousse G, Cabana J, Doublet M L and Tarascon J M 2019 Charge transfer band gap as an indicator of hysteresis in Li-disordered rock salt cathodes for Li-ion batteries *J. Am. Chem. Soc.* **141** 11452–64
[652] Clément R J, Lun Z and Ceder G 2020 Cation-disordered rocksalt transition metal oxides and oxyfluorides for high energy lithium-ion cathodes *Energy Environ. Sci.* **13** 345–73
[653] Nytén A, Abouimrane A, Armand M, Gustafsson T and Thomas J O 2005 Electrochemical performance of Li_2FeSiO_4 as a new Li-battery cathode material *Electrochem. Commun.* **7** 156–60
[654] Sirisopanaporn C, Dominko R, Masquelier C, Robert Armstrong A, Mali G and Bruce P G 2011 Polymorphism in Li_2(Fe, Mn)SiO_4: a combined diffraction and NMR study *J. Mater. Chem.* **21** 17823–31
[655] Saiful Islam M, Dominko R, Masquelier C, Sirisopanaporn C, Robert Armstrong A and Bruce P G 2011 Silicate cathodes for lithium batteries: alternatives to phosphates? *J. Mater. Chem.* **21** 9811–8
[656] Padhi A K, Nanjundaswamy K S, Masquelier C and Goodenough J B 1997 Mapping of transition metal redox energies in phosphates with NASICON structure by lithium intercalation *J. Electrochem. Soc.* **144** 2581
[657] Tygesen A S, Chang J H, Vegge T and García-Lastra J M 2020 Computational framework for a systematic investigation of anionic redox process in Li-rich compounds *npj Comput. Mater.* **6** 1–9
[658] Robert Armstrong A and Bruce P G 1996 Synthesis of layered $LiMnO_2$ as an electrode for rechargeable lithium batteries *Nature* **381** 499–500
[659] Mosbah A, Verbaere A and Tournoux M 1983 Phases $Li_xMnO_{2\lambda}$ rattachees au type spinelle *Mater. Res. Bull.* **18** 1375–81
[660] Dittrich G and Hoppe R 1969 Zur kristallstruktur von $LiMnO_2$ *Z. Anorg. Allg. Chem.* **368** 262–70
[661] Gao P, Ishikawa R, Tochigi E, Kumamoto A, Shibata N and Ikuhara Y 2017 Atomic-scale tracking of a phase transition from spinel to rocksalt in lithium manganese oxide *Chem. Mater.* **29** 1006–13
[662] Chen B, Ben L, Yu H, Chen Y and Huang X 2018 Understanding surface structural stabilization of the high-temperature and high-voltage cycling performance of Al^{3+}-modified $LiMn_2O_4$ cathode material *ACS Appl. Mater. Interfaces* **10** 550–9
[663] Reed J, Ceder G and Van Der Ven A 2001 Layered-to-spinel phase transition in Li_xMnO_2 *Electrochem. Solid-State Lett.* **4** A78
[664] Bruce P G, Scrosati B and Tarascon J-M 2008 Nanomaterials for rechargeable lithium batteries *Angew. Chem., Int. Ed. Engl.* **47** 2930–46
[665] Franger S, Benoit C, Bourbon C and Le Cras F 2006 Chemistry and electrochemistry of composite $LiFePO_4$ materials for secondary lithium batteries *J. Phys. Chem. Solids* **67** 1338–42
[666] Ellis B, Kan W H, Makahnouk W R M and Nazar L F 2007 Synthesis of nanocrystals and morphology control of hydrothermally prepared $LiFePO_4$ *J. Mater. Chem.* **17** 3248–54
[667] Malik R, Burch D, Bazant M and Ceder G 2010 Particle size dependence of the ionic diffusivity *Nano Lett.* **10** 4123–7
[668] Ledwaba R S, Ngoepe P and Sayle D 2018 Modeling diffusion-induced stress in Li-Mn-O nanocomposite cathode materials *APS March Meeting Abstracts* vol 2018 p E20.006
[669] Sayle T X T, Rapela Maphanga R, Ngoepe P E and Sayle D C 2009 Predicting the electrochemical properties of MnO_2 nanomaterials used in rechargeable Li batteries: simulating nanostructure at the atomistic level *J. Am. Chem. Soc.* **131** 6161–73
[670] Gupta P K, Bhandari A, Bhattacharya J and Pala R G S 2018 Correlating voltage profile to molecular transformations in ramsdellite MnO_2 and its implication for polymorph engineering of lithium ion battery cathodes *J. Phys. Chem.* C **122** 11689–700
[671] Gupta P K, Bhandari A, Bhattacharya J and Pala R G S 2020 Higher voltage, wider voltage plateau, longer cycle life and faster kinetics via thermally modulated interfaces between ramsdellite and pyrolusite MnO_2 for lithium-ion battery cathodes *J. Power Sources* **450** 227619
[672] Moriwake H, Kuwabara A, Fisher C A J, Huang R, Hitosugi T, Ikuhara Y H, Oki H and Ikuhara Y 2013 First-principles calculations of lithium-ion migration at a coherent grain boundary in a cathode material, $LiCoO_2$ *Adv. Mater.* **25** 618–22
[673] Dixit M, Engel H, Eitan R, Aurbach D, Levi M D, Kosa M and Major D T 2015 Classical and quantum modeling of Li and Na diffusion in $FePO_4$ *J. Phys. Chem.* C **119** 15801–9
[674] Morgan D, Van der Ven A and Ceder G 2004 Li conductivity in Li_xMPO_4 (M = Mn, Fe, Co, Ni) olivine materials *Electrochem. Solid-State Lett.* **7** A30–A32
[675] Ouyang C, Shi S, Wang Z, Huang X and Chen L 2004 First-principles study of Li ion diffusion in $LiFePO_4$ *Phys. Rev.* B **69** 104303

[676] Saiful Islam M, Driscoll D J, Fisher C A J and Slater P R 2005 Atomic-scale investigation of defects, dopants and lithium transport in the $LiFePO_4$ olivine-type battery material *Chem. Mater.* **17** 5085–92
[677] Amin R, Balaya P and Maier J 2006 Anisotropy of electronic and ionic transport in $LiFePO_4$ single crystals *Electrochem. Solid-State Lett.* **10** A13
[678] Van der Ven A and Ceder G 2000 Lithium diffusion in layered Li_xCoO_2 *Electrochem. Solid-State Lett.* **3** 301
[679] Thackeray M M 1997 Manganese oxides for lithium batteries *Prog. Solid State Chem.* **25** 1–71
[680] Proell J, Kohler R, Mangang A, Ulrich S, Ziebert C and Pfleging W 2012 3D structures in battery materials *J. Laser Micro Nanoeng.* **7** 97
[681] Nishimura S-ichi, Kobayashi G, Ohoyama K, Kanno R, Yashima M and Yamada A 2008 Experimental visualization of lithium diffusion in Li_xFePO_4 *Nat. Mater.* **7** 707–11
[682] Van der Ven A, Thomas J C, Xu Q, Swoboda B and Morgan D 2008 Nondilute diffusion from first principles: Li diffusion in Li_xTiS_2 *Phys. Rev.* B **78** 104306
[683] Bhattacharya J and Van der Ven A 2011 First-principles study of competing mechanisms of nondilute Li diffusion in spinel Li_xTiS_2 *Phys. Rev.* B **83** 144302
[684] Bhattacharya J and Van der Ven A 2010 Phase stability and nondilute Li diffusion in spinel $Li_{1+x}Ti_2O_4$ *Phys. Rev.* B **81** 104304
[685] Van Der Ven A, Bhattacharya J and Belak A A 2013 Understanding Li diffusion in Li-intercalation compounds *Acc. Chem. Res.* **46** 1216–25
[686] Van der Ven A and Ceder G 2001 Lithium diffusion mechanisms in layered intercalation compounds *J. Power Sources* **97** 529–31
[687] Choi S H, Shlyakhtin O A, Kim J and Yoon Y S 2005 Structural and electrochemical properties of $Li1_{1+x}Ni_{0.5}Mn_{0.5}O_{2+\delta}$ $(0 \leqslant x \leqslant 0.7)$ cathode materials for lithium-ion batteries *J. Power Sources* **140** 355–60
[688] Kang K, Meng Y S, Breger J, Grey C P and Ceder G 2006 Electrodes with high power and high capacity for rechargeable lithium batteries *Science* **311** 977–80
[689] Laubach S, Laubach S, Schmidt P C, Gröting M, Albe K, Jaegermann W and Wolf W 2009 Structure, electronic structure and defect formation energies of $Li_xCo_{1-y}Ni_yO_2$ as a function of x $(0 < x < 1)$ and y $(y = 0, 0.5, 1)$ *Z. Phys. Chem.* **223** 1327–40
[690] Lee E and Persson K A 2013 Solid-solution Li intercalation as a function of cation order/disorder in the high-voltage $Li_xNi_{0.5}Mn_{1.5}O_4$ spinel *Chem. Mater.* **25** 2885–9
[691] Hao S, Lu Z and Wolverton C 2016 Quaternary phase diagrams of spinel $Li_y\square_{1-y}Mn_xNi_{2-x}O_4$ and composite cathode voltages for concentration gradient materials *Phys. Rev.* B **94** 014114
[692] Capsoni D, Bini M, Chiodelli G, Mustarelli P, Massarotti V, Azzoni C B, Mozzati M C and Linati L 2002 Inhibition of Jahn–Teller cooperative distortion in $LiMn_2O_4$ spinel by Ga^{3+} doping *J. Phys. Chem.* B **106** 7432–8
[693] Singh G, Gupta S L, Prasad R, Auluck S, Gupta R and Sil A 2009 Suppression of Jahn–Teller distortion by chromium and magnesium doping in spinel $LiMn_2O_4$: a first-principles study using GGA and GGA+U *J. Phys. Chem. Solids* **70** 1200–6
[694] Padhi A K, Nanjundaswamy K S and Goodenough J B 1997 Phospho-olivines as positive-electrode materials for rechargeable lithium batteries *J. Electrochem. Soc.* **144** 1188–94
[695] Thackeray M M, David W I F, Bruce P G and Goodenough P G 1983 Lithium insertion into manganese spinels *Mater. Res. Bull.* **18** 461–72
[696] Koga H, Croguennec L, Menetrier M, Douhiol K, Belin S, Bourgeois L, Suard E and Weill F 2013 Reversible oxygen participation to the redox processes revealed for $Li_{1.20}Mn_{0.54}Co_{0.13}Ni_{0.13}O_2$ *J. Electrochem. Soc.* **160** A786–92
[697] Sathiya M, Lerich J-B, Salager E, Gourier D, Tarascon J-M and Vezin H 2015 Electron paramagnetic resonance imaging for real-time monitoring of Li-ion batteries *Nat. Commun.* **6** 6276
[698] McCalla E *et al* 2015 Visualization of OO peroxo-like dimers in high-capacity layered oxides for Li-ion batteries *Science* **350** 1516–21
[699] Cao T, Shi C, Zhao N, He C, Li J and Liu E 2015 Understanding the electrochemical properties of Li-rich cathode materials from first-principles calculations *J. Phys. Chem.* C **119** 28749–56
[700] Shimoda K *et al* 2016 Oxidation behaviour of lattice oxygen in Li-rich manganese-based layered oxide studied by hard x-ray photoelectron spectroscopy *J. Mater. Chem.* A **4** 5909–16
[701] Chen H and Saiful Islam M 2016 Lithium extraction mechanism in Li-rich Li_2MnO_3 involving oxygen hole formation and dimerization *Chem. Mater.* **28** 6656–63
[702] Luo K *et al* 2016 Charge-compensation in 3D-transition-metal-oxide intercalation cathodes through the generation of localized electron holes on oxygen *Nat. Chem.* **8** 684–91
[703] Muhammad S *et al* 2016 Evidence of reversible oxygen participation in anomalously high capacity Li- and Mn-rich cathodes for Li-ion batteries *Nano Energy* **21** 172–84
[704] Zhan C *et al* 2017 Enabling the high capacity of lithium-rich anti-fluorite lithium iron oxide by simultaneous anionic and cationic redox *Nat. Energy* **2** 963–71
[705] Zheng J, Myeong S, Cho W, Yan P, Xiao J, Wang C, Cho J and Zhang J G 2017 Li- and Mn-rich cathode materials: challenges to commercialization *Adv. Energy Mater.* **7** 1601284
[706] Ben Yahia M, Vergnet J, Saubanère M and Doublet M-L 2019 Unified picture of anionic redox in Li/Na-ion batteries *Nat. Mater.* **18** 496–502
[707] Hua W *et al* 2019 Structural insights into the formation and voltage degradation of lithium- and manganese-rich layered oxides *Nat. Commun.* **10** 5365
[708] Li L *et al* 2019 Probing electrochemically induced structural evolution and oxygen redox reactions in layered lithium iridate *Chem. Mater.* **31** 4341–52
[709] Eum D *et al* 2020 Voltage decay and redox asymmetry mitigation by reversible cation migration in lithium-rich layered oxide electrodes *Nat. Mater.* **19** 419–27
[710] Gent W E, Abate I I, Yang W, Nazar L F and Chueh W C 2020 Design rules for high-valent redox in intercalation electrodes *Joule* **4** 1369–97
[711] Sathiya M, Ramesha K, Rousse G, Foix D, Gonbeau D, Prakash A S, Doublet M L, Hemalatha K and Tarascon J M 2013 High performance $Li_2Ru_{1-y}Mn_yO_3$ $(0.2 \leqslant y \leqslant 0.8)$ cathode materials for rechargeable lithium-ion batteries: their understanding *Chem. Mater.* **25** 1121–31
[712] Xiao R, Li H and Chen L 2012 Density functional investigation on Li_2MnO_3 *Chem. Mater.* **24** 4242–51
[713] Hong J *et al* 2019 Metal–oxygen decoordination stabilizes anion redox in Li-rich oxides *Nat. Mater.* **18** 256–65
[714] Davies D W, Morgan B J, Scanlon D O and Walsh A 2020 Low-cost descriptors of electrostatic and electronic contributions to anion redox activity in batteries *IOP SciNotes* **1** 024805

[715] Xiao Y et al 2018 Insight into the origin of lithium/nickel ions exchange in layered Li ($Ni_xMn_yCo_z$)O_2 cathode materials *Nano Energy* **49** 77–85
[716] Sun H and Zhao K 2017 Electronic structure and comparative properties of $LiNi_xMn_yCo_zO_2$ cathode materials *J. Phys. Chem.* C **121** 6002–10
[717] Dixit M, Markovsky B, Schipper F, Aurbach D and Major D T 2017 Origin of structural degradation during cycling and low thermal stability of Ni-rich layered transition metal-based electrode materials *J. Phys. Chem.* C **121** 22628–36
[718] Hoang K and Johannes M 2016 Defect physics and chemistry in layered mixed transition metal oxide cathode materials: (Ni, Co, Mn) vs (Ni, Co, Al) *Chem. Mater.* **28** 1325–34
[719] Dixit M, Markovsky B, Aurbach D and Major D T 2017 Unraveling the effects of Al doping on the electrochemical properties of $LiNi_{0.5}Co_{0.2}Mn_{0.3}O_2$ using first principles *J. Electrochem. Soc.* **164** A6359
[720] Lu Z, Donaberger R A and Dahn J R 2000 Superlattice ordering of Mn, Ni and Co in layered alkali transition metal oxides with P2, P3 and O3 structures *Chem. Mater.* **12** 3583–90
[721] Du T, Xu B, Wu M, Liu G and Ouyang C 2016 Insight into the vibrational and thermodynamic properties of layered lithium transition-metal oxides $LiMO_2$ (M = Co, Ni, Mn): a first-principles study *J. Phys. Chem.* C **120** 5876–82
[722] Shang S L, Wang Y, Mei Z G, Hui X D and Liu Z K 2012 Lattice dynamics, thermodynamics and bonding strength of lithium-ion battery materials $LiMPO_4$ (M = Mn, Fe, Co and Ni): a comparative first-principles study *J. Mater. Chem.* **22** 1142–9
[723] Sagotra A K, Chu D and Cazorla C 2019 Influence of lattice dynamics on lithium-ion conductivity: a first-principles study *Phys. Rev. Mater.* **3** 035405
[724] Puligheddu M, Xia Y, Chan M and Galli G 2019 Computational prediction of lattice thermal conductivity: a comparison of molecular dynamics and Boltzmann transport approaches *Phys. Rev. Mater.* **3** 085401
[725] Mattila N and Karttunen A J 2020 Lattice thermal conductivity of $NaCoO_2$ and $LiCoO_2$ intercalation materials studied by hybrid density functional theory *Mater. Res. Express* **7** 075502
[726] Feng T, O'Hara A and Pantelides S T 2020 Quantum prediction of ultra-low thermal conductivity in lithium intercalation materials *Nano Energy* **75** 104916
[727] Qian X, Gu X, Dresselhaus M S and Yang R 2016 Anisotropic tuning of graphite thermal conductivity by lithium intercalation *J. Phys. Chem. Lett.* **7** 4744–50
[728] Wei Z, Yang F, Bi K, Yang J and Chen Y 2018 Tunable anisotropic thermal conductivity and elastic properties in intercalated graphite via lithium ions *J. Phys. Chem.* C **122** 1447–55
[729] Xia Y, Hegde V I, Pal K, Hua X, Gaines D, Patel S, He J, Aykol M and Wolverton C 2020 High-throughput study of lattice thermal conductivity in binary rocksalt and zinc blende compounds including higher-order anharmonicity *Phys. Rev.* X **10** 041029
[730] Zhang Q, Uchaker E, Candelaria S L and Cao G 2013 Nanomaterials for energy conversion and storage *Chem. Soc. Rev.* **42** 3127–71
[731] Kramer D and Ceder G 2009 Tailoring the morphology of $LiCoO_2$: a first principles study *Chem. Mater.* **21** 3799–809
[732] Xu B, Fell C R, Chi M and Meng Y S 2011 Identifying surface structural changes in layered Li-excess nickel manganese oxides in high voltage lithium ion batteries: a joint experimental and theoretical study *Energy Environ. Sci.* **4** 2223–33
[733] Dahéron L, Martinez He, Dedryvere R, Baraille I, Ménétrier M, Denage C, Delmas C and Gonbeau D 2009 Surface properties of $LiCoO_2$ investigated by XPS analyses and theoretical calculations *J. Phys. Chem.* C **113** 5843–52
[734] Kim Y, Lee H and Kang S 2012 First-principles and experimental investigation of the morphology of layer-structured $LiNiO_2$ and $LiCoO_2$ *J. Mater. Chem.* **22** 12874–81
[735] Benedek R and Thackeray M M 2011 Simulation of the surface structure of lithium manganese oxide spinel *Phys. Rev.* B **83** 195439
[736] Karim A, Fosse S and Persson K A 2013 Surface structure and equilibrium particle shape of the $LiMn_2O_4$ spinel from first-principles calculations *Phys. Rev.* B **87** 075322
[737] Leung K 2012 First-principles modeling of the initial stages of organic solvent decomposition on $Li_xMn_2O_4$ (100) surfaces *J. Phys. Chem.* C **116** 9852–61
[738] Tompsett D A, Parker S C, Bruce P G and Islam M S 2013 Nanostructuring of β-MnO_2: the important role of surface to bulk ion migration *Chem. Mater.* **25** 536–41
[739] Qian D, Hinuma Y, Chen H, Du L-S, Carroll K J, Ceder G, Grey C P and Meng Y S 2012 Electronic spin transition in nanosize stoichiometric lithium cobalt oxide *J. Am. Chem. Soc.* **134** 6096–9
[740] Hong L, Hu L, Freeland J W, Cabana J, Öğüt S and Klie R F 2019 Electronic structure of $LiCoO_2$ surfaces and effect of al substitution *J. Phys. Chem.* C **123** 8851–8
[741] Abbaspour-Tamijani A, Bennett J W, Jones D T, Cartagena-Gonzalez N, Jones Z R, Laudadio E D, Hamers R J, Santana J A and Mason S E 2020 DFT and thermodynamics calculations of surface cation release in $LiCoO_2$ *Appl. Surf. Sci.* **515** 145865
[742] Deng Y-P, Yin Z-W, Wu Z-G, Zhang S-J, Fu F, Zhang T, Li J-T, Huang L and Sun S-G 2017 Layered/spinel heterostructured and hierarchical micro/nanostructured Li-rich cathode materials with enhanced electrochemical properties for Li-ion batteries *ACS Appl. Mater. Interfaces* **9** 21065–70
[743] Deng Y-P, Fu F, Wu Z-G, Yin Z-W, Zhang T, Li J-T, Huang L and Sun S-G 2016 Layered/spinel heterostructured Li-rich materials synthesized by a one-step solvothermal strategy with enhanced electrochemical performance for Li-ion batteries *J. Mater. Chem.* A **4** 257–63
[744] Long B R, Croy J R, Park J S, Wen J, Miller D J and Thackeray M M 2014 Advances in stabilizing 'layered-layered' $xLi_2MnO_3{\cdot}(1\text{-}x)LiMO_2$ (M = Mn, Ni, Co) electrodes with a spinel component *J. Electrochem. Soc.* **161** A2160
[745] Wang D, Belharouak I, Zhou G and Amine K 2013 Nanoarchitecture multi-structural cathode materials for high capacity lithium batteries *Adv. Funct. Mater.* **23** 1070–5
[746] Warburton R E, Castro F C, Deshpande S, Madsen K E, Bassett K L, Reis R D, Gewirth A A, Dravid V P and Greeley J 2020 Oriented $LiMn_2O_4$ particle fracture from delithiation-driven surface stress *ACS Appl. Mater. Interfaces* **12** 49182–91
[747] Liang C, Longo R C, Kong F, Zhang C, Nie Y, Zheng Y and Cho K 2018 *Ab initio* study on surface segregation and anisotropy of Ni-rich $LiNi_{1-2y}Co_yMn_yO_2$ (NCM) ($y \leqslant 0.1$) cathodes *ACS Appl. Mater. Interfaces* **10** 6673–80
[748] Chen G, Song X and Richardson T J 2006 Electron microscopy study of the $LiFePO_4$ to $FePO_4$ phase transition *Electrochem. Solid-State Lett.* **9** A295
[749] Saiful Islam M 2010 Recent atomistic modelling studies of energy materials: batteries included *Phil. Trans. R. Soc.* A **368** 3255–67
[750] Tankhilsaikhan B, Gorfman S, Tungalag N, Tuvjargal N, Davaasambuu J and Pietsch U 2019 Density functional theory study of the energy landscapes for the channeling of Li in $LiFePO_4$ *Solid State Phenom.* **288** 98–103
[751] Xu G, Zhong K, Yang Y, Zhang J-M and Huang Z 2019 Insight into delithiation process on the $LiFePO_4$ (010) surface from a novel viewpoint of the work function *Solid State Ion.* **338** 25–30

[752] Zhang Y, Alarco J A, Nerkar J Y, Best A S, Snook G A, Talbot P C and Cowie B C C 2020 Observation of preferential cation doping on the surface of $LiFePO_4$ particles and its effect on properties *ACS Appl. Energy Mater.* **3** 9158–67
[753] Li Y *et al* 2018 Fluid-enhanced surface diffusion controls intraparticle phase transformations *Nat. Mater.* **17** 915–22
[754] Edström K, Gustafsson T and Thomas J O 2004 The cathode-electrolyte interface in the Li-ion battery *Electrochim. Acta* **50** 397–403
[755] Bhandari A, Bhattacharya J and Pala R G S 2020 Adsorption preference of HF over ethylene carbonate leads to dominant presence of fluoride products in $LiFePO_4$ cathode–electrolyte interface in Li-ion batteries *J. Phys. Chem.* C **124** 9170–7
[756] Tebbe J L, Fuerst T F and Musgrave C B 2015 Mechanism of hydrofluoric acid formation in ethylene carbonate electrolytes with fluorine salt additives *J. Power Sources* **297** 427–35
[757] Tebbe J L, Holder A M and Musgrave C B 2015 Mechanisms of $LiCoO_2$ cathode degradation by reaction with HF and protection by thin oxide coatings *ACS Appl. Mater. Interfaces* **7** 24265–78
[758] Bhandari A, Gupta P K, Bhattacharya J and Pala R G S 2019 Higher energy barrier for interfacial Li-ion transfer from EC/$LiPF_6$ electrolyte into (010) $LiFePO_4$ cathode surface than bulk Li-ion diffusion within both cathode and electrolyte *J. Electrochem. Soc.* **166** A2966–72
[759] Tebbe J L, Fuerst T F and Musgrave C B 2016 Degradation of ethylene carbonate electrolytes of lithium ion batteries via ring opening activated by $LiCoO_2$ cathode surfaces and electrolyte species *ACS Appl. Mater. Interfaces* **8** 26664–74
[760] Xu S, Luo G, Jacobs R, Fang S, Mahanthappa M K, Hamers R J and Morgan D 2017 *Ab initio* modeling of electrolyte molecule ethylene carbonate decomposition reaction on Li(Ni,Mn,Co)O_2 cathode surface *ACS Appl. Mater. Interfaces* **9** 20545–53
[761] Malmgren S, Rensmo H, Gustafsson T, Gorgoi M and Edström K 2010 Non-destructive depth profiling of the solid electrolyte interphase on $LiFePO_4$ and graphite electrodes *ECS Trans.* **25** 201–10
[762] Dathar G K P, Sheppard D, Stevenson K J and Henkelman G 2011 Calculations of Li-ion diffusion in olivine phosphates *Chem. Mater.* **23** 4032–7
[763] Li W, Erickson E M and Manthiram A 2020 High-nickel layered oxide cathodes for lithium-based automotive batteries *Nat. Energy* **5** 26–34
[764] Li W, Dolocan A, Oh P, Celio H, Park S, Cho J and Manthiram A 2017 Dynamic behaviour of interphases and its implication on high-energy-density cathode materials in lithium-ion batteries *Nat. Commun.* **8** 14589
[765] Li W, Liu X, Celio H, Smith P, Dolocan A, Chi M and Manthiram A 2018 Mn versus Al in layered oxide cathodes in lithium-ion batteries: a comprehensive evaluation on long-term cyclability *Adv. Energy Mater.* **8** 1703154
[766] Middlemiss L A, Rennie A J R, Sayers R and West A R 2020 Characterisation of batteries by electrochemical impedance spectroscopy *Energy Rep.* **6** 232–41
[767] Li J, Murphy E, Winnick J and Kohl P A 2001 Studies on the cycle life of commercial lithium ion batteries during rapid charge–discharge cycling *J. Power Sources* **102** 294–301
[768] Song J Y, Lee H H, Wang Y Y and Wan C C 2002 Two-and three-electrode impedance spectroscopy of lithium-ion batteries *J. Power Sources* **111** 255–67
[769] McTurk E, Birkl C R, Roberts M R, Howey D A and Bruce P G 2015 Minimally invasive insertion of reference electrodes into commercial lithium-ion pouch cells *ECS Electrochem. Lett.* **4** A145–7
[770] Belt J R, Bernardi D M and Utgikar V 2014 Development and use of a lithium-metal reference electrode in aging studies of lithium-ion batteries *J. Electrochem. Soc.* **161** A1116–26
[771] Li J and Manthiram A 2019 A comprehensive analysis of the interphasial and structural evolution over long-term cycling of ultrahigh-nickel cathodes in lithium-ion batteries *Adv. Energy Mater.* **9** 1902731
[772] Kim J-S, Johnson C S, Vaughey J T, Thackeray M M, Hackney S A, Yoon W and Grey C P 2004 Electrochemical and structural properties of $x\mathrm{Li_2}\mathbf{M}'\mathrm{O_3} \cdot (1-x)\mathrm{LiMn_{0.5}Ni_{0.5}O_2}$ electrodes for lithium batteries ($\mathbf{M}'$= Ti, Mn, Zr; $0 \leqslant x \leqslant 0.3$) *Chem. Mater.* **16** 1996–2006
[773] Robert Armstrong A, Holzapfel M, Novák P, Johnson C S, Kang S-H, Thackeray M M and Bruce P G 2006 Demonstrating oxygen loss and associated structural reorganization in the lithium battery cathode Li $[\mathrm{Ni_{0.2}Li_{0.2}Mn_{0.6}}]\mathrm{O_2}$ *J. Am. Chem. Soc.* **128** 8694–8
[774] Bhandari A and Bhattacharya J 2016 Review—manganese dissolution from spinel cathode: few unanswered questions *J. Electrochem. Soc.* **164** A106–27
[775] Nakayama K, Ishikawa R, Kobayashi S, Shibata N and Ikuhara Y 2020 Dislocation and oxygen-release driven delithiation in Li_2MnO_3 *Nat. Commun.* **11** 4452
[776] Deringer V L, Caro M A and Csányi G 2019 Machine learning interatomic potentials as emerging tools for materials science *Adv. Mater.* **31** 1902765
[777] Assat G, Glazier S L, Delacourt C and Tarascon J-M 2019 Probing the thermal effects of voltage hysteresis in anionic redox-based lithium-rich cathodes using isothermal calorimetry *Nat. Energy* **4** 647–56
[778] Grimsmann F, Brauchle F, Gerbert T, Gruhle A, Knipper M and Parisi J 2017 Hysteresis and current dependence of the thickness change of lithium-ion cells with graphite anode *J. Energy Storage* **12** 132–7
[779] Zheng T, McKinnon W R and Dahn J R 1996 Hysteresis during lithium insertion in hydrogen-containing carbons *J. Electrochem. Soc.* **143** 2137–45
[780] Edge J S *et al* 2021 Lithium ion battery degradation: what you need to know *Phys. Chem. Chem. Phys.* **23** 8200–21
[781] Birkl C R, Roberts M R, McTurk E, Bruce P G and Howey D A 2017 Degradation diagnostics for lithium ion cells *J. Power Sources* **341** 373–86
[782] Zúlke A, Li Y, Keil P, Burrell R, Belaisch S, Nagarathinam M, Mercer M P and Hoster H E 2021 High-energy nickel-cobalt-aluminium oxide (NCA) cells on idle: anode- versus cathode-driven side reactions *Batteries Supercaps* **4** 934–47
[783] Symington A R, Molinari M, Dawson J A, Statham J M, Purton J, Canepa P and Parker S C 2021 Elucidating the nature of grain boundary resistance in lithium lanthanum titanate *J. Mater. Chem.* A **9** 6487–98
[784] Vicent-Luna J M, Ortiz-Roldan J M, Hamad S, Tena-Zaera R, Calero S and Anta J A 2016 Quantum and classical molecular dynamics of ionic liquid electrolytes for Na/Li-based batteries: molecular origins of the conductivity behavior *ChemPhysChem* **17** 2473–81
[785] Choi Y-S, Park J-H, Ahn J-P and Lee J-C 2017 Interfacial reactions in the Li/Si diffusion couples: origin of anisotropic lithiation of crystalline Si in Li–Si batteries *Sci. Rep.* **7** 14028